Design and preparation of degradable organosilica particles for biomedical applications

Pierre Picchetti

To cite this version:

Pierre Picchetti. Design and preparation of degradable organosilica particles for biomedical applications. Biochemistry, Molecular Biology. Université de Strasbourg, 2020. English. NNT : 2020STRAF058 . tel-03641291

HAL Id: tel-03641291
https://theses.hal.science/tel-03641291

Submitted on 14 Apr 2022

UNIVERSITÉ DE STRASBOURG

ÉCOLE DOCTORALE DES SCIENCES CHIMIQUES

Institute de Science et d´Ingénierie Supramoléculaires

THÈSE présentée par :

Pierre PICCHETTI

soutenue le : **30 Octobre 2020**

pour obtenir le grade de : **Docteur de l'université de Strasbourg**

Discipline/ Spécialité : Chimie

Design and Preparation of Degradable Organosilica Particles for Biomedical Applications

THÈSE dirigée par :

Mme DE COLA Luisa	Professeur, Université de Strasbourg

RAPPORTEURS :

Mr MARTÍNEZ MAÑEZ Ramón	Professeur, Universidad Politécnica de Valencia
Mr BONNEVIOT Laurent	Professeur, Université de Lyon

AUTRES MEMBRES DU JURY :

Mr JOSÈ LUIS Capelo Martínez	Ass. Prof, Universidade NOVA de Lisboa
Mr LODEIRO ESPIÑO Carlos	Ass. Prof, Universidade NOVA de Lisboa

Table of contents

Résumé de la thèse

Chapitre 1 : Introduction

L'émergence des nanotechnologies dans les années 80 a non seulement changé notre perception de la matière à petite échelle, mais a également contribué à des nouvelles découvertes dans presque tous les domaines scientifiques. En appliquant les outils et les connaissances issus des avancées nanotechnologiques à la médecine pour la détection, la prévention et le traitement des maladies, ces deux sciences ont convergé et créé la nanomédecine. Des matériaux à l'échelle nanométrique ont été étudiés pour obtenir des thérapies supérieures contre les maladies. Les objets à l'échelle nanométrique (c'est-à-dire les nanoparticules) possèdent au moins une de leurs dimensions extérieures dans la gamme de 1 à 100 nm[1,2] et présentent des propriétés physico-chimiques caractéristiques qui ne sont pas observées dans le matériaux de base. Des nombreux auteurs, en particulier dans le domaine de la nanomédecine, étendent souvent le terme "nanomatériau" pour inclure les particules de plus de 100 nm (jusqu'à 1 µm), tant que de nouveaux effets biologiques ou physico-chimiques sont observés qui ne sont pas autrement obtenus avec le matériau brut.[3] Le changement des propriétés physico-chimiques des nanoparticules dans ce régime de taille peut conduire au développement de nouveaux agents d'imagerie et de systèmes d'administration de médicaments, qui peuvent en principe, surpasser les thérapies actuelles en termes d'efficacité et de rendement. Depuis l'approbation en 1995 par la FDA (U.S. Food and Drug Administration) du premier Doxil®, plus de 50 nouveaux nanomédicaments ont été mis à la disposition des cliniques. En 2019, ONPATTRO® est devenu le premier nanothérapeutique à base de siRNA/RNAi utilisé en clinique, ce qui démontre une fois de plus l'importance des nanotechnologies pour l'avenir de la médecine.[4,5] Bien que la nanomédecine soit un domaine de recherche encore relativement jeune, elle a déjà prouvé qu'elle contribuait au développement de nouveaux médicaments.Grâce à cette recherche, on obtient de nouvelles connaissances sur la manière dont les nanomatériaux sont produits, modifiés et interagissent dans un environnement biologique. Ce sont des connaissances pertinentes non seulement pour la nanomédecine, mais aussi pour d'autres branches de la science. Malgré leur succès évident, les formulations de médicaments liposomiques souffrent de plusieurs propriétés sous-optimales, telles que la stabilité à court terme, la libération prématurée du médicament ou le ciblage limité; tous ces aspects sont cruciaux pour améliorer les propriétés pharmacocinétiques optimales globales des thérapies basées sur les liposomes.[6–9] La recherche sur les nanomatériaux alternatifs pour les applications biomédicales peut non seulement améliorer les thérapies actuelles basées sur les nanomédicaments liposomiques, mais promet aussi d'améliorer l'efficacité de médicaments auparavant inadaptés, permettant ainsi la renaissance de molécules thérapeutiques abandonnées. Le taux de réussite des petites molécules atteignant les normes de la FDA pour les essais cliniques de phase I est de 9 % et cette faible valeur est principalement liée au manque d'efficacité et à la faible sécurité clinique observés.[10] L'encapsulation de ces petites molécules dans une particule porteuse de la taille du nanomètre pourrait aider à acheminer la cargaison spécifiquement vers le site malade, ce qui améliorerait considérablement l'efficacité du médicament tout en réduisant les effets secondaires indésirables. Outre les applications d'administration de médicaments, les nanoparticules sont très intéressantes pour les techniques de bio-imagerie. Par exemple, l'encapsulation de colorants fluorescents à l'intérieur de nanoparticules entraîne une amélioration de leur durée de vie en circulation, de leur stabilité chimique et de leurs propriétés photophysiques, rendant les fluorophores de pointe encore plus efficaces pour les applications d'imagerie. Des agents de contraste supérieurs peuvent être obtenus simplement par la nature même de la nanoparticule, comme cela a été démontré avec succès avec des matériaux magnétiques adaptés aux techniques d'imagerie par résonance magnétique ou par des points quantiques dans les techniques d'imagerie optique déclenchées par l'infrarouge proche.[11] Grâce à une conception intelligente des nanoparticules, il est possible de combiner l'imagerie multimodale et les propriétés d'administration de médicaments, créant ainsi des particules pour une utilisation en théranostique.

Bien que les particules de silice mésoporeuse (MSP) aient déjà fait l'objet de recherches pour des applications biomédicales,[12] les thérapies basées sur les MSP n'ont pas encore fait la transition vers des applications cliniques. La raison principale en est la faible clairance des particules observée chez les organismes vivants après injection intraveineuse, qui ne répond pas aux exigences de dégradabilité totale fixées par la FDA.[13] Bien que les MSP se dégradent en milieu aqueux en raison de l'hydrolyse de la structure de silice amorphe en fonction de la taille, de la porosité, de la procédure de préparation (comme la valeur du pH pour la préparation et la présence de co-solvants) et des fonctionnalités de surface supplémentaires des particules, la dissolution complète n'est pas obtenue et la plupart du temps la dissolution reste lente.[14] Le développement de particules organosiliciques mésoporeuses (MON), avec un groupe de pontage organique cassable dans leur structure, possède un grand potentiel pour surmonter le problème de dégradation et d'élimination des nanocarriers à base de silice. L'introduction de groupes de pontage réagissant aux stimuli dans le cadre des MON permet de régler avec précision la dégradation et la libération de la charge utile.[15] La présence d'un déclencheur externe devrait faciliter la désintégration des particules, permettant une libération contrôlée de la charge utile sur une période définie, essentielle pour le développement de nouveaux systèmes d'administration de médicaments pour un traitement optimisé des maladies. Une meilleure dégradation entraîne une meilleure élimination des matières des organismes vivants, ce qui permet de développer des vecteurs de médicaments plus sûrs.

Les travaux présentés dans cette thèse portent sur la conception et la préparation de particules organosiliciques poreuses et sensibles aux stimuli pour des applications d'administration de médicaments. L'accent a été mis sur la possibilité d'utiliser la lumière UV pour déclencher la dégradation des particules organosiliciques mésoporeuses, où la lumière UV est un bon stimulant dans les systèmes d'administration de médicaments pour l'administration topique. L'absorption de la lumière UV nocive, tout en permettant l'administration de molécules bioactives hydrophobes, telles que la provitamine D_3, était le principal objectif visé en ce qui concerne le développement de particules organosiliciques mésoporeuses dégradables par la lumière. Des carences physiopathologiques en vitamine D_3 sont souvent observées chez les personnes souffrant de dysfonctionnements hépatiques, rénaux ou thyroïdiens, et la distribution de provitamine D_3 par des applications topiques, dans lesquelles la formation active de la vitamine D_3 peut se produire sur place, est intéressante.[16] En outre, les maladies de la peau telles que le mélanome ou les inflammations peuvent être traitées avec des nanoparticules chargées de médicaments, permettant une pénétration plus profonde à travers la peau (comme les canaux des follicules pileux).[17] Comme la lumière UV pénètre dans les parties supérieures de la peau (épiderme et derme), les particules organosiliciques dégradables par la lumière UV peuvent servir de systèmes de libération prolongée de médicaments hydrophobes photosensibles.

D'autres travaux présentés dans cette thèse sont axés sur l'étude de l'utilisation de nouvelles particules organosiliciques de 20 nm de taille semblables à des cages comme vecteurs de médicaments pour l'administration intraveineuse. Ces particules n'ont pas été décrites auparavant dans la littérature, les propriétés physico-chimiques et le comportement biologique in vitro et in vivo de la matière ont donc été étudiés. Une attention particulière a été accordée à la caractérisation physique du matériau, comme sa morphologie, ses capacités de charge des médicaments hydrophiles ou hydrophobes et la fonctionnalisation de sa surface avec de petits peptides. Des recherches ont été menées afin de comprendre comment la taille, la morphologie et la fonctionnalisation affectent la biodistribution in vivo chez les souris saines. Les avantages et les obstacles de l'utilisation de particules organosilicielles de petite taille, semblables à des cages, sont en cours d'évaluation.

Enfin, la possibilité d'introduire des oligonucléotides d'ADN ou d'ANP dans les particules de silice a été étudiée, en vue de développer de nouveaux matériaux hybrides et biocompatibles capables de reconnaître et de réagir à la présence de biomarqueurs spécifiques dans les organismes vivants. L'accent a été mis sur la synthèse de nouveaux dérivés d'alcoxysilane d'ADN et d'ANP et leur utilisation pour la préparation de particules d'organosilice par différentes méthodologies. Outre les stratégies de modélisation douce dans lesquelles les alcoxysilanes d'ADN/ANP sont hydrolysés et co-condensés à côté d'une source de silice commune afin de préparer des particules d'organosilice, une méthode directe, guidée par l'interaction d'oligonucléotides complémentaires, a été étudiée pour la préparation de particules hybrides. Une attention supplémentaire a été portée sur le comportement de réponse aux stimuli résultant de la présence d'oligonucléotides d'ADN ou de PNA dans le cadre de la silice.

Chapitre 2: Particules organosiliciques mésoporeuses cassables par la lumière

Les particules organosiliciques mésoporeuses représentent de futurs vecteurs de médicaments très attrayants, en raison de leur non-toxicité générale et de leurs propriétés physico-chimiques facilement réglables, telles que leur taille, leur forme, leur porosité et leur dégradabilité. L'intégration d'un groupe fonctionnel organique dans la structure des particules permet de préparer des particules organosiliciques poreuses cassables. Diverses sources de stimulation, telles que des agents réducteurs,[18–20] des changements de pH[21,22] ou une activité enzymatique,[23,24] peuvent être utilisées. La lumière représente un stimulus intéressant en raison de sa nature non invasive et de son contrôle spatio-temporel simple. Parmi les matériaux dégradables par la lumière signalés précédemment, on trouve les hydrogels,[25,26] les polymères,[27] les systèmes micellaires[28] et les cristaux colloïdaux.[29] Plusieurs nanoparticules à base de silice photosensible ont été précédemment rapportés et comprennent des colloïdes photosensibles[30] et des particules de silice mésoporeuses à grille, [31,32] ainsi que des supports de médicaments photocopiés à base de silice.[33] En revanche, des particules organosiliciques mésoporeuses qui se brisent lors de l'irradiation lumineuse n'ont jamais été rapportées. Nous avons conçu un nouveau bis-alcoxysilane, portant un groupe nitrobenzyle photolabile, à utiliser comme fraction organique de pontage dans la préparation de particules organosiliciques mésoporeuses cassables par la lumière (**LB-MSPs**). La fraction photolabile utilisée dans ce travail est un groupe 2-nitrobenzyle éther, qui est connu pour subir une réaction Norrish de type II lors de l'irradiation par la lumière UV qui conduit à son clivage[34,35]. Afin d'intégrer par covalence un groupe fonctionnel organique photolabile dans des particules organosiliciques mésoporeuses, un bis-alcoxysilane hydrolysable, portant le groupe 2-nitrobenzyle, a été synthétisé. Ce bis-alcoxysilane **1** photolabile a été préparé (Figure 1a) et sa dégradation déclenchée par la lumière lors de l'irradiation aux UV a été caractérisée avec succès par spectroscopie d'absorption UV-Vis (Figures 1b et c) et par spectroscopie RMN ^{1}H. La formation du produit de photodégradation **3** a été confirmée par la comparaison de ses spectres UV-Vis caractéristiques avec les résultats rapportés dans la littérature[34] et des calculs de théorie fonctionnelle de densité dépendante du temps (TD-DFT) en utilisant la suite de calculs Gaussian09®. De l´actinométrie sur le composé **1** a montré que la réaction de photodégradation se produit avec des rendements quantiques de réaction de 30 %.

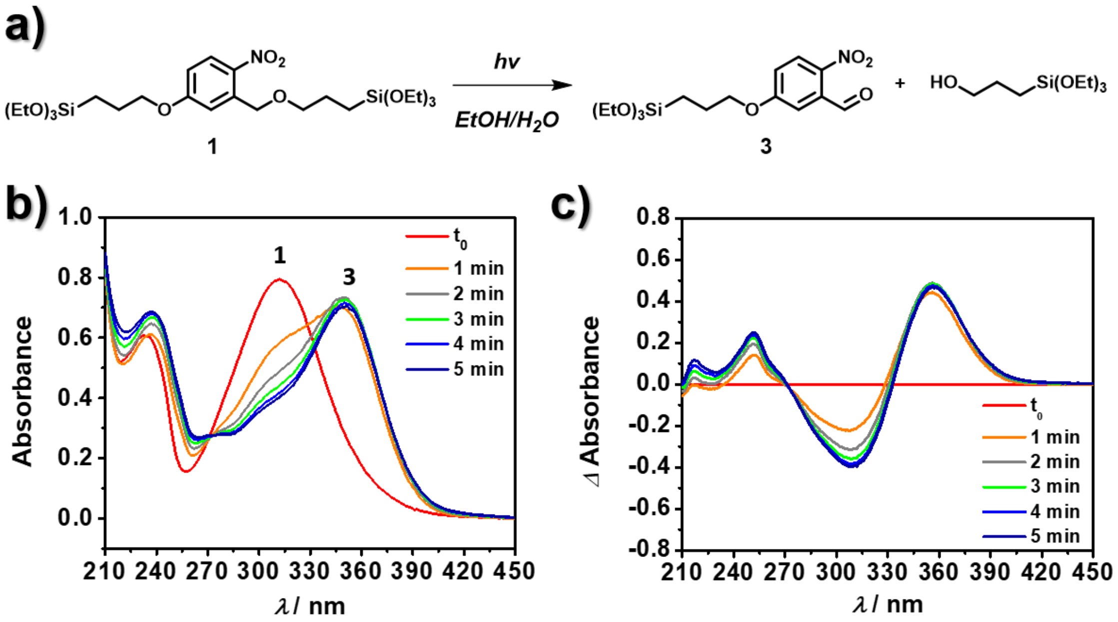

Figure 1. a) Réaction de photodégradation Norrish de type II de **1** induite par l'irradiation par la lumière UV. b) Evolution des spectres d'absorption UV-Vis par l'irradiation par la lumière UV de **1** (0,11mM dans EtOH/H_2O 1:1 *v*/*v*). c) Différence des spectres d'absorption signalés pour visualiser l'évolution spectrale.

Le composé **1** a été utilisé pour préparer les **LB-MSPs** via le protocole de synthèse Stöber modifié.[36] Des **LB-MSPs** sphériques d'un diamètre moyen de 303 ± 34 nm ont été obtenues. L'intégration covalente réussie du lieur dégradable par la lumière dans les particules a été confirmée par analyse thermogravimétrique, par spectroscopie photoélectronique des rayons X et par spectroscopie d'absorption UV-Vis. La dégradation réussie de la particule sous irradiation UV a été prouvée par microscopie électronique (Figure 2), spectroscopie d'absorption UV-Vis et porosimétrie. Aucune dégradation des **LB-MSPs** n'a été observée en l'absence d'irradiation lumineuse, comme le confirment les images de microscopie électronique et la spectroscopie d'absorption UV-Vis.

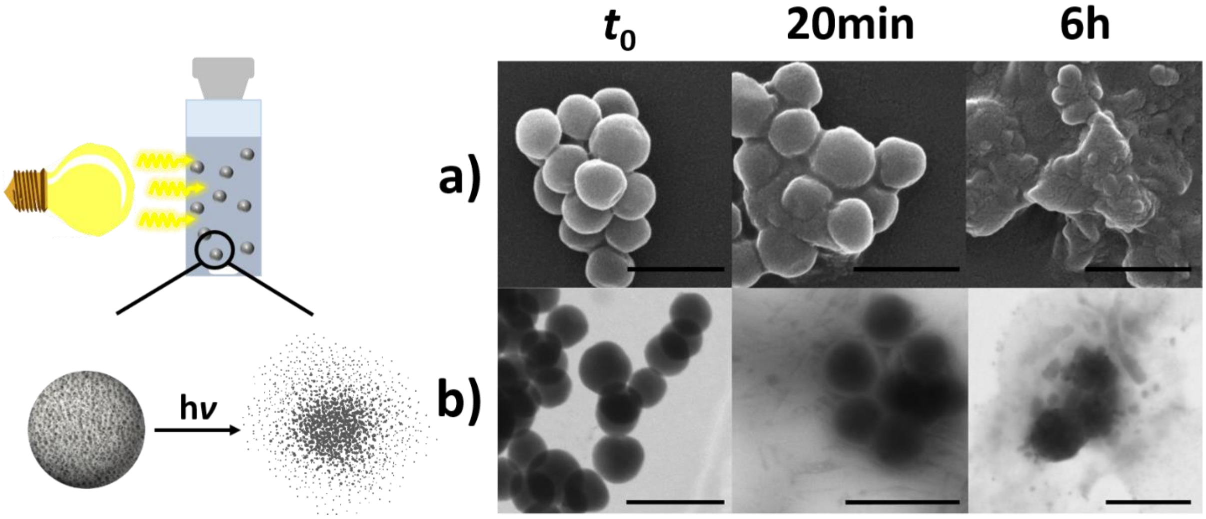

Figure 2. Dégradation des **LB-MSP** déclenchée par la lumière. a) images MEB et b) images STEM des **LB-MSP** à t_0 et après 20 min et 6 h d'irradiation par la lumière UV à 327 nm, barres d'échelle = 500 nm.

Enfin, la possibilité de charger les particules avec des molécules bioactives a été explorée. Du 7-déhydrocholestérol (**7-DH**), un précurseur naturel de la vitamine D3, a été chargée dans des **LB-MSPs** poreuses (charge de **7-DH**=23 % en poids). Sa libération déclenchée par la lumière, due à la dégradation de la particule, a été prouvée avec succès par spectroscopie d'absorption UV-Vis. Comme le montre la Figure 3, une libération accrue de **7-DH** par les **LB-MSPs** a pu être observée lors de l'irradiation aux UV, ce qui peut s'expliquer par la progression de la dégradation des **LB-MSPs** et donc par la libération du médicament. En l'absence de lumière, seule une faible quantité de **7-DH** a été libérée, très probablement en raison de la diffusion passive de la molécule chargée dans les pores ou physioadsorbée à la surface de la particule.

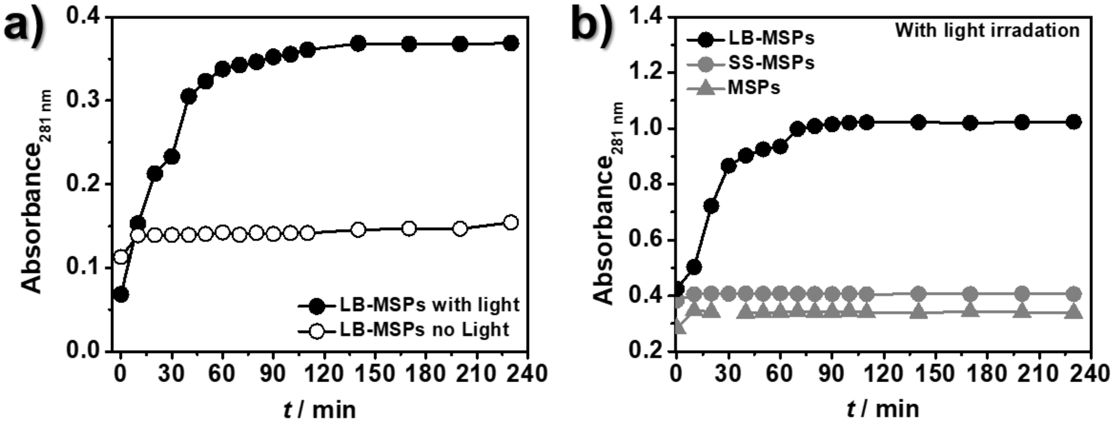

Figure 3. a) Libération de **7-DH** contrôlée à 281 nm des **LB-MSPs** avec et sans irradiation lumineuse à λ_{irr}=327 nm. b) Libération de **7-DH** des **LB-MSPs** comparée à celle des SS-MSPs et des MSPs vierges sous irradiation lumineuse à λ_{irr}=327 nm.

Dans ce travail, la préparation et la caractérisation d'un nouveau bis-alcoxysilane clivable à la lumière et son utilisation pour la préparation de particules organosiliciques mésoporeuses sphériques qui se dégradent lors de l'exposition à la lumière ont été présentées. Des tests préliminaires de cytotoxicité ont en outre montré que les particules et leurs produits de photodégradation ne provoquent pas de cytotoxicité grave à l'égard des cellules HeLa, ce qui indique une bonne cytocompatibilité de ce matériau. Dans les travaux futurs, la capacité des **LB-MSPs** à servir de systèmes d'administration de médicaments pour des applications topiques sera d'un grand intérêt, car les particules assurent une protection contre la lumière UV, en absorbant les rayonnements nocifs tout en libérant simultanément une molécule bioactive, utilisée pour des applications thérapeutiques.

Chapitre 3: Cages organosiliciques biodégradables comme nouveaux nanocarriers pour les applications biomédicales

En ce qui concerne les particules poreuses de silice et d'organosilice, beaucoup d'efforts ont été déployés pour réduire la taille de la particule finale par des voies de formation dirigées par les tensioactifs, tout en maintenant une bonne homogénéité de la distribution des tailles. [37–39] Très récemment, Wiesner et ses collaborateurs ont signalé la préparation de particules de silice inorganiques en cage de moins de 20 nm, très symétriques, qui n'avaient jamais été observées auparavant pour les particules de silice poreuse.[40] Ces particules, qui possèdent une morphologie et une taille uniques, pourraient offrir de nouvelles possibilités pour le développement de systèmes de distribution de médicaments à base de silice. Inspirés par ces derniers travaux, nous avons envisagé la préparation de particules organosiliciques en forme de cage de 20 nm, portant des ponts disulfure biodégradables dans le cadre de la silice, qui, à notre connaissance, n'ont pas encore été décrits dans la littérature. La condensation d'un disulfure contenant du bis-alcoxysilane avec une source de silice commune et en présence du tensioactif CTAB a permis la préparation de cages organosiliceuses à ponts disulfure (**OSCs**). Comme le montre la Figure 4a, bien que la dispersion finale des **OSCs** obtenue après purification ait été très concentrée (c=3 mg·mL^{-1}), un colloïde transparent et stable a été obtenu. Une analyse par diffusion dynamique de la lumière (DLS) a révélé que le diamètre hydrodynamique moyen de la particule était de 23 nm (figure 4d). Ces particules ont ensuite été entièrement caractérisées à l'aide de techniques standards pour les matériaux poreux, telles que la spectroscopie photoélectronique à rayons X, l'analyse thermogravimétrique, la mesure de l'adsorption de N_2, la spectroscopie d'absorption UV-Vis et la spectroscopie de fluorescence. La structure en cage a été prouvée par la reconstruction 3D d'images de particules TEM individuelles à l'aide du programme d'élucidation de structure Relion® (Figure 4c).[41]

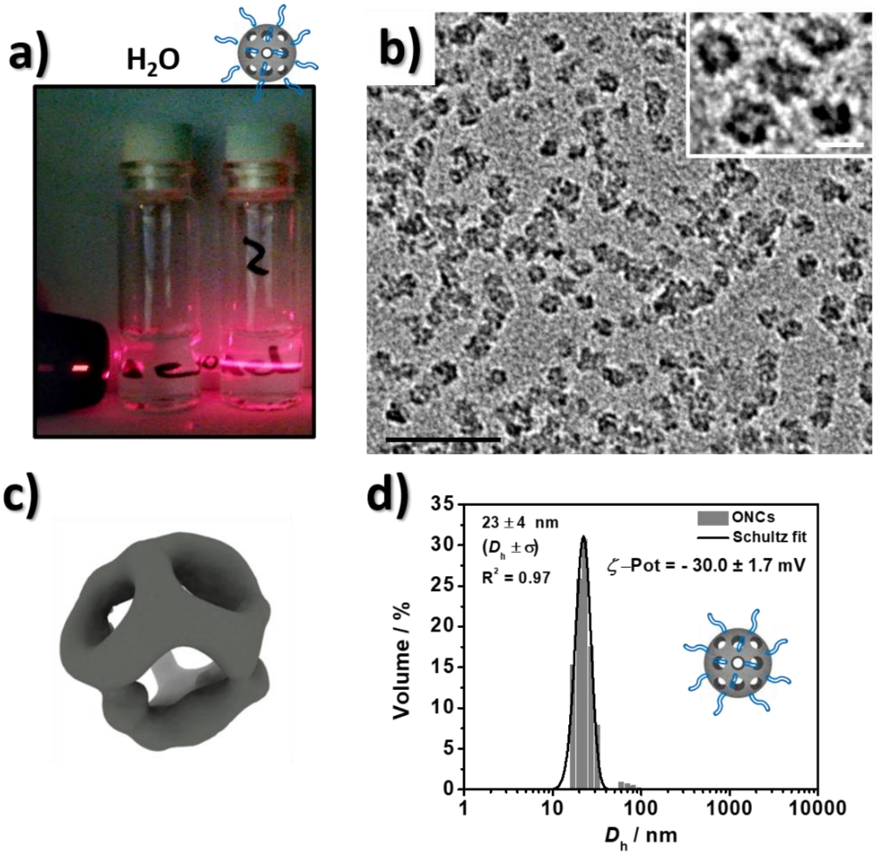

Figure 4. a) Images de la dispersion colloïdale des **OSCs** (Fiole 2). Lorsque les particules sont irradiées par une lumière laser, l'effet Tyndall peut être observé. b) Images TEM de **OSCs** (barre d'échelle=100 nm) et encart montrant une image TEM de **OSCs** à un grossissement plus élevé (barre d'échelle=20 nm). b) Modèle 3D obtenu à partir de la reconstruction des images TEM de **OSCs**, en utilisant Relion®. d) Diamètre hydrodynamique et ζ-potentiel de **OSCs**.

L'intégration des groupes fonctionnels disulfure dans le cadre de la silice rend les **OSCs** dégradables en présence de thiolates en raison des réactions d'échange thiol/disulfure qui se produisent.[42] Le glutathion (GSH), un tripeptide endogène contenant un thiol, est l'un des principaux médiateurs de l'homéostasie redox cellulaire et est capable de réduire le pont disulfure au sein des **OSCs**. Il est connu pour être présent en concentrations relativement élevées dans l'espace intracellulaire (1-10 mM). Comme le montre la Figure 5, une dégradation rapide des particules a été observée sur les images TEM (Figure 5b), comme l'indique la formation de débris plus petits lorsque le glutathion est présent dans la dispersion de la particule. La dégradation relativement rapide qui s'est produite au cours des 2 premières heures peut probablement s'expliquer par la petite taille des particules et la structure en cage des **OSCs**, qui offre une grande surface et une diffusion facile du GSH. Les **OSCs** ont été chargées avec le colorant hydrophile HOECHST 33258 (HE) et sa libération en présence de GSH par spectroscopie de fluorescence a été utilisée pour mettre en évidence la dégradation des particules, confirmant ainsi la capacité des **OSCs** à servir de vecteurs de médicaments sensibles aux stimuli.

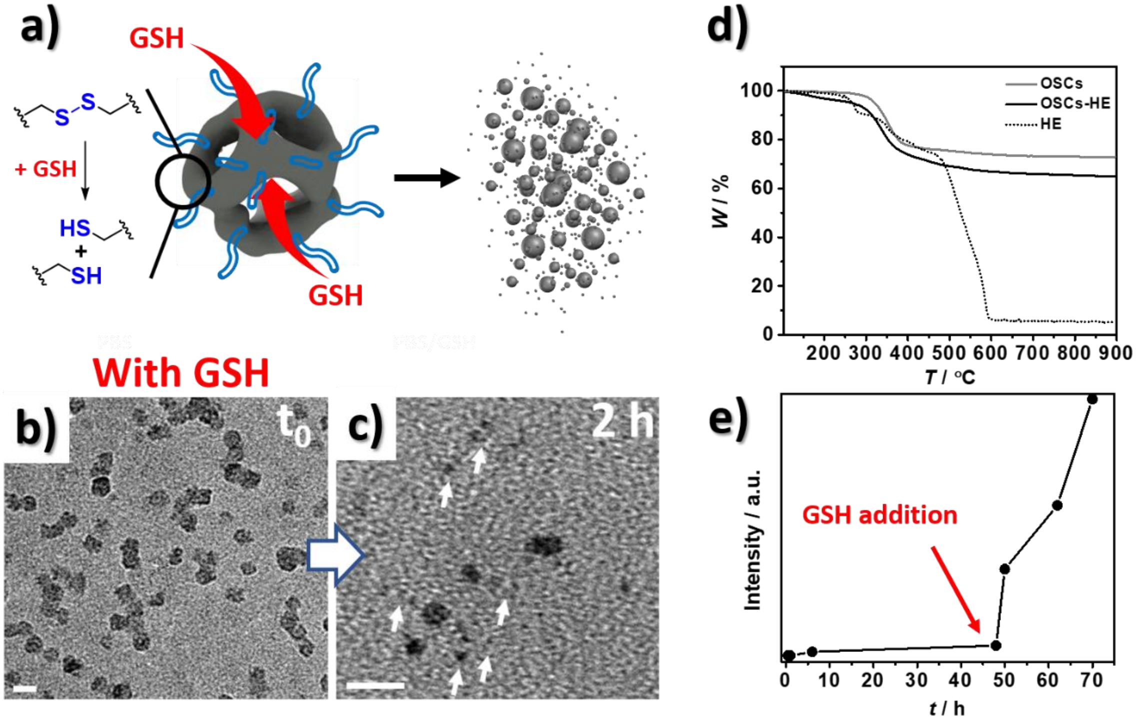

Figure 5. a) Représentation schématique de la dégradation des **OSCs** en présence de l'agent réducteur glutathion (GSH). Dans des conditions physiologiques, le GSH est capable de réduire les ponts disulfure de la particule, ce qui entraîne leur rupture. b) Images TEM des **OSCs** (c=0,1 mg·mL^{-1}) à t_0 et c) après 2 h, lorsqu'ils sont incubés dans du PBS à 37 °C, avec et en l'absence de GSH (10 mM). Toutes les barres d'échelle=20 nm. d) Thermogrammes enregistrés sur les **OSCs**, les **OSCs** chargées de HE (**OSCs-HE**) et HE. e) Expériences de libération de HE enregistrant l'émission de fluorescence (λ_{em}=492 nm, λ_{ex}=350 nm), avant et après l'ajout de GSH.

Après avoir préparé les nanoparticules, la capacité à fonctionnaliser davantage les **OSCs** par des techniques de greffe post-synthèse avec des molécules biologiquement pertinentes, telles que des sucres et des peptides, a été démontrée. Après avoir observé l'instabilité colloïdale de la particule lors de la modification de la surface des **OSCs**, des procédures de greffe de surface optimisées pour ces particules, visant à conserver la stabilité colloïdale, ont été explorées. La chimie des alcoxysilanes a d'abord été sélectionnée pour fonctionnaliser les **OSCs** avec de la D-(+)-glucosamine (**OSCs-Sucre**) et la réaction de cycloaddition azide-alcyne sans cuivre (SPAAC) a été utilisée pour greffer la surface de la particule avec le tripeptide Arg-Gly-Asp (RGD). La possibilité de fonctionnaliser ces nouveaux types de particules organosiliciques en forme de cage avec une variété de petites molécules bioactives a été démontrée, tout en maintenant leur stabilité colloïdale dans les dispersions aqueuses.

La biodistribution des petites particules organosiliciques en forme de cage est encore inexplorée et une première évaluation de leur comportement in vivo est donc intéressante, puisqu'un comportement de biodistribution distinct selon la taille et la forme des nanomatériaux a été signalé.[43] Les études de biodistribution ont également porté sur des particules fonctionnalisées de glucosamine, car la présence d’une fraction desucre peut augmenter l'absorption cellulaire lors de l'interaction avec les récepteurs de surface des cellules GLUT présents sur la couche endothéliale de la barrière hémato-encéphalique (BHE), ce qui pourrait permettre une meilleure adhérence des particules sur cette barrière biologique. Les premières études de biodistribution des **OSCs** ont été réalisées sur un modèle de souris CD1 en bonne santé. La présence de sCy5 sur les **OSCs** s'est avérée idéale puisque l'imagerie se produit dans la région rouge des spectres électromagnétiques, ce qui diminue le signal d'autofluorescence des corps des souris tout en réduisant davantage l'atténuation induite par l'oxygène. Les résultats obtenus par l'imagerie optique ex vivo des particules dans divers organes sont illustrés dans la Figure 6a. Les signaux fluorescents représentés sont normalisés pour la souris à laquelle seule une solution saline a été administrée (véhicule). Il est intéressant de noter que, dans le foie, l'accumulation entre les **OSCs** et les **OSCs-Sucre** n'a pas montré de différence statistique, ce qui indique que la présence du sucre à la surface de la particule n'a pas affecté la cinétique ou l'absorption hépatique. Plus intéressant encore, l'immunohistologie du foie a indiqué que les **OSCs** et les **OSCs-Sucre** ne s'accumulaient pas dans les macrophages hépatiques (cellules de Kupffer) habituellement impliqués dans l'élimination des nanoparticules du foie. Comme le montrent les Figures 6b et c, aucune colocalisation des particules (rouge) avec les macrophages (vert), qui ont été colorés avec des anticorps CD68 marqués à la fluorescéine, n'a été observée. Cette accumulation différenciée a indiqué la possibilité que les particules soient absorbées par d'autres cellules du foie, très probablement des cellules épithéliales. Ces résultats suggèrent que les particules pourraient servir au développement de vecteurs de médicaments pour le traitement des cancers du foie.

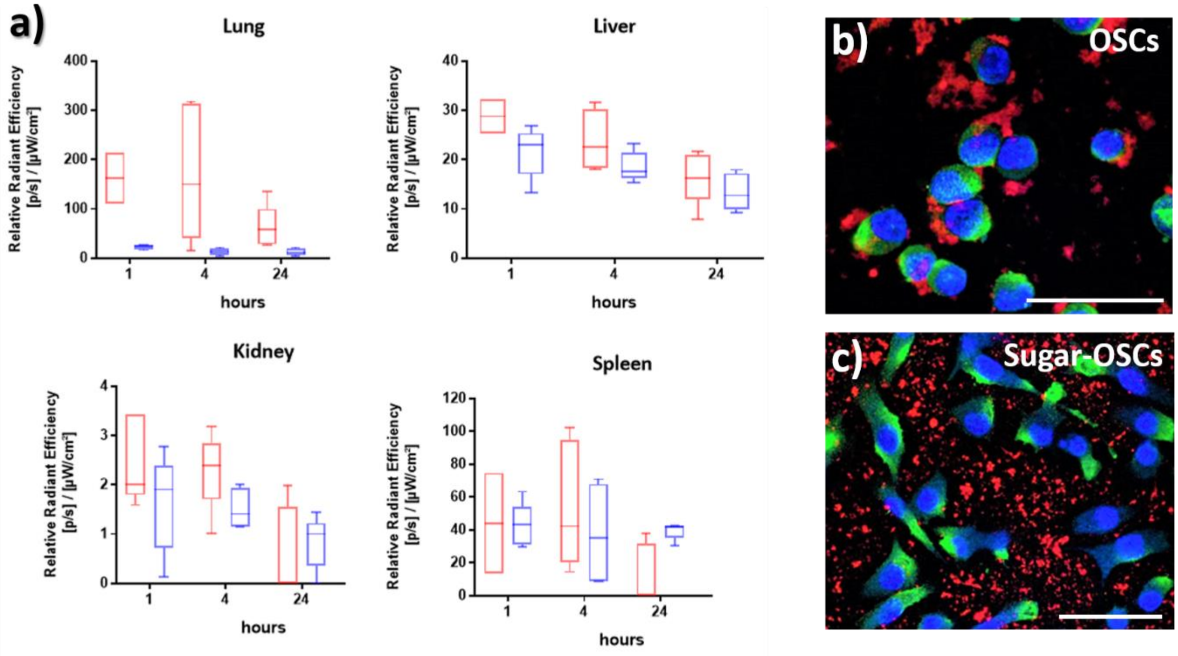

Figure 6. a) Biodistribution ex vivo des **OSCs** (barres rouges) et des **OSCs-Sucre** (barres bleues) à 1h, 4h et 24h. Les efficacités radiantes relatives des **OSCs** et des **OSCs-Sucre** sont indiquées dans le poumon, le foie, le rein et la rate. Efficacité radiante où toutes les valeurs sont normalisées au groupe de véhicules (injection de solution saline)=1. b) et c) Immunohistologie du foie après 4h du traitement par spectroscopie de fluorescence. Bleu : noyau coloré au DAPI, rouge : **OSCs** et **OSCs-Sucre** et vert : cellules de Kupffer. Échelle des barres=50 µm.]

Les signaux fluorescents ex vivo sur les échantillons de cerveau des souris qui ont été traitées avec des CSE, n'ont révélé qu'un signal mineur provenant du cerveau, qui après 24h était comparable aux intensités mesurées pour le véhicule (Figure 7a). En outre, aucune variation statistique significative concernant le signal détecté entre les **OSCs** et les **OSCs-Sucre** n'a été observée. Pour obtenir une information plus quantitative sur la présence des particules dans le cerveau, une spectroscopie d'émission atomique à plasma inductif (ICP-AES) a été effectuée sur les échantillons de cerveau après 4h de traitement. Les résultats de l'ICP-AES obtenus sont illustrés sur la Figure 7b, qui indique qu'un nombre mineur de particules ont pu traverser la BHE, indépendamment de la présence d'une fraction de sucre à la surface des particules. Bien que les expériences in vitro précédemment rapportées utilisant des modèles de BHE aient suggéré un croisement accru de la BHE avec des nanoparticules à fonction sucre, nos expériences ont confirmé que cet effet est négligeable et presque absent dans les modèles in vivo,[44,45] ce qui est en accord avec les résultats récemment publiés par Kataoka et ses collègues. [46,47]

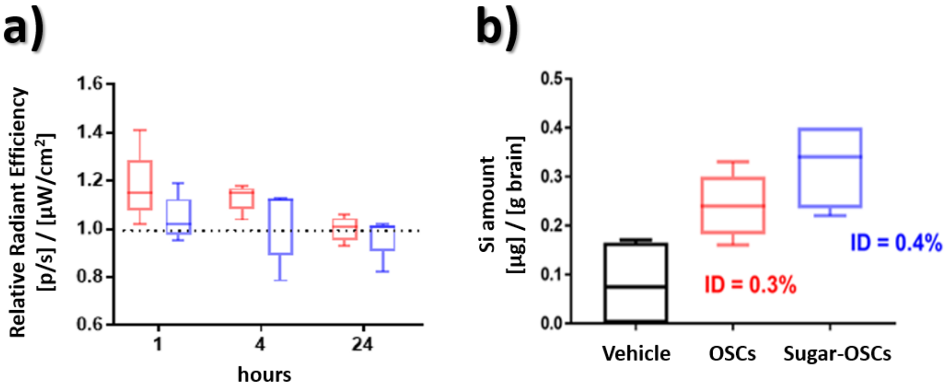

Figure 7. a) Analyse des émissions fluorescentes ex vivo d'échantillons de cerveaux de souris de **OSCs** (barres rouges) et de **OSCs-Sucre** (barres bleues) à 1h, 4h et 24h après le traitement. Efficacité radiante où toutes les valeurs sont normalisées par rapport au groupe du véhicule (injection de solution saline)=1. b) Résultats ICP-AES obtenus à partir d'échantillons de cerveau après 4 h de traitement ; **OSCs** (barres rouges) et **OSCs-Sucre** (barres bleues).

Ce travail a présenté la préparation et la caractérisation de nouvelles particules organosiliciques poreuses en forme de cage. Les particules se sont avérées biodégradables en raison de la présence d'un pont disulfure réductible dans le cadre de la silice, et ont montré des taux de dégradation rapides en raison de leur petite taille et de leur cavité interne très accessible. Il a également été démontré que les particules peuvent être chargées avec des molécules hydrophiles et hydrophobes, ce qui montre la libération déclenchée par des stimuli en présence d'un agent réducteur, tel que le glutathion tripeptide endogène. De plus, des procédures de fonctionnalisation faciles et douces ont été mises en place pour fonctionnaliser les **OSCs**, ce qui prouve la conjugaison covalente réussie des molécules bioactives à la surface de la particule. Des expériences biologiques préliminaires ont indiqué que les particules sont non toxiques et, lors de l'injection intraveineuse chez des souris saines, la bioaccumulation des particules a été étudiée.

Il est intéressant de noter que dans le foie, les **OSCs** ne se sont pas co-localisées avec les macrophages, ce qui rend ces particules intéressantes pour le développement de vecteurs de médicaments contre les cancers du foie.

Chapitre 4: Construire particules organosiliciques avec des oligonucléotides

Particules organosiliciques à pont ADN et PNA

De nombreux groupes fonctionnels organiques différents peuvent être intégrés dans la structure de silice des particules organosiliciques (OSP) par le biais de la chimie sol-gel en utilisant des organo-bisalcoxysilanes, ce qui permet d'ajouter différentes propriétés physico-chimiques.[15] La préparation d'OSP poreuses et sensibles aux stimuli est un vecteur intéressant pour le développement de futures nanomédicaments à sécurité biologique améliorée. Parmi les exemples de molécules inexplorées pour la préparation d'OSP, citons les oligonucléotides à base d'acide désoxyribonucléique simple brin (ssDNA) et d'acide nucléique peptidique simple brin (ssPNA). Ces molécules présentent des groupes fonctionnels organiques intéressants pour la préparation des OSP en raison de leurs propriétés physico-chimiques uniques, telles que la complémentarité programmable des paires de bases et la dégradabilité enzymatique. En outre, grâce à l'utilisation de séquences d'ADN spécifiquement conçues, telles que les aptamères, une variété de petites molécules, de métaux et même de cellules vivantes peuvent être détectées avec une grande sélectivité.[48,49] L'intégration des oligonulcéotides dans un cadre inorganique peut donc conduire à la préparation de matériaux hybrides ayant de fortes propriétés dépendantes des stimuli, allant de la dégradation sensible aux stimuli à la liaison sélective de petites molécules ou même de cellules.

Pour intégrer le groupe de pontage de l'ADN et de l'ANP dans les OSP, des dérivés de bis-alcoxysilane (voir le chapitre 4 de cette thèse) ont été préparés, qui ont ensuite été hydrolysés et co-condensés à côté du tétraéthylorthosilicate (TEOS), source commune de silice, pour former des nanoparticules organosilicielles pontées par l'ADNs ou l'ANPs, marquées respectivement comme ADNs et ANPs (Figure 8).

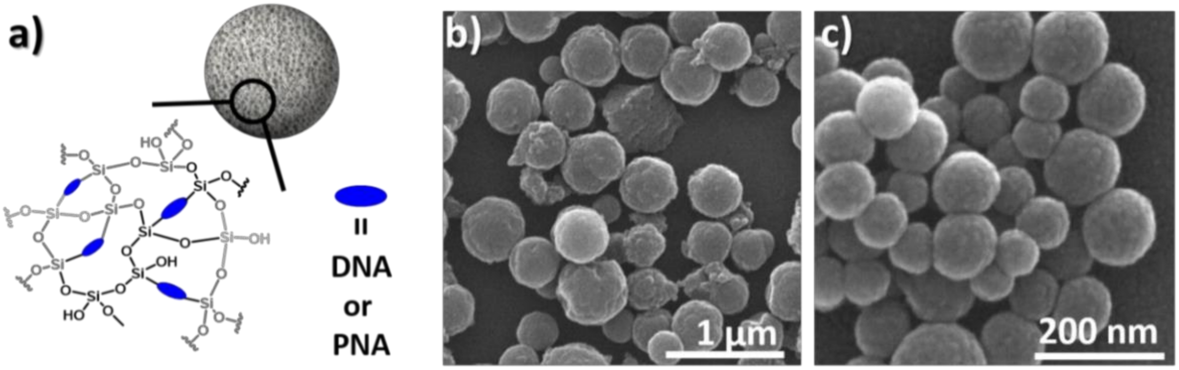

Figure 8. a) Représentation schématique des particules organosiliciques pontées par l'ADN et l'ARN. b) Image MEB de l'ADN **ssDNA-OSPs**. c) Images MEB de l'ANP **ssPNA-OSPs**.

Il a été démontré que les **ssDNA-OSPs** sont dégradables par l'activité enzymatique de la DNase I, une endonucléase qui hydrolyse les liaisons phosphordiester de l'ADN, et la dégradation des particules a été suivie par analyse MEB (Figure 9a) et DLS (Figure 9b).

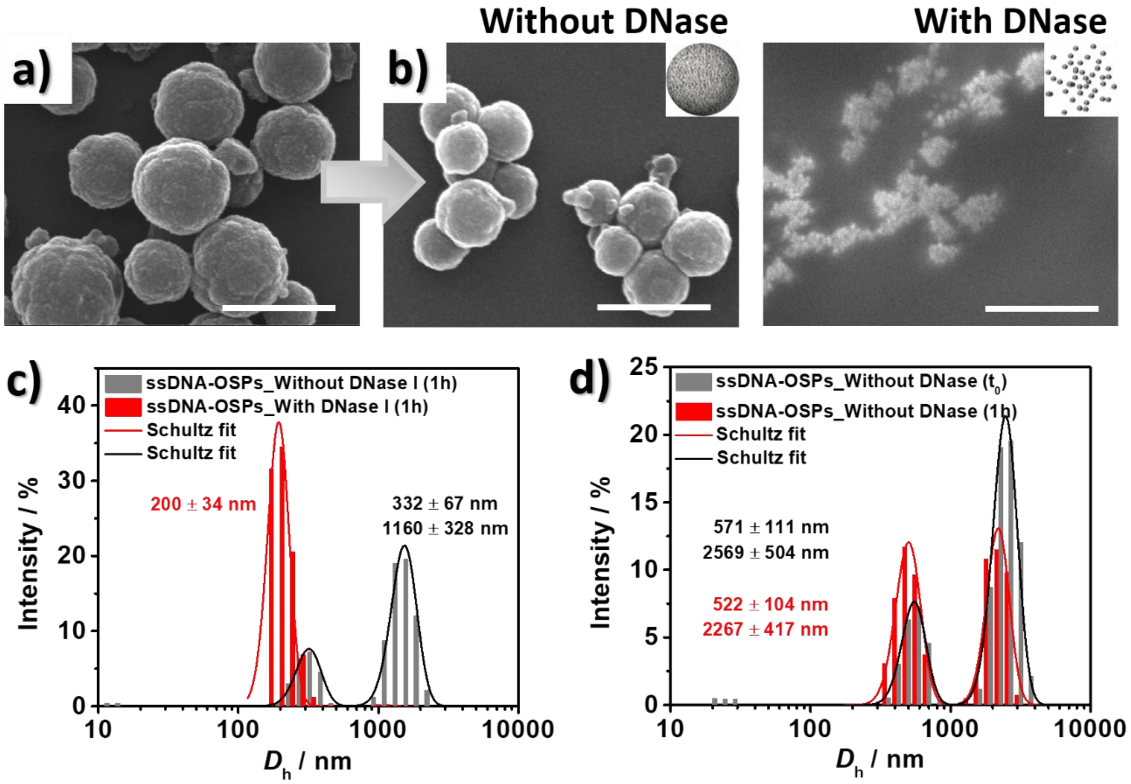

Figure 9. Étude de la dégradation par MEB des **ssDNA-OSPs** en présence ou en absence de DNase I. a) Image MEB des **ssDNA-OSPs** à t_0. b) Images MEB des **ssDNA-OSPs** après 1h sans (image de gauche) ou lorsqu'il est incubé avec la DNase I. c) Mesure DLS sur des **ssDNA-OSPs** qui ont été agités pendant 1h avec et sans la présence de DNase. d) Mesure DLS sur des **ssDNA-OSPs** à t_0 et qui ont été agités pendant 1h en l'absence de DNase.

En outre, il a été démontré que les **ssDNA-OSPs** étaient capables d'hybrider des oligonucléotides d'ADNs complémentaires grâce à des expériences de transfert d'énergie de résonance de Förster (FRET) (Figure 10). Comme le montre la Figure 10a, seuls les brins d'ADN hybridé peuvent transférer l'énergie de l'état excité de l'ADN marqué Cy3 dans les **ssDNA-OSPs** (donneur FRET) au Cy5 marqué d'un brin complémentaire (accepteur FRET), ce qui entraîne l'extinction de Cy3 et l'émission résultante de Cy5. Les expériences FRET ont été réalisées en ajoutant différentes quantités de l´accepteur FRET à des dispersions des **ssDNA-OSPs** (c=0,96 µg·mL^{-1} dans du PBS contenant du Mg^{2+}) tout en surveillant le processus FRET en excitant la partie donneuse à λ_{ex} = 520 nm tout en enregistrant les spectres d'émission du donneur et de l'accepteur. Comme le montre la figure 10c, l'ajout de l´accepteur FRET à la dispersion de particules a entraîné une émission éteinte du donneur en fonction de la concentration, tandis qu'une émission sensibilisée de l'accepteur a été enregistrée, confirmant ainsi la présence du processus FRET due à l'hybridation de l'ADN.

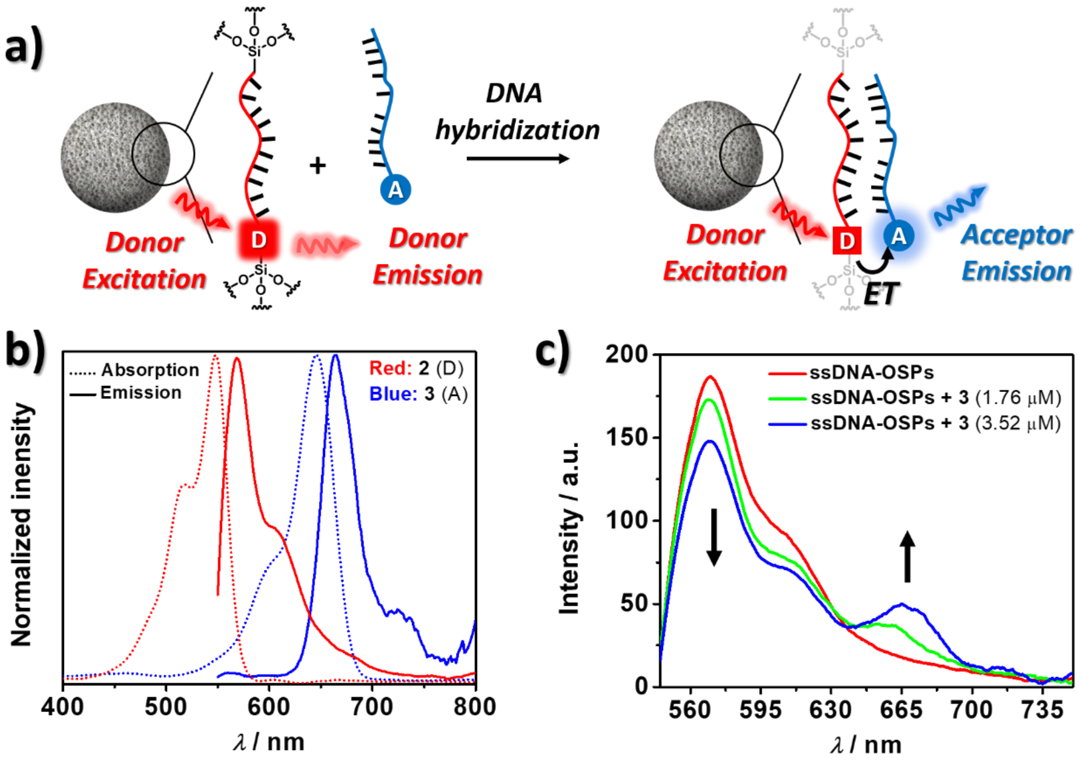

Figure 10. a) Représentation schématique du processus FRET se produisant lors de l'hybridation des brins d'ADN marqués Cy3 (donneur) et Cy5 (accepteur). b) Spectres d'absorption et d'émission normalisés de l'ADN marqué Cy3 et l´accepteur FRET dans le PBS ; λ_{ex} (l'ADN marqué Cy3) = 520 nm et λ_{ex} (accepteur FRET) = 650 nm. c) Expérience FRET avec des **ssDNA-OSPs** (c=0,96 µg·mL^{-1}) et diverses concentrations d'accepteur FRET (1,76 µM et 3,52 µM).

Les images de microscopie électronique des **ssDNA-OSPs** suggèrent que la présence de l'ADN pendant la synthèse des particules altère la voie de formation des particules. La morphologie finale modifiée des **ssDNA-OSPs**, comparée aux MSPs obtenues à partir de la synthèse modèle, pourrait s'expliquer par l'ADN fortement chargé négativement qui interagit fortement avec d'autres espèces chargées, au cours du protocole de synthèse Stöber modifié, tandis que le rôle de la longueur de l'ADN a été confirmé pour influer sur la porosité des particules. Pour préparer des particules organosiliciques pontées par des oligonucléotides avec une distribution de taille uniforme, l'utilisation d'acide nucléique peptidique (ssANP). Les ssANP possèdent les mêmes nucléobases que l'ADN mais le squelette du brin n'est pas composé de groupes phosphodiester mais d'unités N-(2-aminoéthyl)-glycine répétitives non chargées liées par des liaisons peptidiques. Lors de l'hydrolyse et de la co-condensation d'un ANP-bisalcoxysilane, à côté d'une source commune de silice et en présence d'un agent tensioactif, on a obtenu des particules organosiliciques sphériques (**ssPNA-OSPs**) plus petites et dispersées de manière plus homogène (Figure 11).

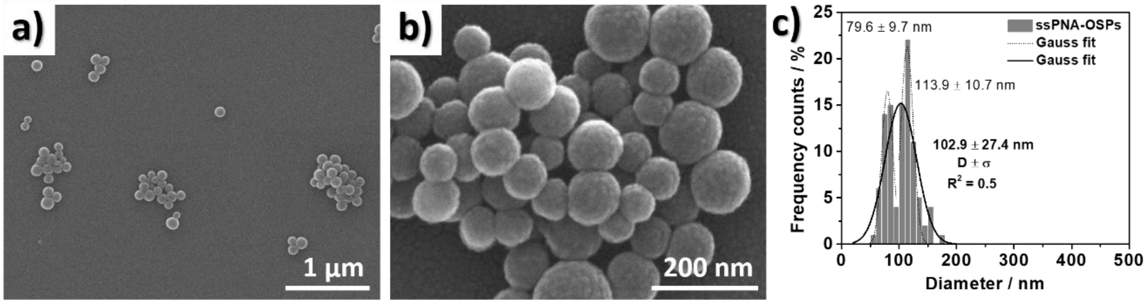

Figure 11. a) et b) Images SEM des **ssPNA-OSPs**. c) Distribution de taille des **ssPNA-OSPs** calculée à partir des images MEB.

Particules organosiliciques à base de PNA préparées en exploitant les interactions supramoléculaires

L'utilisation d'oligonucléotides ssANP complémentaires pour préparer des assemblages supramoléculaires de bis-organoalkocysilanes a été envisagée pour produire des matériaux possédant des propriétés similaires à celles des polymères à liaisons hybrides (HBP).[50] Après avoir évalué la capacité des brins d'ANP à s'auto-assembler, leurs dérivés alcoxysilanes correspondants ont été préparés (voir le chapitre 4 pour plus de détails). Par la suite, les deux brins de dérivés d'alcoxysilane ont été mélangés, ce qui a donné lieu à la formation du bis-alcoxysilane **Supra-PNA-Si** assemblé et à base de ANP (Figure 12a). Le **Supra-PNA-Si** a été utilisé pour la préparation de particules organosiliciques, avec ou sans la présence d'orthosilicate de tétraéthyle (TEOS), source supplémentaire de silice, après son hydrolyse et sa polycondensation catalysées par une base dans un mélange H_2O/EtOH, ce qui a conduit à la formation de particules organosiliciques **Supra-OSPs** (Figure 12b et c).

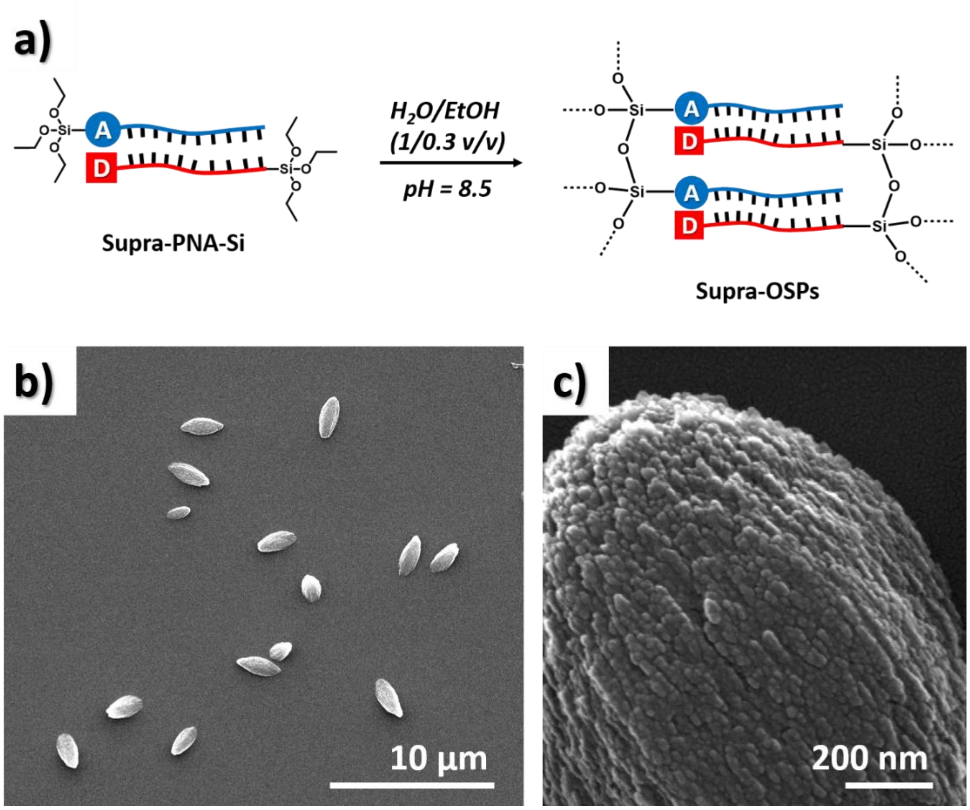

Figure 12. Représentation schématique de l'hydrolyse et de la condensation de **Supra-PNA-Si** pour préparer les **Supra-OSPs**.

En plus de l'analyse spectroscopique UV-Vis et IR, la présence du pont PNA supramoléculaire au sein des **Supra-OSPs** a été étudiée par l'analyse FRET (Figure 13). Une dispersion de particules de **Supra-OSPs** (c=0,008 mg·mL^{-1}) dans du PBS (pH=5,8) a été excitée à 450 nm et la photoluminescence a été enregistrée. Comme le montre la Figure 13c, l'excitation de la fraction du donneur FRET à λ_{ex} = 450 nm (fraction F-PNA) a permis d'éteindre l'émission du donneur ($\lambda_{em,F\text{-}PNA}$ = 517 nm) tandis que l'émission de l'accepteur FRET (fraction T-PNA) $\lambda_{em,T\text{-}PNA}$ = 590 nm a été observée, indiquant l'hybridation des PNAs dans les **Supra-OSPs**. Ensuite, la possibilité de dissocier l'hybridation des ANP au sein des **Supra-OSPs** lors du chauffage a été étudiée par analyse FRET. Comme le montre la Figure 13a, des températures élevées peuvent perturber les interactions supramoléculaires de l'ANP dans les **Supra-OSPs** et, par conséquent, perturber le FRET. Une dispersion de **Supra-OSPs** a été chauffée à 60 °C pendant 10 minutes et la dispersion de particules a ensuite été excitée avec une lumière de 450 nm tout en surveillant l'émission. Comme le montre la Digure 13d, on a constaté que le chauffage interrompait le FRET entre les fractions donneuse et acceptrice, comme l'indique l'augmentation de l'intensité de l'émission observée pour le brin donneur (F-PNA). Ces expériences indiquent que lors de l'hydrolyse et de la condensation du **Supra-PNA-Si**, des particules organosiliciques sont formées. Celles-ci possèdent des PNA hybrides comme groupes de pontage dans leur cadre, et peuvent être dissociées en présence d'un stimulus externe, tel que de la chaleur.

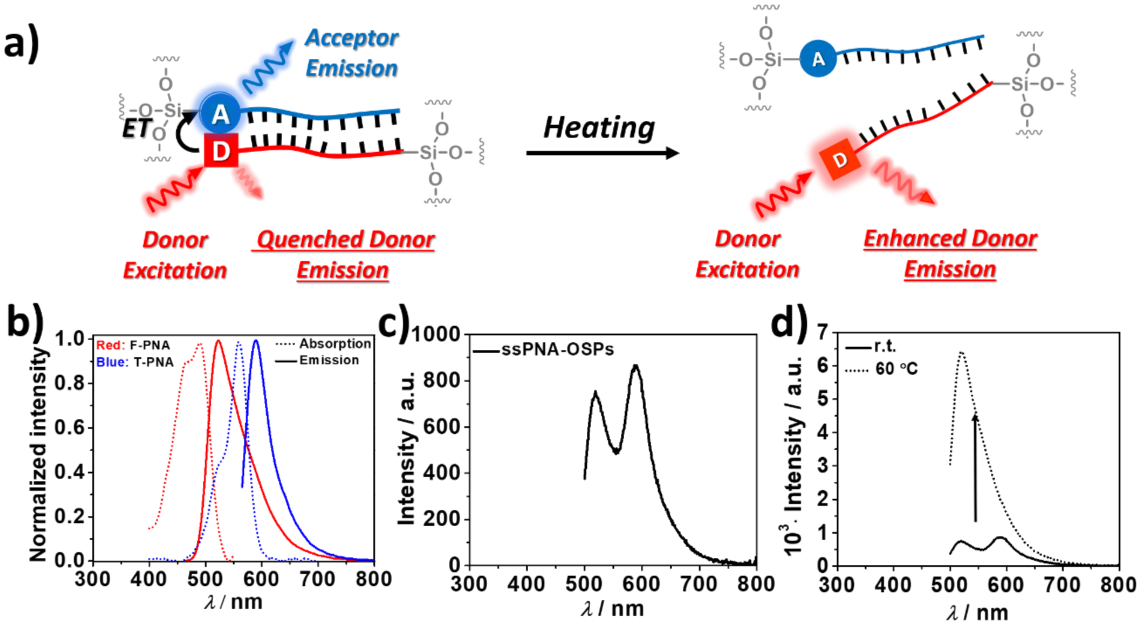

Figure 13. a) Représentation schématique de la perturbation du processus FRET lors du chauffage d'une dispersion de **Supra-OSPs** due à la dissociation des brins de ANP. b) Spectres d'absorption et d'émission normalisés des brins de F- et T-PNA dans le tampon PBS à pH=5,8. c) Expérience FRET sur une dispersion de **Supra-OSPs** (c=0,008 mg·mL^{-1}) dans du PBS (pH=5,8) après excitation à λ_{ex}=450 nm. d) Expériences FRET dépendantes de la température sur une dispersion de **Supra-OSPs** (c=0,008 mg-mL^{-1}) dans du PBS (pH=5,8) après excitation à λ_{ex} = 450 nm.

Particules organosiliciques préparées par des interactions supramoléculaires hybrides ADN-ANP

Le succès de la préparation des organosilices à base d'ANP a incité à préparer des organosilices répondant aux stimuli. Par conséquent, la possibilité d'utiliser l'auto-assemblage d'un assemblage ANP-ADN-ANP comme groupe de pontage réagissant aux stimuli pour la préparation de particules organosiliciques, confirmée par ces expériences, est étudiée dans ce sous-chapitre. La combinaison de l'utilisation de l'interaction ADN et ANP repose sur le fait que la partie ADN permet d'interagir précisément, selon la séquence de base de l'ADN, avec les biomolécules. Comme le montre la figure 14, le mélange de deux ANP-alcoxysilanes monocaténaires (PNA-Si1 et PNA-Si2), conçus pour être complémentaires de 10 régions de longueur mer à l'extrémité 5' et 3' d'un ADN monocaténaire de 45 mer (ssADN), permet d'obtenir un bis-alcoxysilane supramoléculaire **Supra-PDP-Si**. Le ssADN de 45 mer a été conçu non seulement pour s'hybrider avec les ANP-silanes, mais il possède en outre une séquence de liaison à l'ATP, comme l'ont rapporté Ricci et ses collègues.[49]

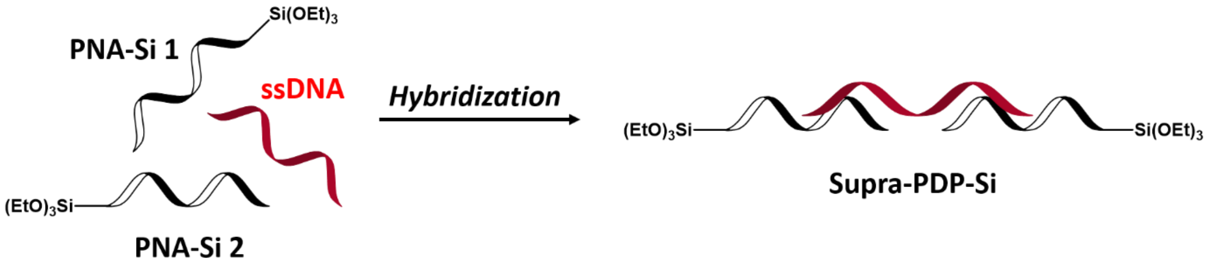

Figure 14. Représentation schématique dans l'utilisation des APN-silanes, qui se lient aux extrémités de l'ADNs pour former le bis-organoalcoxysilane **Supra-PDP-Si** assemblé au niveau supramoléculaire.

Pour préparer le composé **Supra-PDP-Si**, les brins ANP aminés ont été fonctionnalisés avec des ICPTES en présence de la base TEA, pour préparer leurs dérivés monoalcoxysilanes (PNA-S 1 et PNA-Si 2, voir la section expérimentale). Par la suite, une quantité équimolaire de PNA-Si 1, PNA-Si 2 et ssADN ont été mélangés pour favoriser leur hybridation, formant ainsi le Supra-PDP-Si. L'hydrolyse et la condensation subséquentes du **Supra-PDP-Si** catalysées par une base avec et sans la source secondaire de silice TEOS, en présence du tensioactif CTAB, ont été étudiées dans un mélange H_2O/EtOH. Pour suivre la formation des particules organosiliciques, des images de microscopie électronique du brut de réaction ont été analysées à différents intervalles de temps. Les images MEB enregistrées des mélanges réactionnels à 1h, 3h et 12h de temps de réaction en l'absence de TEOS sont présentées à la Figure 15a-c. Comme le montre la Figure 15a, après 1h, des structures fibreuses de moins de 1 µm (entourées en noir) ont été observées, qui ont continué à se développer après 3h de temps de réaction pour devenir de grandes structures fibreuses, très probablement en raison d'une hydrolyse et d'une condensation retardées d'organoalcoxysilanes volumineux. Après 12h de temps de réaction, les structures fibreuses ont commencé à se dégrader en structures fibreuses plus petites, très probablement en raison de l'instabilité des interactions supramoléculaires du groupe de pontage supramoléculaire ANP-ADN-ANP. Lorsque des organosilices ont été préparées à partir de **Supra-PDP-Si** avec une quantité équimolaire de TEOS (Figure 15d-f), aucune structure fibreuse n'a pu être imagée après 1h de temps de réaction. Après 3h, de grandes structures fibreuses ont été observées (Figure 15e), et des structures fibreuses stables ont encore été observées à 12h de temps de réaction (Figure 15f). La stabilité accrue des structures fibreuses d'organosilice peut s'expliquer par la co-condensation du TEOS en **Supra-PDP-Si** et la présence du CTAB, qui a stabilisé les silicates en milieu aqueux contre la dépolymérisation.

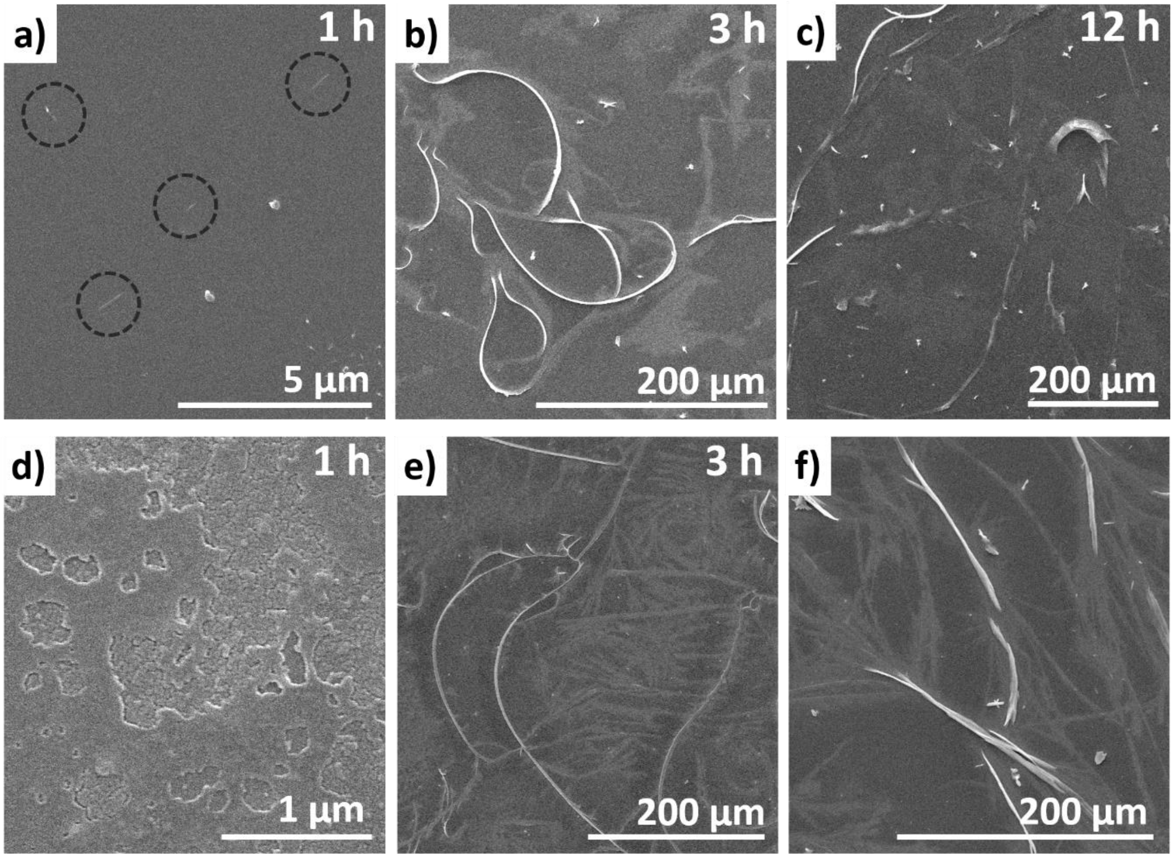

Figure 15. Images MEB des mélanges réactionnels bruts pour la formation d'organosilices à partir de **Supra-PDP-Si**. a-c) Images MEB du brut réactionnel à différents intervalles de temps lorsqu'aucune source de silice supplémentaire n'a été ajoutée dans la réaction d'hydrolyse et de condensation de **Supra-PDP-Si**. d-f) Images MEB du brut réactionnel à différents intervalles de temps lorsqu'une quantité équimolaire de TEOS a été ajoutée à la réaction.

Ce travail a permis d'étudier la possibilité d'utiliser des éléments constitutifs à base d'ADN et d'ARN pour préparer une variété de particules organosiliciques sensibles aux stimuli. La préparation initiale de bis-organoalcoxysilanes à base d'ADN et d'ANP et leur utilisation ultérieure pour préparer des particules de silice pontées par des composés organiques ont été démontrées. Les particules organosiliciques à pont d'ADN préparées ont la capacité de reconnaître des molécules d'ADN complémentaires et de se dégrader en présence d'enzymes telles que des hydrolyses. L'avantage de l'utilisation de bis-alcoxysilanes à base d'ANP réside dans la formation de particules plus uniformes. Deuxièmement, la possibilité d'auto-assembler des alcoxysilanes ANP complémentaires pour former un organo-bis-alcoxysilane supramoléculaire à base de PNA à utiliser pour la préparation de polymères à liaison hybride a été démontrée. L'intégration réussie de liaisons supramoléculaires, au sein d'une structure rigide à base de silice, a été démontrée avec succès, en montrant la faisabilité de préparer des organosilices qui possèdent des liaisons supramoléculaires au sein de leur structure. En outre, il a été démontré que les particules obtenues conservent les fragments supramoléculaires, qui se désassemblent à la chaleur. Enfin, l'utilisation d'un organo-alcoxysilane à base d'ANP-ADN-ANP, maintenu ensemble par des interactions supramoléculaires, pour préparer des organosilices a été étudiée. La formation réussie de structures semblables à des fibres a été confirmée et les futures expériences fourniront des informations supplémentaires sur les propriétés physico-chimiques des organosilices à base d'ANP-ADN-ANP.

Références

(1) Vert, M.; Doi, Y.; Hellwich, K.-H.; Hess, M.; Hodge, P.; Kubisa, P.; Rinaudo, M.; Schué, F. Terminology for Biorelated Polymers and Applications (IUPAC Recommendations 2012). *Pure Appl. Chem.* **2012**, *84* (2), 377–410.

(2) European Commission, *Off. J. Eur. Union* **2011**, *275*, 38–40. https://eur-lex.europa.eu/legal-content/EN/TXT/PDF/?uri=CELEX:32011H0696&from=EN

(3) Wagner, V.; Dullaart, A.; Bock, A. K.; Zweck, A. The Emerging Nanomedicine Landscape. *Nat. Biotechnol.* **2006**, *24* (10), 1211–1217. DOI: 10.1038/nbt1006-1211.

(4) Anselmo, A. C.; Mitragotri, S. Nanoparticles in the Clinic: An Update. *Bioeng. Transl. Med.* **2019**, *4* (3), 1–16. DOI: 10.1002/btm2.10143.

(5) He, H.; Liu, L.; Morin, E. E.; Liu, M.; Schwendeman, A. Survey of Clinical Translation of Cancer Nanomedicines - Lessons Learned from Successes and Failures. *Acc. Chem. Res.* **2019**, *52* (9), 2673–2683. DOI: 10.1021/acs.accounts.9b00228.

(6) Che, H.; Van Hest, J. C. M. Stimuli-Responsive Polymersomes and Nanoreactors. *J. Mater. Chem. B* **2016**, *4* (27), 4632–4647. DOI: 10.1039/c6tb01163b.

(7) Rideau, E.; Dimova, R.; Schwille, P.; Wurm, F. R.; Landfester, K. Liposomes and Polymersomes: A Comparative Review towards Cell Mimicking. *Chem. Soc. Rev.* **2018**, *47* (23), 8572–8610. DOI: 10.1039/c8cs00162f.

(8) Dawidczyk, C. M.; Kim, C.; Park, J. H.; Russell, L. M.; Lee, K. H.; Pomper, M. G.; Searson, P. C. State-of-the-Art in Design Rules for Drug Delivery Platforms: Lessons Learned from

FDA-Approved Nanomedicines. *J. Control. Release* **2014**, *187*, 133–144. DOI: 10.1016/j.jconrel.2014.05.036.

(9) Caracciolo, G. Clinically Approved Liposomal Nanomedicines: Lessons Learned from the Biomolecular Corona. *Nanoscale* **2018**, *10* (9), 4167–4172. DOI: 10.1039/c7nr07450f.

(10) Smietana, K.; Siatkowski, M.; Møller, M. Trends in Clinical Success Rates. *Nat. Rev. Drug Discov.* **2016**, *15* (6), 379–380. DOI: 10.1038/nrd.2016.85.

(11) Han, X.; Xu, K.; Taratula, O.; Farsad, K. Applications of Nanoparticles in Biomedical Imaging. *Nanoscale* **2019**, *11* (3), 799–819. DOI: 10.1039/c8nr07769j.

(12) Manzano, M.; Vallet-Regí, M. Mesoporous Silica Nanoparticles for Drug Delivery. *Adv. Funct. Mater.* **2020**, *30* (2), 3–5. DOI: 10.1002/adfm.201902634.

(13) Croissant, J. G.; Fatieiev, Y.; Khashab, N. M. Degradability and Clearance of Silicon, Organosilica, Silsesquioxane, Silica Mixed Oxide, and Mesoporous Silica Nanoparticles. *Adv. Mater.* **2017**, *29* (9). DOI: 10.1002/adma.201604634.

(14) Möller, K.; Bein, T. Degradable Drug Carriers: Vanishing Mesoporous Silica Nanoparticles. *Chem. Mater.* **2019**, *31* (12), 4364–4378. DOI: 10.1021/acs.chemmater.9b00221.

(15) Croissant, J. G.; Fatieiev, Y.; Almalik, A.; Khashab, N. M. Mesoporous Silica and Organosilica Nanoparticles: Physical Chemistry, Biosafety, Delivery Strategies, and Biomedical Applications. *Adv. Healthc. Mater.* **2018**, *7* (4), 1–75. DOI: 10.1002/adhm.201700831.

(16) Audran, M.; Kumar, R. The Physiology and Pathophysiology of Vitamin D. *Mayo Clin. Proc.* **1985**, *60* (12), 851–866. DOI: 10.1016/S0025-6196(12)64791-0.

(17) Papakostas, D.; Rancan, F.; Sterry, W.; Blume-Peytavi, U.; Vogt, A. Nanoparticles in Dermatology. *Arch. Dermatol. Res.* **2011**, *303* (8), 533–550. DOI: 10.1007/s00403-011-1163-7.

(18) Croissant, J.; Cattoën, X.; Man, M. W. C.; Gallud, A.; Raehm, L.; Trens, P.; Maynadier, M.; Durand, J. O. Biodegradable Ethylene-Bis(Propyl)Disulfide-Based Periodic Mesoporous Organosilica Nanorods and Nanospheres for Efficient in-Vitro Drug Delivery. *Adv. Mater.* **2014**, *26* (35), 6174–6180. DOI: 10.1002/adma.201401931.

(19) Shao, D.; Li, M.; Wang, Z.; Zheng, X.; Lao, Y. H.; Chang, Z.; Zhang, F.; Lu, M.; Yue, J.; Hu, H.; Yan, H.; Chen, L.; Dong, W. fei; Leong, K. W. Bioinspired Diselenide-Bridged Mesoporous Silica Nanoparticles for Dual-Responsive Protein Delivery. *Adv. Mater.* **2018**, *30* (29), 1–8. DOI: 10.1002/adma.201801198.

(20) Maggini, L.; Cabrera, I.; Ruiz-Carretero, A.; Prasetyanto, E. A.; Robinet, E.; De Cola, L. Breakable Mesoporous Silica Nanoparticles for Targeted Drug Delivery. *Nanoscale* **2016**, *8* (13), 7240–7247. DOI: 10.1039/c5nr09112h.

(21) Liu, L.; Kong, C.; Huo, M.; Liu, C.; Peng, L.; Zhao, T.; Wei, Y.; Qian, F.; Yuan, J. Schiff Base Interaction Tuned Mesoporous Organosilica Nanoplatforms with PH-Responsive

Degradability for Efficient Anti-Cancer Drug Delivery: In Vivo. *Chem. Commun.* **2018**, *54* (66), 9190–9193. DOI: 10.1039/c8cc05043k.

(22) Travaglini, L.; Picchetti, P.; Totovao, R.; Prasetyanto, E. A.; De Cola, L. Highly Degradable Imine-Doped Mesoporous Silica Particles. *Mater. Chem. Front.* **2019**, *3* (1). DOI: 10.1039/c8qm00438b.

(23) Fatieiev, Y.; Croissant, J. G.; Julfakyan, K.; Deng, L.; Anjum, D. H.; Gurinov, A.; Khashab, N. M. Enzymatically Degradable Hybrid Organic-Inorganic Bridged Silsesquioxane Nanoparticles for in Vitro Imaging. *Nanoscale* **2015**, *7* (37), 15046–15050. DOI: 10.1039/c5nr03065j.

(24) Maggini, L.; Travaglini, L.; Cabrera, I.; Castro-Hartmann, P.; De Cola, L. Biodegradable Peptide-Silica Nanodonuts. *Chem. - A Eur. J.* **2016**, *22* (11), 3697–3703. DOI: 10.1002/chem.201504605.

(25) Kloxin, A. M.; Kasko, A. M.; Salinas, C. N.; Anseth, K. S. Photodegradable Hydrogels for Dynamic Tuning of Physical and Chemical Properties. *Science (80-.).* **2009**, *324* (5923), 59–63. DOI: 10.1126/science.1169494.

(26) Raman, R.; Hua, T.; Gwynne, D.; Collins, J.; Tamang, S.; Zhou, J.; Esfandiary, T.; Soares, V.; Pajovic, S.; Hayward, A.; Langer, R.; Traverso, G. Light-Degradable Hydrogels as Dynamic Triggers for Gastrointestinal Applications. *Sci. Adv.* **2020**, *6* (3), 1–12. DOI: 10.1126/sciadv.aay0065.

(27) Roppolo, I.; Chiappone, A.; Angelini, A.; Stassi, S.; Frascella, F.; Pirri, C. F.; Ricciardi, C.; Descrovi, E. 3D Printable Light-Responsive Polymers. *Mater. Horizons* **2017**, *4* (3), 396–401. DOI: 10.1039/c7mh00072c.

(28) Cao, J.; Huang, S.; Chen, Y.; Li, S.; Li, X.; Deng, D.; Qian, Z.; Tang, L.; Gu, Y. Near-Infrared Light-Triggered Micelles for Fast Controlled Drug Release in Deep Tissue. *Biomaterials* **2013**, *34* (26), 6272–6283. DOI: 10.1016/j.biomaterials.2013.05.008.

(29) Zhu, J.; Lin, H.; Kim, Y.; Yang, M.; Skakuj, K.; Du, J. S.; Lee, B.; Schatz, G. C.; Van Duyne, R. P.; Mirkin, C. A. Light-Responsive Colloidal Crystals Engineered with DNA. *Adv. Mater.* **2020**, *1906600*, 1–6. DOI: 10.1002/adma.201906600.

(30) Li, S.; Moosa, B. A.; Croissant, J. G.; Khashab, N. M. Electrostatic Assembly/Disassembly of Nanoscaled Colloidosomes for Light-Triggered Cargo Release. *Angew. Chemie - Int. Ed.* **2015**, *54* (23), 6804–6808. DOI: 10.1002/anie.201501615.

(31) He, D.; He, X.; Wang, K.; Cao, J.; Zhao, Y. A Light-Responsive Reversible Molecule-Gated System Using Thymine-Modified Mesoporous Silica Nanoparticles. *Langmuir* **2012**, *28* (8), 4003–4008. DOI: 10.1021/la2047504.

(32) Aznar, E.; Oroval, M.; Pascual, L.; Murguía, J. R.; Martínez-Máñez, R.; Sancenón, F. Gated Materials for On-Command Release of Guest Molecules. *Chem. Rev.* **2016**, *116* (2), 561–718. DOI: 10.1021/acs.chemrev.5b00456.

(33) Lin, Q.; Huang, Q.; Li, C.; Bao, C.; Liu, Z.; Li, F.; Zhu, L. Anticancer Drug Release from a Mesoporous Silica Based Nanophotocage Regulated by Either a One- or Two-Photon Process. *J. Am. Chem. Soc.* **2010**, *132* (31), 10645–10647. DOI: 10.1021/ja103415t.

(34) Il'ichev, Y. V.; Schwörer, M. A.; Wirz, J. Photochemical Reaction Mechanisms of 2-Nitrobenzyl Compounds: Methyl Ethers and Caged ATP. *J. Am. Chem. Soc.* **2004**, *126* (14), 4581–4595. DOI: 10.1021/ja039071z.

(35) Klán, P.; Šolomek, T.; Bochet, C. G.; Blanc, A.; Givens, R.; Rubina, M.; Popik, V.; Kostikov, A.; Wirz, J. Photoremovable Protecting Groups in Chemistry and Biology: Reaction Mechanisms and Efficacy. *Chem. Rev.* **2013**, *113* (1), 119–191. DOI: 10.1021/cr300177k.

(36) Grün, M.; Lauer, I.; Unger, K. K. The Synthesis of Micrometer- and Submicrometer-Size Spheres of Ordered Mesoporous Oxide MCM-41. *Adv. Mater.* **1997**, *9* (3), 254–257. DOI: 10.1002/adma.19970090317.

(37) Ma, K.; Werner-Zwanziger, U.; Zwanziger, J.; Wiesner, U. Controlling Growth of Ultrasmall Sub-10 Nm Fluorescent Mesoporous Silica Nanoparticles. *Chem. Mater.* **2013**, *25* (5), 677–691. DOI: 10.1021/cm303242h.

(38) Zhang, J.; Wang, X.; Wen, J.; Su, X.; Weng, L.; Wang, C.; Tian, Y.; Zhang, Y.; Tao, J.; Xu, P.; Lu, G.; Teng, Z.; Wang, L. Size Effect of Mesoporous Organosilica Nanoparticles on Tumor Penetration and Accumulation. *Biomater. Sci.* **2019**, *7* (11), 4790–4799. DOI: 10.1039/c9bm01164a.

(39) Zhao, T.; Elzatahry, A.; Li, X.; Zhao, D. Single-Micelle-Directed Synthesis of Mesoporous Materials. *Nat. Rev. Mater.* **2019**, *4* (12), 775–791. DOI: 10.1038/s41578-019-0144-x.

(40) Ma, K.; Gong, Y.; Aubert, T.; Turker, M. Z.; Kao, T.; Doerschuk, P. C.; Wiesner, U. Self-Assembly of Highly Symmetrical, Ultrasmall Inorganic Cages Directed by Surfactant Micelles. *Nature* **2018**, *558* (7711), 577–580. DOI: 10.1038/s41586-018-0221-0.

(41) Scheres, S. H. W. RELION: Implementation of a Bayesian Approach to Cryo-EM Structure Determination. *J. Struct. Biol.* **2012**, *180* (3), 519–530. DOI: 10.1016/j.jsb.2012.09.006.

(42) Fernandes, P. A.; Ramos, M. J. Theoretical Insights into the Mechanism for Thiol/Disulfide Exchange. *Chem. - A Eur. J.* **2004**, *10* (1), 257–266. DOI: 10.1002/chem.200305343.

(43) Decuzzi, P.; Godin, B.; Tanaka, T.; Lee, S. Y.; Chiappini, C.; Liu, X.; Ferrari, M. Size and Shape Effects in the Biodistribution of Intravascularly Injected Particles. *J. Control. Release* **2010**, *141* (3), 320–327. DOI: 10.1016/j.jconrel.2009.10.014.

(44) Gromnicova, R.; Davies, H. A.; Sreekanthreddy, P.; Romero, I. A.; Lund, T.; Roitt, I. M.; Phillips, J. B.; Male, D. K. Glucose-Coated Gold Nanoparticles Transfer across Human Brain Endothelium and Enter Astrocytes in Vitro. *PLoS One* **2013**, *8* (12). DOI: 10.1371/journal.pone.0081043.

(45) Jiang, X.; Xin, H.; Ren, Q.; Gu, J.; Zhu, L.; Du, F.; Feng, C.; Xie, Y.; Sha, X.; Fang, X. Nanoparticles of 2-Deoxy-d-Glucose Functionalized Poly(Ethylene Glycol)-Co-

Poly(Trimethylene Carbonate) for Dual-Targeted Drug Delivery in Glioma Treatment. *Biomaterials* **2014**, *35* (1), 518–529. DOI: 10.1016/j.biomaterials.2013.09.094.

(46) Anraku, Y.; Kuwahara, H.; Fukusato, Y.; Mizoguchi, A.; Ishii, T.; Nitta, K.; Matsumoto, Y.; Toh, K.; Miyata, K.; Uchida, S.; Nishina, K.; Osada, K.; Itaka, K.; Nishiyama, N.; Mizusawa, H.; Yamasoba, T.; Yokota, T.; Kataoka, K. Glycaemic Control Boosts Glucosylated Nanocarrier Crossing the BBB into the Brain. *Nat. Commun.* **2017**, *8* (1). DOI: 10.1038/s41467-017-00952-3.

(47) Min, H. S.; Kim, H. J.; Naito, M.; Ogura, S.; Toh, K.; Hayashi, K.; Kim, B. S.; Fukushima, S.; Anraku, Y.; Miyata, K.; Kataoka, K. Systemic Brain Delivery of Antisense Oligonucleotides across the Blood–Brain Barrier with a Glucose-Coated Polymeric Nanocarrier. *Angew. Chemie - Int. Ed.* **2020**, *59* (21), 8173–8180. DOI: 10.1002/anie.201914751.

(48) Keefe, A. D.; Pai, S.; Ellington, A. Aptamers as Therapeutics. *Nat. Rev. Drug Discov.* **2010**, *9* (7), 537–550. DOI: 10.1038/nrd3141.

(49) Del Grosso, E.; Ragazzon, G.; Prins, L. J.; Ricci, F. Fuel-Responsive Allosteric DNA-Based Aptamers for the Transient Release of ATP and Cocaine. *Angew. Chemie - Int. Ed.* **2019**, *58* (17), 5582–5586. DOI: 10.1002/anie.201812885.

(50) Yu, Z.; Tantakitti, F.; Yu, T.; Palmer, L. C.; Schatz, G. C.; Stupp, S. I. Simultaneous Covalent and Noncovalent Hybrid Polymerizations. *Science (80-.).* **2016**, *351* (6272), 497–502. DOI: 10.1126/science.aad4091.

List of abbreviations

7-DH=7-Dehydrocholesterol

APTES=(3-Aminopropyl)triethoxysilane

ATP=Adenosine triphosphate

ATR=Attenuated total reflectance

AzTMS=3-Azidopropyltrimethoxysilane

BBB=Blood-brain barrier

BCN-NHS=((1R,8S,9S)-bicyclo[6.1.0]non-4-yn-9-ylmethyl N-succinimidyl carbonate)

BET=Brunauer-Emmett-Teller

CM=Cell membrane

CMC=Critical micelle concentration

CQDs=Carbon quantum dots

CT=Computed tomography

CTAB=Cetyltrimethylammonium bromide

Cy3=Cyanine 3

Cy5=Cyanine 5

DFT=Density functional theory

DLS=Dynamic light scattering

DMF=Dimethylformamide

DMSO=Dimethyl sulfoxide

DNA=Deoxyribonucleic acid

DT=Docetaxel

DTT=Dithiothreitol

EMA=European Medicine Agency

ESI=Electrospray ionization

FDA=Food and Drug Administration

F-PNA=5-Carboxyfluorescein labelled PNA strand

F-PNA-Si=F-PNA alkoxysilane

FRET=Förster resonance energy transfer

FTIR=Fourier-transform infrared spectroscopy

GSH=Glutathione

HBPs=Hybrid bonding polymers

HE=HOECHST 33258

HMONs=Hollow organo-bridged mesoporous silica particles

HR-MS=High resolution mass-spectrometry

ICP-AES=Inductively coupled plasma atomic emission spectroscopy

ICPTES=3-(Triethoxysilyl)propyl isocyanate

LB-MSPs=Light-breakable mesoporous organosilica particles

LED=Light emitting diode

MCM-41=Mobile composition of matter No.41

MONs=Mesoporous organosilica nanoparticles

MRI=Magnetic resonance imaging

MSPs=mesoporous silica particles

MZ=Marginal zone

NBA=2-nitrobenzoic acid

NMR=Nuclear magnetic resonance

NPs=Nanoparticles

OSCs=Organosilica cages

OSPs=Organosilica particles

PEG=Polyethylene glycol

PNA=Peptide nucleic acid

PNA-Si=PNA alkoxysilane

PQ=9,10-Phenantrenequinone

QDs=Quantum dots

RGD=Arg-Gly-Lys

RNA=Ribonucleic acid

RNAi=Ribonucleic acid interference

RP=Red pulp

SAXS=Small-angle X-ray scattering

sCy5=Sulfo-cyanine 5

SEM=Scanning electron microscopy

siRNA=Small interfering ribonucleic acid

ssDNA=Single stranded deoxyribonucleic acid

ssDNA-OSPs=ssDNA-bridged organosilica particles

SS-MSPs=Disulfide-bridged mesoporous organosilica particles

ssPNA=Single stranded peptide nucleic acid

ssPNA-OSPs=ssPNA-bridged organosilica particles

STEM=Scanning transmission electron microscopy

Supra-OSPs=Supramolecular-bridged organosilica particles

Supra-PDP-Si=Supramolecular PNA-DNA-PNA bis-alkoxysilane

Supra-PNA-Si=Supramolecular PNA bis-alkoxysilane

TAMRA=5-Carboxytetramethylrhodamine

TD-DFT=Time-dependent density functional theory

TEA=Triethylamine

TEEA=Triethylammonium acetate

TEM=Transmission electron microscopy

TEOS=Tetraethyl orthosilicate

TGA=Thermogravimetric analysis

T-PNA=5-Carboxytetramethylrhodamine-labelled PNA strand

T-PNA-Si=T-PNA alkoxysilane

Tris=Tris(hydroxymethyl)aminomethane

usMSPs=Ultrasmall mesoporous silica particles

UV=Ultraviolet

Vis=Visible

WP=White Pulp

wt%=Mass fraction

XPS=X-ray photoelectron spectroscopy

Chapter 1

General introduction

In this chapter, a general introduction of nanomedicine will be given, focusing in particular on the use of porous organosilica particles for biomedical applications. Although there is a wide selection of materials that are currently investigated for new nanomedicines, silica-based materials possess promising properties that are useful for the development of next generation carriers for drug-delivery and bioimaging applications. After a general overview of the current investigations on nanoparticles for medical use, the advantages of organosilica particles for drug delivery applications will be discussed while providing some insight into their preparation, physicochemical characteristics and biological properties. Finally, the aim of the work reported in this thesis will be presented.

1.1. What is “nano” in nanomedicine?

The emergence of nanotechnology in the 1980s has not only changed the way we perceive matter at the small scale but has also contributed to new discoveries in almost every field of science. By applying the tools and knowledge gained from nanotechnological advances to medicine for the detection, prevention, and treatment of diseases, these two sciences have converged and created nanomedicine. In the field of nanomedicine, nanoscale materials are being researched for the development of superior therapies against diseases. Nanoscaled objects (i.e. nanoparticles) are defined as having at least one of their external dimensions in the range of 1 to 100 nm (IUPAC and EU definition of a nanomaterial)[1,2] and feature characteristic physicochemical properties that are not observed in the bulk phase. Many authors, especially in the field of nanomedicine, often extend the term “nanoparticle” to include particles bigger than 100 nm (up to 1 µm), as long as novel biological or physicochemical properties are observed that are otherwise not obtained from the bulk (Figure 1).[3] The change in physicochemical properties of nanoparticles in this size regime can lead to the development of novel imaging agents and drug delivery systems, which hold the potential to outperform current therapies in terms of efficiency and efficacy. In fact, since the FDA approval of the first nanomedicine Doxil® in 1995, more than 50 new nanomedicines have reached clinical use.[4] In 2019, ONPATTRO® became the first siRNA/RNAi based nanotherapeutic to pass clinical testing, further demonstrating the importance of nanotechnology in the future of medicine.[5] Although nanomedicine is still a relatively young research field, it has already contributed to the development of new materials for biomedical applications and to an understanding on how nanomaterials interact with cells. Therefore, further research into the production, modification and the interaction of nanomaterials with the biological environment will lead to a better understanding of these materials, which is not uniquely relevant to the biomedical field, but will affect also other branches of science that work with nanoparticles.

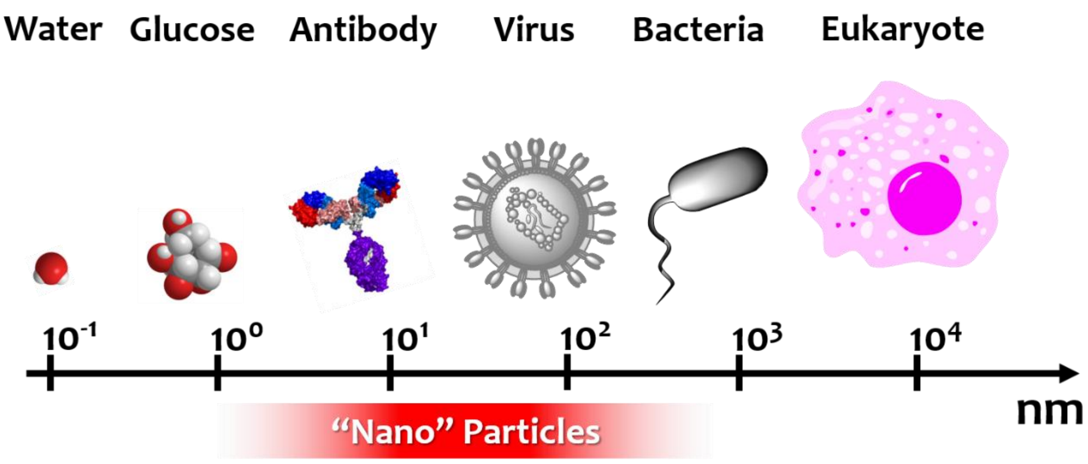

Figure 1. Comparison of sizes for different objects. Nano-objects require that at least one of their size domains lie between 1–100 nm. This definition is not consequently applied throughout the literature, since different physiochemical characteristic of the material regarding its bulk may not strictly be limited to this definition—therefore, the borders remain somewhat undefined.

1.2. Nanoparticles for biomedical applications

The use of nanoparticles for biomedical applications has been shown to be a powerful strategy for the targeted transport of drugs or imaging agents within a living organism. Upon the precise delivery of therapeutic molecules within an organism, unwanted toxicity related to molecular diffusion of the drug in biological healthy tissues can be minimized, resulting in the development of safer and more efficient therapies. Most of the current FDA and EMA nanomedicines in clinical trials or which are already used in clinics, are based on liposomal or polymeric reformulations of previously approved drugs.[6] Despite their obvious success, liposomal drug formulations suffer from several suboptimal properties, such as short term stability, premature drug release, and/or limited possibilities of active-targeting; all aspects that are critical for optimal pharmacokinetic performance of liposomal based therapeutics.[7–10] Research into alternative nanomaterials for biomedical applications can address the shortcomings of current therapies that are based on liposomal nanomedicines, while holding promise to improve the efficacy of previously unsuitable drugs, allowing for the revival of abandoned therapeutic molecules. The success rate of small-molecules reaching the FDA standards for phase I clinical trials lies at 9%, where the low approval rate generally results from an observed lack of drug efficacy and poor biological safety.[11] Encapsulation of such small molecules within a nanometer-sized carrier particle could help to deliver the cargo specifically to the diseased site, greatly improving drug efficacy while reducing unwanted side effects. Encapsulation of fluorescent dyes used in imaging studies within nanoparticles leads to an improvement in their circulation lifetimes, chemical stability and photophysical properties, rendering state of the art fluorophores even more efficient for imaging applications.[12–14] Due to their small size, nanoparticles itself can become superior contrasts agents as successfully demonstrated with magnetic materials suitable for magnetic-resonance-imaging techniques or by quantum dots in near-infrared triggered optical imaging techniques.[15–17] Upon intelligent design of nanoparticles, multimodal imaging and drug-delivery properties can be combined, creating particles for theranostic use.

1.2.1. Physicochemical considerations for nanoparticles

Physiochemical properties such as size, morphology, and chemical composition are known to influence a material's therapeutic or diagnostic efficacy and biological fate (Figure 2).

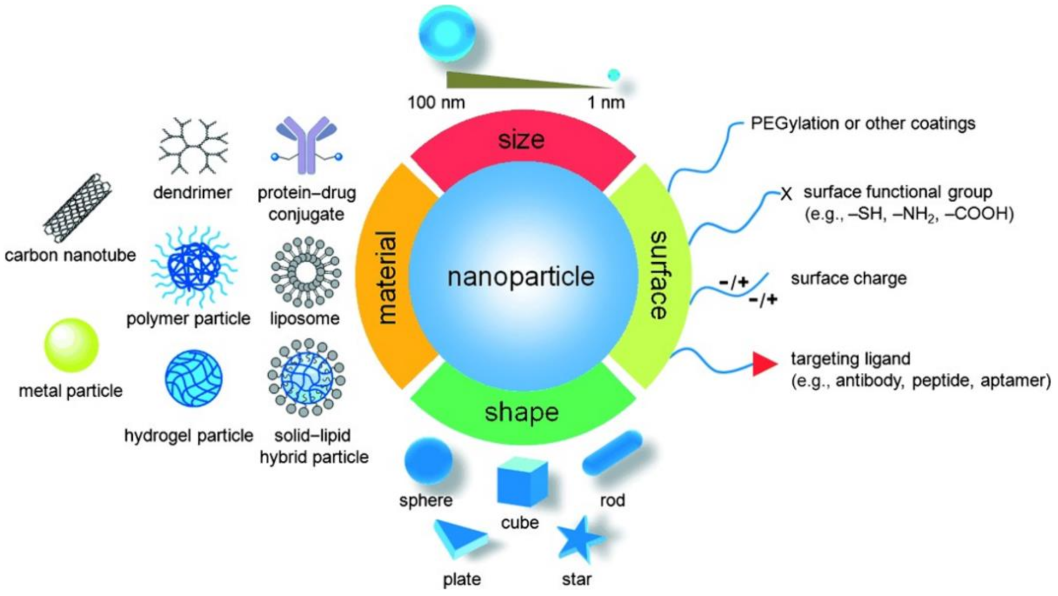

Figure 2. Nanoparticles researched for biomedical applications with different physicochemical properties. Copyright 2014, John Wiley and Sons. Reproduced with permission from Ref 18.

For example, intravenously injected nanoparticles are known to bioaccumulate based on their particle size, morphology and surface charge (Figure 3).[18–23] Relatively small particles with sizes below 5 nm are effectively cleared out from body by the kidneys, while larger particles tend to accumulate in the liver (50–200 nm) and spleen (generally bigger than 200 nm), organs commonly associated with general particle clearance. Positive charges on the nanoparticle surface have been shown to increase nanoparticle uptake by the mononuclear phagocyte system, sequestering nanomaterials preferentially in the liver.

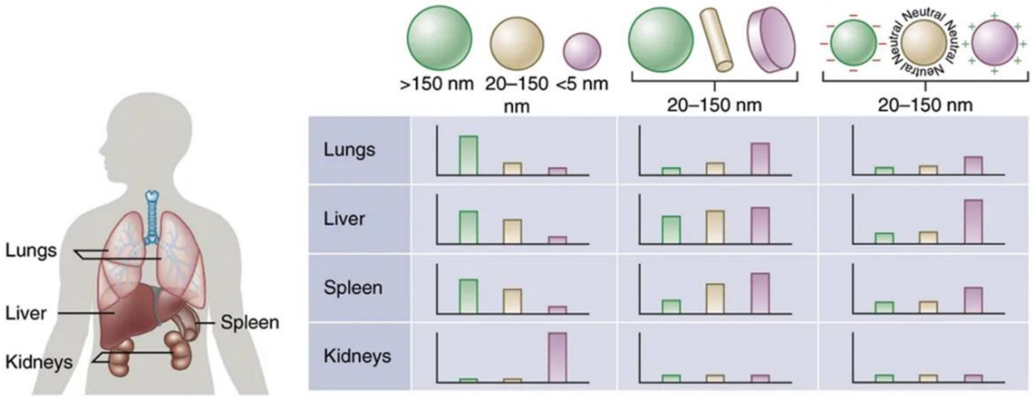

Figure 3. Biodistribution of nanoparticles according to size, morphology, and surface charge. Reproduced with permission from Ref 23. Copyright 2015, Springer Nature.

Surface functionalization has also been demonstrated to greatly influence a particle’s pharmacokinetic properties. Surface functionalization with polymers such as polyethylene glycol[24,25], or with protein-coatings that decrease the particle´s sequestration by the mononuclear phagocyte system[26–28], are effectively used to enhance the particles blood-circulation lifetime and in vivo stability. Another important concept in nanomedicine is active targeting, where surface functionalization with ligands specific to the surface receptors of the target cell leads to improved accumulation at the desired site. Actively targeting liposomal formulations, such as SGT-53 that possesses transferrin targeting antibodies on its surface, are currently in clinical studies and showed promising bioaccumulation effects due to the presence of the targeting unit.[29] Small peptides have been shown to deliver nanoparticles to tumors when they are specific antigens of cell-surface receptors. For example, the RGD (Arg-Asp-Gly) motif was successfully used in order to prove in vivo targeting of nanoparticles to tumor sites.[30–33] More recently it was observed that functionalization of nanoparticles with the tumor-homing peptide (AR) causes a selective accumulation of the material in breast tumors in mice.[34,35] Caruso and coworkers showed that upon functionalization of poly(ethylene glycol) nanoparticles (PEG) with the $\alpha_v\beta_3$-integring ligand RGD peptide causes selective accumulation of the materials in the tumor site of U-87 MG xenografted mice when the particles were intravenously administered (Figure 4).[36] When the RGD sequence was instead modified to RDG, no tumor accumulation was observed, confirming the active targeting role of cell receptor ligands on the nanoparticles.

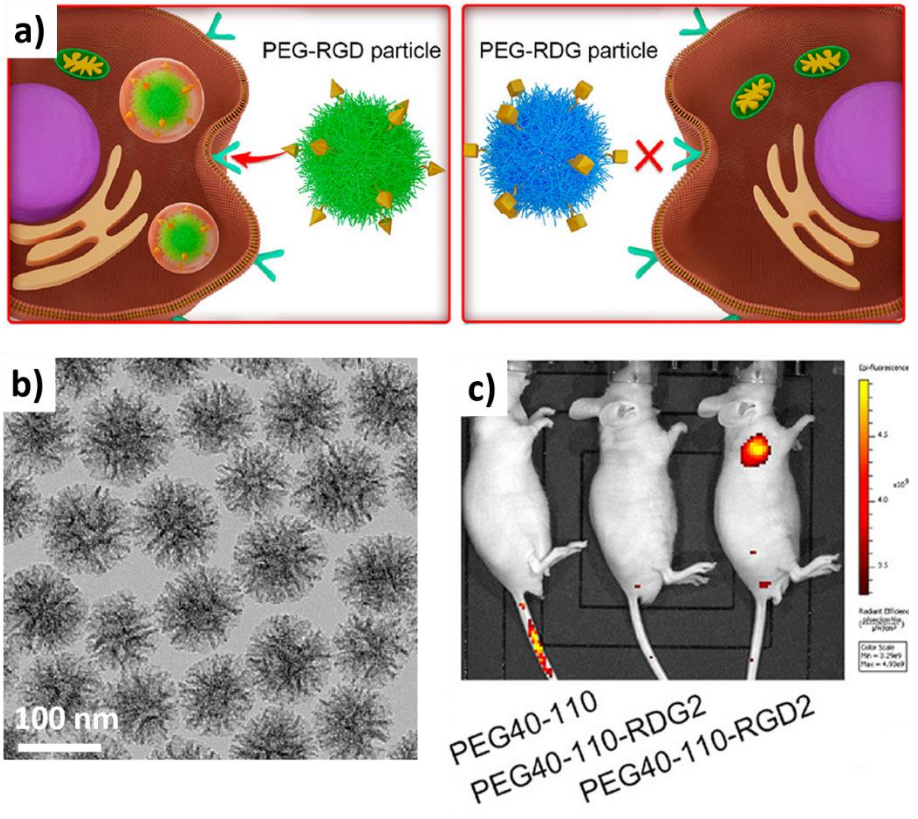

Figure 4. a) Schematic representation of RGD mediated uptake by $\alpha_v\beta_3$-integring expressing cells. RDG functionalized particles are not able to interact with $\alpha_v\beta_3$-integrings du to the receptors sequence-specific recognition of the RGD motive. b) TEM images of PEG particles. c) In vivo fluorescent images with dye labelled PEG, PEG-RGD and PEG-RDG nanoparticles. Only RGD functionalized particles accumulate in U-87 MG tumor cells within mice. Adapted with permission from Ref 36. Copyright 2019, American Chemical Society.

1.2.2. Examples of nanomaterials currently studied for biomedical applications

When it comes to the choice of the nanomaterial used for biomedical applications, one can classify the particles according to their specific properties that emerge from their small size. Magnetic particles, such as iron oxide nanoparticles, have been studied for magnetic resonance imaging (MRI),[37–42] drug delivery,[43–45] hypothermal treatments,[46,47] immunomodulation[48,49] and magneto-mechanical attenuation of cells.[50,51] Cheon and coworkers investigated 15 nm sized exchange-coupled $CoFe_2O_4$ core-shell $MnFe_2O_4$ particles ($CoFe_2O_4@MnFe_2O_4$), where the combination of two materials characterized by hard (core) and soft (shell) magnetic phases led to greater induction heat enhancement when compared to Ferrite® iron oxide nanoparticles (Figure 5).[46] The resulting enhanced heating power of $CoFe_2O_4@MnFe_2O_4$ in the presence of an alternating external magnetic field was used for hypothermal treatment of tumors in mice and the particles showed superior tumor reduction ability compared to Ferrite® particles or doxorubicin.

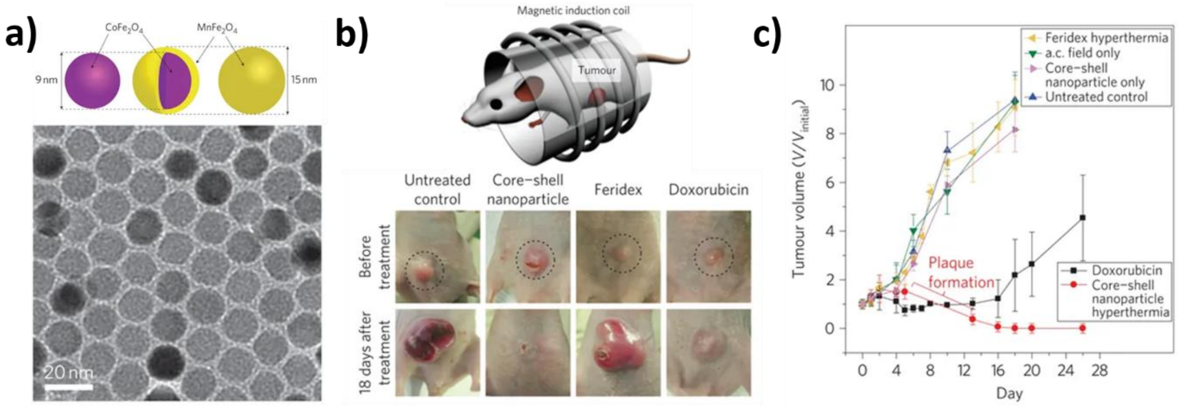

Figure 5. a) Schematic depiction of 15 nm sized $CoFe_2O_4$ core–shell $MnFe_2O_4$ nanoparticles ($CoFe_2O_4@MnFe_2O_4$) and TEM image of $CoFe_2O_4@MnFe_2O_4$. b) Schematic representation of the in vivo hypothermal treatment setup done with tumor-bearing mice after intravenous particle injection. Images of tumor bearing mice before hypothermal treatment (top row, dot circle indicates tumor location) and after treatment (18 days, bottom row). c) Tumor volume versus days after treatment using $CoFe_2O_4@MnFe_2O_4$ particles with and without (untreated) hypothermia, Ferrite® particles combined with hypothermia, and doxorubicin. Adapted with permission from Ref 46. Copyright 2011, Springer Nature.

Nobel-metal-based nanoparticles, such as gold nanoparticles (AuNPs) have gained attention in the biomedical field, since their morphology and surface functionalization can be easily tuned and control over their surface plasmon resonance properties can be precisely adjusted.[52–54] Therefore, AuNPs are extensively investigated for photothermal therapy,[55–57] since the particles possess strong absorption in the NIR region, and are further considered as promising contrast agents for CT imaging applications.[58,59] Zhang and coworkers prepared immunological AuNPs (AuNP@DCB$_{16}$F$_{10}$) derived from melanoma tumor cells (B$_{16}$F$_{10}$ cells), encapsulated within a dendrimer derived vesicle (DC$_{10}$) that showed improved anti-cancer activity when used for photothermal treatment of melanoma in mice (Figure 6).[60] Due to the presence of melanoma antigens on AuNP@DCB$_{16}$F$_{10}$, these particles were able to activate a systematic anti-cancer immune response, which in combination with the photothermal activity of the AuNPs core upon NIR-light irradiation led to the successful reduction of melanoma cancer.

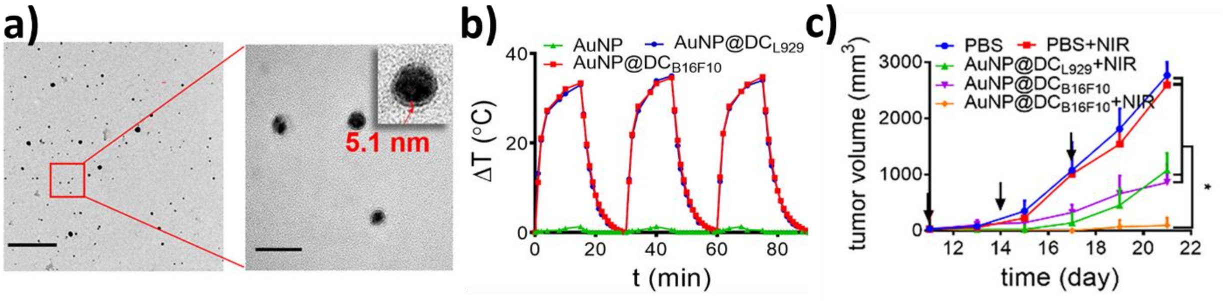

Figure 6. a) TEM images of AuNP@DCB$_{16}$F$_{10}$. TEM images at higher magnification (right) indicate the presence of the dendritic cell derived vesicle with a size of ca. 5 nm. Scale bars 500 and 50 nm, respectively. b) Photothermal effect of AuNPs and immunological AuNPs. Pristine AuNPs showed decreased photothermal activity due to a lack of absorbance in the NIR region. c) Melanoma tumor growth measured with different treatments with or without laser irradiation (2 W·cm^{-2}). Adapted with permission from Ref 60. Copyright 2019, American Chemical Society.

Colloidal semiconductor nanocrystals (QDs) are studied for the development of novel optical imaging probes for biomedical applications due to their high fluorescent quantum yields and superior photostability. The photoluminescence properties of QDs are highly dependent on size, chemical composition and shell thickness.[61,62] The majority of research on QDs is focused on their use as luminescent probes,[63–65] although coverage of QDs with porous polymers or an inorganic shell has shown the possibility to perform drug release.[66,67] The main disadvantages in the use of QDs is their toxicity related to the inclusion of metal ions, such as Cd^{2+}, Pb^{2+} or Hg^{2+}. For example, Kim and coworkers prepared PbS core–shell CdS-QDs (PbS/CdS-QDs) for real-time in vivo imaging in the second near infrared region (NIR-II, 1000–1700 nm).[65] The authors found that the particles photophysical properties could be varied by altering the PbS core-sized of PbS/CdS-QDs, allowing for multiplex imaging upon injection of particles with different core size (λ_{em1}=1080 and λ_{em2}=1280 nm). In order to reduce the particles toxicity, the material was covered with a biocompatible polymer (PQDs) that also allowed for the folic acid functionalization of PQDs, which served as tumor targeting moiety on the surface of PQDs (Figure 7).

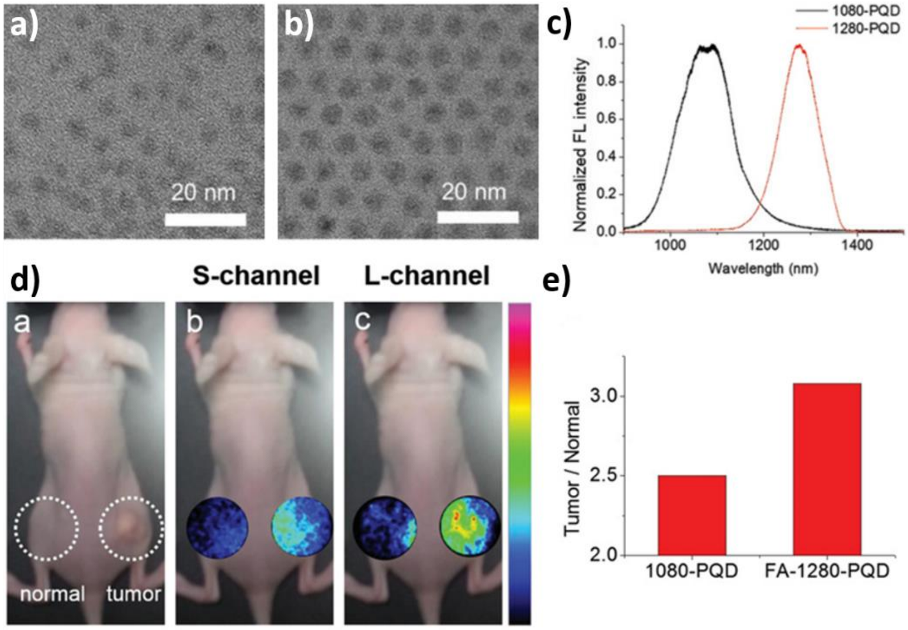

Figure 7. a) TEM image of PbS/CdS-QDs with 4.2 nm core size. b) TEM image of PbS/CdS-QDs with 5.1 nm core size. c) Normalized florescence spectra of PbS/CdS-QDs with 4.2 nm core size (λ_{em}=1080 nm) and 5.1 core-size (λ_{em}=1280 nm) in water. d) In vivo NIR-II multiplexed imaging in tumor xenografted rodents with two polymer-coated and folic acid functionalized PbS/CdS-QDs probes of different core size. Adapted with permission from Ref 65. Copyright 2018, John Wiley and Sons.

The use of carbon quantum dots (CQDs), also called carbon dots, represents an attractive, nontoxic alternative to QDs, though the current generation of CQDs possess inferior photoluminescence quantum yields when compared to traditional QDs.[68,69] Other carbon-based materials currently investigated for biomedical applications include fullerenes,[70–72] graphene oxide[73–75] and carbon nanotubes. Carbon nanotubes (CNTs) are especially interesting since their inner cavity can be loaded with molecules allowing for possible delivery.[76–78] The so-called "soft-materials", such as polymeric aggregates, DNA nanoobjects, nanogels and dendrimers are further researched for future nanomedicines and possess great potential for successful translation into clinics, as indicated on the number of polymeric nanoparticles that are currently under clinical trials for drug-delivery applications.[79] Monomers for the preparation of polymeric nanoparticles can be derived from natural sources or be synthetic. The latter allow for the precise tuning of the particle´s size, morphology, and chemical functionality. Upon the introduction of stimuli-responsive functional groups within the macromolecular monomer, cargo release can be triggered precisely in the presence of external stimuli, such as a change in pH,[80,81] enzymatic activity,[82,83] temperature[84,85] or the presence of reducing agents[86–88]. Recently, Langer and coworkers reported the preparation of hybrid lipid-polymeric nanoparticles for RNAi therapy (Figure 8).[89] RNAi therapy aims to deliver siRNA in order to silence gene expression at the post-transcriptional level and has been shown to be a powerful strategy to treat diseases, leading to the first FDA-approved RNAi-based treatment with ONPATTRO® in 2019. The authors used a polymer-based nanoparticle that enables efficient siRNA delivery to lung endothelial cells at low doses effectively reducing lung tumor growth and metastasis.

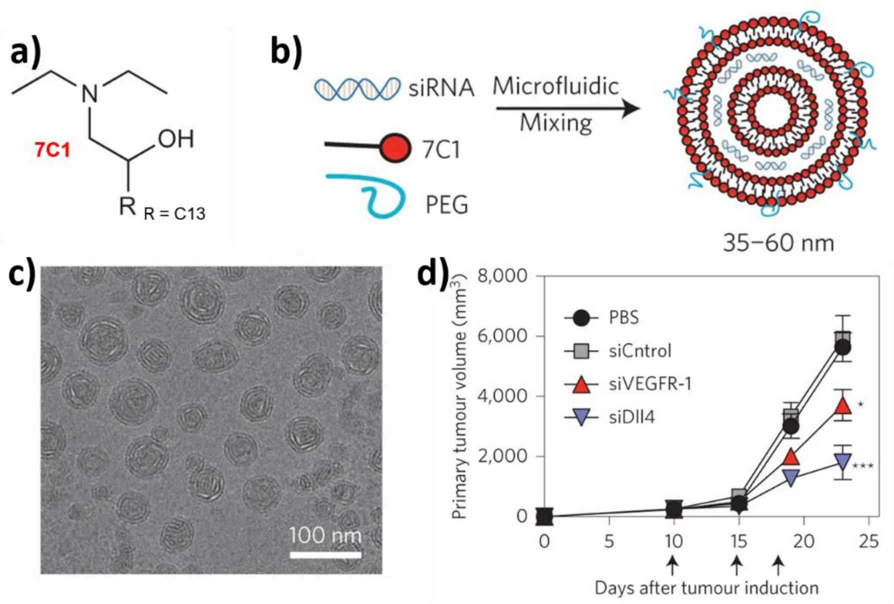

Figure 8. a) Structure of 7C1 lipid used in combination with PEG polymer for the preparation of lipid-polymer hybrid nanoparticles. B) Schematic representation of the lipid-polymer siRNA loaded carrier. c) Cryo-TEM images of lipid-polymer siRNA loaded carrier. d) Primary Lewis lung carcinoma (LLC) growth following three 1.0 mg·kg^{-1} treatments with siRNA loaded lipid-polymer nanoparticles (siRNAs used to silence protein expressions: siLuciferase in siCntrol formulation; siVascular endothelial growth factor receptor-1 in siVEGFR-1 silencing formulation; siDelta-like ligand 4 in siDll4 silencing formulation). Adapted with permission from Ref 89. Copyright 2014, Springer Nature.

A very appealing approach for the development of soft nanoparticles for biomedical application is the use of particles which have been developed in the field of structural DNA nanotechnology.[90] The bottom-up assembly of synthetic oligonucleotide strands via tile-based construction strategies or DNA-origami procedures allows for the preparation of well-defined 3D nano-sized DNA-objects, in which the self-assembly of single oligonucleotide strands occurs with high precision due to Watson–Crick base pairing and π–π stacking interactions. Favorable advantages in the use of synthetic DNA are its biocompatibility and programmable assembly, which allows controlling the precise number of functional groups on the final nanoobject. For example, DNA nanotubes[91] have been studied for in vivo cancer therapy, serving as vehicles for the delivery of doxorubicin to human breast cancer cell lines. In addition, DNA-icosahedra[92] have been proven able to deliver anticancer drugs to tumor cells in vitro. Despite the great control over the assembly of nanoobjects obtained by DNA nanotechnology, their biological stability and the difficultly in unambiguously tracking these nanoobjects in a biological environment represents a critical problem that must be solved in order to facilitate their successful translation for in vivo applications.[93,94] In this respect, Gang and coworkers were able to show that by covering octahedral DNA-origami with peptoids increases their stability against enzymatic degradation (Figure 9).[95] Furthermore, the potential to use octahedral DNA origami for drug-delivery application was shown by encapsulating BSA within the octahedral cavity. Moreover, by suitably functionalizing the peptoids that surround the DNA nanoobject, antibodies and fluorescent marker have been successfully covalently linked, thereby demonstrating the possibility to use these constructs for imaging and targeted drug-delivery applications.

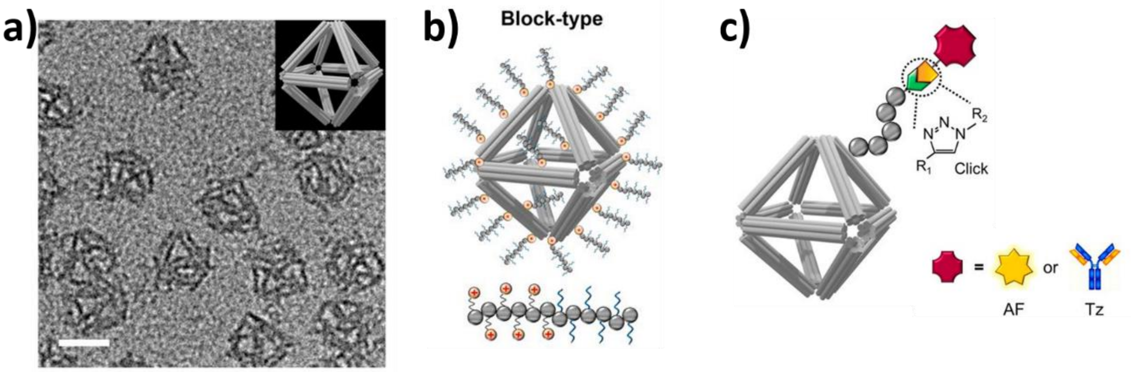

Figure 9. a) TEM image of octahedral DNA origami nanostructures. Scale bar=50 nm. b) Schematic representation of peptoid-protected octahedral DNA-origami. c) Schematic representation of the use of peptoids for selective antibody and/or fluorescent marker functionalization of the nanostructure. AF=Azide-Fluor 488 dye; Tz=Trastuzumab antibody. Adapted from Gang and coworkers Ref 95. Copyright 2020 the Author´s CC BY-NC-ND 4.0, published by National Academy of Sciences.

Other inorganic nanocarriers investigated for biomedical applications are silica-based particles. Ease of preparation and functionalization as well as their good biocompatibility make them attractive platforms for imaging and drug-delivery applications. Sub-10 nm sized silica core–shell PEG nanoparticles (C´Dots), functionalized with the tumor targeting peptide RGD are currently in FDA-approved human clinical trials for tumor mapping applications via fluorescence (Phase II: ClinicalTrials.gov identifier: NCT02106598) and PET-based (Phase I: ClinicalTrials.gov identifier: NCT03465618) imaging techniques. C´-Dots, which have been developed by the group of Prof. Ulrich Wiesner, possess high fluorescent quantum yields per particle and are easily prepared via sol-gel chemistry, allowing for further functionalization of the particles with cell-targeting peptides or contrast agents used for PET imaging techniques (Figure 10).[32,96,97] The small size of the particles ensures efficient renal clearance from the body without causing undesired bioaccumulation in non-targeted tissues.

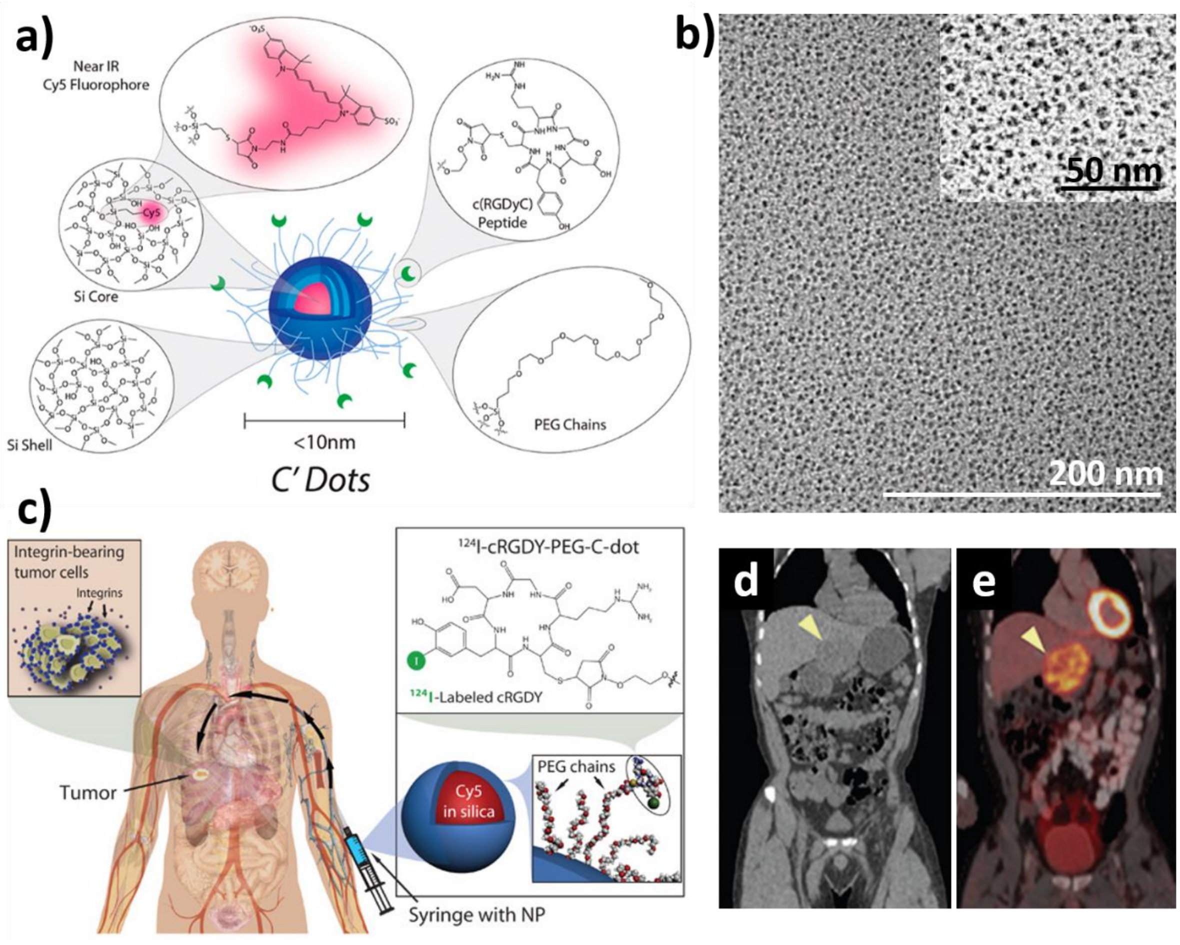

Figure 10. a) Schematic representation of the general structure of sub 10 nm C´-Dots. Within an amorphous silica-core, the red-emissive dye cyanine 5 is covalently incorporated, and the surface of the particle is functionalized with PEG-chains and the tumor homing peptide cRGD. The layered core structure indicates that, according to the synthetic procedure applied, the diameter of C´-Dots can be varied upon further silica growth. b) TEM images of 4.5 nm big C´-Dots. Adapted with permission from Ref 96. Copyright 2015, American Chemical Society. c) Human trials with ^{124}I-labeled and cRGD functionalized C´-Dots for tumor imaging. d) Coronal CT of a patient demonstrates a hypo dense left hepatic lobe metastasis (arrowhead). e) Whole-body PET imaging after 24 h of ^{124}I-labeled C´-Dots. Hepatic metastasis is indicated by the yellow arrow. Adapted with permission from Ref 32. Copyright 2014, The American Association for the Advancement of Science.

With regard to silica-based particles, the most efficient strategy to deliver therapeutic drugs is the use of porous nanoparticles, since high payloads can in principle be achieved. For instance, porous silicon nanoparticles (mSiNPs) have been used and have been approved for pharmaceutical applications by the FDA, given the biocompatibility of both mSiNPs and their degradation products.[98] mSiNPs are produced from silicon-wafers by electrochemical etching and subsequent sonication cycles, allowing for control over the final particle's size and porosity. The tunable porosity of mSiNPs is especially advantageous for the delivery of large bioactive drugs used for example in RNAi therapy. In this regard, Sailor and coworkers have recently reported the preparation of 50 nm-sized and highly porous mSiNPs, with high siRNA loading (25 wt%) for brain delivery applications (Figure 11).[99] The high loading could be retained upon capping of the loaded pores with calcium silicate precipitate. An advantageous feature of mSiNPs is that the particles are photoluminescent upon light excitation[100] and can therefore be easily followed by optical imaging techniques, allowing for their unambiguous identification in biological tissues. To achieve in vitro targeted delivery of the siRNA payload to neuronal cells, mSiNPs have been functionalized with a virus-derived peptide able to target the acetylcholine receptor of neuronal cells, and positive cell targeting ability was confirmed. An enhanced in vivo accumulation on brain injury sites was observed by optical imaging, indicating the potential for these particles to image leaky BBB regions of the brain of injured mice.

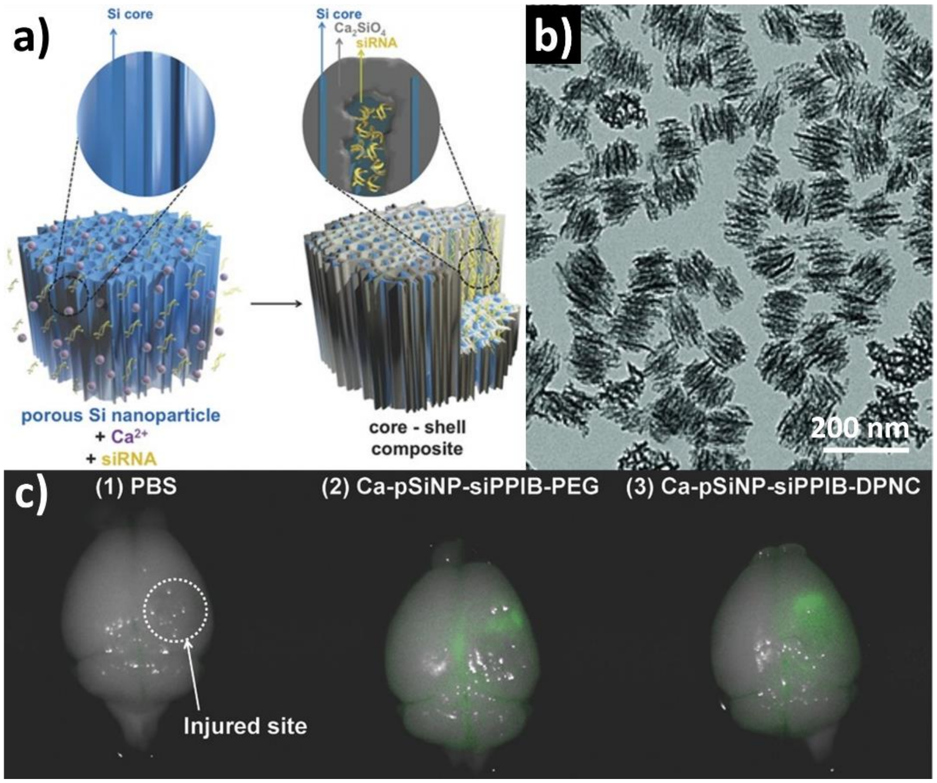

Figure 11. a) Schematic representation of siRNA loading and subsequent calcium silicate capping of nSiNPs. b) TEM images of mSiNPs. c) Ex vivo fluorescence images of brain samples treated with PBS (1), calcium silicate capped, and siRNA loaded mSiNPs functionalized with PEG chains (2) and calcium silicate capped, and siRNA loaded mSiNPs functionalized with the acetylcholine targeting peptide. siPPIB=siRNA for silencing the gene for peptidylprolyl isomerase B expression; DPNC=dual peptide nanocomplex composed of a rabies virus glycoprotein sequence and the transportan-based peptide. Adapted with permission from Ref 99. Copyright 2016, John Wiley and Sons.

The variety of materials that can be used for the preparation of novel nanomedicines is vast, although only a few reach clinical use. As mentioned before, a major obstacle for their translation remains the effective nanoparticle clearance from the body after administration, which is necessary to prevent bioaccumulation and subsequent undesired chronic toxicities. Effective renal clearance of nanomaterials is possible when the particles are generally smaller than 10 nm, which on the other hand limits their application for high payload delivery of bioactive molecules. When bigger particles are used, they must be rendered degradable to facilitate their biological elimination. In this regard, a promising approach to solve the degradability problem of larger particles is the use of mesoporous organosilica particles. The preparation of mesoporous organosilica particles allows for the facile introduction of stimuli-responsive organic bridging groups, which enables the particle's framework to degrade in the presence of a specific external stimulus (e.g. pH change, enzymatic activity or the presence of reducing agents). In the next subchapter, the use of mesoporous organosilica particles for biomedical applications is discussed, by giving a general introduction in the preparation of this type of materials. Further recent developments in the preparation of stimuli-responsive organosilica particles and their use in biomedical applications are also presented.

1.3. Mesoporous stimuli-responsive organosilica particles for biomedical applications

1.3.1. Preparation of mesoporous silica particles

According to the IUPAC definition, mesoporous materials possess pores with sizes ranging from 2 to 50 nm. Since the discovery of ordered mesoporous silicas, such as MCM-41 aluminosilicates by Kresge et al.[101] and Yanagisawa et al.[102] in the early 1990s by surfactant-templated approach, great effort has been devoted to developing new methodologies to tune the size, shape and pore size of mesoporous silica nanoparticles. Pioneering works in the development of nanosized mesoporous silica particles were first published in the 2000s, showing that precise control over synthetic parameters during the particle formation (e.g. pH, temperature, water content and type of surfactant used) enabled the preparation of porous silica with different morphologies.[103–105] Notably, Yano and coworkers modified the Stöber synthesis[106] by introducing a positively charged surfactant and prepared monodisperse and mesoporous silica particles with radially aligned pores.[107] As explained more in detail below, the addition of positively charged surfactants aids in the formation of mesoporous silica particles that form from the base-catalyzed hydrolysis and polycondensation of a silica source, such as tetraethyl orthosilicate (TEOS), in an aqueous or alcohol/water medium. Quaternary ammonium salts are commonly used for the preparation of mesoporous silica particles (MSPs), cetyltrimethylammonium bromide (CTAB) being one of the most used surfactants. In aqueous mixtures, CTAB forms different positively charged aggregates and phases depending on its concentration. For example, at relatively low concentrations, that is, in the range between its critical micelle concentrations (CMC) CMC 1 (in pure water that is 1.0 mM at T=25°C) and CMC 2 (in pure water that is ca. 20 mM at T=25°C), CTAB forms spherical micelles.[108] The CTAB concentration will therefore strongly affect the appearance of the final mesophase in MSPs in terms of pore-order and arrangement (depending on the CTAB concentration used, hexagonal, cubic or worm-like pore structures can be obtained). However, the MSP formation mechanism depends on a number of other variable parameters, including the nature of surfactant and silica source, the solvent mixture, the concentration of the single reaction components, pH, temperature, catalyst or the presence of salts and organic additives. Generally, the formation of mesoporous silica can be explained by using two models: 1) the liquid crystal templated pathway[101,109], which was first established by researchers at the now ExxonMobil company and normally provide bulk silica, and the 2) cooperative self-assembly pathway, which was proposed by Stucky and coworkers and according to which mesoporous silica nanoparticles form.[110] Figure 12 shows a graphical representation of the simplified formation mechanism of MSPs according to the cooperative self-assembly mechanism. Hydrolysis and polycondensation of the silica source (e.g. TEOS) occur catalyzed by the presence of a base. At the same time, the polymeric silicate anions assemble with the positively charged surfactant (e.g. CTAB) micelles through electrostatic interactions, leading to nucleation and subsequent growth. This results in the formation of mesoporous particles whose pores are filled by surfactant molecules. Removal of unreacted starting materials and the surfactantcan occur through calcination, dialysis or extractions in organic solvents providing purified mesoporous particles.

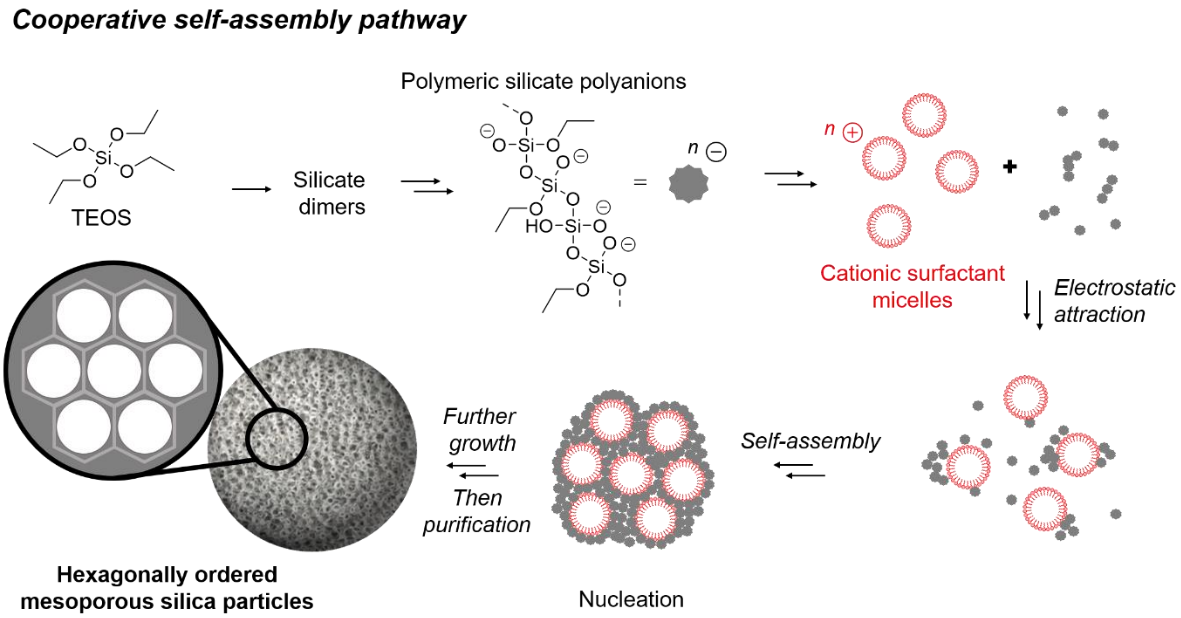

Figure 12. Schematic representation of the cooperative self-assembly pathway for the formation of MSPs.

The hydrolysis and condensation mechanism of alkoxysilanes, such as TEOS, has been excellently described by Brinker and Scherer in their book *Sol-Gel Science – The Physics and Chemistry of Sol-Gel Processing* (1990 Academic Press, Inc). The base-catalyzed hydrolysis of TEOS is initialized by the nucleophilic attack of the hydroxide anion ($^{-}$OH) according to a S_N-like mechanism on the silicon atom of the alkoxysilane. A negatively charged pentacoordinated hypervalent intermediate forms, which then decays through a second transition state by displacing an ethoxide anion (Figure 13a). Since the transition states accumulate either partial or net negative charges, the base catalyzed hydrolysis of TEOS experiences inductive effects from the ligands. In fact, ethoxide groups are less able to stabilize negative charges when compared to hydroxyl groups, resulting in relatively slow initial hydrolysis reaction rates for TEOS (for example when compared to hydrolysis rates of TEOS in acid-catalyzed reactions or other silica sources such as tetramethyl orthosilicate, TMOS). Upon greater ethoxy substitution with stronger electron-withdrawing hydroxyl ligands that can stabilize better the partial negative charges on the silicon atoms, hydrolysis rates increase. Condensation reactions (Figure 13b) involve the nucleophilic attack of deprotonated silanols on the silicon atom of another TEOS molecule or partially hydrolyzed polyalkoxysilanes, in which a S_N2 mechanism is believed to be involved. Since the hydrolysis reaction speeds up upon increased ethoxy substitution, the formation of highly branched polysilicates is promoted, which will eventually be electrostatically attracted by the positively charged CTAB micelles.

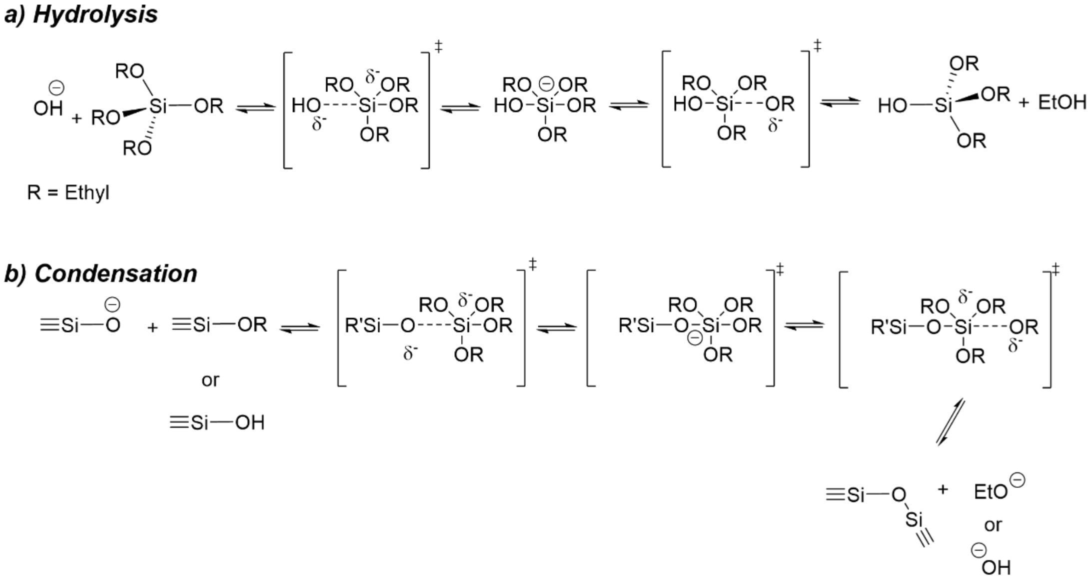

Figure 13. a) Base-catalyzed hydrolysis of TEOS. b) Base-catalyzed condensation of TEOS.

The surfactant-templated approach for the preparation of mesoporous particles is a powerful methodology to prepare a variety of different particles that differ in size, shape, pore geometry and pore size. Upon variation of synthesis parameters and nature of the surfactant used, mesoporous materials are prepared, possessing typically high surface areas (up to ca. 1000 $m^2 \cdot g^{-1}$), tunable pore sizes (2-30 nm) and high total pore volumes (up to 1 $cm^3 \cdot g^{-1}$). In Figure 14 examples of MSPs with different size, morphology and mesopore arrangement obtained by modifying synthetic parameters are shown.

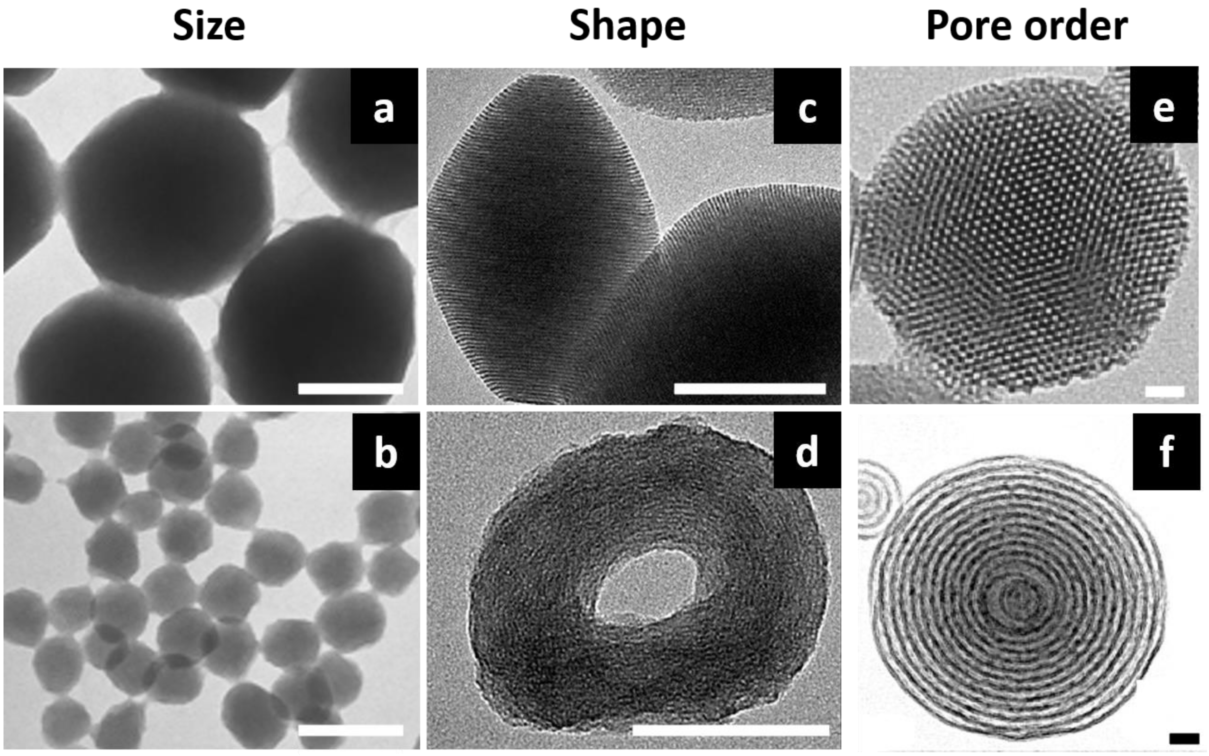

Figure 14. TEM images of MSPs with different size, shape, and pore arrangement. a) Spherical particles of a) 170 nm and b) 50 nm in dimeter. Adapted with permission from Ref 111, Copyright 2013, Royal Society of Chemistry (Great Britain). Particles with c) oval and d) toroidal shape. Adapted from Ref 112. MSPs with e) highly hexagonally ordered mesopores (adapted with permission from Ref 113, Copyright 2012, Elsevier) and f) MSPs with concentrically aligned pores (adapted with permission from Ref 114, Copyright 2013, American Chemical Society). All scale bars = 100 nm.

Of great interest for the development of nanomedicines, is the development of sub-20 nm sized, or so-called, ultra-small mesoporous silica particles (usMSPs). The small size of usMSPs can potentially result in an accelerated hydrolysis of the silica in biological media due to the particle's increased surface area, rendering the them less persistent in biological tissues and making their use safer for biological applications when compared to that of bigger silica particles. Furthermore, smaller particles are less likely to be sequestered by macrophages of the reticuloendothelial system (RES), allowing for improved delivery efficacy of the nanomaterial to diseased sites after intravenous injection. After the pioneering work reported in small amorphous SiO_2 particles,[115,116] Wiesner and coworkers successfully reported the preparation of 10 nm sized single-pore usMSPs (Figure 15a),[117] and more recently the preparation of 10–20 nm-sized highly ordered cage-like silica particles (Figure 15b),[118] a newly observed morphology for porous silica particles.

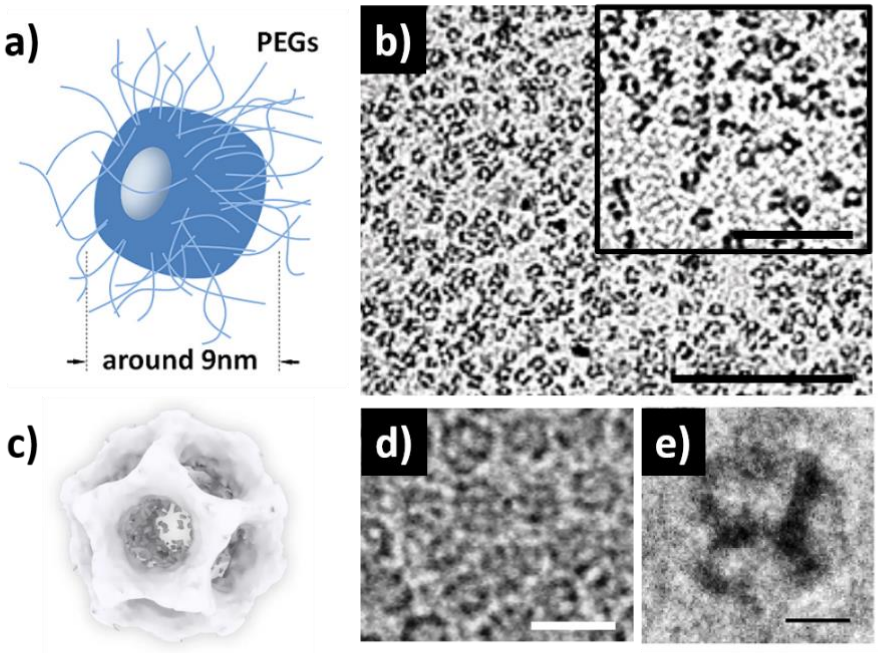

Figure 15. a) Schematic representation of single pore usMSPs and b) TEM images of usMSPs (scale bars = 100 nm and 50 nm for inset). c) 3D reconstructed representation of one cage-like silica particle class obtained from cryo-TEM images. d) TEM and (scale bar = 20 nm) e) Cryo-TEM images of cage-like silica particles (scale bars = 5 nm). Images reproduced with permission: Copyright 2012, American Chemical Society. Images a) and b) adapted with permission from Ref 117; Copyright 2018, Springer nature. Images c-e) adapted with permission from Ref 118.

1.3.2. Preparation and functionalization of mesoporous organosilica particles

The principles that are valid for the surfactant-templated preparation of porous silica particles by alkoxysilane chemistry can be applied to the preparation of mesoporous organosilica particles (MONs). MONs are porous silica-based particles, which possess organic functional groups as bridging units within their silica framework (Figure 16). In order to introduce an organic bridging group within the particle structure, an organo-bis(alkoxy)silane is hydrolyzed and co-condensed with a common alkoxysilane (e.g. TEOS) in the presence of a positively charged surfactant.[119] MONs are generally purified by dialysis or extraction methods, following the removal of the unreacted species and the surfactant.

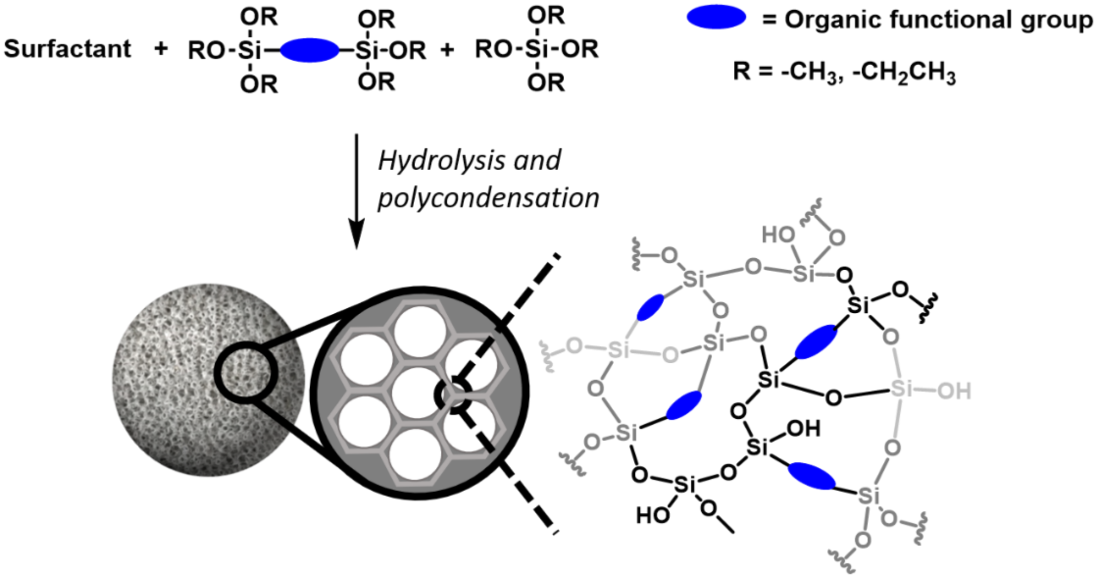

Figure 16. Schematic representation of the preparation for porous organosilica particles. As for the preparation of porous silica particles, porous organosilicas are prepared upon a surfactant templated hydrolysis of alkoxysilanes under acid or base catalysis.

As for the preparation of MSPs, upon variation of synthetic parameters (surfactant, silica source, pH, presence of additives/salts), size, shape and porosity of the final organosilica particles can be finely tuned (Figure 17). The introduction of organic functional groups provides the particles with new physicochemical properties that depend on the nature of the organic bridging molecule that was integrated within the silica framework. The role and importance of these porous organosilica particles in the biomedical field will be discussed in the next subchapter.

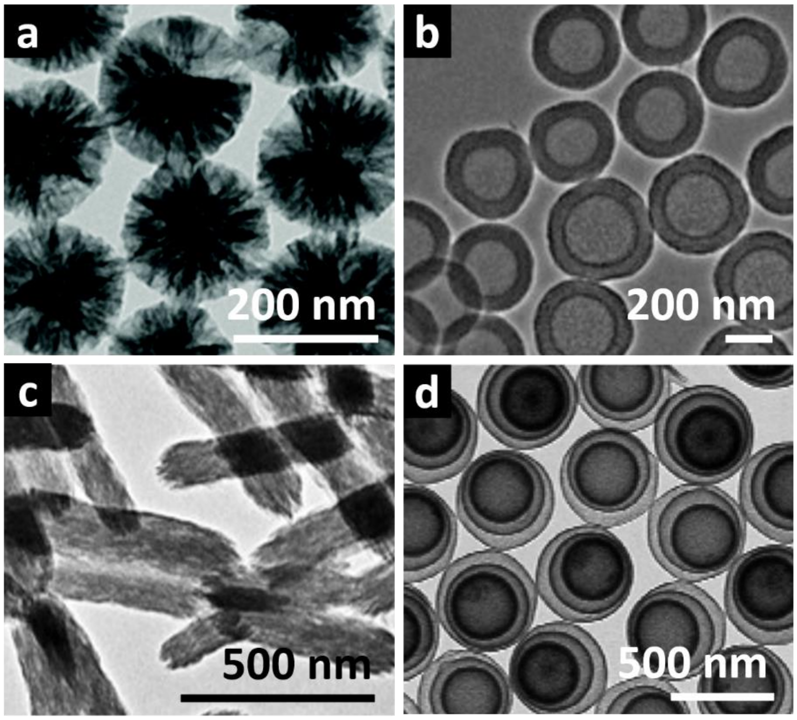

Figure 17. TEM images of organosilica particles with different size, morphology and porosity. a) Spherical particles with radially oriented large pores. Adapted with permission from Ref 120. Copyright 2013, Royal Society of Chemistry (Great Britain). b) Spherical and hollow organosilica particles. Adapted with permission from Ref 121. Copyright 2013, John Wiley and Sons. c) Rod-shaped mesoporous organosilica particles. Adapted with permission from Ref 122. Copyright 2017, John Wiley and Sons. d) Multiple-shelled mesoporous organosilica particles. Adapted with permission from Ref 123. Copyright 2012, American Chemical Society.

The sol–gel based surfactant-templated preparation of MSPs and MONs represents an easy and relatively low-priced synthetic strategy to produce porous carriers for theranostic applications. Additionally, since the particles possess hydroxyl groups on their surface, easy post-synthesis grafting with various functional groups is possible by using simple alkoxysilane chemistry. Furthermore, the functionalization can occur selectively solely on the particle surface when the surfactant has not been extracted from the pores of MSPs/MONs. As depicted in Figure 18, the outer surface of the particle can be selectively functionalized with specific functional groups when the pores are still occupied by surfactant molecules. Once the template has been removed, a selective functionalization, with different functional groups, of the pore inner surface can be achieved, thus allowing for the preparation of complex and multifunctional drug delivery carriers. Surface functionalization is in fact a crucial factor that has to be considered in order to enhance particle biocompatibility and in vivo circulation lifetime or to obtain active targeting. For example, functionalization of MONs with polyethylene glycol chains imparts enhanced in vivo circulation lifetimes due to reduced reticuloendothelial system (RES) related clearance of the particles. When targeting peptides or antibodies are desired, the possibility to modify the particles with functional groups suitable for bioconjugation (e.g. amines, thiols, azides, carboxylic acids) reactions is essential.

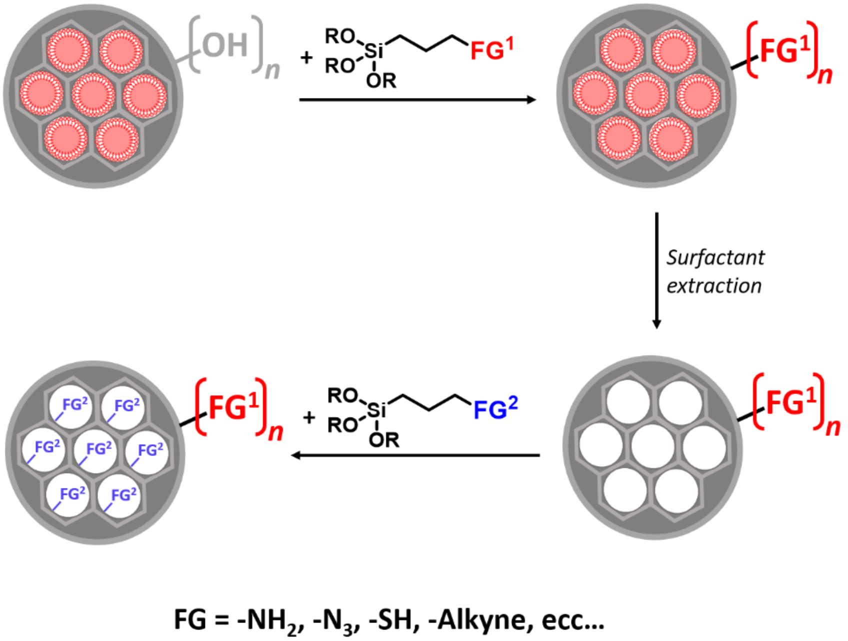

Figure 18. Selective surface and pore functionalization of MSPs or MONs using alkoxysilane chemistry.

1.3.3. Mesoporous organosilica particles for biomedical applications

Although MSPs have been previously investigated for biomedical applications,[124] MSPs-based therapies have yet to find success in clinical applications. The main reason for this issue lies in the observed poor clearance of these particles from living organisms once intravenously injected, which does not meet the requirements of total degradability set by the FDA.[98] Although MSPs degrade in aqueous environments due to the hydrolysis of the amorphous silica framework depending on the size, porosity, preparation procedure (such as pH-value for the preparation and presence of co-solvents) and additional surface functionalities of the particles, complete dissolution is not achieved and slow dissolution is frequently observed.[125] The development of MONs with a cleavable organic bridging group in their structure holds great potential to overcome the degradability and clearance issues of silica-based nanocarriers. In fact, upon the introduction of stimuli-responsive bridging groups within the framework of MONs, precise degradation and payload release can be tuned (Figure 9)

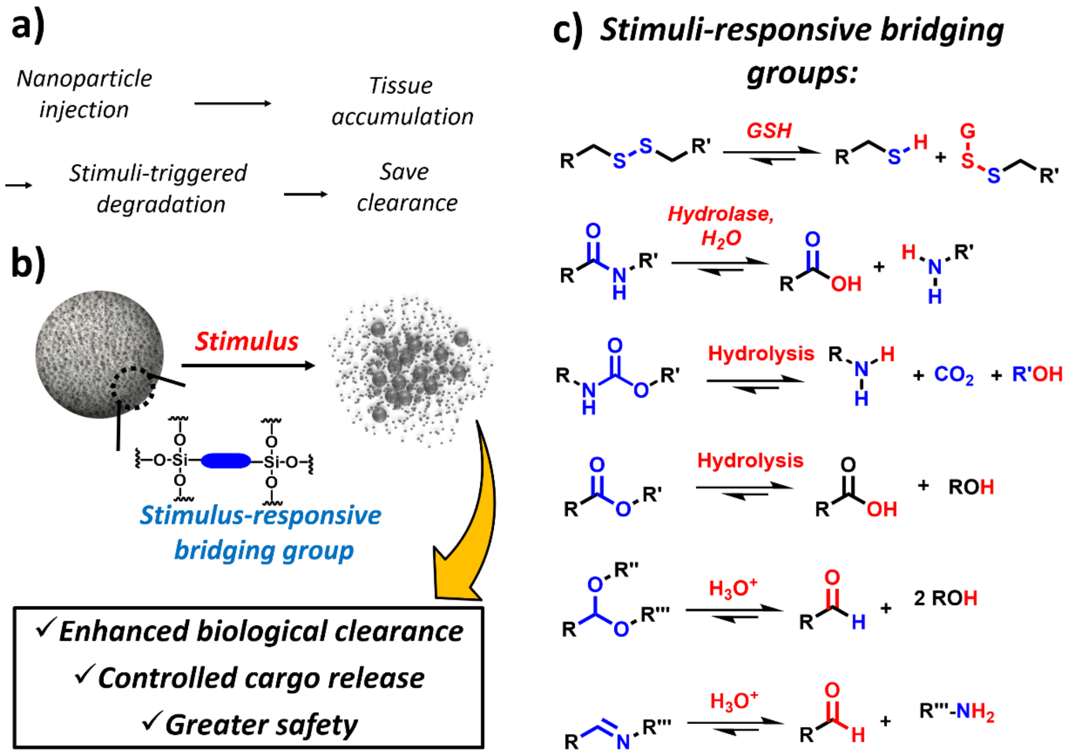

Figure 19. a) The use of breakable MONs allows the delivery of nanoparticles on-site of the disease and their stimuli-triggered degradation, therefore promoting the efficient clearance of small debris from a living organism. b) Stimuli responsive bridging groups integrated within the silica framework allow the stimuli triggered degradation of MONs into small degradation products. C) Stimuli-responsive bridging groups that can be integrated MONs, rendering them breakable in biological environments are shown. The various functional groups can be redox-responsive (e.g. disulfide bonds), sensible to enzymatic hydrolysis (e.g. ester and amide bonds) or sensible to acidic pH-values (e.g. acetal or imine bonds).

After Inagaki and coworkers reported the preparation of mesoporous organosilica for the first time,[126] the group of Prof. Coradin was able to report the synthesis of disulfide-bridged organosilicas and demonstrated their in vitro degradation within cells.[127] The authors were able to demonstrate that disulfide bond reduction occurs upon the exposure of the particles to the reducing agent dithiothreitol (DTT), causing particle disintegration, as observed through electron microscopy. In fact, the disulfide-bridged organosilica particles began degrading also after cell-internalization due to the presence of a cytosolic reducing agent, that is, the tripeptide glutathione (GSH). Since the first preparation of disulfide-bridged organosilicas, great effort has been devoted to the preparation of mesoporous disulfide-bridged organosilica particles (SS-MSPs), as their use for stimuli-responsive in vitro and in vivo drug delivery applications has been successfully proven (Figure 20).[128–130]

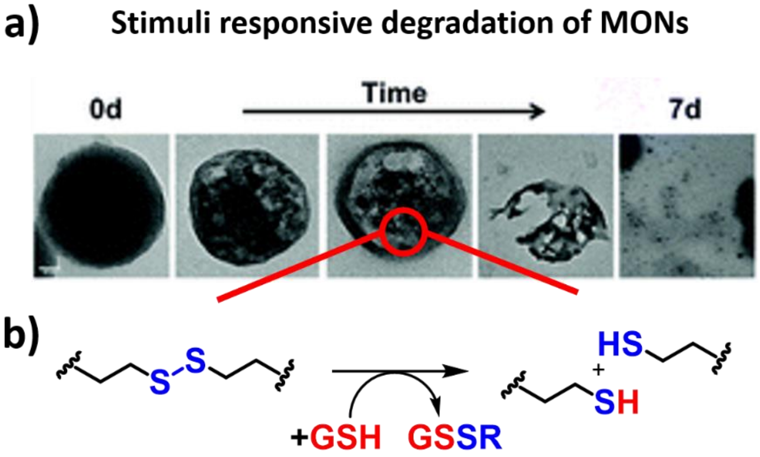

Figure 20. a) TEM images of stimuli responsive disulfide-bridged mesoporous organosilica particles which degrade upon the presence of the reducing agent glutathione (GSH). Adapted with permission from Ref 129. Copyright 2016, Royal Society of Chemistry (Great Britain). b) GSH reduces the disulfide bond and leads to its cleavage, hence triggering the degradation of the particles.

Since the stimuli-responsiveness of the MONs is dictated by the chemistry of the organic bridging group, many different breakable particles for drug-delivery applications have been investigated employing different stimuli, such as pH,[131] enzymatic activity[132,133] or reactive oxygen species[134] in order to trigger the degradation of MONs. More recently Leong and coworkers prepared bioinspired diselenide-bridged MONs, which were able to degrade in cells upon the presence of the reducing agent GSH or reactive oxygen species (Figure 21).[135] Furthermore, the authors showed homologous in vivo targeting upon encapsulation of the particles in cancer-cell-derived cellular membranes, and anticancer activity was investigated upon loading the particles with a cytotoxic RNAse enzyme.

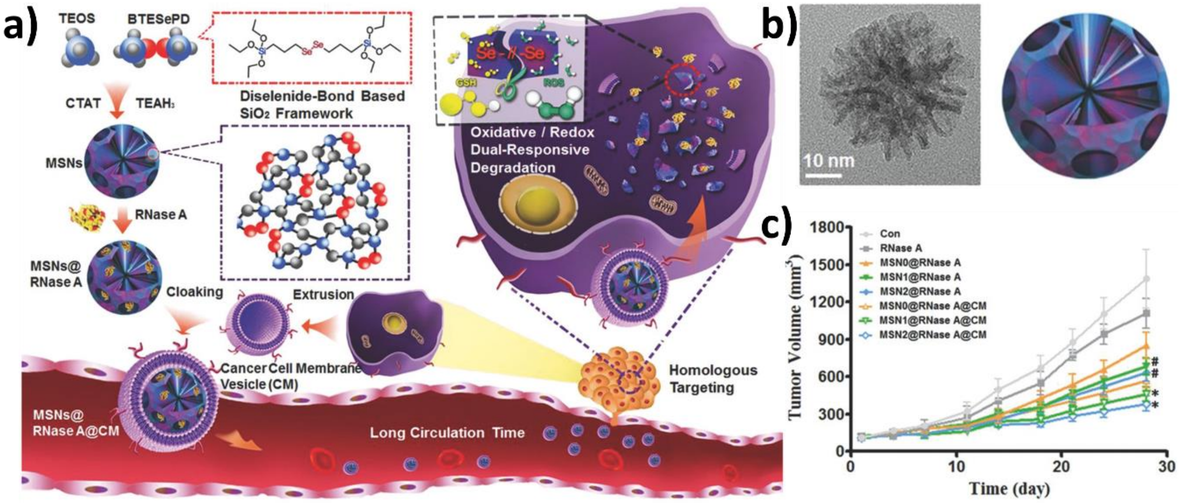

Figure 21. a) Schematic representation of antitumor activity of RNAse A loaded and cell membrane (CM) encapsulated degradable MONs. When intravenously injected the particles actively target the tumor due to CM mediated recognition and upon cellular uptake the particles are degraded and release the cytotoxic cargo. b) TEM image of diselenide-bridged organosilica particles. c) In vivo anti-tumor activity of RNAse A loaded diselenide-bridged nanoparticles. Adapted with permission from Ref 135. Copyright 2018, John Wiley and Sons.

Given that morphology and porosity of MONs can be easily tuned, efforts have been devoted to developing degradable particles characterized by a high cargo loading efficiency, and the capability to accommodate large molecules like proteins and enzymes. To this end, stimuli-responsive hollow mesoporous organosilica silica particles (HMONs) and organosilica capsules have been developed. In order to prepare hollow or capsule-like organosilica particles either hard-templated approaches or liquid-interface assembly methodologies have been employed.[136] Shi and coworkers prepared dual-functionalized HMONs with enhanced doxorubicin loading capacity (148 mg per gram of particles, 14.8 wt%) for in vivo antitumor studies on mice (Figure 22).[137] The hollow structure was prepared via hard-templating method by co-condensation of two organoalkoxysilanes containing benzene and tridisulfide functional groups as bridging units.

It has been shown that the integration of the benzene bridging group not only enhanced the loading capacity, due to enhanced π–π interaction with doxorubicin, but also resulted in decreased hemolytic activity of HMONs, since less Si-OH groups are present on the particle surface. Furthermore, beside the GSH triggered-degradability of HMONs the authors showed that the particles could also release their payload when triggered by the influence of high-intensity focused ultrasound; the authors attributed the enhanced drug release upon ultrasound presence to induced tridisulfide bond cleavage and ultrasonic cavitation effects.

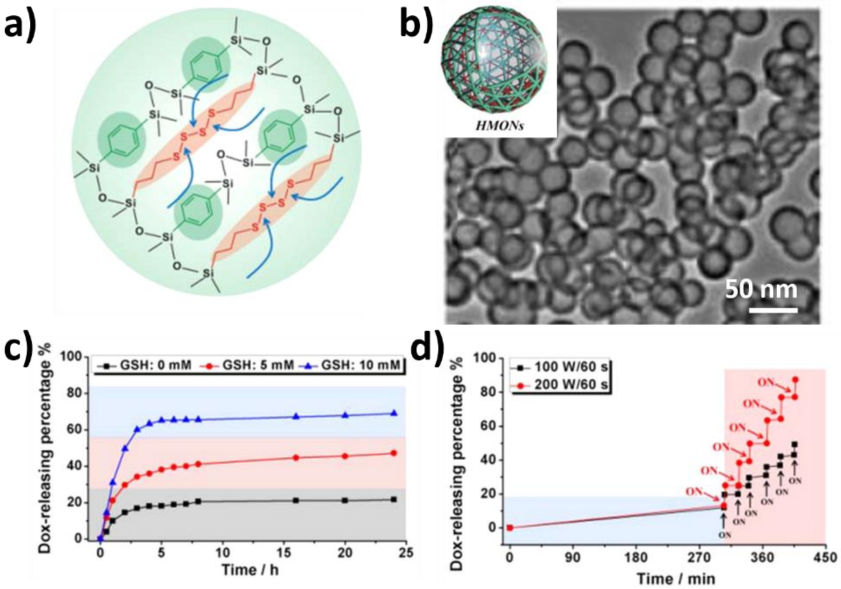

Figure 22. a) Schematic representation of trisulfide and benzene bridged HMONs. b) TEM images of HMONs. c) GSH triggered doxorubicin release form degradable HMONs. d) Doxorubicin release from HMONs upon application of intensity focused ultrasounds. Adapted with permission from Ref 137. Copyright 2014, American Chemical Society.

1.4. Applying supramolecular concepts on organoalkoxysilane chemistry: New opportunities in the preparation of smart organosilica particles

1.4.1. Supramolecular polymers in biomedical research

A major hurdle for current nanomedicines to reach clinical application are safety issues caused by the limited degradation and clearance of nanoparticles from living organisms.[138,139] To solve this safety issue, degradable hard and soft nanomaterials, such as organosilica[119] and polymeric particles,[140] possessing breakable stimuli-responsive functional groups within their framework are currently investigated. Supramolecular polymers prepared by the self-assembly of natural synthetic or natural occurring monomers through noncovalent interactions, such as H-bonds, π–π stacking or electrostatic interactions, have gained much attention in the development of dynamic and smart materials in electronic devices or for biomedical applications.[141] Pioneering work in the preparation of supramolecular polymers by Lehn and coworkers used H-bonds between bifunctional diamidopyridines and uracil derivatives to form linear polymers (Figure 23a).[142] The preparation of more stable supramolecular polymers was later reported by Meijer and coworkers, upon increasing the number of H-bonding motifs present in the monomers used for the preparation of the supramolecular polymer.[143] The authors showed that by introducing a bifunctional monomer containing two 2-ureido-4-pyrimidon units, stronger interactions mediated by four hydrogen bonds, yielded higher polymerization degrees in the final polymer as compared to monomers with less H-bond moieties (Figure 23b). Beside H-bonds, *π-π* interactions between conjugated compounds (Figure 23c) or coordination bonds of metal complexes (Figure 23d) have been used to prepare a variety of new supramolecular materials.[144–146]

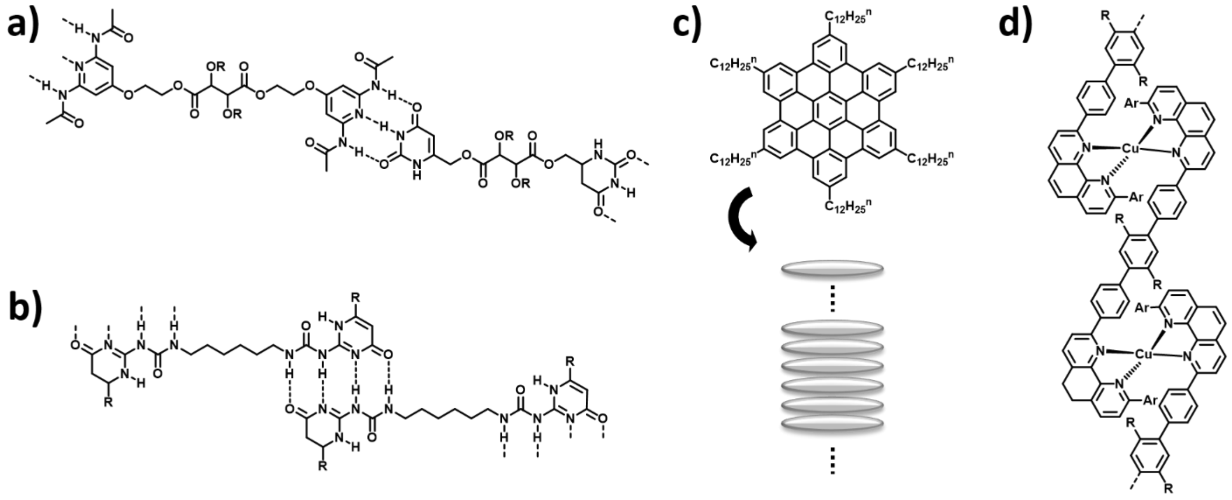

Figure 23. Non-covalent interactions which have been used in the preparation of supramolecular polymers. a) Supramolecular polymer formed between diamidopyridines and uracil derivatives and b) 2-ureido-4-pyrimidon units, via H-bonding interactions. b) Supramolecular polymer formed by *π-π*

interactions between hexa-peri-hexabenzocoronene.[144] c) Supramolecular polymer formed via metal-ligand coordination bond from Cu(I)-o-phenanthroline complexes.[145]

Supramolecular polymers based on macromolecular building blocks represent attractive materials for biomedical applications, such as drug delivery and tissue engineering, allowing the possibility to introduce stimuli-responsive behavior.[147] For example, Langer and coworkers reported the use of a pH-responsive supramolecular gels for the development of gastric devices that were envisioned for use in oral drug delivery given that they possessed prolonged retention and safe gastrointestinal passage (Figure 24).[148] The authors show that while the supramolecular polymer prepared from poly(acryloyl 6-aminocaproic acid) and poly(methacrylic acid-co-ethyl acrylate) is stable in acidic media, it degrades at neutral pH values, allowing for safe excretion of the device.

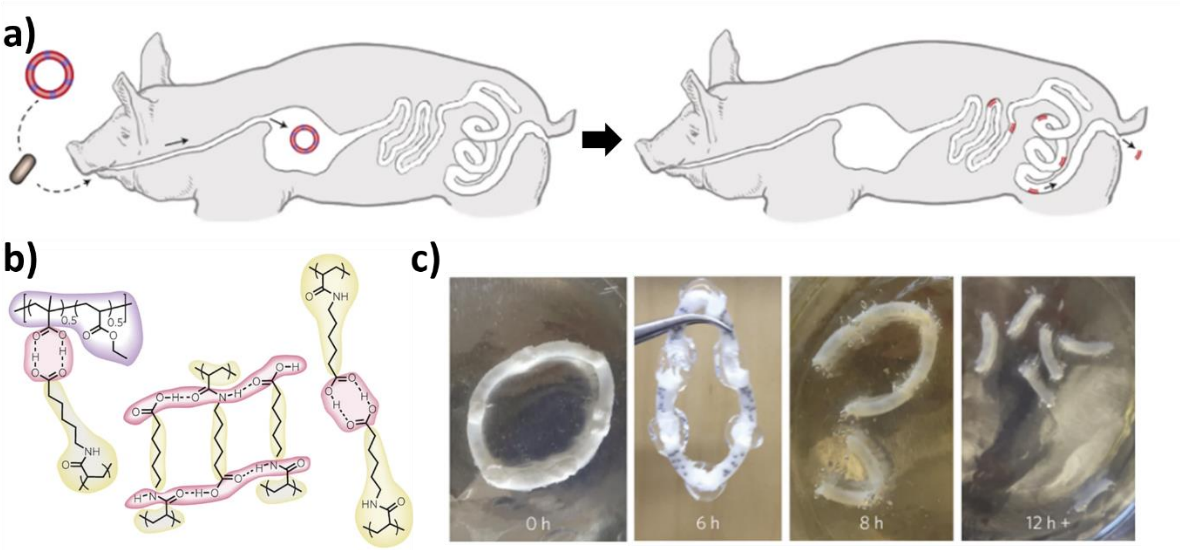

Figure 24. a) Schematic representation in the use of a supramolecular based gastric device in a pig animal model. After oral administration of the encapsulated gastric device within a gelatin capsule, it is retained in the pig's stomach after the dissolution of the gelatin capsule. When translocated to the small and large intestine, the gastric device is degraded, facilitating its safe excretion. b) Chemical structure of poly(acryloyl 6-aminocaproic acid) and poly(methacrylic acid-co-ethyl acrylate)polymer and their supramolecular interactions via H-bonding. c) Degradation of the gastric device at neutral pH-values over time. Adapted with permission from Ref 148.Copyright 2015, Springer Nature.

The use of macromolecular starting materials for the preparation of supramolecular polymers has been proven to yield relatively stable polymers, which can be used for biomedical applications. A drawback in the use of macromolecular precursors in the preparation of supramolecular polymers lies in the limited number of functional groups available for supramolecular assemblies, greatly limiting the preparation of multicomponent assemblies. In contrast, the use of small molecules allows the introduction of multiple unique functionalities within the final supramolecular polymer. For example, small molecule-based supramolecular polymers have been described by Dankers and coworkers as a platform for the intracellular delivery of therapeutic siRNA molecules (Figure 25).[149] The authors showed that the assembly of positively charged 1,3,5-benzenetricarboxamide derivatives which possessed several different functional groups lead to the preparation of multicomponent supramolecular polymers. The resulting fibers were able to physically entrap hydrophobic molecules within the fiber's lipophilic core, while siRNA was electrostatically adsorbed on the outer surface of the aggregate. Further in vitro experiments showed that the supramolecular assembly was internalized into cells and colocalized with the endoplasmic reticulum of the cells. Although small-molecule-based supramolecular polymers allow for the facile preparation of multicomponent assemblies, their monomer design must be optimized to enhance the polymer's mechanical stability, while maintaining its dynamic properties. In fact, compared to macromolecular based monomers, small-molecule-assemblies suffer from poor mechanical properties when biomedical applications are aimed.[147,150]

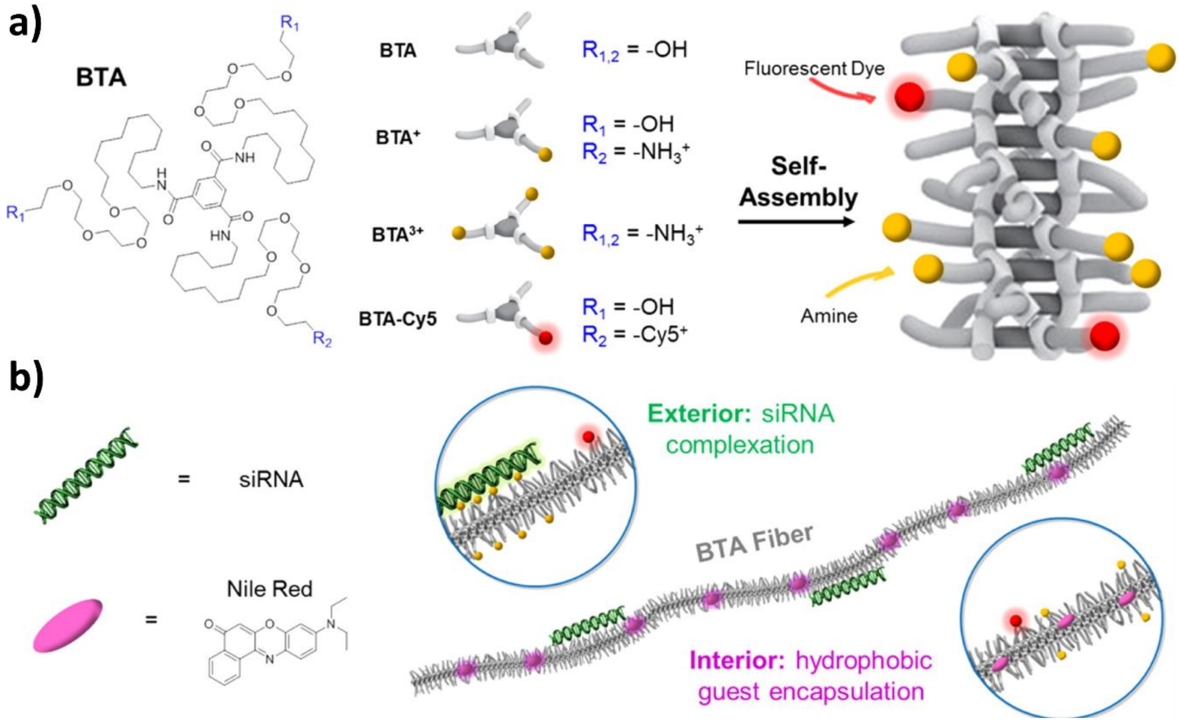

Figure 25. a) Schematic representation in the use of 1,3,5-benzenetricarboxamide derivatives for the preparation of supramolecular polymers. b) Supramolecular assemblies bearing the hydrophobic guest molecule nile red and negatively charged siRNA. Adapted with permission from Ref 149. Copyright 2016, American Chemical Society.

A possibility to prepare small-molecule-based supramolecular aggregates with increased mechanical properties, while retaining their dynamic properties, is the preparation of so-called hybrid bonding polymers (HBP). This this type of material is constituted of molecules that possess the ability to self-assemble via supramolecular interactions and to polymerize by forming covalent bonds.[151] In this regard, Stupp and coworkers reported the preparation of HBPs formed by the covalent and noncovalent polymerization of monomers bearing aromatic dialdehyde, diamine and a peptide sequence (Figure 26).[152] Interestingly, the authors showed that a supramolecular assembly could be reversibly formed and removed on a preexisting covalently linked polymeric fiber.

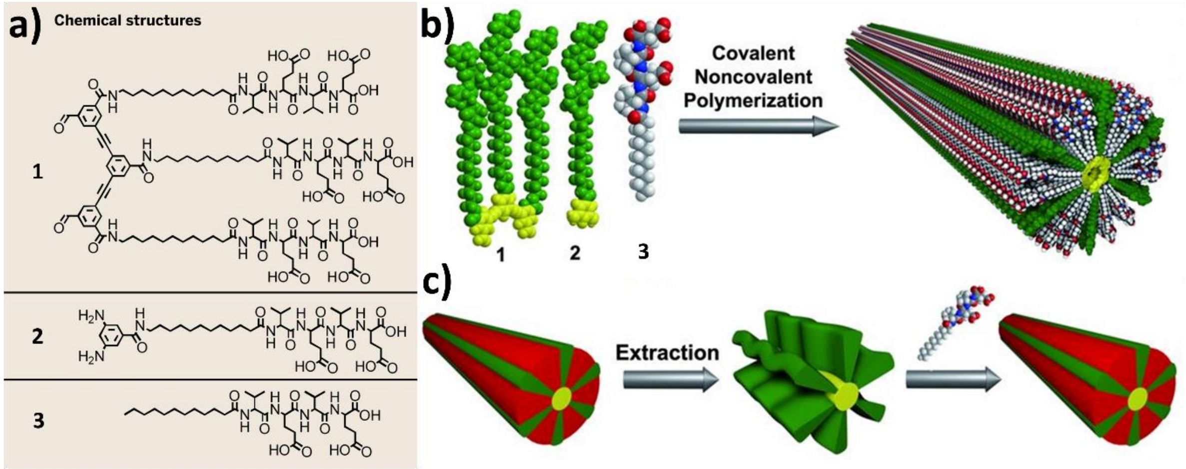

Figure 26. a) Chemical structures of the monomers used for the preparation of HBPs. b) Schematic representation of the formation of the fiber-like HBPs upon supramolecular aggregation and covalent polymerization between monomer 1 and 2, while monomer 3 co-assembles driven only by non-covalent interactions. Adapted with permission from Ref 152. Copyright 2016, American Association for the Advancement of Science.

1.4.2. Self-assembly of organoalkoxysilanes

The self-assembly of organoalkoxysilanes has also been studied[153–155] and reported for the preparation of 2D surface coatings,[156,157] but to date their use has not been considered to develop of new stimuli-responsive materials for biomedical applications or for the preparation of HBPs with dynamic properties. Beside the fabrication of 2D-materials from self-assembled organoalkoxysilanes, a remarkable approach for the preparation of hybrid micellar nanocrystals was described by Fan and coworkers (Figure 27).[158] In this work, the authors self-assembled octadecyldimethyl(3-trimethoxysilylpropyl)ammonium chloride on the surface of hydrophobic gold nanoparticles mediated by hydrophobic interactions. After the assembly, the alkoysilane groups were hydrolyzed and subsequently condensed to form 3D assemblies of hybrid nanocrystals, while retaining the desired plasmon resonance properties of the gold nanoparticle core. The use of organosilica particles, which self-assemble on hydrophobic nanocrystals, represented a novel approach described by the authors, for the preparation of functionalized nanocrystals.

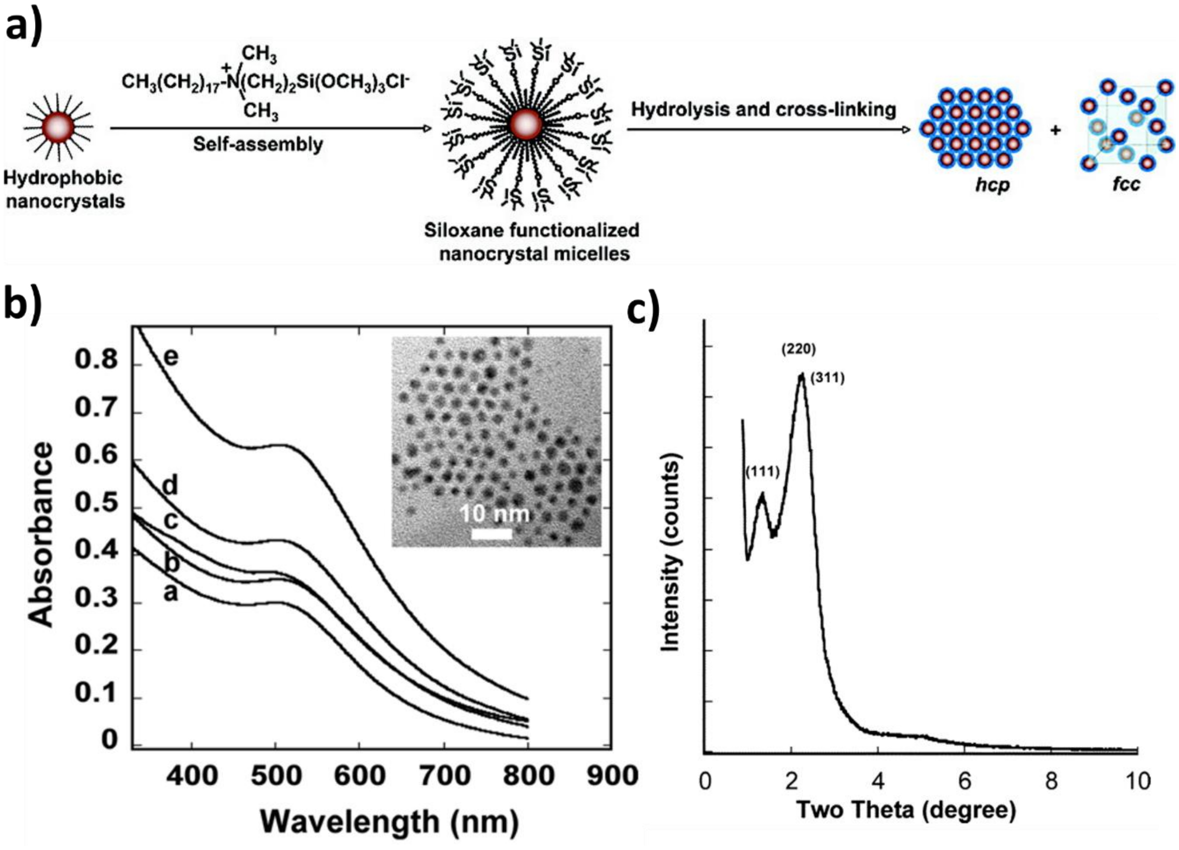

Figure 27. a) Schematic representation in the organoalkoxysilane self-assembly process onto hydrophobic nanocrystals and subsequent crosslinking of the hydrolysable alkoxy-groups in acidic aqueous solution to form hexagonally or cubic arranged hybrid nanocrystals. b) UV-Vis absorption spectra of hybrid nanocrystals, in which the characteristic absorption of the surface resonance band is still visible, even after functionalization. The inset represents a TEM image of hybrid nanocrystals. c) X-ray diffraction pattern of 3D ordered hybrid nanocrystals. Adapted with permission form Ref 158. Copyright 2005, American Chemical Society.

Another example of the use of organoalkoxysilanes for the preparation of self-assembling hybrid structures was reported by Kikuchi and coworkers, which reported the preparation of hybrid-bonding liposomes, named cerasomes (Figure 28). [159] Cerasomes were prepared upon the self-assembly of amphiphilic organoalkoxysilanes, which formed liposomal structures in aqueous solutions. After subsequent polymerization of the liposome alkoxysilane head group, a rigid silicate layer was obtained on the liposomal structure, thus resulting in the formation of stable liposomal structures.

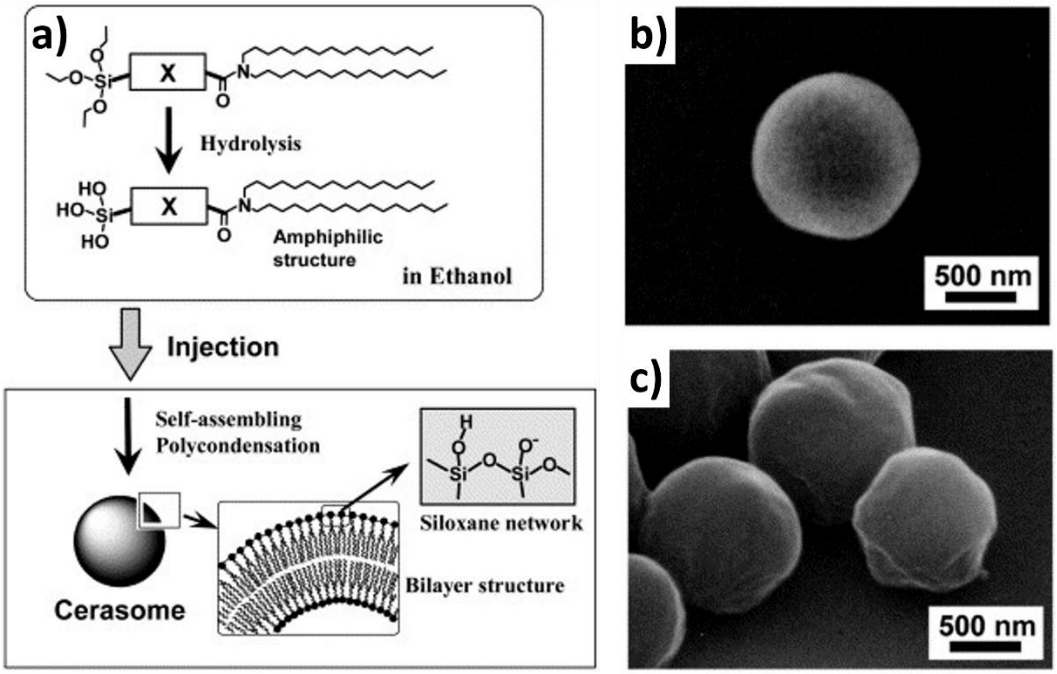

Figure 28. a) Schematic representation of the preparation of cerasomes. SEM image of b) a cerasome particle and c) of a cerasome particle coated with Pt. Adapted with permission from Ref 159. Copyright 2003, Elsevier.

A relatively new and attractive approach to prepare supramolecular structures is the use of oligonucleotides, such as deoxyribonucleic acids (DNAs) or peptide nucleic acids (PNAs). The use of DNA as supramolecular building blocks for the preparation of nanoobjects has been previously demonstrated, providing a power means of developing novel nanotechnologies[160,161] Oligonucleotides are one of the most programmable molecules with self-assembly behavior. DNA self-assembly is dictated by the oligonucleotide nucleobase sequence, involving H-bonding through Watson–Crick base pairs and π–π stacking interactions (Figure 29). PNA oligonucleotides possess a repeating N-(2-aminoethyl)-glycine unit linked via amide bonds as the backbone (Figure 29) and lack therefore the negatively charged phosphodiester backbone as in DNA. Since PNA lacks a negatively charged backbone, it is especially easy to work with in organic solvents, such as DMSO or DMF, and PNA assembly is strong due to the absence of electrostatic repulsions.[162] Further additional features of PNAs is their excellent stability against hydrolases, such as DNases and proteases, a good stability over a wide range of pH values and no need of divalent cations for hybridizations to occur.[163,164]

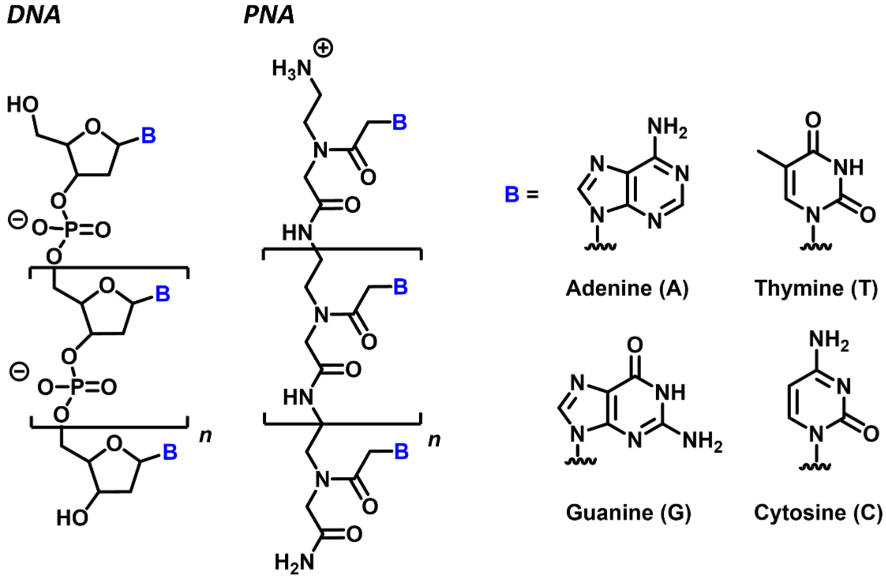

Figure 29. Structure of DNA and PNA oligonucleotides.

The preparation of self-assembled nanostructure from PNA has been extensively reviewed by Gazit and coworkers.[165] Zhang and coworkers have reported the synthesis of PNA-based amphiphilic structures and their use for the preparation of spherical micelles by tuning both, the PNA's Watson–Crick base pairing, the π–π stacking interactions and intermolecular hydrophilic/hydrophilic interactions (Figure 30).[166]

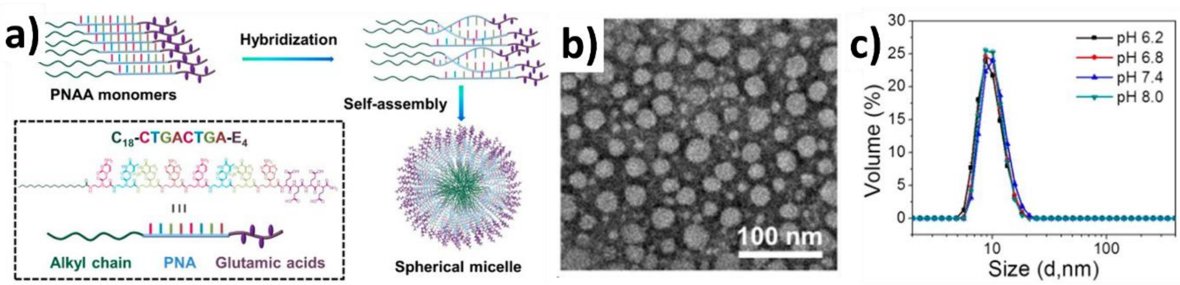

Figure 30. a) Schematic representation of PNA-based monomers to PNA-based micelles. b) TEM images of PNA-based spherical micelles. c) Hydrodynamic diameter measured for PNA-based micelles. Adapted with permission from Ref 166. Copyright 2004, American Chemical Society.

DNA-PNA hybrid nanoparticles have been reported by Kwak and coworkers and studied for their use in the immunological treatment of cancer.[167] As depicted in Figure 31, the hybrid DNA-PNA-aggregate (INA) was constructed upon the self-assembly of 3 components. The final construct was built on a primary micelle formed by the self-assembly of amphiphilic lipid-DNA (U4T), able to hybridize with the adjuvant DNA, the immune activator and a PNA-labeled antigen (e.g.: pOVA). Due to good in-vitro serum stability, the DNA-PNA aggregates were able to reduce the tumor growth in mice through the delivery of immunostimulants.

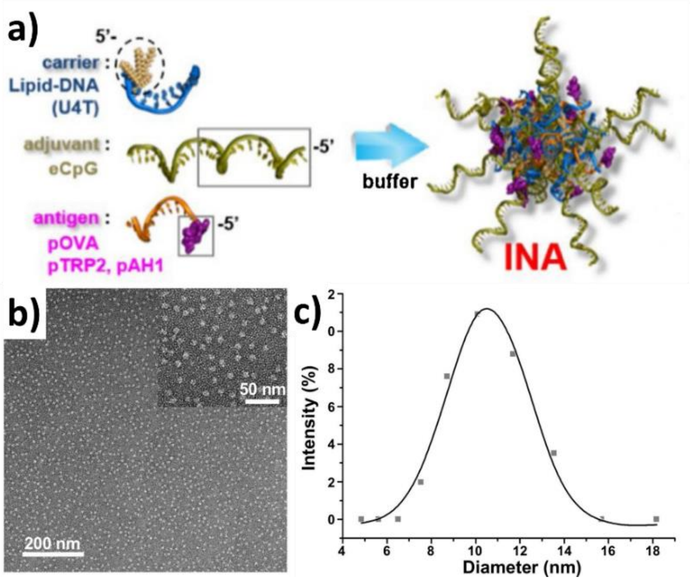

Figure 31. a) Schematic representation in the self-assembly driven formation of an immunostimulant based on DNA-PNA hybrid micelle (INA), formed by mixing of two DNA and a PNA component. b) TEM images of INAs. c) Hydrodynamic radius of INAs. Adapted with permission from Ref 167. Copyright 2019, Elsevier.

1.5. Aim of the thesis

The work presented in this thesis aimed to design and prepare novel porous and stimuli-responsive organosilica particles for drug-delivery applications. In particular, novel bis-alkoxysilanes have been synthesized and used in the preparation of organosilica particles through different methodologies, that is, soft-templating using surfactants or direct self-assembly of organoalkoxysilanes and their subsequent polycondensation. Furthermore, focus was put on the development of morphologically new organosilica particles for theranostic applications.

In the second chapter, the development of new light-degradable mesoporous organosilica particles for potential topical delivery is presented. A new UV-light-responsive bis-alkoxysilane was designed, synthesized, and successfully incorporated in the particle structure. The idea behind this project was to absorb harmful UV light while simultaneously delivering a hydrophobic bioactive molecule, namely provitamin D_3. Pathophysiological vitamin D_3 deficiencies are often observed in people having liver, renal or thyroidal dysfunctions; provitamin D_3 delivery by topical application, in which the active vitamin D_3 formation can occur on site, is therefore of great interest.[168] In addition, skin-related diseases, such as melanoma or inflammations, can be treated with drug-loaded nanoparticles, allowing for deeper penetration through the skin (e.g. through hair follicle canals).[169] Given that UV light is known to penetrate the upper skin layers (epidermis and dermis), UV-light-degradable organosilica particles have potential to serve as breakable drug-delivery systems for sustained release of photosensitive hydrophobic drugs.

In the third chapter, novel cage-like 20 nm sized organosilica particles were prepared and investigated as drug delivery carriers for intravenous administration. Special focus was put on the material physicochemical characterization, such as morphology, loading capacities of hydrophilic or hydrophobic drugs and surface functionalization with small peptides. To understand how size, morphology and functionalization affect the biological behavior both in vitro and in vivo studies were carried out. Biodistribution in healthy mice showed the particle ability to strongly accumulate in the endothelial layer of the liver, avoiding macrophage capture, suggesting the possibility to use them for the treatment of small liver tumors. With the research presented the advantages and hurdles in the use of small-sized cage-like organosilica particles are being assessed.

In the fourth chapter, the possibility to prepare organosilica particles with alkoxysilane derivatives of DNA or PNA oligonucleotides was investigated. The aim was to develop novel hybrid and biocompatible materials able to recognize specific biomarkers (e.g. enzymes, complementary strands) and to react in their presence. To prepare organosilica particles with DNA- or PNA-alkoxysilanes, three different preparation methodologies were investigated: 1) Stöber synthesis, 2) modified Stöber synthesis employing surfactants as structure-directing agents and 3) the possibility to form organosilicas via supramolecular interactions between the PNA-alkoxysilane molecules, inspired by the preparation of hybrid bonding polymers as discussed in section 1.4.[152] To the best of our knowledge, the preparation of oligonucleotide bridged organosilica particles has been scarcely investigated in the literature. Special focus was put on the preparation of bis-alkoxysilanes from mono-PNA-alkoxysilanes driven by supramolecular interactions, namely Watson–Crick base pairing, and their use to prepare organosilicas, which possess dynamic supramolecular moieties within their framework. The results show that, by using alkoxysilane chemistry, it is possible to develop new materials that bear site-specific binding moieties and that can react with specific oligonucleotides, which could pave the way to possible sensing applications.

1.6. References

(1) Vert, M.; Doi, Y.; Hellwich, K.-H.; Hess, M.; Hodge, P.; Kubisa, P.; Rinaudo, M.; Schué, F. Terminology for Biorelated Polymers and Applications (IUPAC Recommendations 2012). *Pure Appl. Chem.* **2012**, *84* (2), 377–410.

(2) European Commission, *Off. J. Eur. Union* **2011**, *275*, 38–40. https://eur-lex.europa.eu/legal-content/EN/TXT/PDF/?uri=CELEX:32011H0696&from=EN.

(3) Wagner, V.; Dullaart, A.; Bock, A. K.; Zweck, A. The Emerging Nanomedicine Landscape. *Nat. Biotechnol.* **2006**, *24* (10), 1211–1217. DOI: 10.1038/nbt1006-1211.

(4) Anselmo, A. C.; Mitragotri, S. Nanoparticles in the Clinic: An Update. *Bioeng. Transl. Med.* **2019**, *4* (3), 1–16. DOI: 10.1002/btm2.10143.

(5) Akinc, A.; Maier, M. A.; Manoharan, M.; Fitzgerald, K.; Jayaraman, M.; Barros, S.; Ansell, S.; Du, X.; Hope, M. J.; Madden, T. D.; Mui, B. L.; Semple, S. C.; Tam, Y. K.; Ciufolini, M.; Witzigmann, D.; Kulkarni, J. A.; van der Meel, R.; Cullis, P. R. The Onpattro Story and the Clinical Translation of Nanomedicines Containing Nucleic Acid-Based Drugs. *Nat. Nanotechnol.* **2019**, *14* (12), 1084–1087. DOI: 10.1038/s41565-019-0591-y.

(6) He, H.; Liu, L.; Morin, E. E.; Liu, M.; Schwendeman, A. Survey of Clinical Translation of Cancer Nanomedicines - Lessons Learned from Successes and Failures. *Acc. Chem. Res.* **2019**, *52* (9), 2673–2683. DOI: 10.1021/acs.accounts.9b00228.

(7) Che, H.; Van Hest, J. C. M. Stimuli-Responsive Polymersomes and Nanoreactors. *J. Mater. Chem. B* **2016**, *4* (27), 4632–4647. DOI: 10.1039/c6tb01163b.

(8) Rideau, E.; Dimova, R.; Schwille, P.; Wurm, F. R.; Landfester, K. Liposomes and Polymersomes: A Comparative Review towards Cell Mimicking. *Chem. Soc. Rev.* **2018**, *47* (23), 8572–8610. DOI: 10.1039/c8cs00162f.

(9) Dawidczyk, C. M.; Kim, C.; Park, J. H.; Russell, L. M.; Lee, K. H.; Pomper, M. G.; Searson, P. C. State-of-the-Art in Design Rules for Drug Delivery Platforms: Lessons Learned from FDA-Approved Nanomedicines. *J. Control. Release* **2014**, *187*, 133–144. DOI: 10.1016/j.jconrel.2014.05.036.

(10) Caracciolo, G. Clinically Approved Liposomal Nanomedicines: Lessons Learned from the Biomolecular Corona. *Nanoscale* **2018**, *10* (9), 4167–4172. DOI: 10.1039/c7nr07450f.

(11) Smietana, K.; Siatkowski, M.; Møller, M. Trends in Clinical Success Rates. *Nat. Rev. Drug Discov.* **2016**, *15* (6), 379–380. DOI: 10.1038/nrd.2016.85.

(12) Wolfbeis, O. S. An Overview of Nanoparticles Commonly Used in Fluorescent Bioimaging. *Chem. Soc. Rev.* **2015**, *44* (14), 4743–4768. DOI: 10.1039/c4cs00392f.

(13) Smith, B. R.; Gambhir, S. S. Nanomaterials for in Vivo Imaging. *Chem. Rev.* **2017**, *117* (3), 901–986. DOI: 10.1021/acs.chemrev.6b00073.

(14) Kohle, F. F. E.; Hinckley, J. A.; Li, S.; Dhawan, N.; Katt, W. P.; Erstling, J. A.; Werner-Zwanziger, U.; Zwanziger, J.; Cerione, R. A.; Wiesner, U. B. Amorphous Quantum Nanomaterials. *Adv. Mater.* **2019**, *31* (5), 1–9. DOI: 10.1002/adma.201806993.

(15) Frey, N. A.; Peng, S.; Cheng, K.; Sun, S. Magnetic Nanoparticles: Synthesis, Functionalization, and Applications in Bioimaging and Magnetic Energy Storage. *Chem. Soc. Rev.* **2009**, *38* (9), 2532–2542. DOI: 10.1039/b815548h.

(16) Han, X.; Xu, K.; Taratula, O.; Farsad, K. Applications of Nanoparticles in Biomedical Imaging. *Nanoscale* **2019**, *11* (3), 799–819. DOI: 10.1039/c8nr07769j.

(17) Matea, C. T.; Mocan, T.; Tabaran, F.; Pop, T.; Mosteanu, O.; Puia, C.; Iancu, C.; Mocan, L. Quantum Dots in Imaging, Drug Delivery and Sensor Applications. *Int. J. Nanomedicine* **2017**, *12*, 5421–5431. DOI: 10.2147/IJN.S138624.

(18) Sun, T.; Zhang, Y. S.; Pang, B.; Hyun, D. C.; Yang, M.; Xia, Y. Engineered Nanoparticles for Drug Delivery in Cancer Therapy. *Angew. Chemie - Int. Ed.* **2014**, *53* (46), 12320–12364. DOI: 10.1002/anie.201403036.

(19) Talamini, L.; Violatto, M. B.; Cai, Q.; Monopoli, M. P.; Kantner, K.; Krpetić, Ž.; Perez-Potti, A.; Cookman, J.; Garry, D.; Silveira, C. P.; Boselli, L.; Pelaz, B.; Serchi, T.; Cambier, S.; Gutleb, A. C.; Feliu, N.; Yan, Y.; Salmona, M.; Parak, W. J.; Dawson, K. A.; Bigini, P. Influence of Size and Shape on the Anatomical Distribution of Endotoxin-Free Gold Nanoparticles. *ACS Nano* **2017**, *11* (6), 5519–5529. DOI: 10.1021/acsnano.7b00497.

(20) Decuzzi, P.; Godin, B.; Tanaka, T.; Lee, S. Y.; Chiappini, C.; Liu, X.; Ferrari, M. Size and Shape Effects in the Biodistribution of Intravascularly Injected Particles. *J. Control. Release* **2010**, *141* (3), 320–327. DOI: 10.1016/j.jconrel.2009.10.014.

(21) Zhu, X.; Vo, C.; Taylor, M.; Smith, B. R. Non-Spherical Micro- and Nanoparticles in Nanomedicine. *Mater. Horizons* **2019**, *6* (6), 1094–1121. DOI: 10.1039/c8mh01527a.

(22) Cataldi, M.; Vigliotti, C.; Mosca, T.; Cammarota, M. R.; Capone, D. Emerging Role of the Spleen in the Pharmacokinetics of Monoclonal Antibodies, Nanoparticles and Exosomes. *Int. J. Mol. Sci.* **2017**, *18* (6). DOI: 10.3390/ijms18061249.

(23) Blanco, E.; Shen, H.; Ferrari, M. Principles of Nanoparticle Design for Overcoming Biological Barriers to Drug Delivery. *Nat. Biotechnol.* **2015**, *33* (9), 941–951. DOI: 10.1038/nbt.3330.

(24) Dai, Q.; Walkey, C.; Chan, W. C. W. Polyethylene Glycol Backfilling Mitigates the Negative Impact of the Protein Corona on Nanoparticle Cell Targeting. *Angew. Chemie - Int. Ed.* **2014**, *53* (20), 5093–5096. DOI: 10.1002/anie.201309464.

(25) Van Vlerken, L. E.; Vyas, T. K.; Amiji, M. M. Poly(Ethylene Glycol)-Modified Nanocarriers for Tumor-Targeted and Intracellular Delivery. *Pharm. Res.* **2007**, *24* (8), 1405–1414. DOI: 10.1007/s11095-007-9284-6.

(26) Schöttler, S.; Becker, G.; Winzen, S.; Steinbach, T.; Mohr, K.; Landfester, K.; Mailänder, V.;

Wurm, F. R. Protein Adsorption Is Required for Stealth Effect of Poly(Ethylene Glycol)- and Poly(Phosphoester)-Coated Nanocarriers. *Nat. Nanotechnol.* **2016**, *11* (4), 372–377. DOI: 10.1038/nnano.2015.330.

(27) Giulimondi, F.; Digiacomo, L.; Pozzi, D.; Palchetti, S.; Vulpis, E.; Capriotti, A. L.; Chiozzi, R. Z.; Laganà, A.; Amenitsch, H.; Masuelli, L.; Mahmoudi, M.; Screpanti, I.; Zingoni, A.; Caracciolo, G. Interplay of Protein Corona and Immune Cells Controls Blood Residency of Liposomes. *Nat. Commun.* **2019**, *10* (1), 1–11. DOI: 10.1038/s41467-019-11642-7.

(28) Simon, J.; Müller, L. K.; Kokkinopoulou, M.; Lieberwirth, I.; Morsbach, S.; Landfester, K.; Mailänder, V. Exploiting the Biomolecular Corona: Pre-Coating of Nanoparticles Enables Controlled Cellular Interactions. *Nanoscale* **2018**, *10* (22), 10731–10739. DOI: 10.1039/c8nr03331e.

(29) Xu, L.; Huang, C.; Huang, W.; Tang, W.; Rait, A.; Yin, Y. Z.; Cruz, I.; Xiang, L.; Pirollo, K. F.; Chang, E. H. Systemic Tumor-Targeted Gene Delivery by Anti-Transferrin. **2002**, *1* (March), 337–346.

(30) Sugahara, K. N.; Teesalu, T.; Karmali, P. P.; Kotamraju, V. R.; Agemy, L.; Girard, O. M.; Hanahan, D.; Mattrey, R. F.; Ruoslahti, E. Tissue-Penetrating Delivery of Compounds and Nanoparticles into Tumors. *Cancer Cell* **2009**, *16* (6), 510–520. DOI: 10.1016/j.ccr.2009.10.013.

(31) Sugahara, K. N.; Scodeller, P.; Braun, G. B.; De Mendoza, T. H.; Yamazaki, C. M.; Kluger, M. D.; Kitayama, J.; Alvarez, E.; Howell, S. B.; Teesalu, T.; Ruoslahti, E.; Lowy, A. M. A Tumor-Penetrating Peptide Enhances Circulation-Independent Targeting of Peritoneal Carcinomatosis. *J. Control. Release* **2015**, *212*, 59–69. DOI: 10.1016/j.jconrel.2015.06.009.

(32) Phillips, E.; Penate-Medina, O.; Zanzonico, P. B.; Carvajal, R. D.; Mohan, P.; Ye, Y.; Humm, J.; Gönen, M.; Kalaigian, H.; Schöder, H.; Strauss, H. W.; Larson, S. M.; Wiesner, U.; Bradbury, M. S. Clinical Translation of an Ultrasmall Inorganic Optical-PET Imaging Nanoparticle Probe. *Sci. Transl. Med.* **2014**, *6* (260). DOI: 10.1126/scitranslmed.3009524.

(33) Juthani, R.; Madajewski, B.; Yoo, B.; Zhang, L.; Chen, P. M.; Chen, F.; Turker, M. Z.; Ma, K.; Overholtzer, M.; Longo, V. A.; Carlin, S.; Aragon-Sanabria, V.; Huse, J.; Gonen, M.; Zanzonico, P.; Rudin, C. M.; Wiesner, U.; Bradbury, M. S.; Brennan, C. W. Ultrasmall Core-Shell Silica Nanoparticles for Precision Drug Delivery in a High-Grade Malignant Brain Tumor Model. *Clin. Cancer Res.* **2020**, *26* (1), 147–158. DOI: 10.1158/1078-0432.CCR-19-1834.

(34) Li, L.; Lu, Y.; Lin, Z.; Mao, A. S.; Jiao, J.; Zhu, Y.; Jiang, C.; Yang, Z.; Peng, M.; Mao, C. Ultralong Tumor Retention of Theranostic Nanoparticles with Short Peptide-Enabled Active Tumor Homing. *Mater. Horizons* **2019**, *6* (9), 1845–1853. DOI: 10.1039/c9mh00014c.

(35) Qu, X.; Qiu, P.; Zhu, Y.; Yang, M.; Mao, C. Guiding Nanomaterials to Tumors for Breast Cancer Precision Medicine: From Tumor-Targeting Small-Molecule Discovery to Targeted

Nanodrug Delivery. *NPG Asia Mater.* **2017**, *9* (12), e452. DOI: 10.1038/am.2017.196.

(36) Cui, J.; Alt, K.; Ju, Y.; Gunawan, S. T.; Braunger, J. A.; Wang, T. Y.; Dai, Y.; Dai, Q.; Richardson, J. J.; Guo, J.; Björnmalm, M.; Hagemeyer, C. E.; Caruso, F. Ligand-Functionalized Poly(Ethylene Glycol) Particles for Tumor Targeting and Intracellular Uptake. *Biomacromolecules* **2019**, *20* (9), 3592–3600. DOI: 10.1021/acs.biomac.9b00925.

(37) Ge, J.; Hu, Y.; Biasini, M.; Beyermann, W. P.; Yin, Y. Superparamagnetic Magnetite Colloidal Nanocrystal Clusters. *Angew. Chemie - Int. Ed.* **2007**, *46* (23), 4342–4345. DOI: 10.1002/anie.200700197.

(38) Smith, B. R.; Heverhagen, J.; Knopp, M.; Schmalbrock, P.; Shapiro, J.; Shiomi, M.; Moldovan, N. I.; Ferrari, M.; Lee, S. C. Localization to Atherosclerotic Plaque and Biodistribution of Biochemically Derivatized Superparamagnetic Iron Oxide Nanoparticles (SPIONs) Contrast Particles for Magnetic Resonance Imaging (MRI). *Biomed. Microdevices* **2007**, *9* (5), 719–727. DOI: 10.1007/s10544-007-9081-3.

(39) Jun, Y. W.; Huh, Y. M.; Choi, J. S.; Lee, J. H.; Song, H. T.; Kim, S.; Yoon, S.; Kim, K. S.; Shin, J. S.; Suh, J. S.; Cheon, J. Nanoscale Size Effect of Magnetic Nanocrystals and Their Utilization for Cancer Diagnosis via Magnetic Resonance Imaging. *J. Am. Chem. Soc.* **2005**, *127* (16), 5732–5733. DOI: 10.1021/ja0422155.

(40) Choi, J. S.; Kim, S.; Yoo, D.; Shin, T. H.; Kim, H.; Gomes, M. D.; Kim, S. H.; Pines, A.; Cheon, J. Distance-Dependent Magnetic Resonance Tuning as a Versatile MRI Sensing Platform for Biological Targets. *Nat. Mater.* **2017**, *16* (5), 537–542. DOI: 10.1038/nmat4846.

(41) Miller, M. A.; Gadde, S.; Pfirschke, C.; Engblom, C.; Sprachman, M. M.; Kohler, R. H.; Yang, K. S.; Laughney, A. M.; Wojtkiewicz, G.; Kamaly, N.; Bhonagiri, S.; Pittet, M. J.; Farokhzad, O. C.; Weissleder, R. Predicting Therapeutic Nanomedicine Efficacy Using a Companion Magnetic Resonance Imaging Nanoparticle. *Sci. Transl. Med.* **2015**, *7* (314), 1–13. DOI: 10.1126/scitranslmed.aac6522.

(42) Weizenecker, J.; Gleich, B.; Rahmer, J.; Dahnke, H.; Borgert, J. Three-Dimensional Real-Time in Vivo Magnetic Particle Imaging. *Phys. Med. Biol.* **2009**, *54* (5). DOI: 10.1088/0031-9155/54/5/L01.

(43) Yu, M. K.; Jeong, Y. Y.; Park, J.; Park, S.; Kim, J. W.; Min, J. J.; Kim, K.; Jon, S. Drug-Loaded Superparamagnetic Iron Oxide Nanoparticles for Combined Cancer Imaging and Therapy in Vivo. *Angew. Chemie - Int. Ed.* **2008**, *47* (29), 5362–5365. DOI: 10.1002/anie.200800857.

(44) Das, M.; Mishra, D.; Dhak, P.; Gupta, S.; Maiti, T. K.; Basak, A.; Pramanik, P. Biofunctionalized, Phosphonate-Grafted, Ultrasmall Iron Oxide Nanoparticles for Combined Targeted Cancer Therapy and Multimodal Imaging. *Small* **2009**, *5* (24), 2883–2893. DOI: 10.1002/smll.200901219.

(45) Mertz, D.; Sandre, O.; Bégin-Colin, S. Drug Releasing Nanoplatforms Activated by Alternating Magnetic Fields. *Biochim. Biophys. Acta - Gen. Subj.* **2017**, *1861* (6), 1617–

1641. DOI: 10.1016/j.bbagen.2017.02.025.

(46) Lee, J. H.; Jang, J. T.; Choi, J. S.; Moon, S. H.; Noh, S. H.; Kim, J. W.; Kim, J. G.; Kim, I. S.; Park, K. I.; Cheon, J. Exchange-Coupled Magnetic Nanoparticles for Efficient Heat Induction. *Nat. Nanotechnol.* **2011**, *6* (7), 418–422. DOI: 10.1038/nnano.2011.95.

(47) Barrera, G.; Allia, P.; Tiberto, P. Temperature-Dependent Heating Efficiency of Magnetic Nanoparticles for Applications in Precision Nanomedicine. *Nanoscale* **2020**, *12* (11), 6360–6377. DOI: 10.1039/c9nr09503a.

(48) Cho, N. H.; Cheong, T. C.; Min, J. H.; Wu, J. H.; Lee, S. J.; Kim, D.; Yang, J. S.; Kim, S.; Kim, Y. K.; Seong, S. Y. A Multifunctional Core-Shell Nanoparticle for Dendritic Cell-Based Cancer Immunotherapy. *Nat. Nanotechnol.* **2011**, *6* (10), 675–682. DOI: 10.1038/nnano.2011.149.

(49) Chiang, C. S.; Lin, Y. J.; Lee, R.; Lai, Y. H.; Cheng, H. W.; Hsieh, C. H.; Shyu, W. C.; Chen, S. Y. Combination of Fucoidan-Based Magnetic Nanoparticles and Immunomodulators Enhances Tumour-Localized Immunotherapy. *Nat. Nanotechnol.* **2018**, *13* (8), 746–754. DOI: 10.1038/s41565-018-0146-7.

(50) Mannix, R. J.; Kumar, S.; Cassiola, F.; Montoya-Zavala, M.; Feinstein, E.; Prentiss, M.; Ingber, D. E. Nanomagnetic Actuation of Receptor-Mediated Signal Transduction. *Nat. Nanotechnol.* **2008**, *3* (1), 36–40. DOI: 10.1038/nnano.2007.418.

(51) Thomas, C. R.; Ferris, D. P.; Lee, J. H.; Choi, E.; Cho, M. H.; Kim, E. S.; Stoddart, J. F.; Shin, J. S.; Cheon, J.; Zink, J. I. Noninvasive Remote-Controlled Release of Drug Molecules in Vitro Using Magnetic Actuation of Mechanized Nanoparticles. *J. Am. Chem. Soc.* **2010**, *132* (31), 10623–10625. DOI: 10.1021/ja1022267.

(52) Hutter, E.; Fendler, J. H. Exploitation of Localized Surface Plasmon Resonance. *Adv. Mater.* **2004**, *16* (19), 1685–1706. DOI: 10.1002/adma.200400271.

(53) Zhuang, Y.; Liu, L.; Wu, X.; Tian, Y.; Zhou, X.; Xu, S.; Xie, Z.; Ma, Y. Size and Shape Effect of Gold Nanoparticles in “Far-Field” Surface Plasmon Resonance. *Part. Part. Syst. Charact.* **2019**, *36* (1), 1–8. DOI: 10.1002/ppsc.201800077.

(54) Chen, Y.; Xianyu, Y.; Jiang, X. Surface Modification of Gold Nanoparticles with Small Molecules for Biochemical Analysis. *Acc. Chem. Res.* **2017**, *50* (2), 310–319. DOI: 10.1021/acs.accounts.6b00506.

(55) Ali, M. R. K.; Wu, Y.; El-Sayed, M. A. Gold-Nanoparticle-Assisted Plasmonic Photothermal Therapy Advances Toward Clinical Application. *J. Phys. Chem. C* **2019**, *123* (25), 15375–15393. DOI: 10.1021/acs.jpcc.9b01961.

(56) Dickerson, E. B.; Dreaden, E. C.; Huang, X.; El-Sayed, I. H.; Chu, H.; Pushpanketh, S.; McDonald, J. F.; El-Sayed, M. A. Gold Nanorod Assisted Near-Infrared Plasmonic Photothermal Therapy (PPTT) of Squamous Cell Carcinoma in Mice. *Cancer Lett.* **2008**, *269* (1), 57–66. DOI: 10.1016/j.canlet.2008.04.026.

(57) Zhang, D.; Wu, T.; Qin, X.; Qiao, Q.; Shang, L.; Song, Q.; Yang, C.; Zhang, Z. Intracellularly Generated Immunological Gold Nanoparticles for Combinatorial Photothermal Therapy and Immunotherapy against Tumor. *Nano Lett.* **2019**, *19* (9), 6635–6646. DOI: 10.1021/acs.nanolett.9b02903.

(58) Popovtzer, R.; Agrawal, A.; Kotov, N. A.; Popovtzer, A.; Balter, J.; Carey, T. E.; Kopelman, R. Targeted Gold Nanoparticles Enable Molecular CT Imaging of Cancer. *Nano Lett.* **2008**, *8* (12), 4593–4596. DOI: 10.1021/nl8029114.

(59) Xi, D.; Dong, S.; Meng, X.; Lu, Q.; Meng, L.; Ye, J. Gold Nanoparticles as Computerized Tomography (CT) Contrast Agents. *RSC Adv.* **2012**, *2* (33), 12515–12524. DOI: 10.1039/c2ra21263c.

(60) Lu, Z.; Long, Y.; Cun, X.; Wang, X.; Li, J.; Mei, L.; Yang, Y.; Li, M.; Zhang, Z.; He, Q. A Size-Shrinkable Nanoparticle-Based Combined Anti-Tumor and Anti-Inflammatory Strategy for Enhanced Cancer Therapy. *Nanoscale* **2018**, *10* (21), 9957–9970. DOI: 10.1039/c8nr01184b.

(61) Michalet, X., Pinaud, F.F., Bentolila, L. . Quantum_dots_for_live_cells__i.PDF. *Science (80-.).* **2005**, *307* (January), 538–544.

(62) Han, H.; Di Francesco, G.; Maye, M. M. Size Control and Photophysical Properties of Quantum Dots Prepared via a Novel Tunable Hydrothermal Route. *J. Phys. Chem. C* **2010**, *114* (45), 19270–19277. DOI: 10.1021/jp107702b.

(63) Tsuboi, S.; Sasaki, A.; Sakata, T.; Yasuda, H.; Jin, T. Immunoglobulin Binding (B1) Domain Mediated Antibody Conjugation to Quantum Dots for in Vitro and in Vivo Molecular Imaging. *Chem. Commun.* **2017**, *53* (68), 9450–9453. DOI: 10.1039/c7cc04966h.

(64) Medintz, I. L.; Stewart, M. H.; Trammell, S. A.; Susumu, K.; Delehanty, J. B.; Mei, B. C.; Melinger, J. S.; Blanco-Canosa, J. B.; Dawson, P. E.; Mattoussi, H. Quantum-Dot/Dopamine Bioconjugates Function as Redox Coupled Assemblies for in Vitro and Intracellular PH Sensing. *Nat. Mater.* **2010**, *9* (8), 676–684. DOI: 10.1038/nmat2811.

(65) Jeong, S.; Jung, Y.; Bok, S.; Ryu, Y. M.; Lee, S.; Kim, Y. E.; Song, J.; Kim, M.; Kim, S. Y.; Ahn, G. O.; Kim, S. Multiplexed In Vivo Imaging Using Size-Controlled Quantum Dots in the Second Near-Infrared Window. *Adv. Healthc. Mater.* **2018**, *7* (24), 1–9. DOI: 10.1002/adhm.201800695.

(66) Hu, R.; Yong, K. T.; Roy, I.; Ding, H.; Law, W. C.; Cai, H.; Zhang, X.; Vathy, L. A.; Bergey, E. J.; Prasad, P. N. Functionalized Near-Infrared Quantum Dots for Invivo Tumor Vasculature Imaging. *Nanotechnology* **2010**, *21* (14). DOI: 10.1088/0957-4484/21/14/145105.

(67) Bruun, K.; Hille, C. Study on Intracellular Delivery of Liposome Encapsulated Quantum Dots Using Advanced Fluorescence Microscopy. *Sci. Rep.* **2019**, *9* (1), 1–15. DOI: 10.1038/s41598-019-46732-5.

(68) Molaei, M. J. Carbon Quantum Dots and Their Biomedical and Therapeutic Applications: A Review. *RSC Adv.* **2019**, *9* (12), 6460–6481. DOI: 10.1039/c8ra08088g.

(69) Du, J.; Xu, N.; Fan, J.; Sun, W.; Peng, X. Carbon Dots for In Vivo Bioimaging and Theranostics. *Small* **2019**, *15* (32), 1–16. DOI: 10.1002/smll.201805087.

(70) Liang, X. J.; Meng, H.; Wang, Y.; He, H.; Meng, J.; Lu, J.; Wang, P. C.; Zhao, Y.; Gao, X.; Sun, B.; Chen, C.; Xing, G.; Shen, D.; Gottesman, M. M.; Wu, Y.; Yin, J. J.; Jia, L. Metallofullerene Nanoparticles Circumvent Tumor Resistance to Cisplatin by Reactivating Endocytosis. *Proc. Natl. Acad. Sci. U. S. A.* **2010**, *107* (16), 7449–7454. DOI: 10.1073/pnas.0909707107.

(71) Montellano, A.; Da Ros, T.; Bianco, A.; Prato, M. Fullerene C60 as a Multifunctional System for Drug and Gene Delivery. *Nanoscale* **2011**, *3* (10), 4035–4041. DOI: 10.1039/c1nr10783f.

(72) Ramos-Soriano, J.; Reina, J. J.; Illescas, B. M.; De La Cruz, N.; Rodríguez-Pérez, L.; Lasala, F.; Rojo, J.; Delgado, R.; Martín, N. Synthesis of Highly Efficient Multivalent Disaccharide/[60]Fullerene Nanoballs for Emergent Viruses. *J. Am. Chem. Soc.* **2019**, *141* (38), 15403–15412. DOI: 10.1021/jacs.9b08003.

(73) Chung, C.; Kim, Y. K.; Shin, D.; Ryoo, S. R.; Hong, B. H.; Min, D. H. Biomedical Applications of Graphene and Graphene Oxide. *Acc. Chem. Res.* **2013**, *46* (10), 2211–2224. DOI: 10.1021/ar300159f.

(74) Liu, Z.; Robinson, J. T.; Sun, X.; Dai, H. PEGylated Nanographene Oxide for Delivery of Water-Insoluble Cancer Drugs. *J. Am. Chem. Soc.* **2008**, *130* (33), 10876–10877. DOI: 10.1021/ja803688x.

(75) Campbell, E.; Hasan, M. T.; Pho, C.; Callaghan, K.; Akkaraju, G. R.; Naumov, A. V. Graphene Oxide as a Multifunctional Platform for Intracellular Delivery, Imaging, and Cancer Sensing. *Sci. Rep.* **2019**, *9* (1), 1–9. DOI: 10.1038/s41598-018-36617-4.

(76) Wang, Y.; Xu, J.; Xia, X.; Yang, M.; Vangveravong, S.; Chen, J.; MacH, R. H.; Xia, Y. SV119-Gold Nanocage Conjugates: A New Platform for Targeting Cancer Cells via Sigma-2 Receptors. *Nanoscale* **2012**, *4* (2), 421–424. DOI: 10.1039/c1nr11469g.

(77) Hong, S. Y.; Tobias, G.; Al-Jamal, K. T.; Ballesteros, B.; Ali-Boucetta, H.; Lozano-Perez, S.; Nellist, P. D.; Sim, R. B.; Finucane, C.; Mather, S. J.; Green, M. L. H.; Kostarelos, K.; Davis, B. G. Filled and Glycosylated Carbon Nanotubes for in Vivo Radioemitter Localization and Imaging. *Nat. Mater.* **2010**, *9* (6), 485–490. DOI: 10.1038/nmat2766.

(78) Lamanna, G.; Battigelli, A.; Ménard-Moyon, C.; Bianco, A. Multifunctionalized Carbon Nanotubes as Advanced Multimodal Nanomaterials for Biomedical Applications. *Nanotechnol. Rev.* **2012**, *1* (1), 17–29. DOI: 10.1515/ntrev-2011-0002.

(79) Ferrari, R.; Sponchioni, M.; Morbidelli, M.; Moscatelli, D. Polymer Nanoparticles for the Intravenous Delivery of Anticancer Drugs: The Checkpoints on the Road from the Synthesis to Clinical Translation. *Nanoscale* **2018**, *10* (48), 22701–22719. DOI: 10.1039/c8nr05933k.

(80) Gao, W.; Chan, J. M.; Farokhzad, O. C. PH-Responsive Nanoparticles for Drug Delivery.

Mol. Pharm. **2010**, *7* (6), 1913–1920. DOI: 10.1021/mp100253e.

(81) Banerjee, R.; Parida, S.; Maiti, C.; Mandal, M.; Dhara, D. PH-Degradable and Thermoresponsive Water-Soluble Core Cross-Linked Polymeric Nanoparticles as Potential Drug Delivery Vehicle for Doxorubicin. *RSC Adv.* **2015**, *5* (102), 83565–83575. DOI: 10.1039/c5ra17158j.

(82) Samarajeewa, S.; Shrestha, R.; Li, Y.; Wooley, K. L. Degradability of Poly(Lactic Acid)-Containing Nanoparticles: Enzymatic Access through a Cross-Linked Shell Barrier. *J. Am. Chem. Soc.* **2012**, *134* (2), 1235–1242. DOI: 10.1021/ja2095602.

(83) Ding, Y.; Kang, Y.; Zhang, X. Enzyme-Responsive Polymer Assemblies Constructed through Covalent Synthesis and Supramolecular Strategy. *Chem. Commun.* **2015**, *51* (6), 996–1003. DOI: 10.1039/c4cc05878j.

(84) Soga, O.; Van Nostrum, C. F.; Fens, M.; Rijcken, C. J. F.; Schiffelers, R. M.; Storm, G.; Hennink, W. E. Thermosensitive and Biodegradable Polymeric Micelles for Paclitaxel Delivery. *J. Control. Release* **2005**, *103* (2), 341–353. DOI: 10.1016/j.jconrel.2004.12.009.

(85) Fan, X.; Cheng, H.; Wang, X.; Ye, E.; Loh, X. J.; Wu, Y. L.; Li, Z. Thermoresponsive Supramolecular Chemotherapy by “V”-Shaped Armed β-Cyclodextrin Star Polymer to Overcome Drug Resistance. *Adv. Healthc. Mater.* **2018**, *7* (7), 1–11. DOI: 10.1002/adhm.201701143.

(86) Yan, Y.; Wang, Y.; Heath, J. K.; Nice, E. C.; Caruso, F. Cellular Association and Cargo Release of Redox-Responsive Polymer Capsules Mediated by Exofacial Thiols. *Adv. Mater.* **2011**, *23* (34), 3916–3921. DOI: 10.1002/adma.201101609.

(87) Lim, W. Q.; Phua, S. Z. F.; Zhao, Y. Redox-Responsive Polymeric Nanocomplex for Delivery of Cytotoxic Protein and Chemotherapeutics. *ACS Appl. Mater. Interfaces* **2019**, *11* (35), 31638–31648. DOI: 10.1021/acsami.9b09605.

(88) Zhao, M.; Biswas, A.; Hu, B.; Joo, K. Il; Wang, P.; Gu, Z.; Tang, Y. Redox-Responsive Nanocapsules for Intracellular Protein Delivery. *Biomaterials* **2011**, *32* (22), 5223–5230. DOI: 10.1016/j.biomaterials.2011.03.060.

(89) Dahlman, J. E.; Barnes, C.; Khan, O. F.; Thiriot, A.; Jhunjunwala, S.; Shaw, T. E.; Xing, Y.; Sager, H. B.; Sahay, G.; Speciner, L.; Bader, A.; Bogorad, R. L.; Yin, H.; Racie, T.; Dong, Y.; Jiang, S.; Seedorf, D.; Dave, A.; Singh Sandhu, K.; Webber, M. J.; Novobrantseva, T.; Ruda, V. M.; Lytton-Jean, A. K. R.; Levins, C. G.; Kalish, B.; Mudge, D. K.; Perez, M.; Abezgauz, L.; Dutta, P.; Smith, L.; Charisse, K.; Kieran, M. W.; Fitzgerald, K.; Nahrendorf, M.; Danino, D.; Tuder, R. M.; Von Andrian, U. H.; Akinc, A.; Panigrahy, D.; Schroeder, A.; Koteliansky, V.; Langer, R.; Anderson, D. G. In Vivo Endothelial SiRNA Delivery Using Polymeric Nanoparticles with Low Molecular Weight. *Nat. Nanotechnol.* **2014**, *9* (8), 648–655. DOI: 10.1038/nnano.2014.84.

(90) Hu, Q.; Li, H.; Wang, L.; Gu, H.; Fan, C. DNA Nanotechnology-Enabled Drug Delivery Systems. *Chem. Rev.* **2019**, *119* (10), 6459–6506. DOI: 10.1021/acs.chemrev.7b00663.

(91) Zhao, Y. X.; Shaw, A.; Zeng, X.; Benson, E.; Nyström, A. M.; Högberg, B. DNA Origami Delivery System for Cancer Therapy with Tunable Release Properties. *ACS Nano* **2012**, *6* (10), 8684–8691. DOI: 10.1021/nn3022662.

(92) Chang, M.; Yang, C. S.; Huang, D. M. Aptamer-Conjugated DNA Icosahedral Nanoparticles as a Carrier of Doxorubicin for Cancer Therapy. *ACS Nano* **2011**, *5* (8), 6156–6163. DOI: 10.1021/nn200693a.

(93) Madhanagopal, B. R.; Zhang, S.; Demirel, E.; Wady, H.; Chandrasekaran, A. R. DNA Nanocarriers: Programmed to Deliver. *Trends Biochem. Sci.* **2018**, *43* (12), 997–1013. DOI: 10.1016/j.tibs.2018.09.010.

(94) Lacroix, A.; Vengut-Climent, E.; De Rochambeau, D.; Sleiman, H. F. Uptake and Fate of Fluorescently Labeled DNA Nanostructures in Cellular Environments: A Cautionary Tale. *ACS Cent. Sci.* **2019**, *5* (5), 882–891. DOI: 10.1021/acscentsci.9b00174.

(95) Wang, S. T.; Gray, M. A.; Xuan, S.; Lin, Y.; Byrnes, J.; Nguyen, A. I.; Todorova, N.; Stevens, M. M.; Bertozzi, C. R.; Zuckermann, R. N.; Gang, O. DNA Origami Protection and Molecular Interfacing through Engineered Sequence-Defined Peptoids. *Proc. Natl. Acad. Sci. U. S. A.* **2020**, *117* (12), 6339–6348. DOI: 10.1073/pnas.1919749117.

(96) Ma, K.; Mendoza, C.; Hanson, M.; Werner-Zwanziger, U.; Zwanziger, J.; Wiesner, U. Control of Ultrasmall Sub-10 Nm Ligand-Functionalized Fluorescent Core-Shell Silica Nanoparticle Growth in Water. *Chem. Mater.* **2015**, *27* (11), 4119–4133. DOI: 10.1021/acs.chemmater.5b01222.

(97) Chen, F.; Ma, K.; Zhang, L.; Madajewski, B.; Zanzonico, P.; Sequeira, S.; Gonen, M.; Wiesner, U.; Bradbury, M. S. Target-or-Clear Zirconium-89 Labeled Silica Nanoparticles for Enhanced Cancer-Directed Uptake in Melanoma: A Comparison of Radiolabeling Strategies. *Chem. Mater.* **2017**, *29* (19), 8269–8281. DOI: 10.1021/acs.chemmater.7b02567.

(98) Croissant, J. G.; Fatieiev, Y.; Khashab, N. M. Degradability and Clearance of Silicon, Organosilica, Silsesquioxane, Silica Mixed Oxide, and Mesoporous Silica Nanoparticles. *Adv. Mater.* **2017**, *29* (9). DOI: 10.1002/adma.201604634.

(99) Kang, J.; Joo, J.; Kwon, E. J.; Skalak, M.; Hussain, S.; She, Z. G.; Ruoslahti, E.; Bhatia, S. N.; Sailor, M. J. Self-Sealing Porous Silicon-Calcium Silicate Core–Shell Nanoparticles for Targeted SiRNA Delivery to the Injured Brain. *Adv. Mater.* **2016**, *28* (36), 7962–7969. DOI: 10.1002/adma.201600634.

(100) Li, Q.; Jin, R. Photoluminescence from Colloidal Silicon Nanoparticles: Significant Effect of Surface. *Nanotechnol. Rev.* **2017**, *6* (6), 601–612. DOI: 10.1515/ntrev-2017-0145.

(101) Kresge, C. T.; Leonowicz, M. E.; Roth, W. J.; Vartuli, J. C.; Beck, J. S. Ordered Mesoporous Molecular Sieves Synthesized by a Lipid-Crystal Template Mechanism. *Nature* **1992**, *359* (22), 710–712. DOI: 10.1038/359710a0.

(102) Yanagisawa, T.; Shimizu, T.; Kuroda, K.; Kato, C. The Preparation of

Alkyltrimethylammonium-Kanemite Complexes and Their Conversion to Microporous Materials. *Bulletin of the Chemical Society of Japan*. 1990, 988–992. DOI: 10.1246/bcsj.63.988.

(103) Fowler, C. E.; Khushalani, D.; Lebeau, B.; Mann, S. Nanoscale Materials with Mesostructured Interiors. *Adv. Mater.* **2001**, *13* (9), 649–652. DOI: 10.1002/1521-4095(200105)13:9<649::AID-ADMA649>3.0.CO;2-G.

(104) Nooney, R. I.; Thirunavukkarasu, D.; Yimei, C.; Josephs, R.; Ostafin, A. E. Synthesis of Nanoscale Mesoporous Silica Spheres with Controlled Particle Size. *Chem. Mater.* **2002**, *14* (11), 4721–4728. DOI: 10.1021/cm0204371.

(105) Cai, Q.; Luo, Z. S.; Pang, W. Q.; Fan, Y. W.; Chen, X. H.; Cui, F. Z. Dilute Solution Routes to Various Controllable Morphologies of MCM-41 Silica with a Basic Medium. *Chem. Mater.* **2001**, *13* (2), 258–263. DOI: 10.1021/cm990661z.

(106) Stöber, W.; Fink, A. Controlled Growth of Monodisperse Silica Spheres in the Micron Size Range. *J. Colloid Interface Sci.* **1968**, *26* (1), 62–69. DOI: 10.1016/0021-9797(68)90272-5.

(107) Yano, K.; Fukushima, Y. Synthesis of Mono-Dispersed Mesoporous Silica Spheres with Highly Ordered Hexagonal Regularity Using Conventional Alkyltrimethylammonium Halide as a Surfactant. *J. Mater. Chem.* **2004**, *14* (10), 1579–1584. DOI: 10.1039/b313712k.

(108) Coppola, L.; Gianferri, R.; Nicotera, I.; Oliviero, C.; Ranieri, G. A. Structural Changes in CTAB/H2O Mixtures Using a Rheological Approach. *Phys. Chem. Chem. Phys.* **2004**, *6* (9), 2364–2372. DOI: 10.1039/b316621j.

(109) Beck, J. S.; Vartuli, J. C.; Roth, W. J.; Leonowicz, M. E.; Kresge, C. T.; Schmitt, K. D.; Chu, C. T. W.; Olson, D. H.; Sheppard, E. W.; McCullen, S. B.; Higgins, J. B.; Schlenker, J. L. A New Family of Mesoporous Molecular Sieves Prepared with Liquid Crystal Templates. *J. Am. Chem. Soc.* **1992**, *114* (27), 10834–10843. DOI: 10.1021/ja00053a020.

(110) Gay, D.; Hoa, S. V; Tsai, S. W. Composite Materials Composite Materials. *Nature* **1994**, *368* (March), 317–321.

(111) Wu, S. H.; Lin, H. P. Synthesis of Mesoporous Silica Nanoparticles. *Chem. Soc. Rev.* **2013**, *42* (9), 3862–3875. DOI: 10.1039/c3cs35405a.

(112) Travaglini, L.; Picchetti, P.; Del Giudice, A.; Galantini, L.; De Cola, L. Tuning and Controlling the Shape of Mesoporous Silica Particles with CTAB/Sodium Deoxycholate Catanionic Mixtures. *Microporous Mesoporous Mater.* **2019**, *279* (August 2018), 423–431. DOI: 10.1016/j.micromeso.2019.01.030.

(113) Lu, J.; Li, Z.; Zink, J. I.; Tamanoi, F. In Vivo Tumor Suppression Efficacy of Mesoporous Silica Nanoparticles-Based Drug-Delivery System: Enhanced Efficacy by Folate Modification. *Nanomedicine Nanotechnology, Biol. Med.* **2012**, *8* (2), 212–220. DOI: 10.1016/j.nano.2011.06.002.

(114) Tarn, D.; Ashley, C. E.; Xue, M.; Carnes, E. C.; Zink, J. I.; Brinker, C. J. Mesoporous Silica Nanoparticle Nanocarriers: Biofunctionality and Biocompatibility. *Acc. Chem. Res.* **2013**, *46* (3), 792–801. DOI: 10.1021/ar3000986.

(115) Huo, Q.; Liu, J.; Wang, L. Q.; Jiang, Y.; Lambert, T. N.; Fang, E. A New Class of Silica Cross-Linked Micellar Core-Shell Nanoparticles. *J. Am. Chem. Soc.* **2006**, *128* (19), 6447–6453. DOI: 10.1021/ja060367p.

(116) van Blaaderen, A.; Vrij, A. Synthesis and Characterization of Colloidal Dispersions of Fluorescent, Monodisperse Silica Spheres. *Langmuir* **1992**, *8* (12), 2921–2931. DOI: 10.1021/la00048a013.

(117) Ma, K.; Sai, H.; Wiesner, U. Ultrasmall Sub-10 Nm near-Infrared Fluorescent Mesoporous Silica Nanoparticles. *J. Am. Chem. Soc.* **2012**, *134* (32), 13180–13183. DOI: 10.1021/ja3049783.

(118) Ma, K.; Gong, Y.; Aubert, T.; Turker, M. Z.; Kao, T.; Doerschuk, P. C.; Wiesner, U. Self-Assembly of Highly Symmetrical, Ultrasmall Inorganic Cages Directed by Surfactant Micelles. *Nature* **2018**, *558* (7711), 577–580. DOI: 10.1038/s41586-018-0221-0.

(119) Croissant, J. G.; Fatieiev, Y.; Almalik, A.; Khashab, N. M. Mesoporous Silica and Organosilica Nanoparticles: Physical Chemistry, Biosafety, Delivery Strategies, and Biomedical Applications. *Adv. Healthc. Mater.* **2018**, *7* (4), 1–75. DOI: 10.1002/adhm.201700831.

(120) Dang, M.; Li, W.; Zheng, Y.; Su, X.; Ma, X.; Zhang, Y.; Ni, Q.; Tao, J.; Zhang, J.; Lu, G.; Teng, Z.; Wang, L. Mesoporous Organosilica Nanoparticles with Large Radial Pores via an Assembly-Reconstruction Process in Bi-Phase. *J. Mater. Chem. B* **2017**, *5* (14), 2625–2634. DOI: 10.1039/C6TB03327J.

(121) Chen, Y.; Xu, P.; Chen, H.; Li, Y.; Bu, W.; Shu, Z.; Li, Y.; Zhang, J.; Zhang, L.; Pan, L.; Cui, X.; Hua, Z.; Wang, J.; Zhang, L.; Shi, J. Colloidal HPMO Nanoparticles: Silica-Etching Chemistry Tailoring, Topological Transformation, and Nano-Biomedical Applications. *Adv. Mater.* **2013**, *25* (22), 3100–3105. DOI: 10.1002/adma.201204685.

(122) Fatieiev, Y.; Croissant, J. G.; Alamoudi, K.; Khashab, N. M. Cellular Internalization and Biocompatibility of Periodic Mesoporous Organosilica Nanoparticles with Tunable Morphologies: From Nanospheres to Nanowires. *Chempluschem* **2017**, *82* (4), 631–637. DOI: 10.1002/cplu.201600560.

(123) Teng, Z.; Su, X.; Zheng, Y.; Zhang, J.; Liu, Y.; Wang, S.; Wu, J.; Chen, G.; Wang, J.; Zhao, D.; Lu, G. A Facile Multi-Interface Transformation Approach to Monodisperse Multiple-Shelled Periodic Mesoporous Organosilica Hollow Spheres. *J. Am. Chem. Soc.* **2015**, *137* (24), 7935–7944. DOI: 10.1021/jacs.5b05369.

(124) Manzano, M.; Vallet-Regí, M. Mesoporous Silica Nanoparticles for Drug Delivery. *Adv. Funct. Mater.* **2020**, *30* (2), 3–5. DOI: 10.1002/adfm.201902634.

(125) Möller, K.; Bein, T. Degradable Drug Carriers: Vanishing Mesoporous Silica Nanoparticles.

Chem. Mater. **2019**, *31* (12), 4364–4378. DOI: 10.1021/acs.chemmater.9b00221.

(126) Inagaki, S.; Guan, S.; Ohsuna, T.; Terasaki, O. An Ordered Mesoporous Organosilica Hybrid Material with a Crystal-like Wall Structure. *Nature* **2002**, *416* (6878), 304–307. DOI: 10.1038/416304a.

(127) Quignard, S.; Masse, S.; Laurent, G.; Coradin, T. Introduction of Disulfide Bridges within Silica Nanoparticles to Control Their Intra-Cellular Degradation. *Chem. Commun.* **2013**, *49* (33), 3410–3412. DOI: 10.1039/c3cc41062e.

(128) Croissant, J.; Cattoën, X.; Man, M. W. C.; Gallud, A.; Raehm, L.; Trens, P.; Maynadier, M.; Durand, J. O. Biodegradable Ethylene-Bis(Propyl)Disulfide-Based Periodic Mesoporous Organosilica Nanorods and Nanospheres for Efficient in-Vitro Drug Delivery. *Adv. Mater.* **2014**, *26* (35), 6174–6180. DOI: 10.1002/adma.201401931.

(129) Maggini, L.; Cabrera, I.; Ruiz-Carretero, A.; Prasetyanto, E. A.; Robinet, E.; De Cola, L. Breakable Mesoporous Silica Nanoparticles for Targeted Drug Delivery. *Nanoscale* **2016**, *8* (13), 7240–7247. DOI: 10.1039/c5nr09112h.

(130) Du, X.; Kleitz, F.; Li, X.; Huang, H.; Zhang, X.; Qiao, S. Z. Disulfide-Bridged Organosilica Frameworks: Designed, Synthesis, Redox-Triggered Biodegradation, and Nanobiomedical Applications. *Adv. Funct. Mater.* **2018**, *28* (26). DOI: 10.1002/adfm.201707325.

(131) Liu, L.; Kong, C.; Huo, M.; Liu, C.; Peng, L.; Zhao, T.; Wei, Y.; Qian, F.; Yuan, J. Schiff Base Interaction Tuned Mesoporous Organosilica Nanoplatforms with PH-Responsive Degradability for Efficient Anti-Cancer Drug Delivery: In Vivo. *Chem. Commun.* **2018**, *54* (66), 9190–9193. DOI: 10.1039/c8cc05043k.

(132) Croissant, J. G.; Fatieiev, Y.; Julfakyan, K.; Lu, J.; Emwas, A. H.; Anjum, D. H.; Omar, H.; Tamanoi, F.; Zink, J. I.; Khashab, N. M. Biodegradable Oxamide-Phenylene-Based Mesoporous Organosilica Nanoparticles with Unprecedented Drug Payloads for Delivery in Cells. *Chem. - A Eur. J.* **2016**, *22* (42), 14806–14811. DOI: 10.1002/chem.201601714.

(133) Maggini, L.; Travaglini, L.; Cabrera, I.; Castro-Hartmann, P.; De Cola, L. Biodegradable Peptide-Silica Nanodonuts. *Chem. - A Eur. J.* **2016**, *22* (11), 3697–3703. DOI: 10.1002/chem.201504605.

(134) Lin, Z.; Xu, L.; Zhang, J.; Li, Z.; Zhao, J. Novel Thioacetal-Bridged Hollow Mesoporous Organosilica Nanoparticles with ROS-Responsive Biodegradability for Smart Drug Delivery. *Nano* **2019**, *14* (11), 1–14. DOI: 10.1142/S1793292019501418.

(135) Shao, D.; Li, M.; Wang, Z.; Zheng, X.; Lao, Y. H.; Chang, Z.; Zhang, F.; Lu, M.; Yue, J.; Hu, H.; Yan, H.; Chen, L.; Dong, W. fei; Leong, K. W. Bioinspired Diselenide-Bridged Mesoporous Silica Nanoparticles for Dual-Responsive Protein Delivery. *Adv. Mater.* **2018**, *30* (29), 1–8. DOI: 10.1002/adma.201801198.

(136) Teng, Z.; Li, W.; Tang, Y.; Elzatahry, A.; Lu, G.; Zhao, D. Mesoporous Organosilica Hollow Nanoparticles: Synthesis and Applications. *Adv. Mater.* **2019**, *31* (38), 1–24. DOI: 10.1002/adma.201707612.

(137) Chen, Y.; Meng, Q.; Wu, M.; Wang, S.; Xu, P.; Chen, H.; Li, Y.; Zhang, L.; Wang, L.; Shi, J. Hollow Mesoporous Organosilica Nanoparticles: A Generic Intelligent Framework-Hybridization Approach for Biomedicine. *J. Am. Chem. Soc.* **2014**, *136* (46), 16326–16334. DOI: 10.1021/ja508721y.

(138) Yang, G.; Phua, S. Z. F.; Bindra, A. K.; Zhao, Y. Degradability and Clearance of Inorganic Nanoparticles for Biomedical Applications. *Adv. Mater.* **2019**, *31* (10), 1–23. DOI: 10.1002/adma.201805730.

(139) Wang, Y.; Byrne, J. D.; Napier, M. E.; DeSimone, J. M. Engineering Nanomedicines Using Stimuli-Responsive Biomaterials. *Adv. Drug Deliv. Rev.* **2012**, *64* (11), 1021–1030. DOI: 10.1016/j.addr.2012.01.003.

(140) Cheng, R.; Meng, F.; Deng, C.; Klok, H. A.; Zhong, Z. Dual and Multi-Stimuli Responsive Polymeric Nanoparticles for Programmed Site-Specific Drug Delivery. *Biomaterials* **2013**, *34* (14), 3647–3657. DOI: 10.1016/j.biomaterials.2013.01.084.

(141) Aida, T.; Meijer, E. W.; Stupp, S. I. Functional Supramolecular Polymers. *Science (80-.).* **2012**, *335* (6070), 813–817. DOI: 10.1126/science.1205962.

(142) Fouquey, C.; Jean-Marie, L.; Anne-Marie, L. Molecular Recognition Directed Self-Assembly of Supramolecular Liquid Crystalline Polymers from Complementary Chiral Components. *Adv. Mater.* **1990**, *2* (5), 254–257. DOI: 10.1002/adma.19900020506.

(143) Li, S. L.; Xiao, T.; Lin, C.; Wang, L. Advanced Supramolecular Polymers Constructed by Orthogonal Self-Assembly. *Chem. Soc. Rev.* **2012**, *41* (18), 5950–5968. DOI: 10.1039/c2cs35099h.

(144) Hasegawa, M.; Iyoda, M. Conducting Supramolecular Nanofibers and Nanorods. *Chem. Soc. Rev.* **2010**, *39* (7), 2420–2427. DOI: 10.1039/b909347h.

(145) Velten, U.; Rehahn, M. First Synthesis of Soluble, Well Defined Coordination Polymers from Kinetically Unstable Copper(I) Complexes. *Chem. Commun.* **1996**, No. 23, 2639–2640. DOI: 10.1039/cc9960002639.

(146) Amabilino, D. B.; Smith, D. K.; Steed, J. W. Supramolecular Materials. *Chem. Soc. Rev.* **2017**, *46* (9), 2404–2420. DOI: 10.1039/c7cs00163k.

(147) Dong, R.; Zhou, Y.; Huang, X.; Zhu, X.; Lu, Y.; Shen, J. Functional Supramolecular Polymers for Biomedical Applications. *Adv. Mater.* **2015**, *27* (3), 498–526. DOI: 10.1002/adma.201402975.

(148) Zhang, S.; Bellinger, A. M.; Glettig, D. L.; Barman, R.; Lee, Y. A. L.; Zhu, J.; Cleveland, C.; Montgomery, V. A.; Gu, L.; Nash, L. D.; Maitland, D. J.; Langer, R.; Traverso, G. A PH-Responsive Supramolecular Polymer Gel as an Enteric Elastomer for Use in Gastric Devices. *Nat. Mater.* **2015**, *14* (10), 1065–1071. DOI: 10.1038/nmat4355.

(149) Bakker, M. H.; Lee, C. C.; Meijer, E. W.; Dankers, P. Y. W.; Albertazzi, L. Multicomponent Supramolecular Polymers as a Modular Platform for Intracellular Delivery. *ACS Nano*

2016, *10* (2), 1845–1852. DOI: 10.1021/acsnano.5b05383.

(150) Zhang, Q.; Deng, Y. X.; Luo, H. X.; Shi, C. Y.; Geise, G. M.; Feringa, B. L.; Tian, H.; Qu, D. H. Assembling a Natural Small Molecule into a Supramolecular Network with High Structural Order and Dynamic Functions. *J. Am. Chem. Soc.* **2019**, *141* (32), 12804–12814. DOI: 10.1021/jacs.9b05740.

(151) Stupp, S. I.; Clemons, T. D.; Carrow, J. K.; Sai, H.; Palmer, L. C. Supramolecular and Hybrid Bonding Polymers. *Isr. J. Chem.* **2020**, *60* (1–2), 124–131. DOI: 10.1002/ijch.202000005.

(152) Yu, Z.; Tantakitti, F.; Yu, T.; Palmer, L. C.; Schatz, G. C.; Stupp, S. I. Simultaneous Covalent and Noncovalent Hybrid Polymerizations. *Science* **2016**, *351*, 497–502. DOI: 10.1126/science.aad4091.

(153) Shimizu, I.; Okabayashi, H.; Hattori, N.; Taga, K.; Yoshino, A.; O’Connor, C. J. 13C- And 1H-NMR and FTIR Spectroscopic Evidence for Aggregate Formation of Organosilanes in Toluene. *Colloid Polym. Sci.* **1997**, *275* (3), 293–297. DOI: 10.1007/s003960050084.

(154) Dieudonné, P.; Man, M. W. C.; Pichón, B. P.; Vellutini, L.; Bantignies, J. L.; Blanc, C.; Creff, G.; Finet, S.; Sauvajol, J. L.; Bied, C.; Moreau, J. J. E. In Situ X-Ray Measurements to Probe a New Solid-State Polycondensation Mechanism for the Design of Supramolecular Organo-Bridged Silsesquioxanes. *Small* **2009**, *5* (4), 503–510. DOI: 10.1002/smll.200800254.

(155) Ni, L.; Chemtob, A.; Croutxé-Barghorn, C.; Brendlé, J.; Vidal, L.; Rigolet, S. Kinetics, Thermodynamics, and Dynamics in Organosilane Self-Assembly. *J. Phys. Chem. C* **2012**, *116* (45), 24320–24330. DOI: 10.1021/jp307274d.

(156) Parikh, A. N.; Schivley, M. A.; Koo, E.; Seshadri, K.; Aurentz, D.; Mueller, K.; Allara, D. L. N-Alkylsiloxanes: From Single Monolayers to Layered Crystals. The Formation of Crystalline Polymers from the Hydrolysis of n-Octadecyltrichlorosilane. *J. Am. Chem. Soc.* **1997**, *119* (13), 3135–3143. DOI: 10.1021/ja963284p.

(157) Han, J. T.; Lee, D. H.; Ryu, C. Y.; Cho, K. Fabrication of Superhydrophobic Surface from a Supramolecular Organosilane with Quadruple Hydrogen Bonding. *J. Am. Chem. Soc.* **2004**, *126* (15), 4796–4797. DOI: 10.1021/ja0499400.

(158) Fan, H.; Chen, Z.; Blinker, C. J.; Clawson, J.; Alam, T. Synthesis of Organo-Silane Functionalized Nanocrystal Micelles and Their Self-Assembly. *J. Am. Chem. Soc.* **2005**, *127* (40), 13746–13747. DOI: 10.1021/ja053795o.

(159) Hashizume, M.; Kawanami, S. I.; Iwamoto, S.; Isomoto, T.; Kikuchi, J. I. Stable Vesicular Nanoparticle “Cerasome” as an Organic-Inorganic Hybrid Formed with Organoalkoxysilane Lipids Having a Hydrogen-Bonding Unit. *Thin Solid Films* **2003**, *438–439* (03), 20–26. DOI: 10.1016/S0040-6090(03)00745-4.

(160) Seeman, N. C.; Sleiman, H. F. DNA Nanotechnology. *Nat. Rev. Mater.* **2017**, *3*. DOI: 10.1038/natrevmats.2017.68.

(161) Jones, M. R.; Seeman, N. C.; Mirkin, C. A. Programmable Materials and the Nature of the DNA Bond. *Science* **2015**, *347*, 840. DOI: 10.1126/science.1260901.

(162) Wu, J. C.; Meng, Q. C.; Ren, H. M.; Wang, H. T.; Wu, J.; Wang, Q. Recent Advances in Peptide Nucleic Acid for Cancer Bionanotechnology. *Acta Pharmacol. Sin.* **2017**, *38* (6), 798–805. DOI: 10.1038/aps.2017.33.

(163) Uhlmann, E.; Peyman, A.; Breipohl, G.; Will, D. W. ChemInform Abstract: PNA: Synthetic Polyamide Nucleic Acids with Unusual Binding Properties. *ChemInform* **2010**, *30* (9), no-no. DOI: 10.1002/chin.199909294.

(164) Ali, A.; Karim, S.; Shakeel, S. Peptide Nucleic Acid (PNA) – a Review. *J. Chem. Technol. Biotechnol.* **2006**, *81*, 892–899. DOI: 10.1002/jctb.1505.

(165) Berger, O.; Gazit, E. Molecular Self-Assembly Using Peptide Nucleic Acids. *Biopolymers* **2017**, *108* (1), 1–6. DOI: 10.1002/bip.22930.

(166) Liu, L. H.; Li, Z. Y.; Rong, L.; Qin, S. Y.; Lei, Q.; Cheng, H.; Zhou, X.; Zhuo, R. X.; Zhang, X. Z. Self-Assembly of Hybridized Peptide Nucleic Acid Amphiphiles. *ACS Macro Lett.* **2014**, *3* (5), 467–471. DOI: 10.1021/mz5001916.

(167) Jin, J. O.; Kim, H.; Huh, Y. H.; Herrmann, A.; Kwak, M. Soft Matter DNA Nanoparticles Hybridized with CpG Motifs and Peptide Nucleic Acids Enable Immunological Treatment of Cancer. *J. Control. Release* **2019**, *315* (October), 76–84. DOI: 10.1016/j.jconrel.2019.09.013.

(168) AUDRAN, M.; KUMAR, R. The Physiology and Pathophysiology of Vitamin D. *Mayo Clin. Proc.* **1985**, *60* (12), 851–866. DOI: 10.1016/S0025-6196(12)64791-0.

(169) Papakostas, D.; Rancan, F.; Sterry, W.; Blume-Peytavi, U.; Vogt, A. Nanoparticles in Dermatology. *Arch. Dermatol. Res.* **2011**, *303* (8), 533–550. DOI: 10.1007/s00403-011-1163-7.

Chapter 2

Light-breakable mesoporous organosilica particles

In this chapter, the preparation and characterization of a novel light-responsive bis-alkoxysilane and its use for the preparation of light-breakable mesoporous organosilica particles is presented. The use of light to trigger the particle degradation is particuarly advantageous, due to its facile spatiotemporal control and non-invasive properties. The light-breakable organosilica particles can be loaded with bioactive molecules and the payload release can be triggered upon light-irradiation. These particles hold potential as cutaneous drug delivery systems, protecting the skin from harmful UV-light radiation, while simultaneously releasing bioactive molecules, such as provitamin D_3.

2.1. Introduction

Mesoporous organosilica particles represent highly attractive drug-delivery carriers for potential biomedical applications, due to their general non-toxicity and easily tunable physicochemical properties, such as size, shape, porosity and degradability. Upon integration of stimuli-responsive organic functional groups within the silica framework, breakable porous organosilica particles can be prepared. In fact, the presence of an external trigger can mediate the particle disintegration, allowing for a controlled payload release over a defined period of time, which is essential for the development of new drug-delivery systems for optimized disease treatment. Improved degradation leads to improved material clearance from living organisms, leading to the development of safer drug carriers.[1–3] A variety of stimuli sources, such as reducing agents,[4–6] pH changes [7,8] or enzymatic activity[9,10], can be used; light represents a particularly attractive stimulus owing to its non-invasive nature and simple spatiotemporal control. Previously reported light-degradable materials include hydrogels[11,12], polymers[13], micellar systems[14] and light-responsive colloidal crystals[15]. Several light-responsive silica-based nanoparticles have been previously reported and include light-responsive colloidosomes[16] and gated mesoporous silica particles[17,18], as well as silica-based photocaged drug carriers[19], but mesoporous organosilica particles that break upon light irradiation have not yet been reported. Previously, Shea and coworkers reported the preparation of photoresponsive bridged-polysilsesquioxanes, that undergo a change in morphology upon light irradiation.[20,21] Inspired by this work, we designed a new bis-alkoxysilane bearing a photolabile nitrobenzyl group to be used as the bridging organic moiety in the preparation of light-breakable mesoporous organosilica particles (**LB-MSPs**). The photolabile moiety used in this work is a 2-nitrobenzyl ether group, which is known to undergo a Norrish type II reaction upon UV-light irradiation that leads to its cleavage[22,23]. The choice to use the nitrobenzyl functional group as the light-responsive moiety was dictated by the fact that this group is widely used, and its photochemical properties have been therefore well studied. In fact, the 2-nitrobenzylgroup serves as the caging group for bioactive molecules[24–26], as the photolabile protecting group in organic synthesis[27,28] or as the photoresponsive gatekeeper[29] for controlled drug release using mesoporous silica particles. In this chapter, the synthesis and thorough photochemical characterization of the new photodegradable bis-alkoxysilane and its use in the preparation of **LB-MSPs** is presented. The particles have been characterized by several techniques and their degradation behavior upon UV-light exposure has been investigated. To demonstrate the applicability of **LB-MSPs** as porous containers for the light-stimulated release of a cargo molecule, the particles were loaded with 7-dehydrocholesterol (**7-DH**), a natural previtamin D_3 precursor, and the triggered release of this molecule upon UV-light exposure was investigated. The preparation of pristine mesoporous silica particles (**MSPs**) and disulfide-bridged mesoporous organosilica particles (**ss-MSPs**) to be used as model particles for comparison in the light-induce degradation and release studies has also been reported. In principle, **LB-MSPs** possess the potential to be used as novel organosilica carriers for topical drug-delivery applications being capable of absorbing harmful UV-light radiation while simultaneously releasing a natural precursor of a previtamin D_3.

2.2. Results and discussion

2.2.1. Synthesis and characterization of the photolabile bis-alkoxysilane

In order to covalently integrate a photolabile organic functional group within the framework of mesoporous organosilica particles, a hydrolysable bis-alkoxysilane bearing the 2-nitrobenzyl group was synthesized. The photolabile bis-alkoxysilane **1** was prepared according to the synthetic path depicted in Scheme 1. The diallyl intermediate **2** was successfully prepared from 5-hydroxy-2-nitrobenzyl alcohol after reaction with allyl bromide, employing sodium hydride as a base. Subsequently, hydrosylilation of compound **2** with triethoxysilane, in the presence of Karstedt´s catalyst, yielded the final compound **1** in good yields (^{1}H and ^{13}C NMR spectra are reported in section 2.4.2)

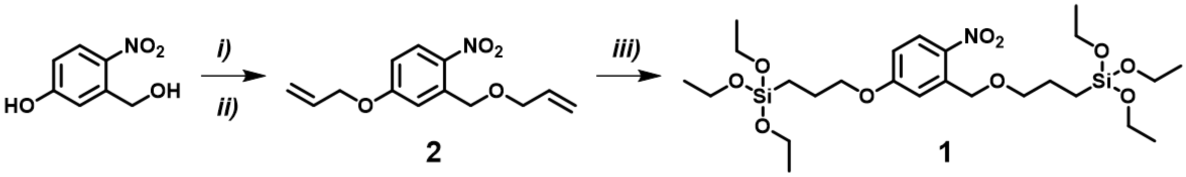

Scheme 1. Synthesis of photolabile bis-alkoxysilane **1**. Reaction conditions: (*i*) NaH, DMF, 0°C; (*ii*) allylbromide, DMF, 0°C to r.t.; (*iii*) Karstedt’s catalyst, triethoxysilane, toluene, 50°C.

As discussed in the introduction, the photodegradable 2-nitrobenzyl ether moiety undergoes a Norrish type II reaction when irradiated with UV light, leading to its specific O_{benz}-C bond cleavage (Figure 1a). The occurrence of this photodegradation reaction in compound **1** was first characterized by using UV-Vis absorption spectroscopy. Therefore, a solution of **1** (0.11 mM) in a EtOH/H_2O mixture (5:1, *v*/*v*) was irradiated with light at λ_{irr}=320 nm and the evolution of the spectra was recorded over time (Figure 1b and c). At t_0 the UV-Vis absorption spectrum of **1** shows the characteristic absorption band of the n–π* transition centered at 312 nm. The profile evolution in time upon light irradiation shows a decrease in intensity of the band at 312 nm, which resulted to be absent after the first 5 min of irradiation, whereas a new n–π* transition band at 352 nm appeared, indicating the formation of the nitroso photodegradation product **3** (Figure 1a). Considering that the developed particles would serve as novel drug-delivery carriers for topical delivery applications, the specific solvent mixture for the UV-Vis absorption spectroscopy studies was chosen in order to contain a water fraction comparable to that present in creams and ointments. Furthermore, the high EtOH/H_2O ratio used for these experiments ensured that, at a later stage when **LB-MSPs** would be tested, no particle degradation could occur due to hydrolysis of the amorphous silica.

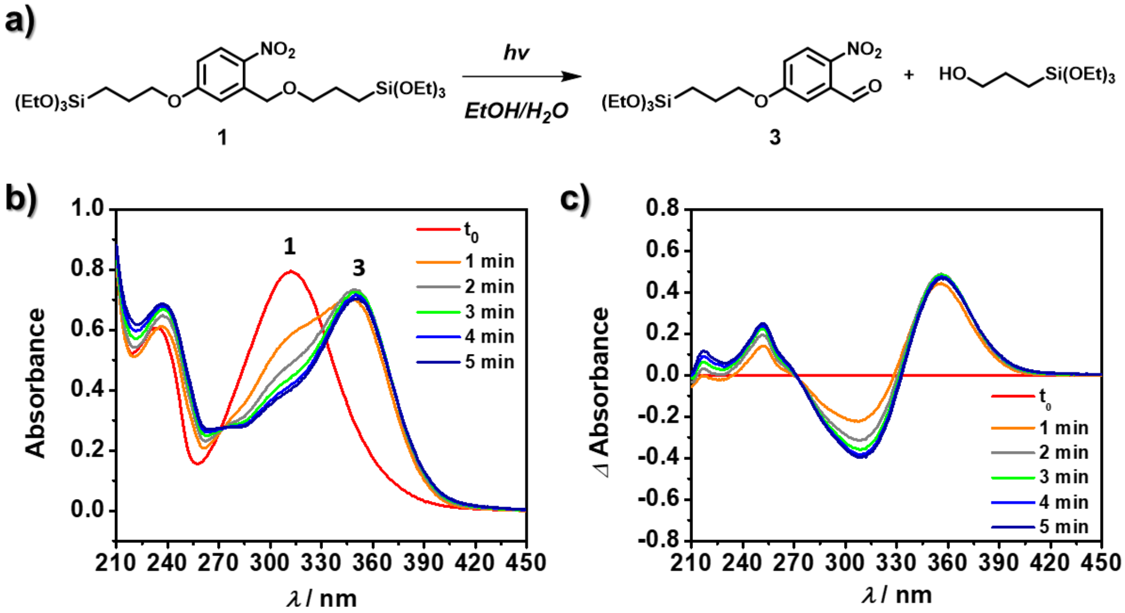

Figure 1. a) Norrish type II photodegradation reaction of **1** induced by UV-light irradiation. b) UV-Vis absorption spectra evolution upon UV-Light irradiation of **1** (0.11mM in EtOH/H_2O 1:1 *v*/*v*). c) Difference absorbance spectra reported to better visualize the spectral evolution.

The formation of the photodegradation product **3** was confirmed by comparing its characteristic UV-Vis spectra with results reported in the literature[22] and by time-dependent density functional theory (TD-DFT) calculations using Gaussian09® calculation suite (see section 2.4.9 for further information). DFT calculations on compound **3** revealed that the lowest and highest molecular frontier orbitals were only located on the conjugated system (Figure 2a), allowing TD-DFT calculations to be performed on the truncated structure (Figure 2b). As predicted, the calculated absorption spectra of this truncated structure matched the experimental results obtained, confirming further the formation of the nitroso benzaldehyde upon light irradiation of **1**.

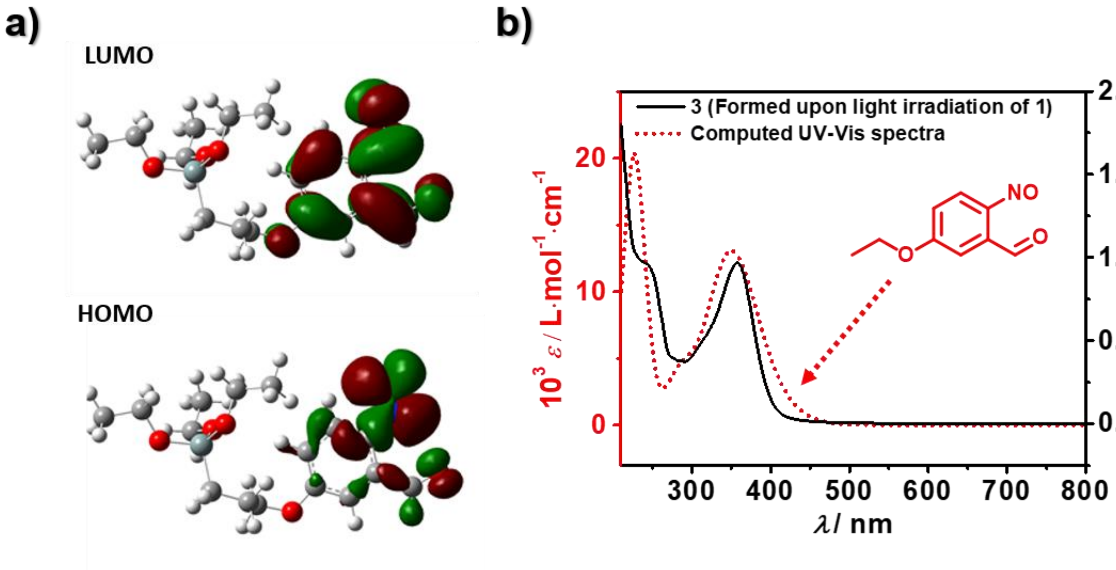

Figure 2. a) Computed frontier molecular orbitals for compound **3**. b) Comparison of the absorption spectra of **3** with the computed absorption spectra of the model nitroso-compound shown in red.

The characteristic photodegradation of **1** was further confirmed by ^{1}H NMR spectroscopy. A solution of **1** in $CDCl_3$ was placed in an NMR tube and irradiated with light at 320 nm and the NMR spectra recorded at different time intervals (see section 2.4.5 for more details). As depicted in Figure 3, the intensity of the benzylic -CH_2- signal at 4.89 ppm and the triplet signal from the -O_{benz}-CH_2-CH_2- aliphatic chain at 3.57 ppm decreased over time, confirming the occurring photodegradation reaction. The formation of the degradation product **3** was instead detected by the appearance of the aldehyde –CHO signal at 10.49 ppm. The use of a non-quartz NMR tube, possessing a sub-optimal UV-cutoff region and the weak light source derived from the spectrophotometer for this experiment explains the relatively long reaction times observed in the above-described NMR experiment compared to the UV-Vis absorption studies.

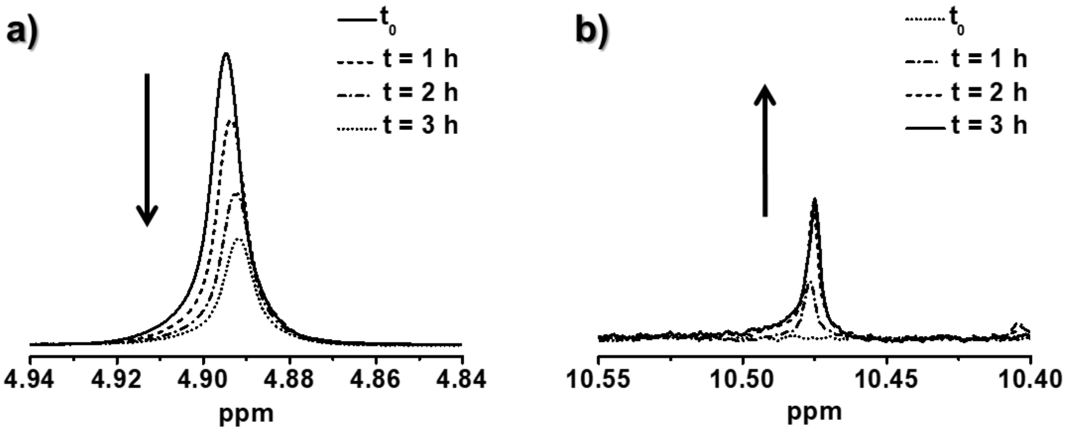

Figure 3. NMR spectra recorded over time upon light-irradiation of **1**. a) Intensity change of the benzylic methylene resonance signal upon light irradiation. b) Intensity change of the aldehyde resonance signal upon light irradiation.

An additional NMR analysis was used to determine the photodegradation quantum yield of **1** through a previously reported NMR-based chemical actinometry method that uses quartz NMR tubes for optimal irradiation conditions (see section 2.4.5 for additional details).[30,31]. The intensity (I_0) of a 365 nm LED light source was calibrated by measuring the photodecay rate of the chemical actinometer 2-nitrobenzaldehyde (NBA) by monitoring changes in the NMR spectra. NBA was selected as the chemical actinometer due to its well-known photochemical degradation quantum yield (φ_{365}) of 0.5 at 365 nm. The degradation rate of the actinometer can be described by first-order kinetics, where the observed rate is equal to the product of the incident light intensity (I_0), the quantum yield (φ_{365}) at 365 nm and the fraction of light absorbed (f) by the sample (Equation 1).

$$v_{NBA} = -\frac{d[NBA]}{dt} = k_0 \cdot [NBA] = I_0 \cdot \ \varphi_{365} \cdot f \tag{1}$$

The fraction of light absorbed by the sample can be reformulated as in Equation 2

$$f = \frac{I_0 - I}{I_0} = 1 - \frac{I}{I_0} \tag{2}$$

The term I/I_0 in Equation 2 can be easily derived from the Lambert–Beer law (Equations 3 and 4) and re-expressed as in Equation 5.

$$A = \log\left(\frac{I_0}{I}\right) = \varepsilon \cdot d \cdot [NBA] \tag{3}$$

$$\log\left(\frac{I}{I_0}\right) = -\varepsilon \cdot d \cdot [NBA] \tag{4}$$

$$\frac{I}{I_0} = 10^{-\varepsilon \cdot d \cdot [NBA]} \tag{5}$$

Combining Equations 5 and 2 in Equation 1 results in the rate law for the disappearance of the actinometer (i.e., NBA) shown in Equation 6, used for the determination of I_0.

$$v_{NBA} = -\frac{d[NBA]}{dt} = I_0 \cdot \ \varphi_{365} \cdot \left(1 - 10^{-\varepsilon \cdot d \cdot [NBA]}\right) \tag{6}$$

In order to extract I_0 from Equation 6, first the initial reaction rates for the photodecay of NBA was determined over a series of starting concentrations (Figure 4a). The initial reaction rate was monitored through the decay of the aldehyde peak in the NMR spectrum, where the area of the residual acetone solvent peak was used as an internal standard. At these short time intervals, the [NBA] decays linearly with time, where the slope of these data corresponds to the initial reaction rate. The reactions rates obtained were plotted against the initial concentrations of NBA (Figure 4b) and the data was fitted with the help of equation 4 in order to extract I_0, with ε=260 L·mol^{-1}·L^{-1}.

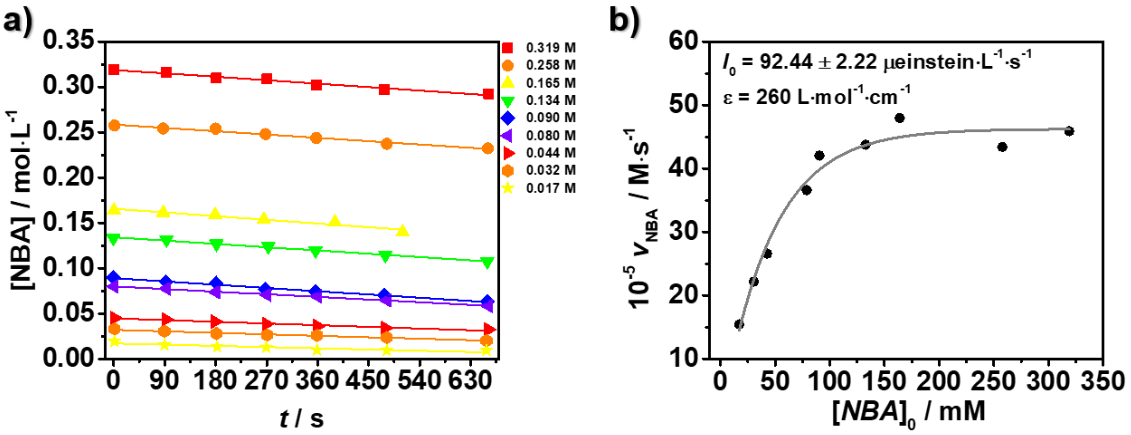

Figure 4. a) Concentration change of NBA over a series of initial different concentrations. b) Reaction rates as a function of initial NBA concentrations.

Once calibrated, the LED was used in subsequent actinometry experiments performed on **1**. For these experiments, $CDCl_3$ was used as the solvent to avoid any undesired hydrolysis and condensation of **1** due to the presence of water. For these experiments, hexamethyldisilane was introduced as the internal standard. The reaction rate $v(\mathbf{1})$ was monitored over time by the decrease in the peak area for the benzylic proton peak. Given the high concentrations used (> 60 mM) and the large extinction coefficient for the compound (6980 L mol-^{1} cm^{-1}), Equation 6 simplifies to Equation 7 and the reaction rate constant for the decay of **1** can be extracted from a linear fit (Figure 5). Applying equation 5 from the rate vs time plot allowed to estimate the reaction quantum yield for **1** having an average value of φ_{365}=0.30±0.09.

$$I_0 = \frac{v(\mathbf{1})}{\varphi_{365}} = \frac{k_0}{\varphi_{365}} \qquad (7)$$

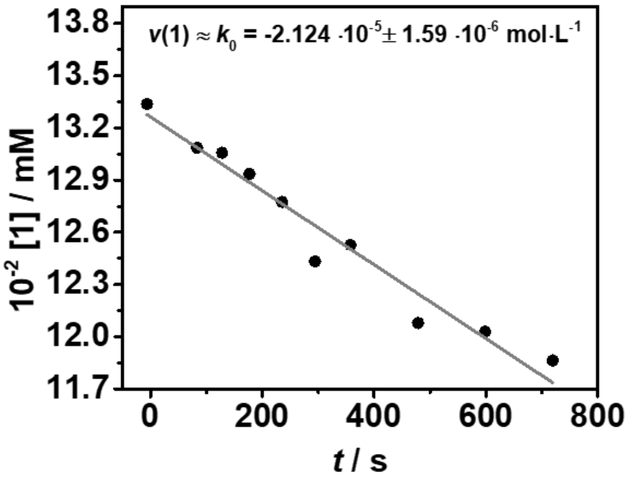

Figure 5. Concentration change of **1** over light irradiation at 365 nm.

2.2.2. Preparation and characterization of light-breakable mesoporous organosilica particles

Light-breakable mesoporous silica particles (**LB-MSPs**) were prepared according to a modified recently reported procedure[8] that employed a modified Stöber synthesis protocol.[32] As depicted in Scheme 2, the photolabile bis-alkoxysilane **1** was hydrolyzed and co-condensed with tetraethyl orthosilicate (TEOS), with a TEOS/**1** molar ratio of 2.25:1, in the presence of the surfactant cetyltrimethylammonium bromide (CTAB) and by using aqueous ammonia as the reaction catalyst. The particle preparation was performed in the dark in order to prevent the degradation of **1** due to ambient light. The particles were collected by centrifugation and the surfactant was removed by extraction in EtOH heated to reflux for 24 h (see section 2.4.3 for further details).

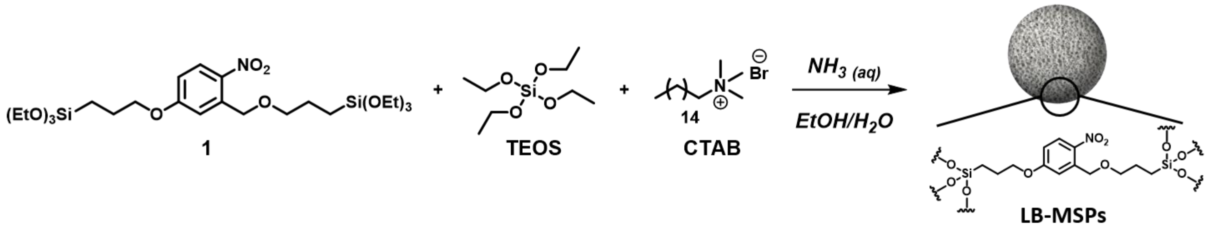

Scheme 2. Schematic representation of the preparation of **LB-MSPs.**

The morphology of the particles was first analyzed by electron microscopy. SEM (Figure 6a) and TEM images (Figure 6b) of **LB-MSPs** revealed the presence of spherical particles with a size of

303±34 nm (Figure 6c). The hydrodynamic diameter (D_h) was determined to be 409±0 nm by DLS analysis (Figure 6d), which indicates a good dispersibility of the particles.

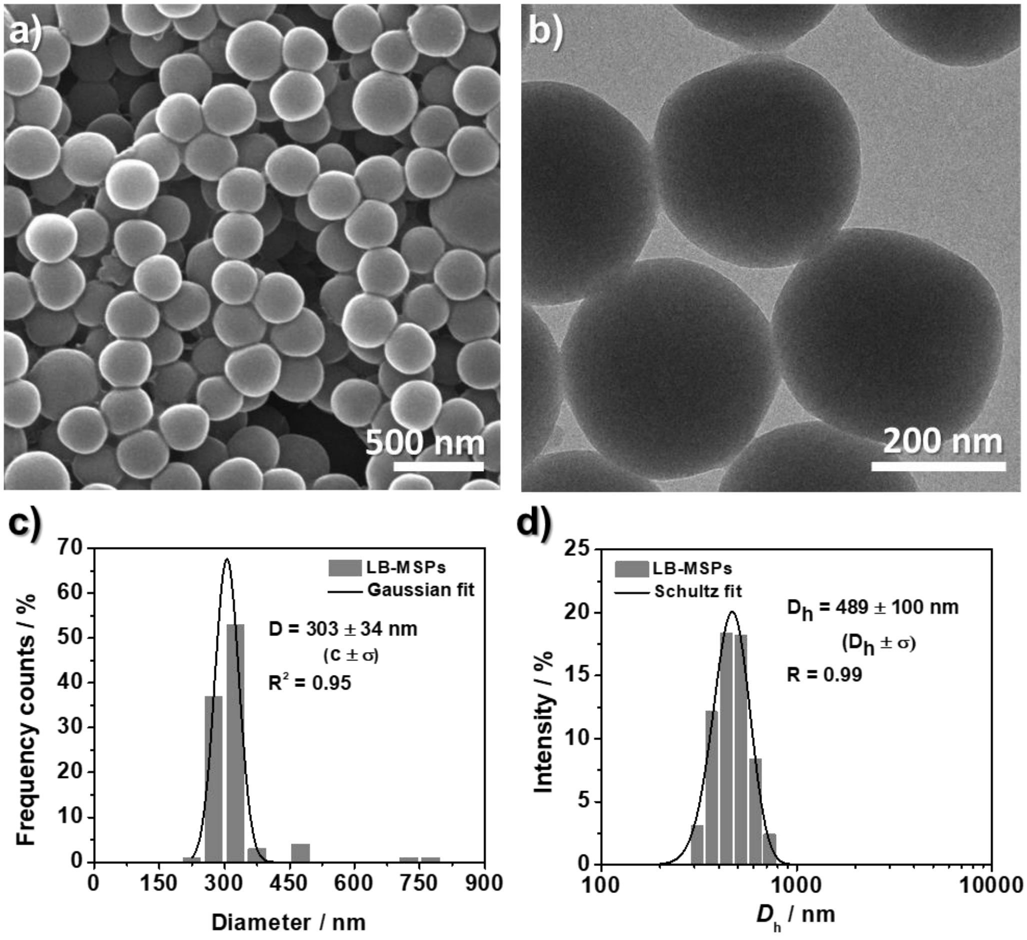

Figure 6. a) SEM and b) TEM images of **LB-MSPs**. c) Size distribution of LB-MSPS calculated from TEM images (N = 100). d) DLS measurements on **LB-MSPs** in water.

TEM images of **LB-MSPs** taken at higher magnification (Figure 7a) indicated the absence of a high-ordered mesoporous phase. From the SAXS pattern (Figure 7b) of **LB-MSPs**, two broad peaks of low intensity centered at q=1.8 and q=2.9 nm^{-1} were found, confirming the absence of an ordered mesoporous phase, which is in agreement with the findings obtained from TEM. The reduced order of the mesoporous phase can be explained by the presence of the bulky organic linker in the reaction mixture during the preparation of **LB-MSPs**, affecting the formation of the porous phase.[33,34]

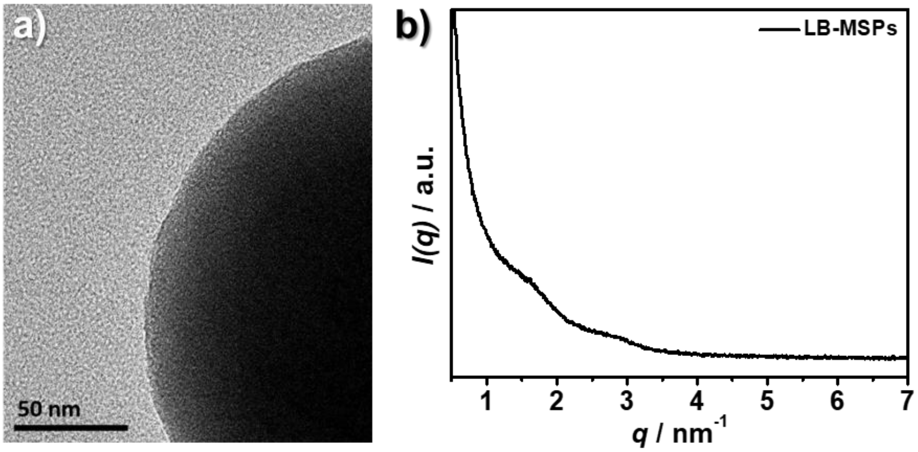

Figure 7. a) TEM images of **LB-MSPs** at higher magnification. b) SAXS pattern on **LB-MSPs**.

N_2 adsorption–desorption sorption measurements were used to characterize the porosity of **LB-MSPs** (Figure 8a), which confirmed the presence of mesopores with an average pore diameter of 2.4 nm, having a total pore volume of 0.26 cm^3g^{-1} (Figure 8b) and a BET specific surface area of 318 m^2g^{-1}.

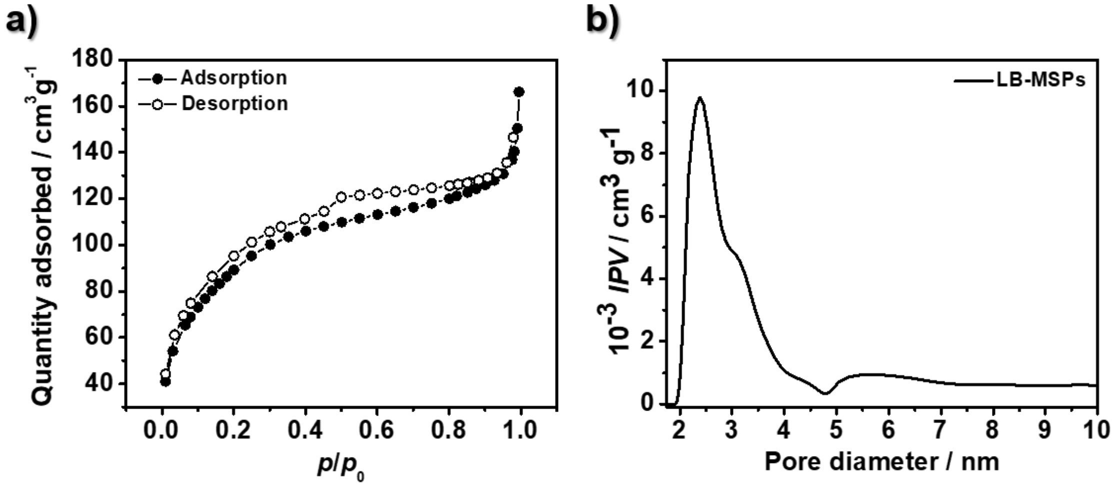

Figure 8. a) N_2 adsorption and desorption isotherms measured on **LB-MSPs.** b) DFT pore size distribution calculated from adsorption branch of the isothermal curve of **LB-MSPs**.

Having assessed the size shape and porosity of the particles, the amount of organic content in **LB-MSPs** was characterized. In **Figure 9a**, the thermograms of the photodegradable linker **1**, **LB-MSPs** and pristine **MSPs** are depicted. **LB-MSPs** possess, compared to **MSPs**, which were prepared in same conditions as **LB-MSPs** but do not contain an organic bridging group in their structure (see section 2.4.3 for preparation procedure), 25 wt% of organic content. The continuous weight loss observed for pristine **MSPs** at temperatures higher than 300 °C can be attributed to the loss of water, caused from further hydroxyl condensation.[35] ATR-FTIR spectroscopy further confirmed the presence of the photolabile linker in **LB-MSPs** (Figure 9b), showing the characteristic transmission bands attributable to the $–NO_2$ stretching modes at 1515 and 1340 cm^{-1}, the aromatic -C–C- stretching modes at 1610 and 1583 cm^{-1} and the C_{sp2}–H and C_{sp3}–H stretching vibrations at 3016, 2978, 2929 and 2887 cm^{-1}.[36] Moreover, the assigned transmission bands identified for **LB-MSPs** match the IR spectrum recorded on the photolabile linker **1** (section 2.4.2).

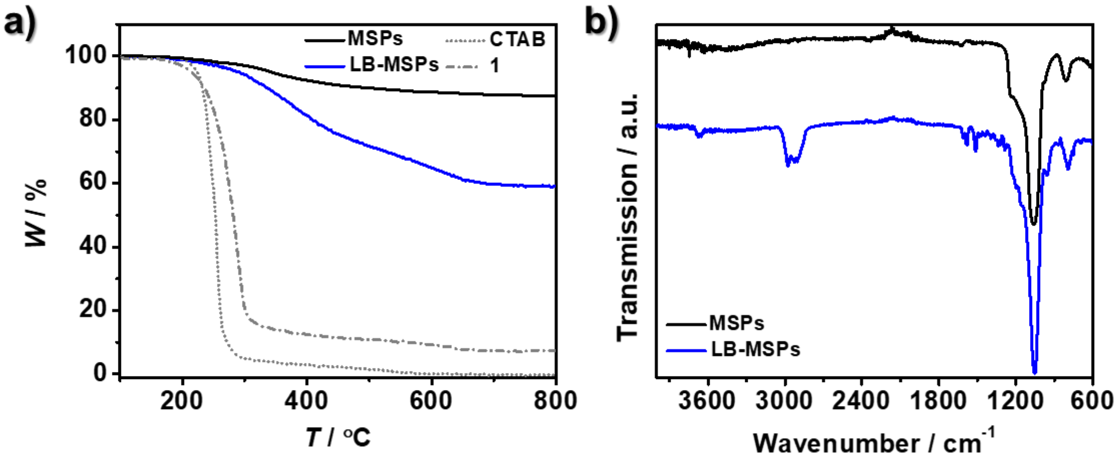

Figure 9. a) TGA analysis showing the characteristic weight losses of **LB-MSPs**, Pristine **MSPs**, **1** and CTAB. b) ATR-FTIR recorded on **LB-MSPs** and Pristine **MSPs**.

The covalent linkage of the linker within the silica framework was confirmed by XPS analysis. The survey spectrum recorded on **LB-MSPs** indicated the presence of C(1s) and N(1s) signals at 285 and 405 eV, respectively (Figure 10a). The deconvolution of the HR scan for the N(1s) peak (Figure 10b) shows the presence of two components, N-1 at 400.2 eV and N-2 at 405.6 eV, in a ratio (area) of 1:3.6. The component N-2 can be attributed to the aromatic $–NO_2$ nitro group, whereas the N-1 component can be assigned to the nitrogen of the –NO nitroso group, which is probably formed on the surface of the particles upon exposure to light during the sample preparation. The analysis of the HR scan of the C(1s) core level (Figure 10c) shows the presence of three components C-1 (284.1 eV), C-2 (284.8 eV) and C-3 (285.9 eV) attributable to the aromatic carbon species, C-C and C-O carbon species, respectively. The assignment is in agreement with data reported in the literature.[37]

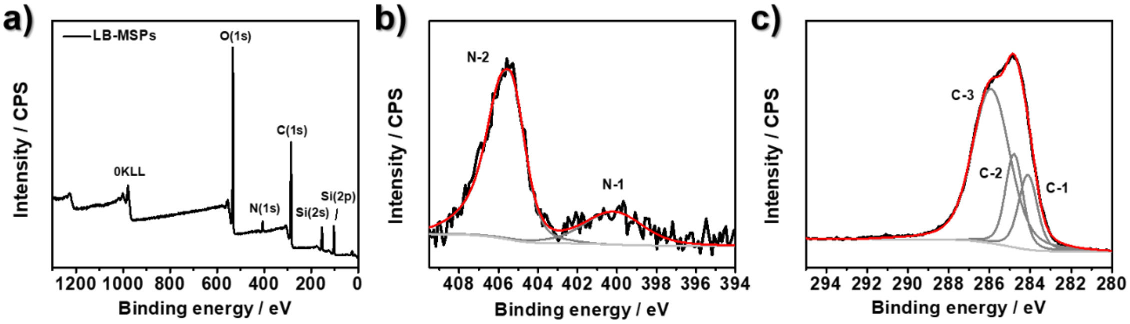

Figure 10. a) XPS survey spectrum on **LB-MSPs.** b) Deconvoluted XPS HR scan of N(1s) level recorded on **LB-MSPs.** c) Deconvoluted XPS HR scan of C(1s) level recorded on **LB-MSPs.**

Finally, the UV-Vis absorption spectra of **LB-MSPs** in an EtOH/H_2O (5:1 *v*/*v*) mixture was recorded (Figure 11a), which showed two bands at 242 and 327 nm reflecting the presence of the photolabile nitrobenzyl functional group within the silica particles. In contrast to the absorption spectra recorded for compound **1** (Figure 11b) in the same solvent mixture, the absorption maxima recorded in **LB-MSPs** are slightly redshifted.

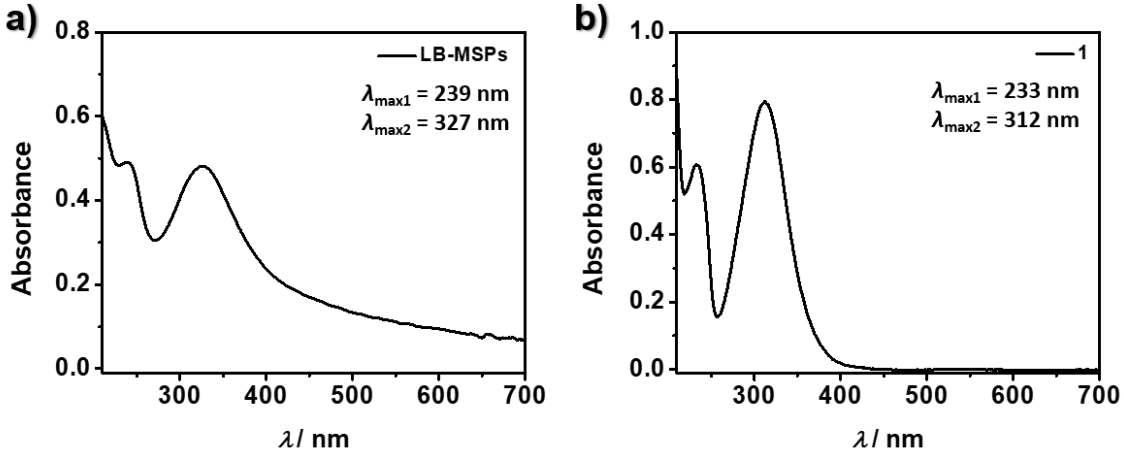

Figure 11. a) UV-Vis absorption spectra of **1** in EtOH/H_2O (5:1 *v*/*v*); *c*(**1**)=0.1 mM. b) UV-Vis absorption spectra of **LB-MSPs** in EtOH/H_2O (5:1 *v*/*v*); *c*(**LB-MSPs**)=0.1 mg·mL^{-1}.

2.2.3. Preparation and characterization of SS-MSPs

Disulfide-bridged mesoporous organosilica particles (**SS-MSPs**) were prepared that possess similar physicochemical properties compared with **LB-MSPs** to used them as model particles for comparison when studying the unique light-triggered degradation and drug release from **LB-MSPs**. **SS-MSPs** were prepared by adapting the synthesis of **LB-MSPs** and replacing the photolabile bis-alkoxysilane with bis[3-(triethoxysilyl)propyl]disulfide (BTPS, see section 2.4.3 for details). As depicted in Scheme 3, BTPS was hydrolyzed and co-condensed with TEOS, with a TEOS/BTPS molar ratio of 2.25:1, in the presence of CTAB and using aqueous ammonia as the basic catalyst.

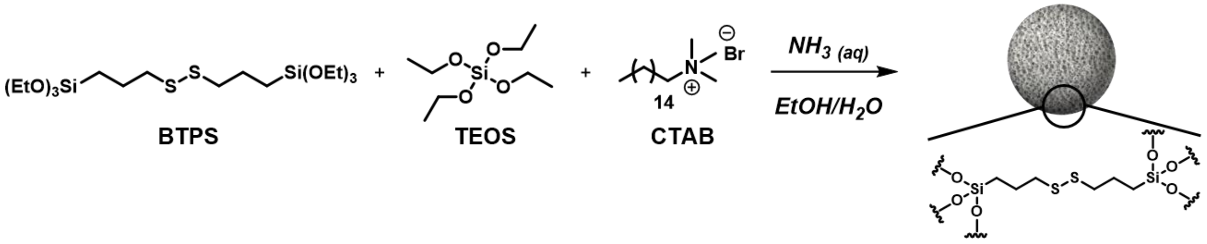

Scheme 3. Schematic representation of the preparation of **SS-MSPs**.

SEM images of **SS-MSPs** showed the spherical morphology of the particles, with a size of 242±17 nm (Figure 12a). STEM images of **SS-MSPs** revealed the absence of a highly ordered mesoporous phase within the particles, which was confirmed by the SAXS pattern obtained from **SS-MSPs**, where no sharp peak could be observed, but only a shoulder centered around q=1.6 nm^{-1}.

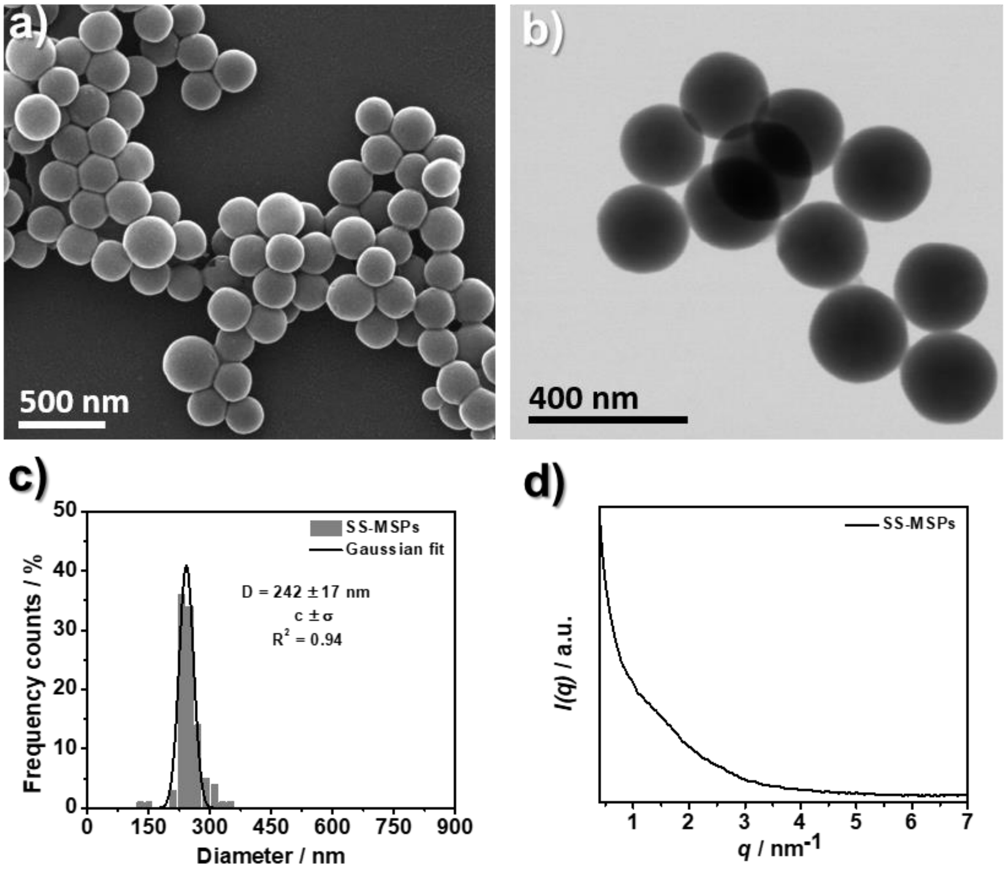

Figure 12. a) SEM and b) STEM images of **SS-MSPs**. c) Calculated size distribution of **SS-MSPs** using STEM images (*N*=100). d) SAXS pattern obtained from **SS-MSPs**.

N_2 adsorption–desorption measurements were used to characterize the porosity of **SS-MSPs** (Figure 14a), which demonstrated the presence of mesopores with an average pore diameter of 2.2 nm (Figure 14 b), having a total pore volume of 0.44 cm^3g^{-1} and a BET specific surface area of 470 m^2g^{-1}.

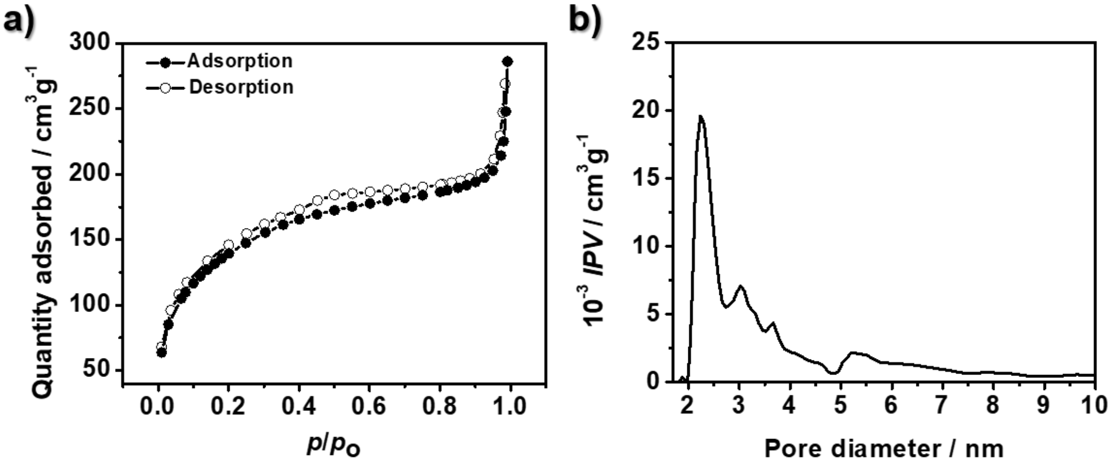

Figure 14. a) N_2 adsorption and desorption isotherms measured on **SS-MSPs.** b) DFT pore size distribution calculated from adsorption branch of the isothermal curve of **SS-MSPs**.

The organic content within **SS-MSPs** was determined by TGA (Figure 15a) and a 28 wt% loss was observed compared to pristine **MSPs.** The covalent linkage of the disulfide linker within the silica framework was confirmed by XPS. The survey spectrum recorded on **SS-MSPs** (Figure 15b) shows the presence of C(1s), S(2s) and S(2p) signals at 285, 228 and 164 eV, respectively. Additionally, the deconvolution of the HR-scan for the S(2p) peak (Figure 15c) shows the presence of the overlapping spin-orbit doublets S-2(S2p$_{1/2}$) (164.8 eV) and S-1 S(S2P$_{3/2}$) (163.6 eV). The deconvolution of the HR-scan for the C(1s) peak (Figure 15d) three components C-1 (284.3 eV), C-2 (284.9 eV) and C-3 (286.2eV), that can be attributed to C–H, C–C and C–S species, respectively.[38]

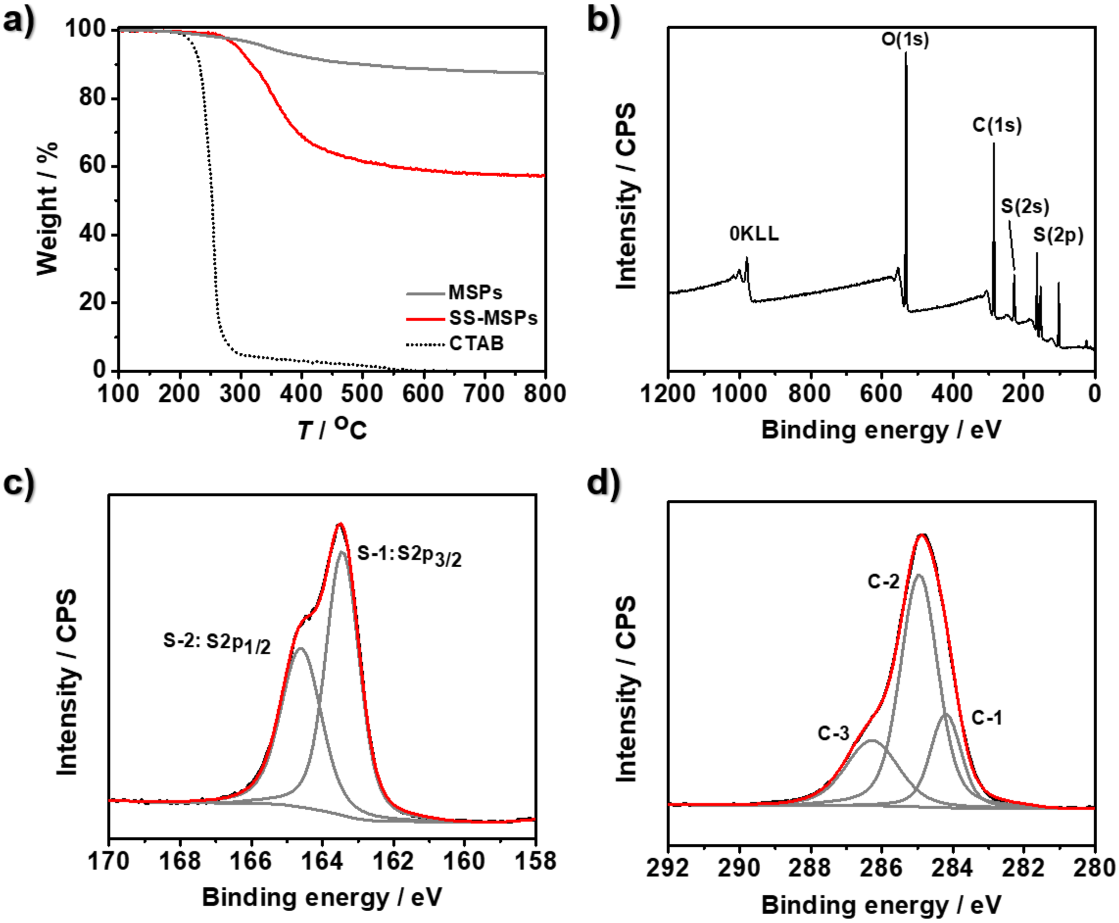

Figure 15. a) Thermogram recorded on **MSPs**, **SS-MSPs** and the surfactant CTAB. b) XPS survey spectrum recorded on **SS-MSPs**. c) Deconvoluted XPS HR scan of S(2p) level recorded on **SS-MSPs.** c) Deconvoluted XPS HR scan of C(1s) level recorded on **SS-MSPs**.

2.2.4. Preparation and characterization of MSPs

Pristine mesoporous silica particles (**MSPs**) have been prepared to compare the photo-responsive behavior of **LB-MSPs** with particles that do not possess an organic functional group within the inorganic structure. The particles have been prepared according to a previously reported procedure (see section 2.4.3 for details).[8] SEM and STEM images of **MSPs** (Figure 16a and b) showed that spherical particles with a size of 209±20 nm (Figure 16c) were obtained and the presence of a relatively ordered porous mesophase was confirmed by the SAXS pattern recorded on **MSPs** (Figure 16d), which shows a broad peak centered at q=1.9 nm^{-1}.

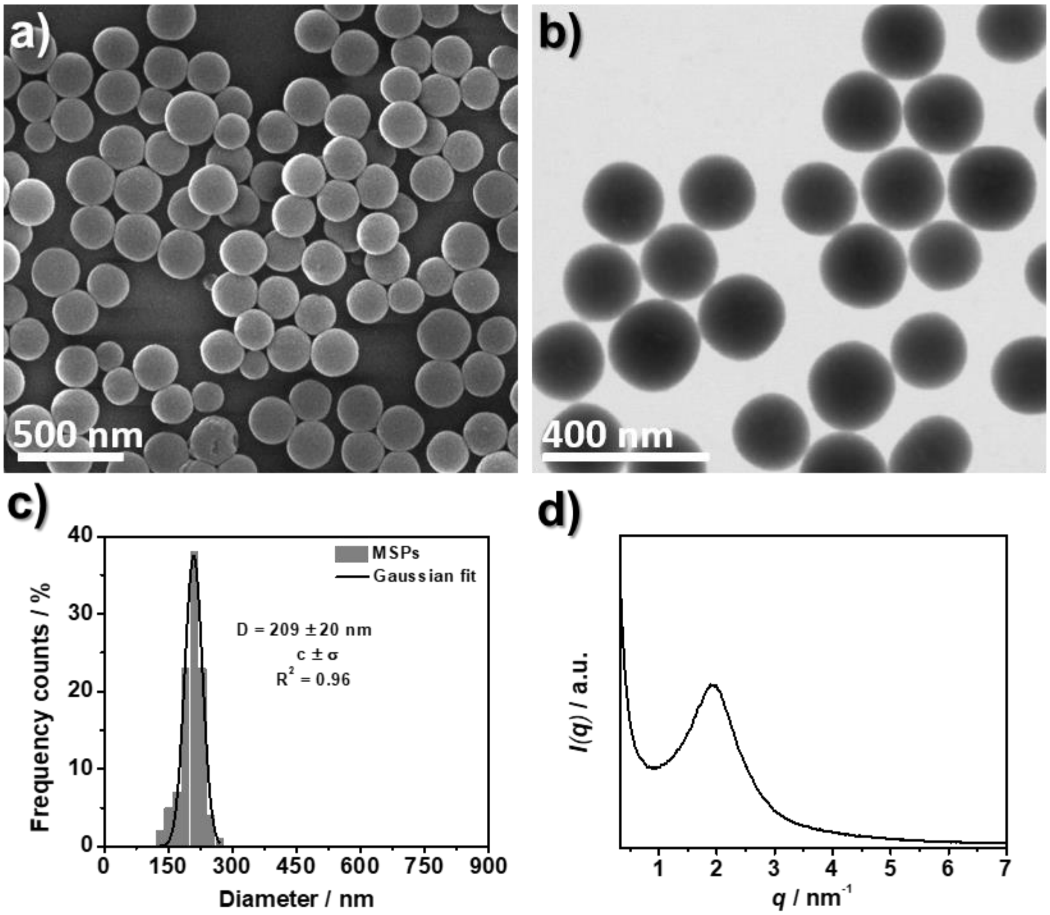

Figure 16. a) SEM and b) STEM images of **MSPs**. c) Calculated size distribution of **MSPs** using STEM images (*N*=100). d) SAXS pattern recorded on **MSPs**.

The porosity of **MSPs** was assessed by N_2 adsorption–desorption experiments. As depicted in Figure 17a, the adsorption branch follows a sigmoidal type IV adsorption branch, typical for mesoporous materials. DFT pore size distributions were calculated from the adsorption branch and an average pore diameter of 2.5 nm having a total pore volume of 0.86 cm^3g^{-1} was calculated for **MSPs**. The specific BET surface area was calculated to be 1243 m^2 g^{-1}. Compared to **LB-MSPs** and **SS-MSPs**, pristine **MSPs** possess more accessible mesopores, which explains the increased specific surface areas and pore volumes for these particles. Since the particles were prepared in the absence of a sterically hindered organic bis-alkoxysilane, the mesoporous phase of the particles was, compared to **SS-MSPs** and **LB-MSPs**, more uniformly dispersed, which reflected in the narrow pore-size distribution obtained from N_2 sorption measurements (Figure 17b).

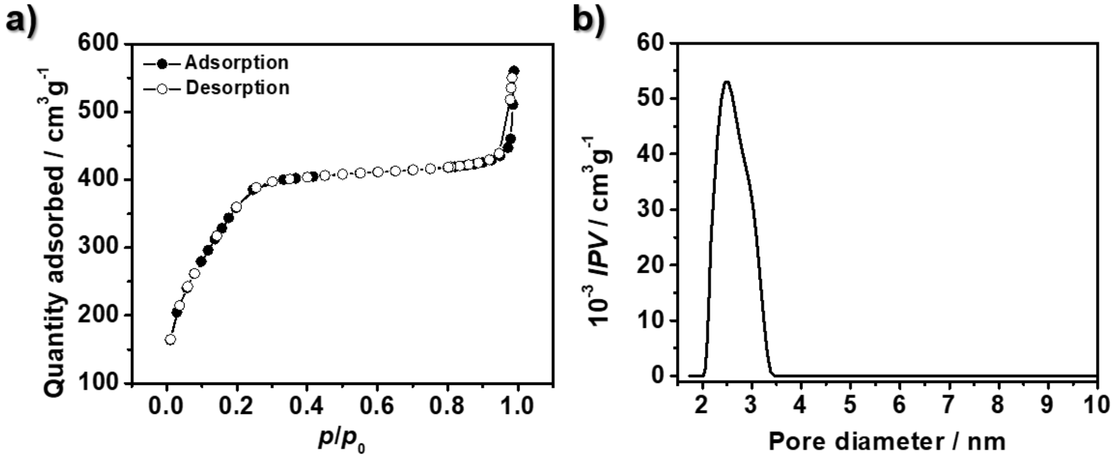

Figure 17. a) N_2 adsorption and desorption isotherms measured on **MSPs.** b) DFT pore size distribution calculated from adsorption branch of the isothermal curve of **MSPs**.

2.2.5. Light-triggered degradation of light-breakable mesoporous organosilica particles

The light-induced degradation of **LB-MSPs** was investigated by irradiating a dispersion of the particles (c=0.1 mg·mL^{-1}) in an EtOH/H_2O mixture (5:1 *v*/*v*) with 327 nm light and by analyzing aliquots of the dispersion by SEM and STEM. UV-Vis absorption spectra of the dispersion were also recorded over time. The specific solvent mixture was selected to have a water content similar to that of creams and ointments, considering the potential use of these particles as drug-delivery carriers for topical applications. In order to exclude the possibility that the particles degrade because of eventual hydrolysis of the amorphous silica control tests in solutions containing 20% of water were also performed. The breakability of the particles upon light-irradiation was followed by electron microscopy images to observe the light-induced change in morphology of **LB-MSPs**. Furthermore, UV-Vis absorption spectroscopy was used to confirm the light-triggered degradation of the light-responsive linker within **LB-MSPs**. As shown in the SEM images (Figure 18a), the surface of **LB-MSPs** became rougher after 20 min of UV-light irradiation and an amorphous material could be visualized due to the degradation of the particles. Prolonged irradiation induced an advanced structural disintegration of the particles, and after 6 h of light irradiation the complete loss of the initial morphology could be seen. The aggregates present in the SEM images could be due to a drying effect on the glass coverslip during sample preparation on the small debris formed upon degradation. STEM images (Figure 18b) recorded on the same samples confirmed the degradation of the particles into small debris. Furthermore, no particles with reduced core densities could be observed suggesting that the degradation process occurs from the exterior of the particle.

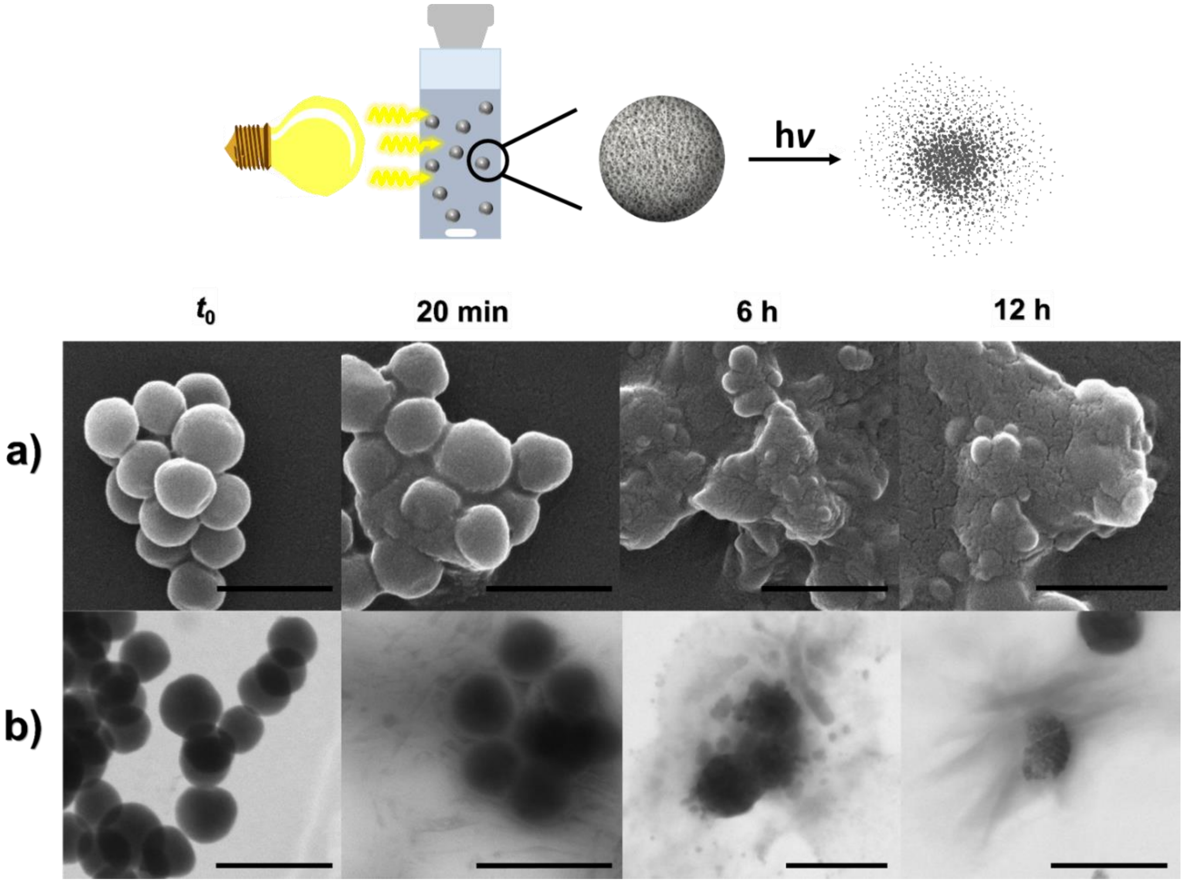

Figure 18. a) SEM and b) STEM images of **LB-MSPs** at t_0 and after 20 min and 6 h of UV-light irradiation at 327 nm, scale bars = 500 nm.

The UV-Vis absorption spectra recorded on **LB-MSPs** upon light irradiation at 320 nm (Figure 19), confirmed the light-induced degradation of the photo-responsive linker in **LB-MSPs**. After 20 min of light irradiation the characteristic absorption band at 327 nm, attributable to the nitrobenzyl group, was absent, thereby indicating its cleavage. This observed change in the UV-Vis spectra of

LB-MSPs upon light irradiation is in agreement with the results obtained for the light-degradable linker **1**.

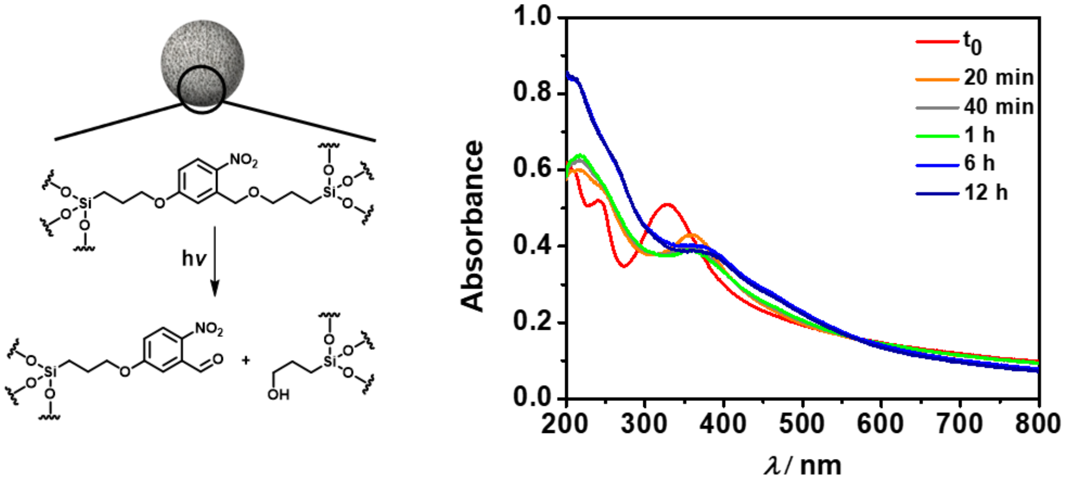

Figure 19. UV–vis absorption spectra recorded over time on a dispersion of **LB-MSPs** (0.1 mg·mL^{-1}) in EtOH/H_2O (5:1, *v*/*v*) upon light irradiation at λ_{irr}=327 nm.

For further confirmation that the particles break upon light irradiation, N_2 sorption experiments were performed on **LB-MSPs**. A **LB-MSPs** dispersion (0.1 mg·mL^{-1} in EtOH/H_2O 5:1, *v*/*v*) was irradiated for 24 h with 327 nm light and subsequently dried prior to measurement. As depicted in Figure 20, after light-irradiation the amount of nitrogen adsorbed by the material decreases significantly and the calculated total pore volume and BET specific surface area decreased substantially to 0.03 cm^{3}g^{-1} and 57 m^{2}g^{-1}. The decrease in total pore volume and specific surface area can be explained by the light-triggered degradation of the particles and as a consequence the loss of the porous structure and spherical morphology, diminishing therefore the amount of nitrogen gas that can be adsorbed on the material.

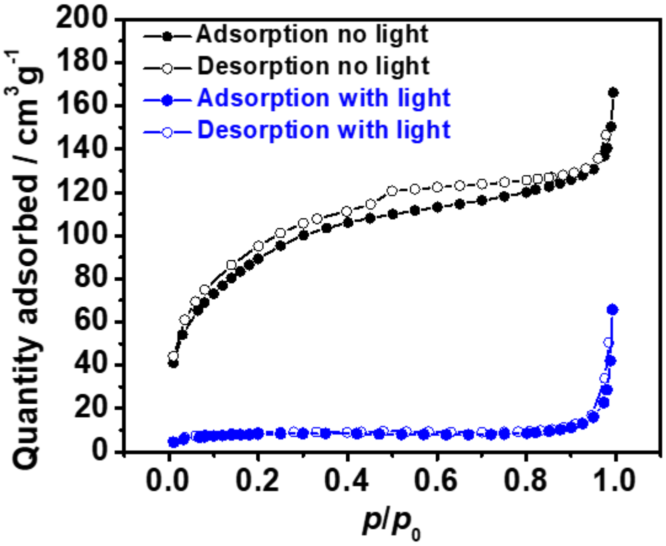

Figure 20. Comparison between the N_2 adsorption–desorption isotherms obtained for **LB-MSPs** (black) before and after UV-light irradiation (blue).

A control experiment was performed in which **LB-MSPs** (c=0.1 mg·mL^{-1}) were stirred in an EtOH/H_2O (5:1 v/v) mixture for 12 h in the dark. SEM (Figure 21a) and STEM (Figure 21b) images of the control experiment indicated that no degradation occurred after 12 h in the absence of light. Also, the UV-Vis absorption spectra of the particles remained unchanged, indicating the integrity of the light-degradable linker within **LB-MSPs** (Figure 21c). This control experiment confirms that the particles disintegration is only caused upon UV-light irradiation and that the solvent mixture has no effect on the particle morphology.

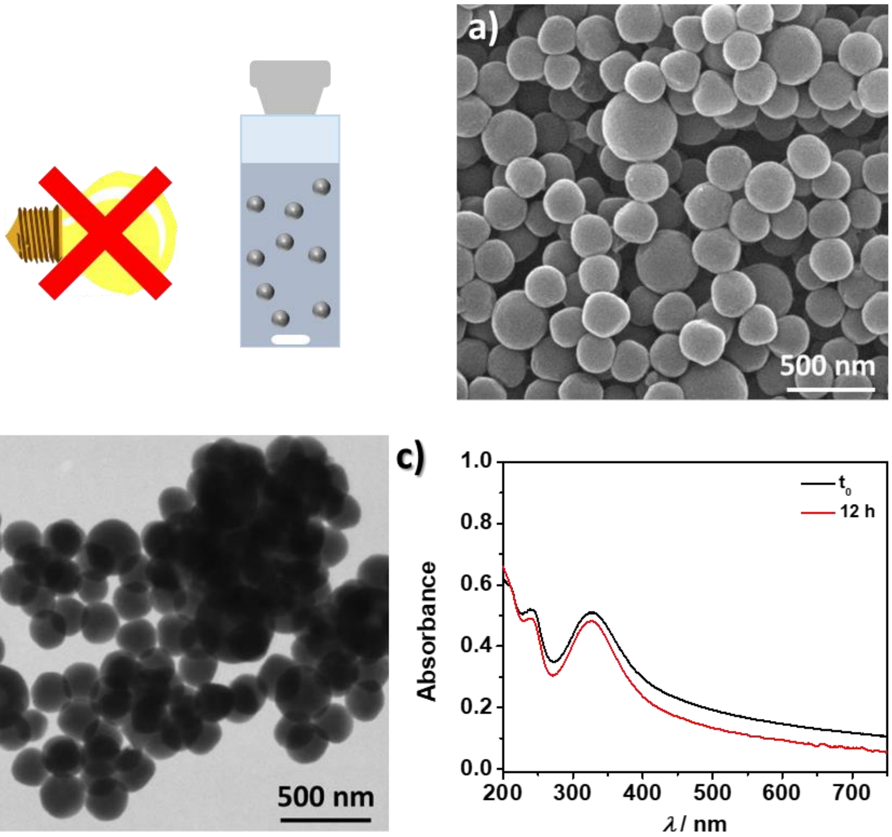

Figure 21. a) SEM and b) STEM images of **LB-MSPs** which have been stirred in the dark. c) UV-Vis absorption spectra of **LB-MSPs** stirred in the dark at t_0 and after 12 h.

2.2.6. Light-triggered cargo release from LB-MSPs

Once the unique light-triggered degradation of **LB-MSPs** has been assessed, the possibility of loading the particles with a bioactive molecule and its release upon light-irradiation were investigated. For this purpose, **LB-MSPs** were loaded with 7-dehydrocholesterol (**7-DH**), a hydrophobic molecule and natural vitamin D_3 precursor. The particles were suspended in a highly concentrated solution of **7-DH** (20 mg·mL^{-1}) in ethanol and stirred in the dark for 24 h. After solvent evaporation, the particles were washed and dried under reduced pressure (see section 2.4.4.). The final drug loading was determined to be 23 wt% by TGA (Figure 22a). For comparison, also **SS-MSPs** and pristine **MSPs** have been loaded with **7-DH** using the same loading protocol as for **LB-MSPs**. The amount of **7-DH** loaded within **SS-MSPs** was determined to be 28 wt% by TGA (Figure 22b), while for **MSPs** it resulted to be 5 wt% (Figure 22c). The cargo loading for **SS-MSPs** was comparable to the one obtained for **LB-MSPs**. The lowerloading efficacy of **7-DH** within **MSPs** could be explained by the particle higher hydrophilicity, since no organic functional groups are present within the silica structure, rendering an adsorption of the hydrophobic **7-DH** onto the pore-walls more difficult.

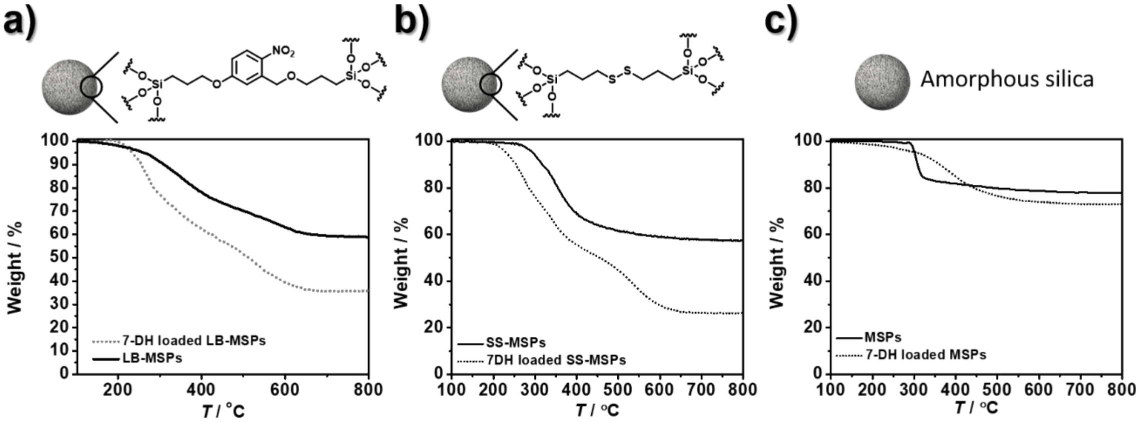

Figure 22. a) Thermogram of **LB-MSPs** and **7-DH** loaded **LB-MSPs**. b) Thermogram of **SS-MSPs** and **7-DH** loaded **SS-MSPs**. c)Thermogram of **MSPs** and **7-DH** loaded **MSPs**.

The release of **7-DH** from **LB-MSPs** upon light irradiation was investigated by UV-Vis absorption spectroscopy. An aqueous particle dispersion (ca. 0.8 mg·mL^{-1}) was prepared and a 500 µL aliquot was placed in a 10 mm path length quartz cuvette equipped with a small stirring bar. A layer of cyclohexane (2 mL) was then added on top of the aqueous particle dispersion in order to extract the released **7-DH**. Under gentle stirring, avoiding to mix the biphasic system, the particle dispersion was irradiated at 327 nm and the variation in absorbance in the cyclohexane layer at λ_{max}=281 nm was monitored over time (see section 2.4.7).

As depicted in Figure 23a, a boosted release of **7-DH** from **LB-MSPs** could be observed upon UV-light irradiation, which can be explained by the progressing degradation of **LB-MSPs** and therefore occurring release of the drug. In the absence of light, only a low amount of **7-DH** was released most probably due to the passive diffusion of the molecule loaded in the pores or physisorbed onto the particle surface (Figure 23a). To further confirm that the release of **7-DH** is triggered by light, the same release experiments were performed by using **MSPs** and **SS-MSPs** as references (See experimental section 2.4.7.). **SS-MSPs** particles possessed comparable particle size, shape and organic content to **LB-MSPs** but had the disulfide linker within their structure, which does not react upon UV-light irradiation. The release experiments showed that, besides the fast passive diffusion of **7-DH** from **SS-MSPs** and **MSPs**, no boosted release of the drug due to light irradiation was observed, demonstrating the unique light-triggered cargo release from **LB-MSPs** (Figure 23b).

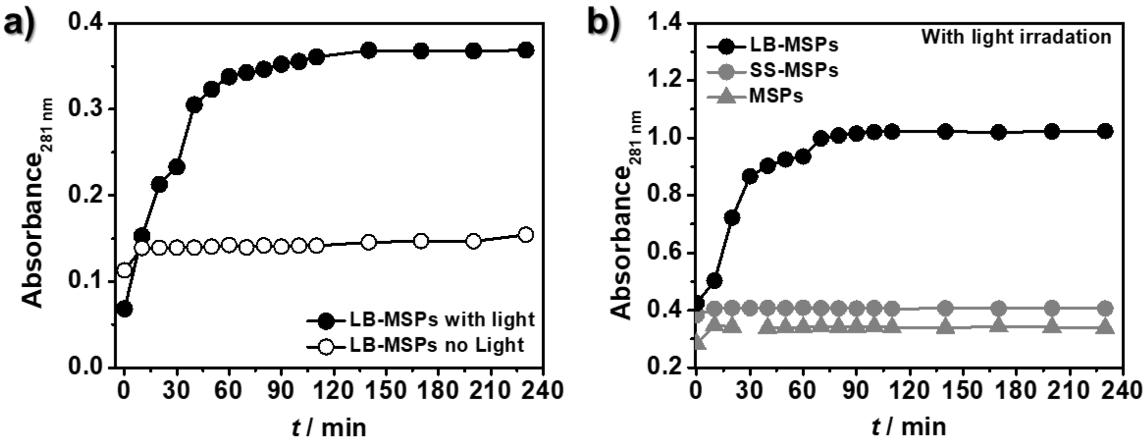

Figure 23. a) **7-DH** release monitored at 281 nm from **LB-MSPs** (c=0.1 mg·mL^{-1}) with and without light irradiation at λ_{irr} = 327 nm. b) **7-DH** release from **LB-MSPs** compared to **SS-MSPs** and pristine **MSPs** upon light irradiation at λ_{irr} = 327 nm; c(particles)=0.78 mg·mL^{-1}.

The amount of **7-DH** released from **LB-MSPs**, with and without light-irradiation, shown in Figure 23a, was calculated by comparing the absorbance values at 281 nm obtained for t=230 min with a calibration curve made from solutions of **7-DH** in cyclohexane at different concentrations (Figure 24). Considering that 0.39 mg of **LB-MSPs** were used and the loading of **7-DH** is 23 wt%, the amount of drug loaded was 0.0897 mg (2.33·10^{-7} mol) of **7-DH**, which corresponds to 100% of drug present in the system. The absorption value of **7-DH** after 230 min of UV-light irradiation was measured to be 0.3685, which corresponds to 7.3·10^{-7} mol, or 31 wt% of **7-DH** released upon light irradiation. In contrast, when no UV light was present, the absorbance measured after 230 min was 0.1540, which corresponded to 2.9·10^{-8} mol, or 12 wt% of **7-DH** released.

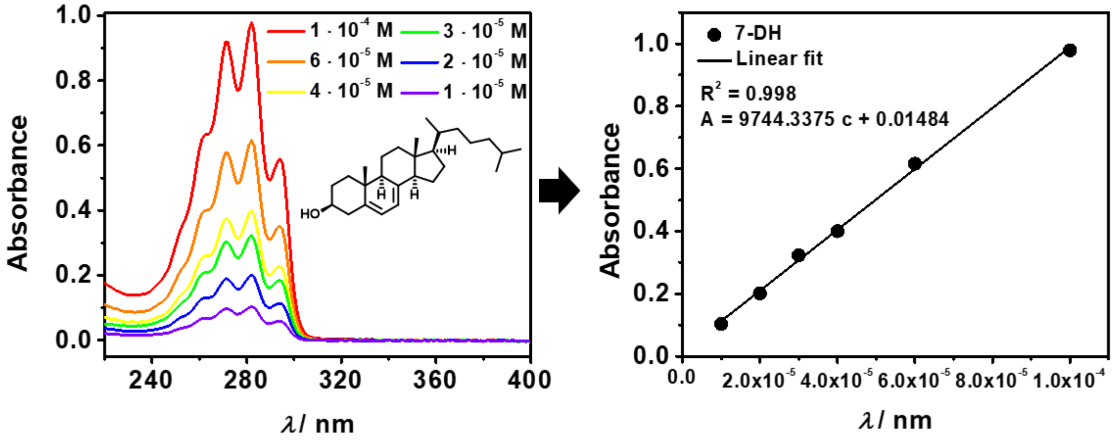

Figure 24. Left: UV-Vis absorption spectra of **7-DH** in cyclohexane recorded at different concentrations. Right: Calibration curve obtained for **7-DH** in order to quantify the amount of cargo release upon and without UV-light irradiation of **LB-MSPs**.

Finally, in order to exclude the possibility that the observed **7-DH** release from **LB-MSPs** may be caused by thermal effects upon light exposure, the particles were irradiated at 500 nm, a wavelength at which the photochemical degradation reaction of the nitrobenzyl moiety does not occur. As depicted in Figure 25a, upon irradiation at 500 nm, no **7-DH** release was observed by monitoring its absorbance at 281 nm. The triggered release of the drug could be detected when changing the irradiation wavelength from 500 nm to 327 nm. The lower overall absorbance measured for **7-DH** compared to the other release experiments here reported was since the particles had been further washed with EtOH/H_2O (1:9 *v*/*v*; 1x500µL). This was done in order to reduce the amount of physisorbed material, and consequently of passive release of **7-DH**, and to better visualize any variation upon light exposure. No light-induced degradation of the light-degradable linker occurred upon light irradiation at 500 nm, indicating that the light-triggered release of **7-DH** is only due to UV-light irradiation (Figure 25b).

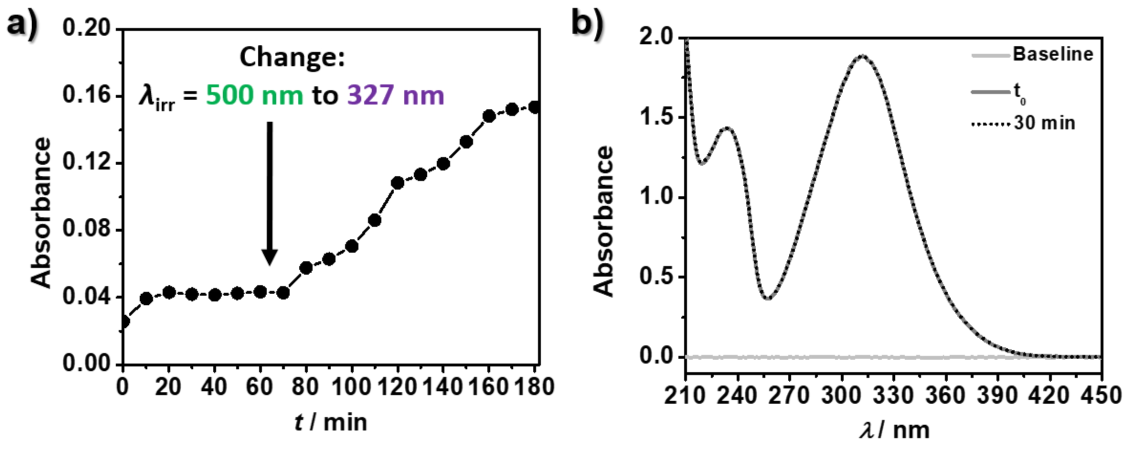

Figure 25. a) **7-DH** release from **LB-MSPs** (*c*=0.1 mg·mL^{-1}) monitored at 281 nm by UV-Vis absorption spectroscopy at two different irradiation wavelengths. b) UV-Vis absorption spectra of **1** irradiated with light of 500 nm at to and after 30 min.

2.2.7. Preliminary cytotoxicity tests

Taking into consideration that the particles could be used for biomedical applications, preliminary cytocompatibility test of the particles and their photodegradation products formed during UV-light irradiation were performed. The preliminary cytotoxicity study of **LB-MSPs** and their degradation products was done on HeLa cells, since this type of cell line is a standard for cytotoxicity experiments and the cells are especially easy to handle. Nevertheless, future cytotoxicity experiments on **LB-MSPs** will be done on healthy endothelial cell lines to simulate the particle´s toxicity when used for topical applications. HeLa cells were incubated for 12 and 24 h with different concentrations of **LB-MSPs** or light-breakable mesoporous organosilica particles that have been irradiated beforehand with UV-light at 320 nm for 12 h (**LB-MSPs_irradiated**) and the AlamarBlue® assay was used for the evaluation of the cytotoxicity (see section 2.4.8). As depicted in Figure 26, no relevant decrease in cell viability was observed for both **LB-MSPs** and **LB-MSPs_irradiated**, concluding that the particles do not show any relevant cytotoxicity at the investigated concentrations.

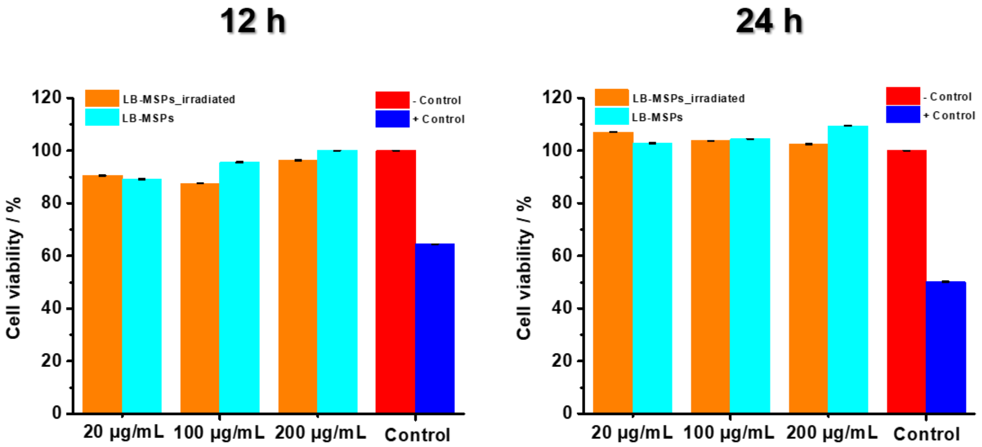

Figure 26. ALamarBlue® cell viability test results of **LB-MSPs** and **LB-MSPs_irradiated** on HeLa cells.

2.3. Conclusions

In this chapter, the preparation and characterization of a novel light-cleavable bis-alkoxysilane and its use for the preparation of spherical mesoporous organosilica particles that degrade upon light exposure has been presented. The cleavage of the nitrobenzyl-group containing bis-alkoxysilane takes place upon UV-light irradiation, with a quantum yield of 0.30±0.09. Incorporation of the linker within the silica structure of mesoporous particles allowed for the preparation of light-breakable particles and their potential as drug-delivery systems for the light-triggered release of provitamin D_3 (7-dehydrocholesterol) was demonstrated. The stability of the particles in the absence of light, while being degradable upon light irradiation, opens new possibilities in the design of novel organosilica carriers that release hydrophobic drug molecules in the presence of a non-chemical stimulus. Preliminary cytotoxicity tests further showed that the particles and their photodegradation products do not provoke any serious cytotoxicity towards HeLa cells, indicating a good cytocompatibility of this material. In future work the ability of **LB-MSPs** to serve as drug-delivery systems for topical applications will be of most interest, since the particles provide UV-light protection by absorbing harmful radiation, while simultaneously releasing a bioactive molecule.

2.4. Experimental section

2.4.1. Instruments

^{1}H, ^{13}C Nuclear magnetic resonance (NMR) spectra were recorded on a Bruker Avance 400 spectrometer. The ^{1}H NMR chemical shifts (δ) are given in ppm and refer to residual protons of the corresponding deuterated solvent. All deuterated solvents were used as received without any further purification. Signal splittings are described as singlet (s), doublet (d), triplet (t), multiplet (m). Coupling constants (J) are given in Hertz (Hz).

Fourier transform infrared (FTIR) transmittance spectra were measured with a Shimadzu IRAffinity-1 spectrometer. The spectrum of **1** was recorded in $CHCl_3$ (ca. 1 mg mL^{-1}, 0.1 mm path length NaCl window cell). The attenuated total reflectance Fourier transform infrared (ATR-FTIR) spectra of the particle samples were collected using a spectral resolution of $\Delta = 4$ cm^{-1}, accumulating 64 scans and the ATR-FTIR spectra were ATR corrected (penetration depth mode).

High resolution mass spectrometry (HR-MS) experiments were performed on a Bruker Daltonics microToF spectrometer (Bruker Daltonik GmgH, Bremen, Germany) with the electrospray ionization (ESI) interface operating in a positive ion mode.

Absorption spectra were measured on a Shimadzu UV-3600 spectrophotometer double-beam UV–VIS–NIR spectrometer and baseline corrected. Quartz cuvettes with path length of 10.0 mm were used for the recording of UV-Vis absorption spectra.

Light-breakability experiments on **LB-MSPs** and the photolabile linker **1** (but not for the quantum yield determination for **1**) were performed with a Horiba Jobin−Yvon IBH FL-322 Fluorolog 3 spectrometer equipped with a 450 W xenon arc lamp, double grating excitation, emission monochromators (2.1 nm/mm of dispersion; 1200 grooves/mm), and a TBX-04 detector. The emission slit opening were set to 14 mm. Quartz cuvettes with 10.0 mm path length were used.

Scanning electron microscopy (SEM) and scanning transmission electron microscopy (STEM) images were recorded with a FEI Quanta FEG 250 instrument (FEI corporate, Hillsboro, S3 Oregon, USA) with an acceleration voltage of 20 kV. The SEM sample were prepared by drop-casting the dispersion of particles in EtOH onto a glass cover slip, subsequently sputter coated with Au (Emitech K575X Peltier cooled) for 60 s at 60 mA prior to fixation on an Al support.

The STEM were prepared drop casting dispersions of particles in EtOH onto Formvar-coated Cu grids (400 mesh) and allowed to dry overnight prior visualization.

Transmission electron microscopy (TEM) samples were analyzed on a FEI/PHILIPS CM120 system operating at 100 kV. Samples were prepared drop casting dispersions of particles in EtOH (ca. 0.1 mg/mL) onto Formvar-coated Cu grids (400 mesh) and allowed to dry overnight prior visualization.

Dynamic light scattering (DLS): the measurements were conducted on a Delsa Nano C Particle Analyzer (Beckman Coulter, operative wavelength 655 nm). The DLS measurements were performed on dispersions of the particles in EtOH (ca. 0.1 mg/mL).

Nitrogen physisorption isotherms were obtained with a Micromeritics ASAP-2020 physisorption instrument. The particles were degassed at 100 °C for 12h. The measurement was performed at -196 °C. The surface areas were calculated by Brunauer–Emmett–Teller (BET) method in the relative pressure range of the adsorption branch at p/p_0 0.06-0.3. The pore size distributions and pore volumes were calculated by density functional theory (DFT) method on the adsorption branch. The adsorption data were analyzed by using the SAIEUS software (model used: N2@77K, cylindrical pores in an oxide surface),8 provided by Micrometrics. The total pore volume was calculated at p/p_0=0.99.

Small-angle X-ray scattering (SAXS) set-up comprised the SAXSess mc2 instrument from Anton Paar GmbH, containing a slit collimation system, and the PW3830 laboratory X-ray generator (40 kV, 50 mA) with a long-fine focus sealed X-ray tube (CuKα wavelength of λ = 0.1542 nm) from PANalytical. Detection was performed with the 2D imaging-plate reader Cyclone® by Perkin Elmer. The measurement was performed on a powder sample for 5 min and the data collected up to a scattering vector q value of 7 nm^{-1}, where q = (4πsinθ)/λ and 2θ is the scattering angle.

The 2D data were converted to 1D data and background-corrected by using SAXSQuant software (Anton Paar GmbH, Austria).

X-Ray photoelectron spectroscopy (XPS) analysis was performed using a K-Alpha™+ X-ray Photoelectron Spectrometer System (Thermo Scientific). Monochromatic Al K alpha X-rays were used (15 keV, 72 W, 200 mm spot diameter). Spectra were measured using pass energy of 200 eV for survey spectra and 50 eV for core level spectra. The samples were analysed as powders. The Advantage software was used for background subtraction (smart-mode), and deconvolution of peaks.

Thermogravimetric analysis (TGA) was conducted on a Netzsch model STA 449 fi Jupiter instrument. The samples (ca. 2 mg) were kept at 100°C for 30 min for stabilization, then heated from 25 to 800 °C at a speed of 10°C/min, before being held at this temperature for further 30 min, and finally cooled. The analyses were performed under a 20 mL/min air flow.

2.4.2. Synthesis of the light-degradable bis-alkoxy silane 1

General information: Compound **1** was prepared according to the reactions shown in Scheme 1. All reactions were carried out under argon atmosphere. The round-bottom flasks used in the reactions were oven-dried at 110 °C prior to use. All reactions were performed in anhydrous solvents as purchased from Sigma–Aldrich. The reaction progress was monitored by thin-layer chromatography (TLC) with silica gel 60 F254 coated on aluminum sheets (Merck). Flash column chromatography was carried out using 60-200 µm silica gel (VWR Chemicals). The solvents used were reagent grade or higher, unless otherwise noted. The following compounds were purchased from the listed supplies at the given purity and were used without further purification: sodium hydride (NaH, Sigma–Aldrich, 90%), 5-hydroxy-2-nitrobenzyl alcohol (Sigma–Aldrich, 97%), *N*,*N*-dimethylformamide (DMF, Sigma–Aldrich, anhydrous, 99.8%), triethoxysilane (Sigma–Aldrich, 95%), platinum(0)-1,3-diviynl-1,1,3,3-tetramethyldisiloxane complex solution (Karstedt's catalyst, Pt∼2 wt% in xylene, Sigma–Aldrich), sodium sulfate (anhydrous, Sigma–Aldrich, ACS reagent), and sodium hydrogen carbonate (Sigma–Aldrich, ACS reagent, >99.7%).

4-(allyloxy)-2-((allyloxy)methyl)-1-nitrobenzene (2): NaH (311 mg, 12.98 mmol) was added portion-wise to a stirring solution of 5-hydroxy-2-nitrobenzyl alcohol (1.00 g, 5.91 mmol) in dry DMF (10 mL) at 0 °C. After the completed addition of NaH, the reaction mixture was further stirred for 10 min at 0 °C. Subsequently, allyl bromide (1.17 mL, 13.52 mmol) was added dropwise to the stirring reaction mixture at 0 °C. The reaction mixture was stirred for 1 h at 0°C and for a further 1 h at room temperature and was then quenched with water (5 mL). The aqueous layer was extracted with ethyl acetate (3×, 20 mL), and the combined organic layers were washed with a saturated Na_2CO_3 solution and brine, and finally dried over anhydrous Na_2SO_4. Subsequently, the solvent was evaporated under reduced pressure and the crude oil was purified by column chromatography (silica gel, EtOAc/cyclohexane=1:2), affording the diallyl intermediate **2** as a yellowish oil (1.05 g, 71%). ^{1}H NMR ($CDCl_3$, 400 MHz): δ 8.16 (d, 1H, *J*=9.1 Hz), 7.37 (m, 1H), 6.87 (m, 1H), 6.09–5.94 (m, 2H), 5.47–5.23 (m, 4H), 4.94 (s, 2H), 4.66–4.64 (m, 2H), 4.17–4.15 ppm (m, 2H). ^{13}C{^{1}H} NMR ($CDCl_3$, 100 MHz): δ 163.1, 139.8, 139.0, 134.2, 132.0, 127.6, 118.6, 117.3, 113.5, 113.3, 71.9, 69.3, 69.0 ppm. ATR-FTIR $\tilde{\nu}_{max}$ [cm^{-1}]: 3861, 2854, 1577, 1508, 1336, 1321, 1282, 1228, 1066, 993, 923, 842, 754. HR-MS (ESI-TOF): *m*/*z* [M+H]$^+$ calcd for $C_{13}H_{16}NO_4$, 250.1079; found, 250.1073.

^{1}H-NMR (400 MHz, $CDCl_3$)

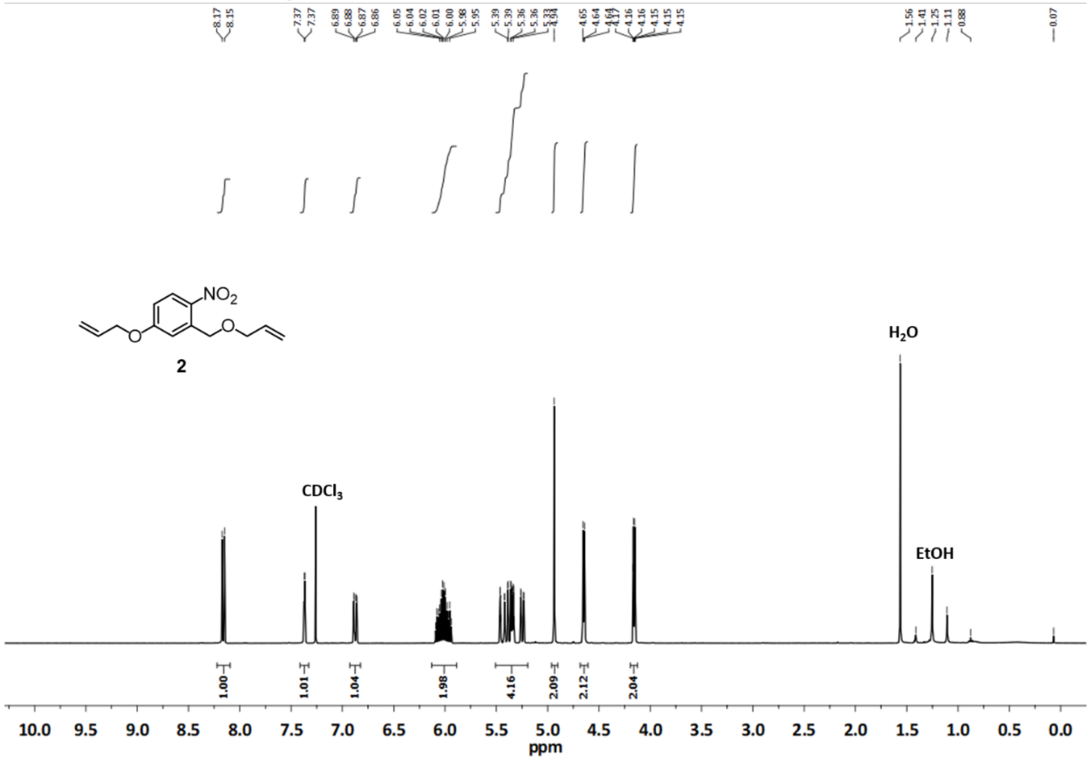

^{13}C-NMR (100 MHz, $CDCl_3$)

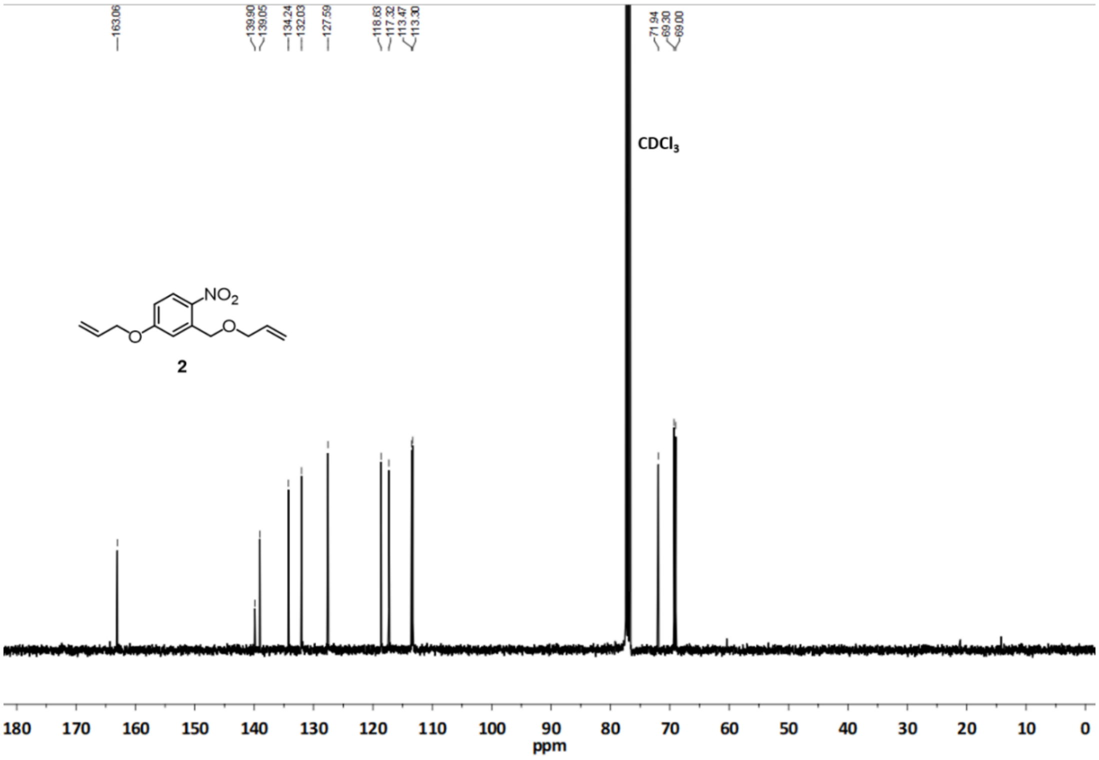

Triethoxy(3-(4-nitro-3-((3-(triethoxysilyl)propoxy)methyl)phenoxy)propyl)silane (1): To a solution of **2** (1.00 g, 4.01 mmol) in dry toluene (9 mL), triethoxysilane (2.02 mL, 10.95 mmol) and platinum(0)-1,3-divinyl-1,1,3,3-tetramethyldisiloxane complex solution (Karstedt's catalyst, Pt∼2 wt% in xylene, 125 µL) were added dropwise in this order. The reaction mixture was stirred at 50°C for 12 h. Additional Karstedt's catalyst solution (100 µL) was added, and the reaction mixture was stirred for a further 12 h at 50°C. The organic solvent was evaporated under reduced pressure, and the crude oil was purified by column chromatography (silica gel, EtOAc/ cyclohexane=1:7), yielding compound **1** as a yellowish oil (692 mg, 63%). ^{1}H NMR (400 MHz, $CDCl_3$): δ 8.14 (d, 1H, *J*=9.1 Hz), 7.31 (m, 1H), 6.83 (m, 1H), 4.90 (s, 2H), 4.04 (t, 2H, *J*=6.7 Hz), 3.86–3.81 (m, 12H), 3.58 (t, 2H, *J*=6.8 Hz), 1.97–1.90 (m, 2H), 1.84–1.77 (m, 2H), 1.23 (t, 18H, J = 7.0 Hz), 0.7–0.75 (m, 2H), 0.7–0.69 ppm (m, 2H). ^{13}C{^{1}H} NMR ($CDCl_3$,100 MHz): δ 163.3, 139.6, 139.3, 127.5, 113.3, 112.7, 73.5, 70.5, 69.6, 58.48, 58.41, 23.1, 22.6, 18.3, 6.6, 6.5 ppm. FTIR ṽ max [cm^{-1}]: 3016, 2978, 2931, 2889, 1583, 1512, 1442, 1388, 1340, 1323, 1286, 1230, 1165, 1103, 1078, 958. HR-MS (ESI-TOF): m/z [M + Na]$^{+}$ calcd for C25H47NO10Si2Na, 600.2636; found, 600.2624.

^{1}H-NMR (400 MHz, $CDCl_3$)

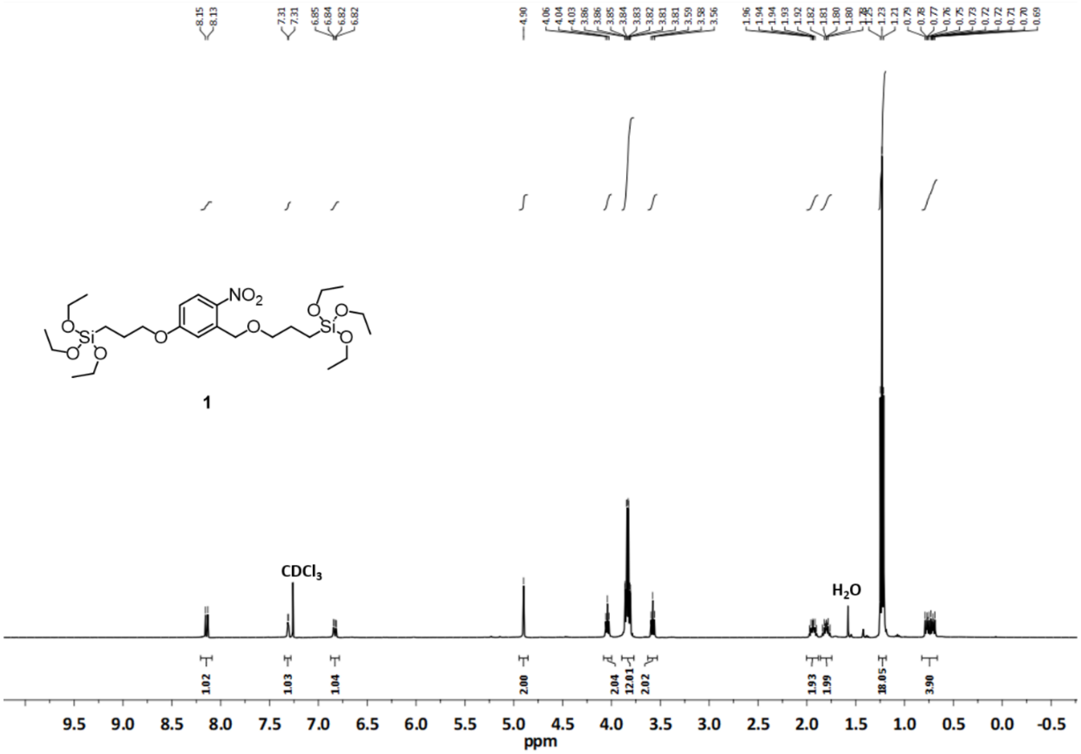

1

^{13}C-NMR (100 MHz, $CDCl_3$)

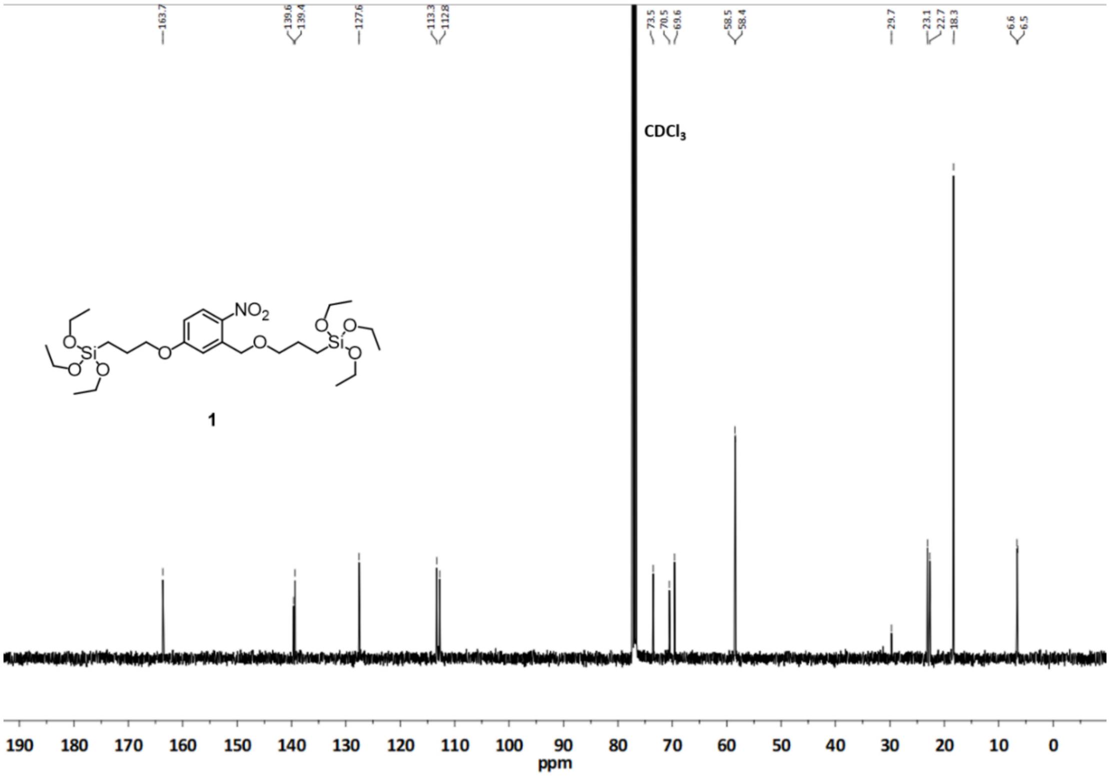

1

2.4.3. Preparation of particles

General information: All the reactions were carried out in a 100 mL round-bottom flask equipped with a magnetic stirring bar (1 cm Teflon-coated cylindrical bar). EtOH from Carlo Erba (ACS reagent), hexadecyltrimethylammonium bromide (CTAB, Acros Organics, 99+%), ammonia solution (VWR, 28%), tetraethyl orthosilicate (TEOS, Sigma–Aldrich, ≥99% GC), and bis[3-(triethoxysilyl)propyl]disulfide (fluorochem, tech grade) were used for the preparation of the particles.

Preparation of light-breakable mesoporous organosilica particles (LB-MSPs). CTAB (50 mg, 0.137 mmol) was added to an EtOH/H_2O mixture (14.5:30, *v*/*v*) and stirred at 250 rpm until its complete dissolution. Subsequently, NH_3 (28 wt%, 350 µL) was added to the mixture under stirring, and the stirring speed was increased to 1000 rpm. A mixture of TEOS (87.3 µL, 0.39 mmol) and compound **1** (100 mg, 0.173 mmol) in EtOH (500 µL) was added, and the mixture was stirred (1000 rpm) at r.t. overnight in the dark. The solution was decanted, leaving behind any material which was adhered to the walls, and the particles were recovered by centrifugation at 20000 ×g (15 min). Subsequent purification and extraction steps were carried out under the exclusion of light. Particles were thoroughly washed by sonication and centrifugation with distilled H_2O/EtOH (1:1, *v*/*v*; 2×) and EtOH (2×). The organic template was removed by heating the particle dispersion in EtOH to reflux for 12 h. The material was recovered by centrifugation, re-dispersed in EtOH, sonicated for 2 min, and centrifuged again. The particles were re-dispersed in EtOH, the dispersion heated to reflux for additional 12 h and finally centrifuged. The particle were washed with EtOH (3×) and dried overnight under reduced pressure.

Preparation of disulfide-bridged mesoporous organosilica particles (SS-MSPs). CTAB (50 mg, 0.137 mmol) was dissolved in an EtOH/H_2O mixture (14.5/30, *v*/*v*) and stirred at 250 rpm until its complete dissolution. Subsequently, NH_3 (28 wt.%, 350 µL) was added to the stirring solution and the stirring speed was increased to 1000 rpm. A mixture of TEOS (87.3 µL, 0.39 mmol) and compound bis[3-(triethoxysilyl)propyl]disulfide (79.75µL, 0.173 mmol) in EtOH (500 µL) were added and the mixture was stirred (1000 rpm) at r.t. overnight. The solution was decanted, leaving behind any material, which was adhered to the walls, and the particles were recovered by centrifugation at 20000 ×g (15 min). Particles were thoroughly washed by sonication and centrifugation with distilled H_2O/EtOH (1:1, *v*/*v*; 2x) and EtOH (2x). The organic template was removed by refluxing the particles in EtOH for 12 h. The material was recovered by centrifugation, re-dispersed in EtOH, sonicated for 2 min, and centrifuged again. The particles were re-dispersed in EtOH, the dispersion heated to reflux for additional 12 h and finally centrifuged. The particle were washed with EtOH (3×) and dried overnight under reduced pressure.

Preparation of mesoporous silica particles (MSPs): CTAB (50 mg, 0.137 mmol) was added to an EtOH/H_2O mixture (15:30, *v*/*v*) and stirred at 250 rpm until its complete dissolution. Subsequently, NH_3 (28 wt%, 350 µL) was added to the stirring solution and the stirring speed was increased to 1000 rpm. A mixture of TEOS (125 µL, 0.56 mmol) were added and the mixture was stirred (1000 rpm) at r.t. overnight. The solution was decanted, leaving behind any material, which was adhered to the walls, and the particles were recovered by centrifugation at 20000 ×g (15 min). Particles were thoroughly washed by sonication and centrifugation with distilled H_2O/EtOH (1:1, *v*/*v*; 2×) and EtOH (2×). The organic template was removed by heating a particle dispersion in EtOH to reflux for 12 h. The material was recovered by centrifugation, re-dispersed in EtOH, sonicated for 2 min, and centrifuged again. The particles were re-dispersed in EtOH, the dispersion heated to reflux for additional 12 h and finally centrifuged. The particle were washed with EtOH (3×) and dried overnight under reduced pressure.

2.4.4. 7-DH loading of MSPs, SS-MSPs and LB-MSPs

A suspension of particles (4 mg) and 7-dehydrocholesterol (**7-DH**; 4 mg) in EtOH (200 µL) was stirred for 24 h at room temperature. Subsequently, the organic solvent was evaporated, the particles were washed with a mixture EtOH/H_2O=1:9 (*v*/*v*; 2×500µL) and dried overnight under reduced pressure.

2.4.5. Light-triggered degradation study of compound 1

Spectroscopic studies: A solution of **1** (0.11 mM in EtOH/H_2O=5:1 *v*/*v*) in a quartz cuvette was irradiated with UV light at λ_{irr}=320 nm using a Horiba Jobin−Yvon IBH FL-322 Fluorolog 3 spectrometer equipped with a 450 W xenon arc lamp. The emission slit opening were set to 14 mm. UV-Vis absorption spectra were recorded at different time intervals. When the degradation of **1** was investigated using NMR spectroscopy, a solution of **1** (2 mg in 0.6 mL of deuterated chloroform) placed in a non-quartz NMR tube was irradiated and spectra were recorded.

Actinometry: In a typical experiment, **1** and the actinometer (NBA=2-nitrobenzoic acid, Sigma–Aldrich 98%) were dissolved each in ca. 0.5 mL of the appropriate (deuterated acetone or $CDCl_3$) deuterated solvent and then added to a quartz NMR tube. The tube was then irradiated with a 365 nm LED (ThorLabs) driven at 550 mA, where the distance between the sample and the light source was kept fixed. Changes in the NMR spectra were monitored as function of irradiation time. Given that NMR integration-based quantitation techniques can be inaccurate if the system is not allowed to fully relax between pulses, a 30-degree pulse with a 4 second delay between pulses was employed to ensure that full relaxation is achieved. Experiments were either performed in a darkened room, or with the sample wrapped in aluminum foil when not in use to reduce stray light exposure. The rate of the light driving decomposition reactions can be described by Equation 6 (section 2.2.1). The LED intensity was calibrated through the quantification of the initial reaction rate for 2-nitrobenzaldehyde performed over a series of starting concentrations prepared in deuterated acetone. The initial reaction rate was monitored through the decay of the aldehyde peak in the NMR spectrum, where the area of the acetone solvent peak was used as an internal standard. The rate was then abstracted through a first-order kinetic fit to these data, Figure 4a. A plot of initial reaction rate vs initial concentration was subsequently modeled by using Equation 6, where ε_{365} = 260 M^{-1} cm^{-1} and, Φ_{365}=0.5 (Figure 4b). Once calibrated, the LED was used in subsequent actinometry experiments performed on **1**. These experiments were performed in $CDCl_3$, where hexamethyldisilane was introduced as an internal standard. The reaction rate was monitored by the decrease in the peak area for the benzylic proton peaks. Given the high concentrations used (> 60 mM) and the large extinction coefficient for the compound (6980 M^{-1} cm^{-1}), Equation 6 simplifies to Equation 7 (section 2.2.1). The initial reaction rate abstracted from a first order kinetic fit (Figure 5, section 2.2.1) were then used to calculate the reaction quantum yield. An average value for Φ_{365}= 0.30±0.09 (mean value±standard deviation, N=3).

2.4.6. Light-triggered degradation study of LB-MSPs

A dispersion of **LB-MSPs** (0.1 mg·mL^{-1}) in EtOH/H_2O (5:1, *v*/*v*) was placed in a quartz cuvette equipped with a magnetic stirrer. The dispersion was kept under stirring and irradiated at λ_{irr}=327 nm using a Horiba Jobin−Yvon IBH FL-322 Fluorolog 3 spectrometer equipped with a 450 W xenon arc lamp. The emission slit opening were set to 14 mm. The UV-Vis absorption spectra were recorded on the dispersion of particles. To follow the degradation by electron microscopy, a dispersion of **LB-MSPs** (0.1 mg·mL^{-1}) in EtOH/H_2O (5:1 *v*/*v*) was placed in a quartz cuvette equipped with a magnetic stirrer. The particle dispersion was irradiated at λ_{irr}=327 nm under stirring and aliquots were taken for SEM and STEM investigations at different time intervals.

2.4.7. Release of 7-DH from LB-MSPs, SS-MSPs and MSPs

Release of 7-DH upon UV-light irradiation from LB-MSPs: Cyclohexane (2 mL) was slowly added to a dispersion of **7-DH** loaded particles (0.39 mg) in H_2O (500 µL) contained in a quartz cuvette equipped with a magnetic stir bar. Under stirring, to avoid the mixing of the two separate phases, the aqueous layer was irradiated with light at 327 nm using a Horiba Jobin−Yvon IBH FL-322 Fluorolog 3 spectrometer equipped with a 450 W xenon arc lamp (the emission slit opening were set to 14 mm) and over time the UV-Vis absorption spectra were recorded on the cyclohexane phase.

Release of 7-DH upon UV-light irradiation from SS-MSPs, MSPs and LB-MSPs: Cyclohexane (2 mL) was slowly added to a dispersion of **7-DH** loaded particles (0.8 mg) in H_2O (500 µL) contained in a quartz cuvette equipped with a magnetic stir bar. Under stirring, avoiding the mixing of the two separate phases, the aqueous layer was irradiated with light at 327 nm using a Horiba Jobin−Yvon IBH FL-322 Fluorolog 3 spectrometer equipped with a 450 W xenon arc lamp (the emission slit opening were set to 14 mm) and over time the UV-Vis absorption spectra were recorded on the cyclohexane phase.

2.4.8. Cell viability assay

The cytotoxicity evaluation of **LB-MSPs** and their degradation products after 12 h of UV-light irradiation (**LB-MSPs_irradiated**) was performed by using HeLa cell line and the AlamarBlue® assay. **LB-MSPs_irradiated** were prepared by irradiating a suspension of **LB-MSPs** (3.2 mg·mL^{-1}) in EtOH/H_2O (5:1, *v*/*v*) at 327 nm for 12 h. The suspension was lyophilized prior to the biological evaluation to remove residual EtOH that was detrimental for the cell growth. The HeLa cells were seeded in a 96-well plate (1.5×104 cells per well) and incubated at 37 °C (5% CO_2) overnight to allow them to attach on the plate surface. The culture medium (CM; Dulbecco's Modified Eagle Medium) was then replaced by fresh CM (100 µL) containing different concentrations of nanoparticles (20, 100, 200 µg·mL^{-1}). After 12- and 24-h incubation, AlamarBlue® (10 µL) was added and the cells were incubated for additional 2 h. A solution of DMSO in CM (10%, *v*/*v*) and CM were used as the positive and negative control, respectively. The percentage of living cells was determined by monitoring the absorbance at 570 and 600 nm by using a microplate reader (Perkin Elmer, VICTOR™ X5).

2.4.9. DFT calculations

DFT calculations were performed using the Gaussian09 calculation suite. Ground state structure optimizations were performed at the B3LYP/6-31+G(d,p) level of theory, using a self-consistent reaction field (SCRF) PCM to model the influence of the surrounding solvent. Optimization into a global minimum was confirmed by the lack of negative vibration modes. Time-dependent (TD)-DFT calculations were performed to calculate electronic excitation energies using the random phase approximation at the B3LYP/6-311+G(2d,p) level of theory. The cartesian coordinates for the truncated nitroso-model were as followed:

C	-1.23112600	-0.33193900	-0.26303900
C	-0.16254500	-1.24352300	-0.19943000
C	1.15409900	-0.80830100	-0.09079400
C	1.42084000	0.58217200	-0.07337200
C	0.35558000	1.48473800	-0.14298300
C	-0.96055200	1.04746700	-0.22917800
H	-0.39329400	-2.30510500	-0.22014700

H	0.59235200	2.54389600	-0.14285600
H	-1.76144300	1.77569200	-0.28101800
N	2.78981000	1.03099000	-0.10107900
C	2.19497700	-1.86954000	0.05535200
H	1.83405100	-2.87583000	-0.25678300
O	3.31229100	-1.72035700	0.49550900
O	-2.45885900	-0.88833800	-0.37372000
C	-3.63532300	-0.06326100	-0.41050800
H	-4.39368800	-0.70834400	-0.86119000
H	-3.47677900	0.78477300	-1.08740100
C	-4.07129500	0.38638500	0.97853300
H	-4.23560100	-0.48198000	1.62390800
H	-3.32423500	1.02965800	1.45354700
H	-5.01007600	0.94727000	0.90868400
O	2.92808300	2.22967700	0.10612700

2.5. References

(1) Cassano, D.; Pocoví-Martínez, S.; Voliani, V. Ultrasmall-in-Nano Approach: Enabling the Translation of Metal Nanomaterials to Clinics. *Bioconjug. Chem.* **2018**, *29* (1), 4–16. DOI: 10.1021/acs.bioconjchem.7b00664.

(2) Croissant, J. G.; Fatieiev, Y.; Almalik, A.; Khashab, N. M. Mesoporous Silica and Organosilica Nanoparticles: Physical Chemistry, Biosafety, Delivery Strategies, and Biomedical Applications. *Adv. Healthc. Mater.* **2018**, *7* (4), 1–75. DOI: 10.1002/adhm.201700831.

(3) Henstock, J. R.; Canham, L. T.; Anderson, S. I. Silicon: The Evolution of Its Use in Biomaterials. *Acta Biomater.* **2015**, *11* (1), 17–26. DOI: 10.1016/j.actbio.2014.09.025.

(4) Croissant, J.; Cattoën, X.; Man, M. W. C.; Gallud, A.; Raehm, L.; Trens, P.; Maynadier, M.; Durand, J. O. Biodegradable Ethylene-Bis(Propyl)Disulfide-Based Periodic Mesoporous Organosilica Nanorods and Nanospheres for Efficient in-Vitro Drug Delivery. *Adv. Mater.* **2014**, *26* (35), 6174–6180. DOI: 10.1002/adma.201401931.

(5) Shao, D.; Li, M.; Wang, Z.; Zheng, X.; Lao, Y. H.; Chang, Z.; Zhang, F.; Lu, M.; Yue, J.; Hu, H.; Yan, H.; Chen, L.; Dong, W. fei; Leong, K. W. Bioinspired Diselenide-Bridged Mesoporous Silica Nanoparticles for Dual-Responsive Protein Delivery. *Adv. Mater.* **2018**, *30* (29), 1–8. DOI: 10.1002/adma.201801198.

(6) Maggini, L.; Cabrera, I.; Ruiz-Carretero, A.; Prasetyanto, E. A.; Robinet, E.; De Cola, L. Breakable Mesoporous Silica Nanoparticles for Targeted Drug Delivery. *Nanoscale* **2016**, *8* (13), 7240–7247. DOI: 10.1039/c5nr09112h.

(7) Liu, L.; Kong, C.; Huo, M.; Liu, C.; Peng, L.; Zhao, T.; Wei, Y.; Qian, F.; Yuan, J. Schiff Base Interaction Tuned Mesoporous Organosilica Nanoplatforms with PH-Responsive Degradability for Efficient Anti-Cancer Drug Delivery: In Vivo. *Chem. Commun.* **2018**, *54* (66), 9190–9193. DOI: 10.1039/c8cc05043k.

(8) Travaglini, L.; Picchetti, P.; Totovao, R.; Prasetyanto, E. A.; De Cola, L. Highly Degradable Imine-Doped Mesoporous Silica Particles. *Mater. Chem. Front.* **2019**, *3* (1). DOI: 10.1039/c8qm00438b.

(9) Fatieiev, Y.; Croissant, J. G.; Julfakyan, K.; Deng, L.; Anjum, D. H.; Gurinov, A.; Khashab, N. M. Enzymatically Degradable Hybrid Organic-Inorganic Bridged Silsesquioxane Nanoparticles for in Vitro Imaging. *Nanoscale* **2015**, *7* (37), 15046–15050. DOI: 10.1039/c5nr03065j.

(10) Maggini, L.; Travaglini, L.; Cabrera, I.; Castro-Hartmann, P.; De Cola, L. Biodegradable Peptide-Silica Nanodonuts. *Chem. - A Eur. J.* **2016**, *22* (11), 3697–3703. DOI: 10.1002/chem.201504605.

(11) Kloxin, A. M.; Kasko, A. M.; Salinas, C. N.; Anseth, K. S. Photodegradable Hydrogels for Dynamic Tuning of Physical and Chemical Properties. *Science (80-.).* **2009**, *324* (5923),

59–63. DOI: 10.1126/science.1169494.

(12) Raman, R.; Hua, T.; Gwynne, D.; Collins, J.; Tamang, S.; Zhou, J.; Esfandiary, T.; Soares, V.; Pajovic, S.; Hayward, A.; Langer, R.; Traverso, G. Light-Degradable Hydrogels as Dynamic Triggers for Gastrointestinal Applications. *Sci. Adv.* **2020**, *6* (3), 1–12. DOI: 10.1126/sciadv.aay0065.

(13) Roppolo, I.; Chiappone, A.; Angelini, A.; Stassi, S.; Frascella, F.; Pirri, C. F.; Ricciardi, C.; Descrovi, E. 3D Printable Light-Responsive Polymers. *Mater. Horizons* **2017**, *4* (3), 396–401. DOI: 10.1039/c7mh00072c.

(14) Cao, J.; Huang, S.; Chen, Y.; Li, S.; Li, X.; Deng, D.; Qian, Z.; Tang, L.; Gu, Y. Near-Infrared Light-Triggered Micelles for Fast Controlled Drug Release in Deep Tissue. *Biomaterials* **2013**, *34* (26), 6272–6283. DOI: 10.1016/j.biomaterials.2013.05.008.

(15) Zhu, J.; Lin, H.; Kim, Y.; Yang, M.; Skakuj, K.; Du, J. S.; Lee, B.; Schatz, G. C.; Van Duyne, R. P.; Mirkin, C. A. Light-Responsive Colloidal Crystals Engineered with DNA. *Adv. Mater.* **2020**, *1906600*, 1–6. DOI: 10.1002/adma.201906600.

(16) Li, S.; Moosa, B. A.; Croissant, J. G.; Khashab, N. M. Electrostatic Assembly/Disassembly of Nanoscaled Colloidosomes for Light-Triggered Cargo Release. *Angew. Chemie - Int. Ed.* **2015**, *54* (23), 6804–6808. DOI: 10.1002/anie.201501615.

(17) He, D.; He, X.; Wang, K.; Cao, J.; Zhao, Y. A Light-Responsive Reversible Molecule-Gated System Using Thymine-Modified Mesoporous Silica Nanoparticles. *Langmuir* **2012**, *28* (8), 4003–4008. DOI: 10.1021/la2047504.

(18) Aznar, E.; Oroval, M.; Pascual, L.; Murguía, J. R.; Martínez-Mánez, R.; Sancenón, F. Gated Materials for On-Command Release of Guest Molecules. *Chem. Rev.* **2016**, *116* (2), 561–718. DOI: 10.1021/acs.chemrev.5b00456.

(19) Lin, Q.; Huang, Q.; Li, C.; Bao, C.; Liu, Z.; Li, F.; Zhu, L. Anticancer Drug Release from a Mesoporous Silica Based Nanophotocage Regulated by Either a One- or Two-Photon Process. *J. Am. Chem. Soc.* **2010**, *132* (31), 10645–10647. DOI: 10.1021/ja103415t.

(20) Zhao, L.; Vaupel, M.; Loy, D. A.; Shea, K. J. Photoresponsive Hybrid Materials: Synthesis and Characterization of Coumarin-Dimer-Bridged Polysilsesquioxanes. *Chem. Mater.* **2008**, *20* (5), 1870–1876. DOI: 10.1021/cm702804r.

(21) Zhao, L.; Loy, D. A.; Shea, K. J. Photodeformable Spherical Hybrid Nanoparticles. *J. Am. Chem. Soc.* **2006**, *128* (44), 14250–14251. DOI: 10.1021/ja066047n.

(22) Il'ichev, Y. V.; Schwörer, M. A.; Wirz, J. Photochemical Reaction Mechanisms of 2-Nitrobenzyl Compounds: Methyl Ethers and Caged ATP. *J. Am. Chem. Soc.* **2004**, *126* (14), 4581–4595. DOI: 10.1021/ja039071z.

(23) Klán, P.; Šolomek, T.; Bochet, C. G.; Blanc, A.; Givens, R.; Rubina, M.; Popik, V.; Kostikov, A.; Wirz, J. Photoremovable Protecting Groups in Chemistry and Biology: Reaction Mechanisms and Efficacy. *Chem. Rev.* **2013**, *113* (1), 119–191. DOI: 10.1021/cr300177k.

(24) Pellois, J. P.; Muir, T. W. A Ligation and Photorelease Strategy for the Temporal and Spatial Control of Protein Function in Living Cells. *Angew. Chemie - Int. Ed.* **2005**, *44* (35), 5713–5717. DOI: 10.1002/anie.200501244.

(25) Elamri, I.; Heumüller, M.; Herzig, L. M.; Stirnal, E.; Wachtveitl, J.; Schuman, E. M.; Schwalbe, H. A New Photocaged Puromycin for an Efficient Labeling of Newly Translated Proteins in Living Neurons. *ChemBioChem* **2018**, *19* (23), 2458–2464. DOI: 10.1002/cbic.201800408.

(26) Lin, Y.; Mazo, M. M.; Skaalure, S. C.; Thomas, M. R.; Schultz, S. R.; Stevens, M. M. Activatable Cell-Biomaterial Interfacing with Photo-Caged Peptides. *Chem. Sci.* **2019**, *10* (4), 1158–1167. DOI: 10.1039/c8sc04725a.

(27) Watson, J. A.; Jarvis, B. B. Total Synthesis of Nominal Diazonamides. Part I: Convergent Preparation of the Structure Proposed for (-)-Diazonamide A. Part 2: On the True Structure and Origin of Natural Isolates. *Chemtracts* **2002**, *15* (9), 481–486.

(28) Kessler, M.; Glatthar, R.; Giese, B.; Bochet, C. G. Sequentially Photocleavable Protecting Groups in Solid-Phase Synthesis. *Org. Lett.* **2003**, *5* (8), 1179–1181. DOI: 10.1021/ol027454g.

(29) Zhang, R.; Li, L.; Feng, J.; Tong, L.; Wang, Q.; Tang, B. Versatile Triggered Release of Multiple Molecules from Cyclodextrin- Modified Gold-Gated Mesoporous Silica Nanocontainers. *ACS Appl. Mater. Interfaces* **2014**, *6* (13), 9932–9936. DOI: 10.1021/am502463h.

(30) Willett, K. L.; Hites, R. A. Chemical Actinometry: Using o-Nitrobenzaldehyde to Measure Light Intensity in Photochemical Experiments. *J. Chem. Educ.* **2000**, *77* (7), 900–902. DOI: 10.1021/ed077p900.

(31) Ji, Y.; DiRocco, D. A.; Hong, C. M.; Wismer, M. K.; Reibarkh, M. Facile Quantum Yield Determination via NMR Actinometry. *Org. Lett.* **2018**, *20* (8), 2156–2159. DOI: 10.1021/acs.orglett.8b00391.

(32) Grün, M.; Lauer, I.; Unger, K. K. The Synthesis of Micrometer- and Submicrometer-Size Spheres of Ordered Mesoporous Oxide MCM-41. *Adv. Mater.* **1997**, *9* (3), 254–257. DOI: 10.1002/adma.19970090317.

(33) Huh, S.; Wiench, J. W.; Yoo, J. C.; Pruski, M.; Lin, V. S. Y. Organic Functionalization and Morphology Control of Mesoporous Silicas via a Co-Condensation Synthesis Method. *Chem. Mater.* **2003**, *15* (22), 4247–4256. DOI: 10.1021/cm0210041.

(34) Atluri, R.; Hedin, N.; Garcia-Bennett, A. E. Hydrothermal Phase Transformation of Bicontinuous Cubic Mesoporous Material AMS-6. *Chem. Mater.* **2008**, *20* (12), 3857–3866. DOI: 10.1021/cm702440n.

(35) Kunc, F.; Balhara, V.; Sun, Y.; Daroszewska, M.; Jakubek, Z. J.; Hill, M.; Brinkmann, A.; Johnston, L. J. Quantification of Surface Functional Groups on Silica Nanoparticles: Comparison of Thermogravimetric Analysis and Quantitative NMR. *Analyst* **2019**, *144*

(18), 5589–5599. DOI: 10.1039/c9an01080g.

(36) Dunkin, I. R.; Gebicki, J.; Kiszka, M.; Sanín-Leira, D. Phototautomerism of O-Nitrobenzyl Compounds: O-Quinonoid Aci-Nitro Species Studied by Matrix Isolation and DFT Calculations. *J. Chem. Soc. Perkin Trans. 2* **2001**, No. 8, 1414–1425. DOI: 10.1039/b009630j.

(37) Yang, G.; Hu, H.; Zhou, Y.; Hu, Y.; Huang, H.; Nie, F.; Shi, W. Synthesis of One-Molecule-Thick Single-Crystalline Nanosheets of Energetic Material for High-Sensitive Force Sensor. *Sci. Rep.* **2012**, *2*, 1–7. DOI: 10.1038/srep00698.

(38) Mekaru, H.; Yoshigoe, A.; Nakamura, M.; Doura, T.; Tamanoi, F. Biodegradability of Disulfide-Organosilica Nanoparticles Evaluated by Soft X-Ray Photoelectron Spectroscopy: Cancer Therapy Implications. *ACS Appl. Nano Mater.* **2019**, *2* (1), 479–488. DOI: 10.1021/acsanm.8b02023.

Chapter 3

Novel biodegradable organosilica cages as nanocarriers for biomedical applications

In this chapter, the preparation and characterization of 20 nm sized cage-like organosilica nanoparticles is presented. The particles possess stimuli-responsive disulfide functional groups within the silica framework, which renders this material degradable upon the presence of endogenous reducing agents, such as the tripeptide glutathione. The possibility to load the particles with hydrophilic and hydrophobic drugs is shown along with the stimuli-triggered cargo release, demonstrating their potential for drug-delivery applications. Moreover, grafting procedures for easy and efficient functionalization of the particles with various biomolecules employing alkoxysilane chemistry are reported that allow ensuring a good particle colloidal stability. Since little is known about the biological fate of cage-like particles intravenous administration in healthy mice models was done and their biological feature were investigated. In-vivo results suggested that the particles do not accumulate preferentially in liver macrophages after occurred injection but are taken up by endothelial cells of the liver. Due to the particles ability to escape the uptake by liver macrophages, their use to treat effectively hepatocellular carcinoma can be envisioned, which will be further investigated in vivo in future experiments.

3.1. Introduction

Although tremendous research efforts have been made to develop nanomaterials for future applications in nanomedicine, only few have met the rigorous standards required for clinical implementation. Degradation represents a major hurdle for hard nanomaterials, where poor degradation leads to prolonged bioaccumulation, which in turn leads to an undesired chronic toxicity in living organisms.[1] Of many degradable nanoparticles currently under study for biomedical applications, porous organosilicas have attracted great interest in recent years due to several attractive physicochemical properties, including the facile tunability of properties, such as size,[2,3]morphology[4–6] and biodegradability[7]. Size represents an important factor in the particle´s biodistribution[8], and small nanoparticles ("small" meaning a diameter below 50 nm) are considered to possess favorable biodistribution properties due to accelerated elimination of these small particles from the body.[9] Regarding porous silica and organosilica particles, much effort has been devoted to decrease the final particle size via surfactant-directed formation pathways, while still maintaining a high degree of dispersibility and colloidal stability.[10–12] Over the past years, many reports have been published on the effect of different nanoparticle shapes on the biodistribution and bioaccumulation,[13–15] nevertheless little is known about the biological behavior of the recently discovered cage-like silica nanoparticles reported by Wiesner and co-workers.[16] These nanoparticles represent an attractive system to be explored for biomedical applications, owing to their small size and unique morphology characterized by a relatively large empty cavity. Inspired by Wiesner's work, we envisioned the preparation of 20 nm sized cage-like organosilica particles bearing biodegradable disulfide bridges within the silica framework, which to the best of our knowledge have not yet been described in the literature. Co-condensation of a disulfide containing bis-alkoxysilane with a common silica source in the presence of the surfactant CTAB and subsequent polyethylene glycol (PEG) and sulfo-cyanine 5 (sCy5) surface-grafting, allowed for the preparation of disulfide-bridged organosilica cages (**OSCs**). These particles have been fully characterized with standard characterization techniques for porous materials and the cage-like structure has been proven by 3D reconstruction of single-particle TEM images. Further it was shown that the cavity of the particles can be loaded with hydrophilic and hydrophobic molecules, proving their applicability for drug delivery applications.

Due to the presence silanol groups on the surface of the particles, fluorescent dyes and bioactive molecules for cellular recognition were successfully grafted on the particle surface using simple alkoxysilane chemistry. Considering the particle´s unique morphology and non-toxicity, preliminary biodistribution studies were performed on **OSCs** in healthy rat models to assess their potential use in biomedical applications, such as drug delivery or imaging. The obtained biodistributions results for **OSCs** in various organs, especially the liver, revealed the potential of these particles for anti-cancer applications in the latter organ, since histological analysis suggested that the particles are not sequestered by liver macrophages. Finally, the particles ability to cross stiff biological barriers, such as the blood–brain barrier, was investigated and future strategies to increase the ability of these particles to accumulate in the brain will be discussed.

3.2. Results and discussion

3.2.1. Preparation and characterization of cage-like organosilica particles

Disulfide-bridged organosilica cages (**OSCs**) were prepared by modifying previously reported procedure for the preparation of 20 nm sized mesoporous organosilica particles.[17] As depicted in Figure 1, the final organosilica cages were obtained through a two-step bottom-up procedure, according to which a disulfide-containing bis-alkoxysilane, namely bis(triethoxysilylpropyl) disulfide (BTDS), was hydrolyzed and co-condensed with tetraethyl orthosilicate (TEOS) in the presence of the surfactant cetylammonium bromide (CTAB) and of the aqueous NH_3 as the basic catalyst. The co-condensation of BTDS ensures the covalent linkage of the disulfide functional groups within the particle framework, thereby rendering the particles degradable in a reducing environment, such as the intracellular space given its high glutathione concentrations (2-10 mM).[18,19] In a second step (Figure 1), after the initial particle formation, the surface functionalization was obtained via alkoxysilane chemistry; polyethylene glycol silane (mean PEG chain length of 6-9 ethyleneoxy groups) and the sulfo-cyanine5-silane (sCy5-silane) have been added to the colloidal particle dispersion, obtaining a covalent grafting of these molecules onto the particle surface. The purification of the particles from unreacted species and the surfactant was obtained via dialysis (see section 3.4.4.)

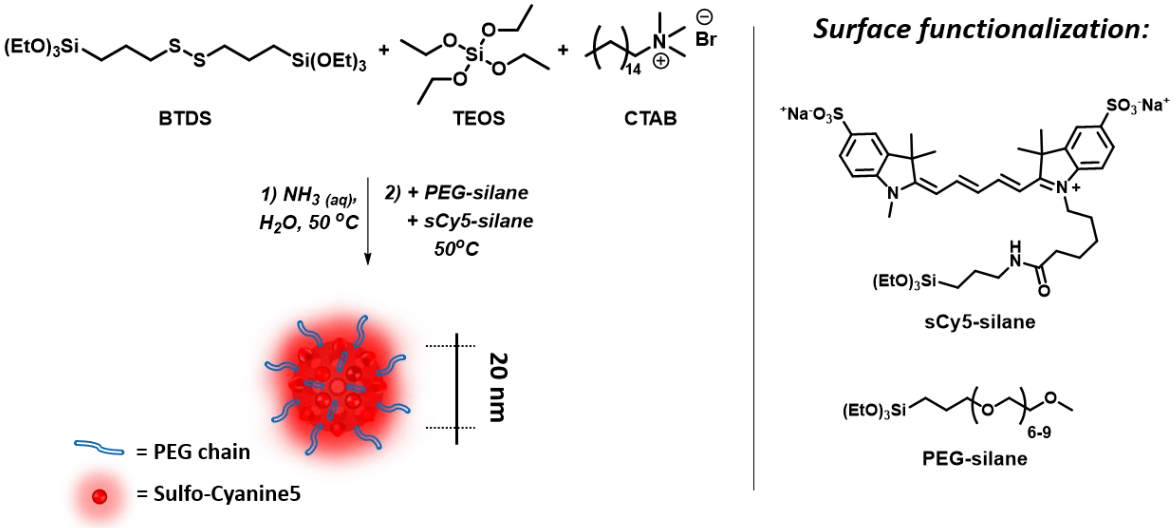

Figure 1. Schematic representation of the preparation and surface functionalization of disulfide-bridged organosilica cages (**OSCs**).

Transmission electron microscopy images (TEM) of **OSCs** (Figure 2a) revealed the cage-like structure of the particles possessing an average diameter of 20 nm (Figure 2b) as seen from the characteristic high and low contrast areas observed (Figure 2a inset). In order to reconstruct the 3D structure of **OSCs**, 17.946 single-particle TEM images were recorded and analyzed using the structure elucidation program Relion®.[20,21] As depicted in Figure 3b, the 3D-reconstruction confirmed the cage-like structure of **OSCs**, revealing the presence of a relatively large inner cavity of around 5 nm in diameter.

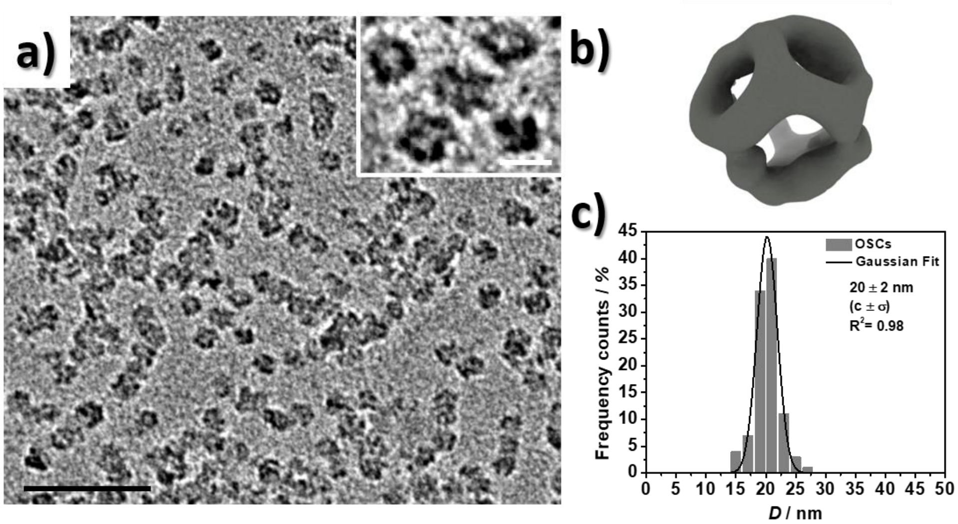

Figure 2. a) TEM images of **OSCs** (scale bar = 100 nm) and inset showing **OSCs** at higher magnification (scale bar=20 nm). b) 3D-model obtained from the reconstruction of **OSCs** TEM images, using Relion®.c) OSCs size-distribution calculated from TEM images (*N*=100).

The presence of an inner cavity within **OSCs** was further confirmed by N_2 adsorption–desorption measurements. Sorption isotherms (Figure 3a) show a characteristic hysteresis indicating the presence of a porous material, and a pore size distribution with an average size of 8 nm (Figure 3b) and an average total pore volume of 0.577 cm3·g^{-1} were calculated. The calculated specific BET surface area of was measured to be 437.0 m^{2}·g^{-1}. The results obtained were comparable with the nitrogen-adsorption data reported by Wiesner and co-workers for cage-like inorganic silica particles.[16]

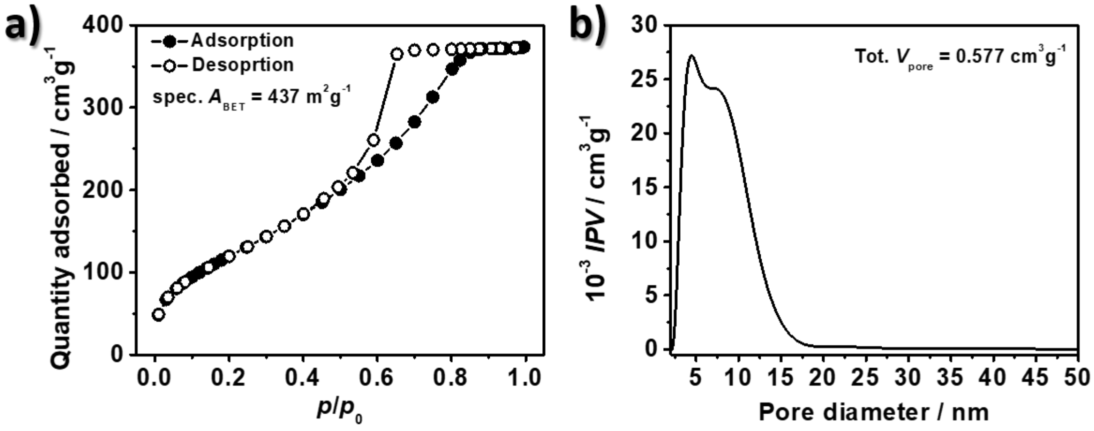

Figure 3. a) N_2 adsorption–desorption isotherms recorded on **OSCs**. b) Pore size distribution calculated on **OSCs**.

Although the final **OSCs** dispersion obtained after purification was highly concentrated (*c*=3 mg·mL^{-1}), a transparent and stable colloid was obtained (Figure 4a) and DLS analysis (Figure 4b) revealed the particle mean hydrodynamic diameter to be a 23 nm. The presence of short PEG-chains (6−9 units) on the particle surface was crucial for the colloidal stability of **OSCs**, since intense aggregation of the particles was observed when prepared without, as confirmed by DLS (Figure 4c). The enhanced colloidal stability upon PEGylation can be explained by steric repulsion between single particles created by the coiled polymers chains.[22,23] In order to investigate the biological features of **OSCs**, the red-emissive dye sulfo-cyanine5 (sCy5) was grafted onto the particles (see section 3.4.2. and 3.4.4. for details). As depicted in Figure 4d, upon sCy5 grafting of the particles surface, **OSCs** showed the characteristic absorption (λ_{max}=650 nm) and emission (λ_{max}=670 nm, λ_{ex}=600 nm) spectra of sCy5, possessing high fluorescent quantum yield of 52%.

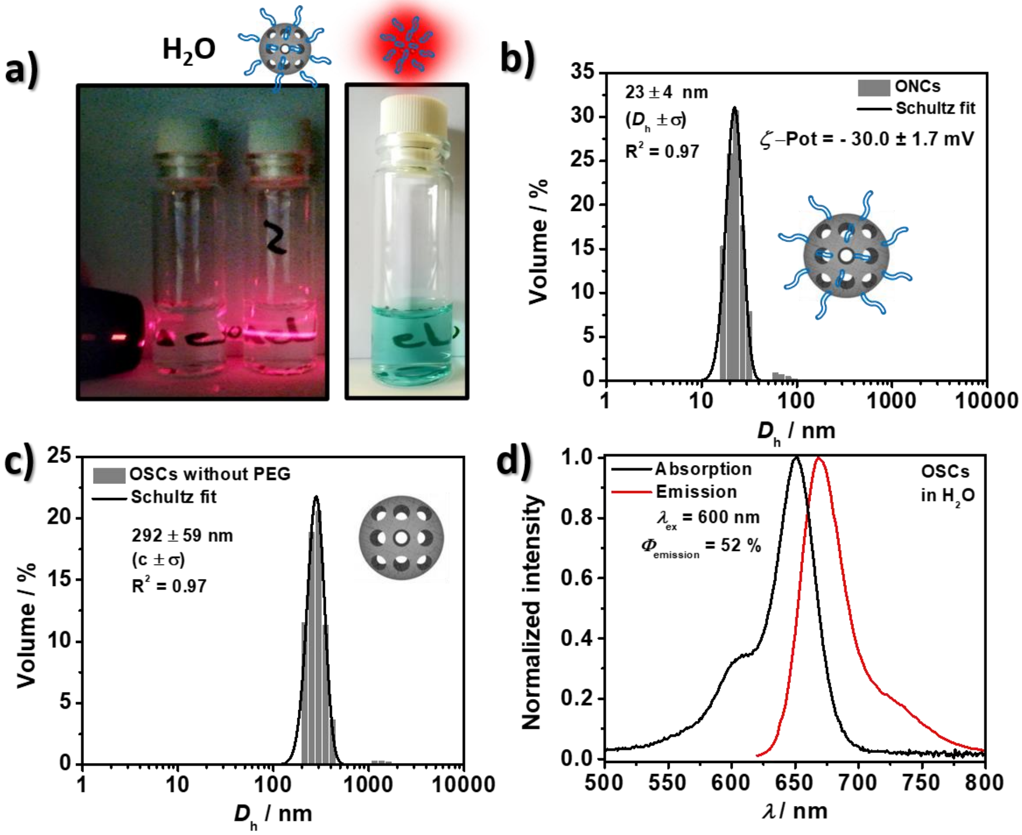

Figure 4. a) Left: images of colloidal dispersions of **OSCs** (c=3 mg·mL^{-1}), showing the characteristic Tyndall effect of colloids when irradiated with a laser. Right: colloidal dispersion of **OSCs** (c=3 mg·mL^{-1}) which were functionalized with the dye sCy5. b) DLS analysis on **OSCs**. c) DLS analysis on **OSCs** which have not been functionalized with PEG-chains. d) UV-Vis absorption (black) end emission (red) spectra of an aqueous **OSCs** dispersion that were functionalized with sCy5.

The organic content of **OSCs** was first investigated by TGA on dried samples (Figure 5a). The overall organic content was determined to be roughly 50 wt%. The amount of disulfide-linker integrated within the silica framework was determined to be 11 wt% by comparing the thermogram of non-functionalized **OSCs** with that of particles prepared analogously but not containing the disulfide bridge. Consequently, the amount of PEG chains grafted onto **OSCs** was calculated to be around 32 wt%, whereas the amount of dye could not be discriminated by TGA, due to the low amount used to functionalize **OSCs**. TGA analysis also confirmed the complete removal of the surfactant upon dialysis. ATR-FTIR spectra (Figure 5b) recorded on dried **OSCs** showed characteristic transmission bands for the -CH_2- wagging and deformation vibration at 1456 and 1354 cm^{-1}, respectively, which could be attributed to the presence of PEG chains. The transmission bands in the 2927–2868 cm^{-1} range could be assigned to the C_{sp3}–H stretching vibration derived from the presence of PEG chains and the disulfide linker within the silica framework of **OSCs**.

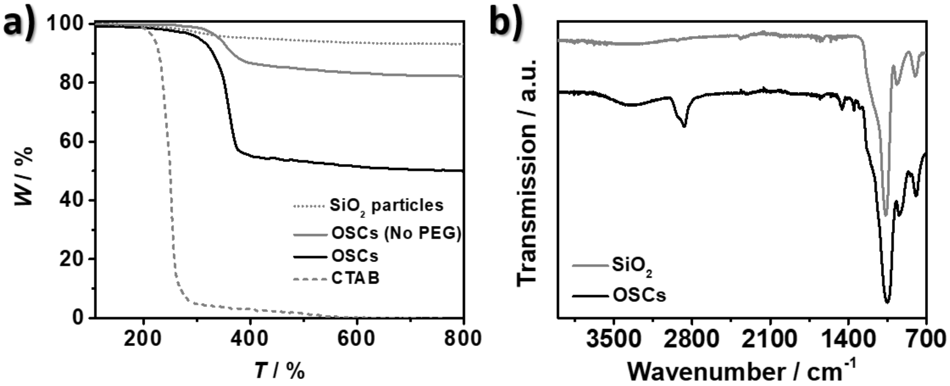

Figure 5. a) Thermogram recorded on silica nanoparticles, non-PEGylated **OSCs**, **OSCs** and the surfactant CTAB. b) ATR-FTIR transmission spectra recorded on **OCSs** and on silica particles that have been prepared analogously as **OSCs**, but not presenting disulfide organic moieties (SiO_2).

The covalent nature of the linkage of the disulfide moieties within the **OSC** silica framework was proven by XPS analysis. The survey spectrum recorded on **OSCs** (Figure 6a) indicates the presence of C(1s) and S(2p) signals at 287 eV and 164 eV, respectively. The deconvoluted HR scan for the C(1s) peak (Figure 6b) shows the presence of two components C-1 at 284.8 eV and C-2 at 286.4 eV, which can be attributed to the presence of C–C and C–O–C species, respectively. The analysis of the HR scan for the S(2p) peak (Figure 6c) shows the presence of the characteristic spin-orbit components of sulfur S-1 at 163.5 eV and S-2 at 164.6 eV, respectively, which are attributable to the disulfide bond present in **OSCs**.[24]

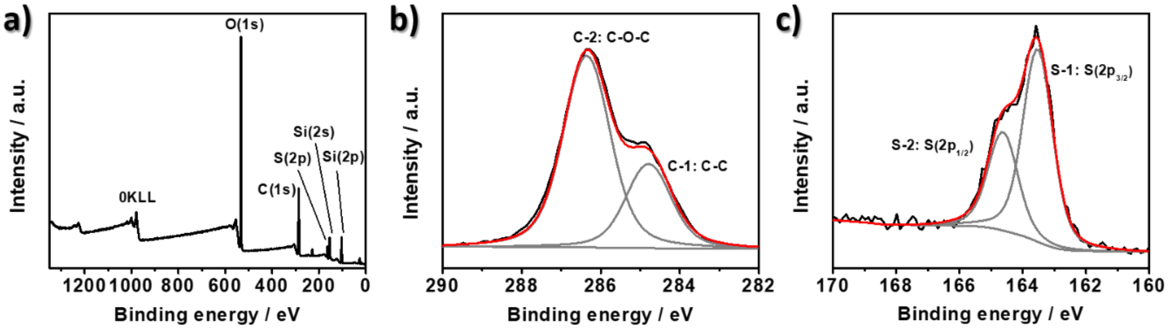

Figure 6. a) XPS survey spectrum recorded on **OSCs**. b) Deconvoluted XPS HR scan for C(1s) level recorded on **OSCs**. c) Deconvoluted XPS HR scan for S(2p) level recorded on **OSCs**.

As previously mentioned, the quantification of dye conjugated onto the particles surface could not be performed by TGA, therefore UV-Vis analysis was used to determine the amount of sCy5 present on **OSCs**. Upon comparison of the UV-Vis absorption spectrum recorded on **OSCs** in water (Figure 7a, c=0.15 mg·mL^{-1}) with a calibration curve obtained by measuring the absorbance of sCy5 at different concentrations, a total amount of 0.17 µg of dye per 1 mg of **OSCs** (25.7 µmol SCy5 per 1 mg of **OSCs**) was determined.

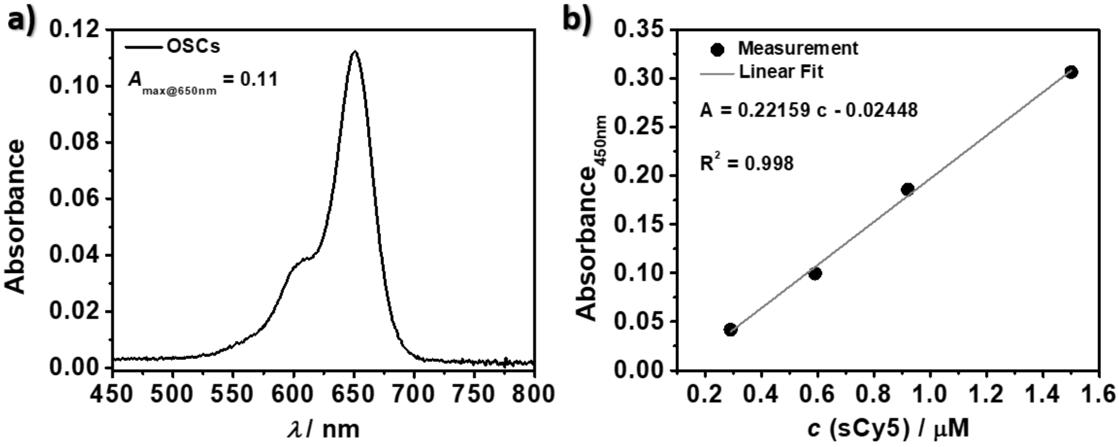

Figure 7.a) UV-Vis absorption spectra of **OSCs** (c=0.15 mg·mL^{-1}) recorded in water. b) Calibration curve obtained from measuring the absorbance of sCy5 at different concentrations.

3.2.2. Degradation studies and stimuli-triggered cargo release

As discussed in the introduction, the integration of disulfide functional groups within the silica framework renders **OSCs** degradable in the presence of thiolates due to occurring thiol–disulfide exchange reactions in the intracellular environment, caused by high concentrations (1−10 mM) of glutathione (GSH),[25] a thiol-containing endogenous tripeptide.[26] GSH is one of the main mediators for cellular redox homeostasis and is able to reduce the disulfide bridge within **OSCs**. In order to investigate the GSH-triggered degradation of **OSCs**, particle dispersions (c=0.1 mg·mL^{-1}) in PBS buffer with and without GSH (10 mM) were prepared and incubated at 37°C. Aliquots of these dispersions were taken at different time points were analyzed by TEM and STEM. As depicted in Figure 8, the formation of small debris was observed, indicating a fast particle degradation. The relatively fast degradation that occurred within the first 2 h ca be explained by the small particle size and the cage-like structure of **OSCs**, which provide a high surface area and therefore facile GSH diffusion. Therefore, the disulfide reduction most likely occurred simultaneously on the inner and outer regions of the particles. STEM images of **OSCs** dispersed in PBS/GSH (10 mM) solution at 37°C indicated the complete degradation of the particles after 12 h (Figure 9) of incubation as visualized by the formation of low-contrast and amorphous degradation products.

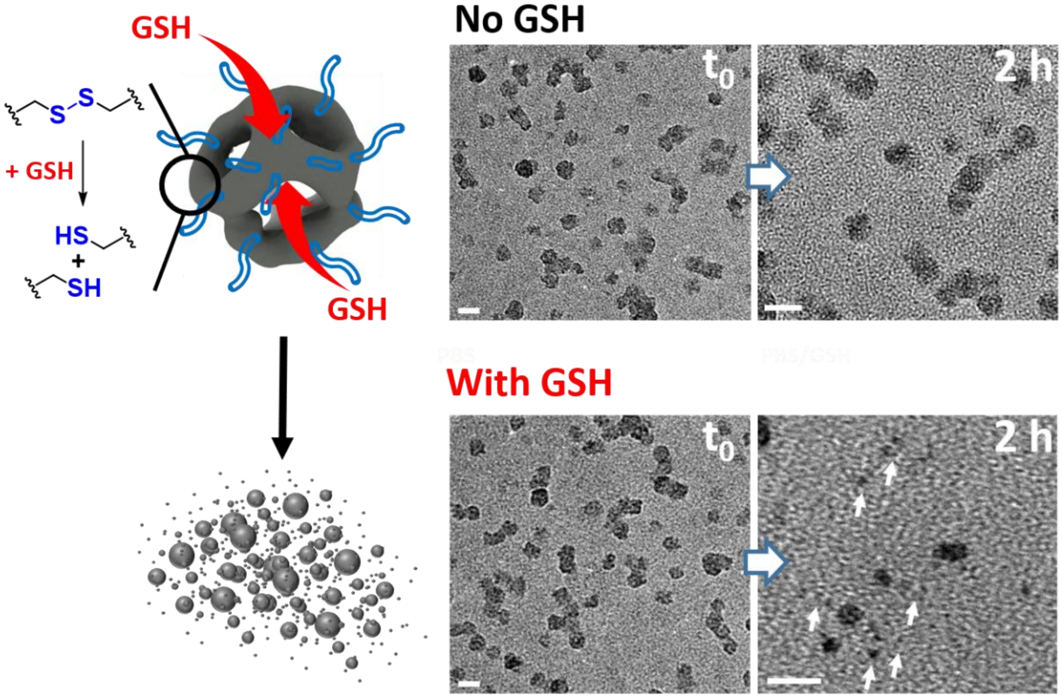

Figure 8. Left: GSH-triggered reduction of disulfide groups within **OSCs**, leading to particle degradation. Right: TEM images of **OSCs** (c=0.1 mg·mL^{-1}) at t_0 and after 2 h, when incubated in PBS at 37 °C, with and without GSH (10 mM). All scale bars=20 nm.

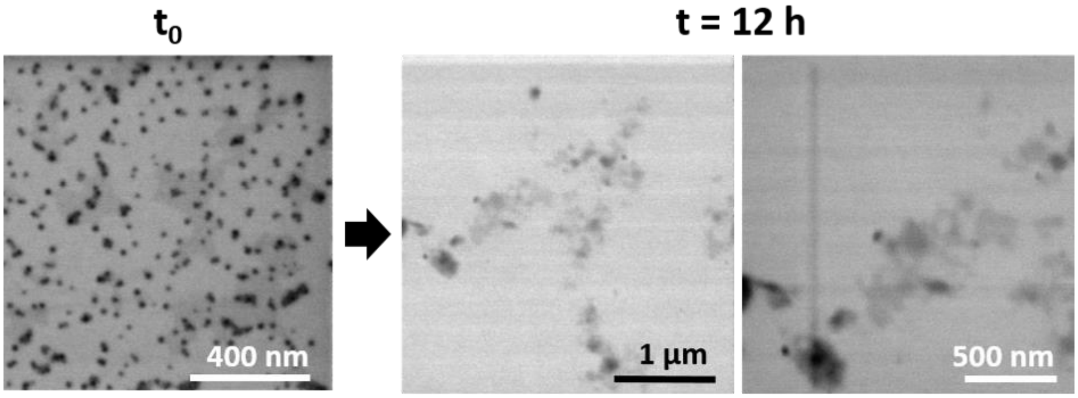

Figure 9. STEM images of **OSCs** (c=0.1 mg·mL^{-1}) dispersed in PBS/GSH (10 mM) solution at t_0 and after 12 h.

The **OSCs** were loaded with the hydrophilic dye HOECHST 33258 (HE) and its release in the presence of GSH was studied by fluorescence spectroscopy to further prove particle degradation. **OSCs** non functionalized with PEG were loaded by impregnation method (see section 3.4.6. for details) with a highly concentrated HE solution and subsequently PEGylated to entrap the dye within the internal cavity (**OSCs-HE**). The particles were subsequently washed to ensure the removal of physiosorbed HE on the particle surface (see section 3.4.6. for details). **OSCs-HE** dispersions (c=0.1 mg·mL^{-1}) in PBS buffer solutions were prepared with and without GSH (10 mM) and the cumulative cargo-release of HE was followed by fluorescence spectroscopy in the supernatant of the particle dispersions (λ_{em}=492 nm, λ_{ex}=350 nm). As depicted in Figure 10a, the cargo loading was estimated to be 10 wt% upon comparison of particles that have been prepared as **OSCs-HE**, but not loaded with the dye. ς-potential analysis of **OSCs-HE** showed that the surface potential became more positive, likely due to charge compensation of loaded HE, since the cargo molecule possesses three positive charges per molecule. Release experiments (Figure 10c) showed that a boosted HE-release was present when **OSCS-HE** particles were dispersed in PBS containing GSH, indicating the particles degradation and subsequent HE-release. The stimuli-triggered release was further confirmed by stirring an **OSCs-HE** dispersion and measuring the HE emission at different time intervals before and after GSH addition and as depicted in Figure 10d. Only upon the addition of GSH to the particle dispersion a boosted HE release was observed, further confirming the exclusive degradation of the particles in the presence of an external reducing agent.

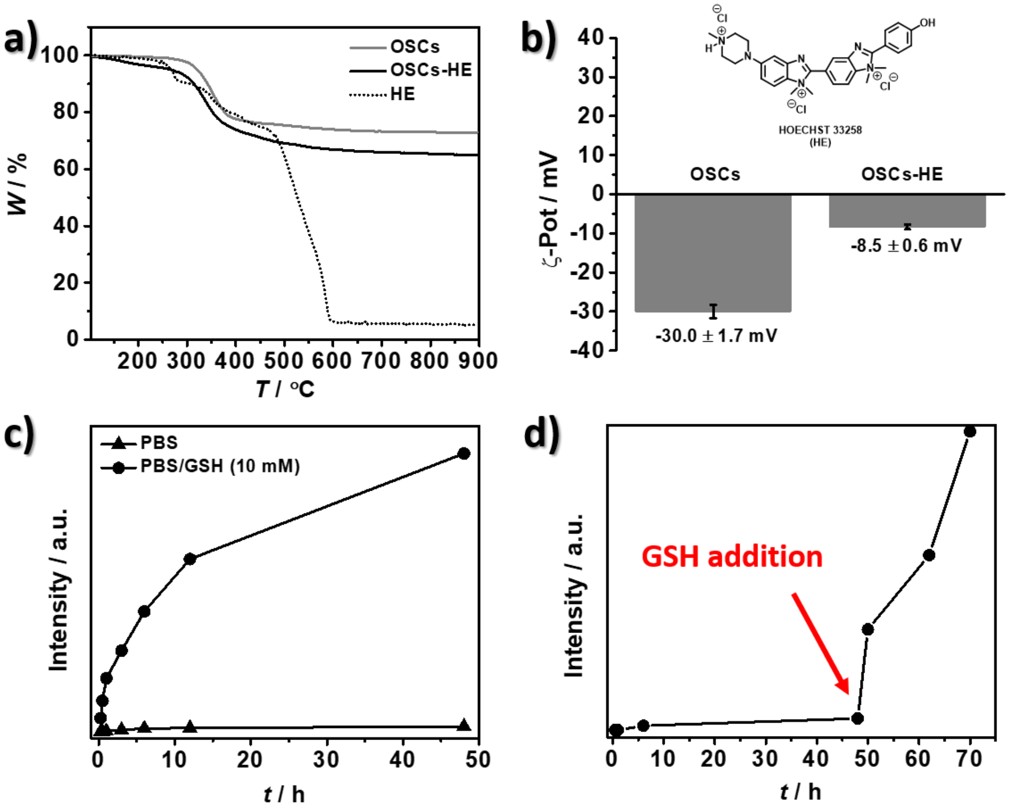

Figure 10. a) Thermograms recorded on **OSCs**, **OSCs-HE** and **HE**. b) ζ-potential measurements on **OSCs** and **OSCs-HE**. c) Cumulative HE-release experiments following the HE fluorescence emission (λ_{em}=492 nm, λ_{ex}=350 nm) from **OSCs-HE** dispersions (c=0.1 mg·mL^{-1}), with and without GSH (10 mM). d) HE-release experiments recording the fluorescence emission (λ_{em}=492 nm, λ_{ex}=350 nm), before and after addition of GSH.

Having assessed the particles stimuli-triggered degradation and cargo release of a model drug molecule, the possibility to load **OSCs** with the hydrophobic anti-cancer drug docetaxel (DT) was investigated. DT, a member of the taxane class of anti-cancer drugs, is widely applicated for the treatment of cancers such as breast, stomach and prostate. Due to its hydrophobic nature, nano-formulations have been developed to increase the efficacy of the drug, resulting in the successful preparation of liposome-based delivery systems. The use of liposomes as carrier vehicle still faces challenges, such as liposome instability, short blood-circulation lifetimes and high productions costs.[27,28] The use of porous organosilicas, such as the here presented **OSCs** would instead provide small (20 nm) delivery system characterized by high stability and a stimuli responsive degradation behavior. Therefore, the particles have been loaded with DT in a two-step procedure. First, the drug was loaded into the particles cavity by stirring non-PEG functionalized **OSCs** in an ethanolic DT solution (1/1 *wt*/*wt*) over night. Subsequently, the particles were functionalized with PEG, ensuring DT entrapment within **OSCs**, and the particles were washed by dispersion–centrifugation cycles to remove any physisorbed drug on the surface, yielding DT loaded **OSCs** (**OSCs-DT**, see section 3.4.6. for details). The removed supernatants were analyzed by UV-Vis absorption spectroscopy, which revealed that the physiosorbed drug was successfully removed from the particles surface, since no absorption of DT was measured in the washing solutions (Figure 11a). TGA allowed to determine a DT loading of 13 wt% (Figure 11b) upon comparison with the thermogram recorded for **OCSs**.

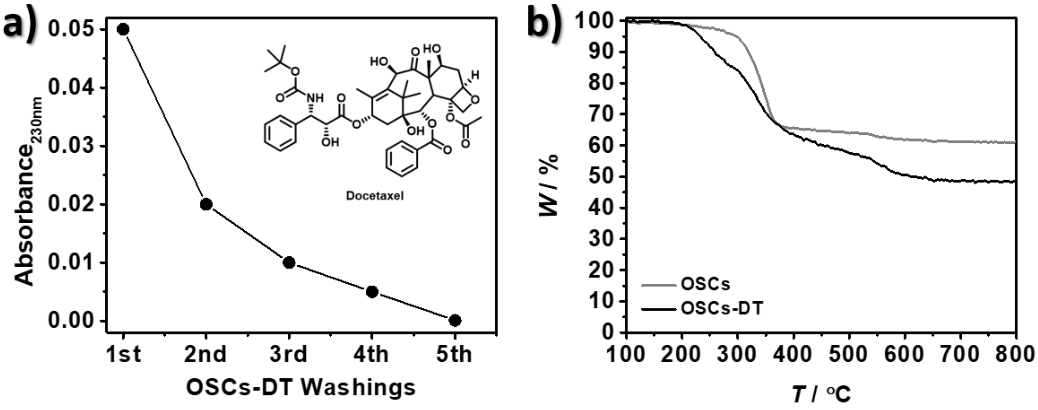

Figure 11. a) UV-absorption of the supernatant washing solutions recorded at λ=320 nm. b) Thermograms recorded on **OSCs** and **OSCs-DT**.

After particle loading, the colloidal stability was not preserved, and massive aggregation was observed. Prolonged sonication and subsequent filtration of **OSCs-DT** dispersion (1 mg·mL^{-1}) with a nylon syringe filter (cut-off 0.2 µm) helped to obtain a colloidal dispersion with a relatively homogeneous size distribution of **OSCs** as confirmed by DLS on purified **OSCs-DT** (Figure 12). The main drawback of the purification method was the high dilution of the purified **OSCs-DT** obtained, unpractical for in vivo experiments when the injection volume should be minimized. Future work will further focus on establishing a robust and efficient methodology to load hydrophobic drugs within **OSCs**, while persevering their colloidal stability. The encapsulation of hydrophobic drugs will be of great interest since its encapsulation in hydrophilic drug carriers, while obtaining high loadings, is still hardly achieved.

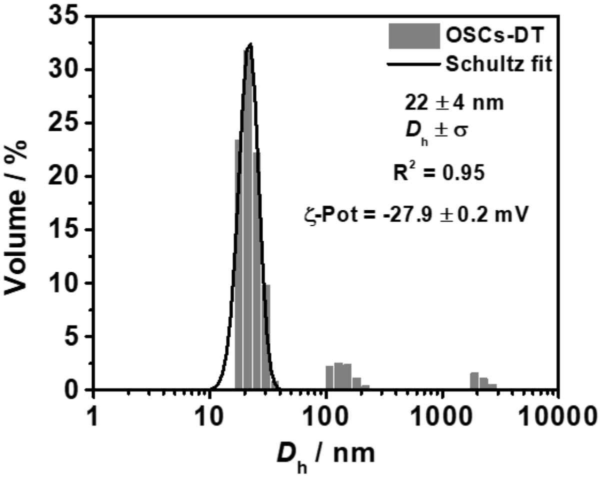

Figure 12. DLS analysis of a filtered **OSCs-DT** particle dispersion in water.

3.2.3. Surface functionalization of cage-like organosilica particles

As already discussed in the general introduction, the functionalization of nanoparticles with biological active molecules, such as cell-targeting peptides or sugar molecules, has the potential to increase the particle´s therapeutic efficacy. To functionalize silica nanoparticles with biological relevant biomolecules, such as sugars or peptides, alkoxysilane chemistry offers an opportune strategy for covalent surface grafting.[29] We aimed therefore to find a working protocol to graft the surface of **OSCs** with the tripeptide Arg–Gly–Asp (RGD) or the sugar D-(+)-glucosamine, aiming for mild functionalization reaction, which retain good colloidal stability of the particles and do not require laborious purification steps. Alkoxysilane chemistry was first selected to functionalize **OSCs** with D-(+)-glucosamine, and copper-free azide-alkyne cycloaddition reaction (SPAAC) was used to graft the particle surface with RGD.

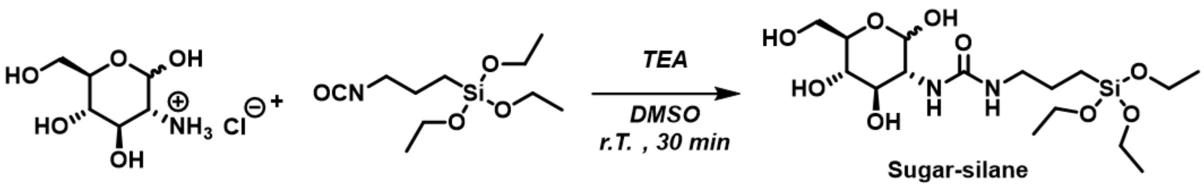

Scheme 1. Reaction scheme for the preparation of the sugar-silane.

The sugar functionalization occurred in a one-step procedure (Scheme 2). Therefore, once the particles formation occurred, the sugar-silane and PEG-silane where added to the stirring colloidal dispersion and the reaction mixture was allowed to stir for 16 h at 50°C. Surfactant removal was achieved through dialysis to yield the sugar-functionalized particles (**Sugar-OSCs**, see section 3.4.2. and 3.4.4. for details).

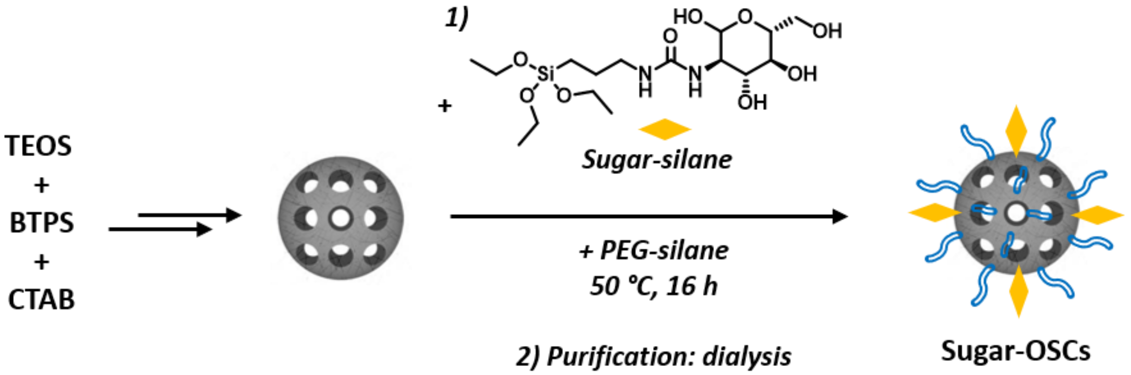

Scheme 2. Glucosamine functionalization of **OSCs** occurred after the initial formation of cage-like organosilica particles.

The amount of glucosamine covalently grafted onto **Sugar-OSCs** was quantified by using a previously reported fluorimetric analysis, in which the reaction of reducing sugars with cyanoacetamide in borate buffer results in the formation of luminescent reaction product.[30] The amount of glucosamine was estimated by measuring the fluorescence intensity of **Sugar-OSCs** (Figure 13) that have been derivatized with 2-cyanoacetamide in borate buffer (c=0.6 mg·mL^{-1}) at the wavelength of emission λ_{em}=383 nm (λ_{ex}=331 nm) and resulted to be 0.89 µg of glucosamine per mg of **Sugar-OSCs** (see section 3.4.5.).

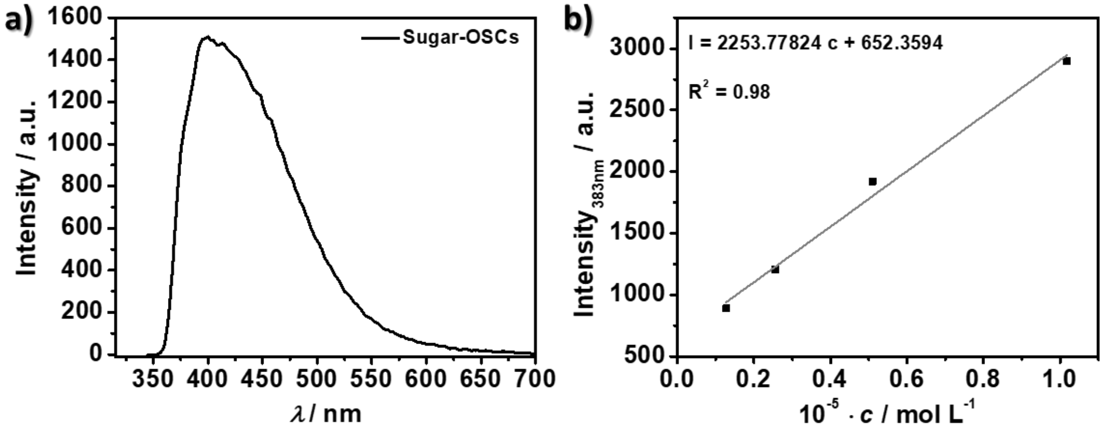

Figure 13. a) Fluorescence emission spectra of **Sugar-OSCs** (c=0.6 mg·mL^{-1}) which have been incubated with 2-cyanoacetamide in borate buffer (λ_{ex}=331 nm).b) Fluorescence emission calibration curve obtained from the reaction of glucosamine at different concentrations (λ_{ex}=331 nm, λ_{em}=383 nm).

After sugar functionalization, the colloidal stability of the particles was investigated by DLS. As depicted in Figure 13, the colloidal stability of **Sugar-OSCs** was confirmed as the hydrodynamic diameter was 28±7 nm (Figure 14a). The ς-potential measured for **Sugar-OSCs** was -23±1 mV, a slightly more positive mean value when compared to that for **OSCs**. The particles morphology after surface functionalization was analyzed by TEM, which indicated that particle morphology was retained after surface functionalization (Figure 13b). The amount of sugar-silane used for the functionalization was 3.5 mg per 100 mg of non-functionalized **OSCs**. Higher amounts of sugar-silane led to the formation of unstable colloidal dispersions of **Sugar-OSCs**, most likely due to the increased presence of H-bonding units, mediating interparticle attraction forces.[31]

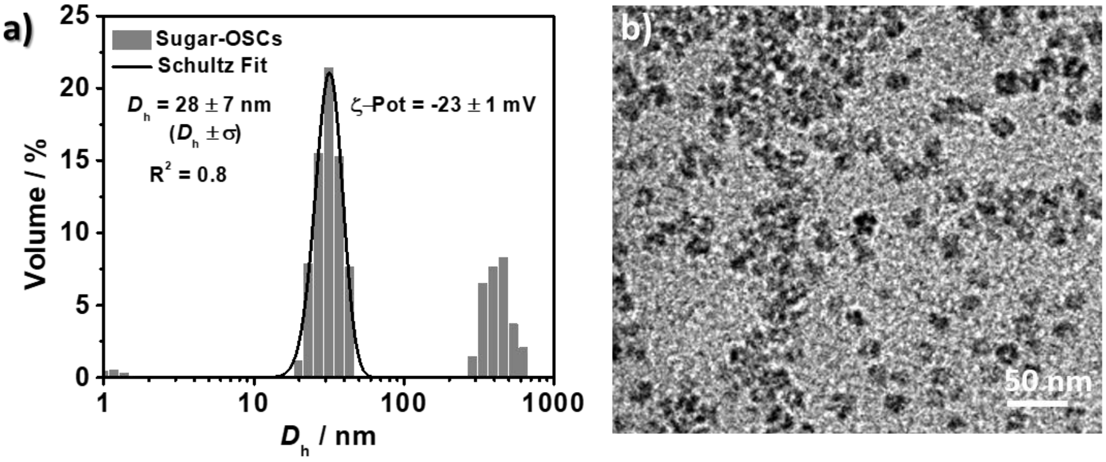

Figure 14. a) DLS analysis of **Sugar-OSCs** and b) TEM images of **Sugar-OSCs**.

Peptide functionalization of **OSCs** was performed by SPAAC since mild grafting protocols are needed when functionalizing colloidal particles. Copper-free click-chemistry is advantageous because, beside the reactants, no additional coupling reagents are needed for covalent conjugation that could otherwise be toxic reagents or destabilize the colloidal dispersion. For this reason, SPAAC was preferred over the functionalization of the particles by amide-bond formation. The tripeptide RGD was used as a model peptide for establishing a working functionalization protocol for **OSCs**. In order to covalently link the model peptide onto the particle´s surface, the alkyne derivative of RGD (Alkyne-RGD) was prepared. The RGD was allowed to react with (1R,8S,9S)-bicyclo[6.1.0]non-4-yn-9-ylmethyl *N*-succinimidyl carbonate (BCN-NHS) in the presence of the base TEA, as depicted in Scheme 3, yielding alkyne-RGD that was used without further purification for particle functionalization (see section 3.4.3 for details).

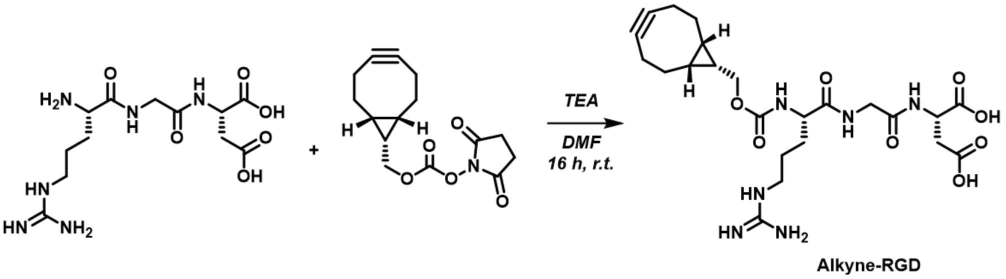

Scheme 3. Depicted synthesis pathway for the preparation of alkyne-RGD.

In order to functionalize the particles with the alkyne-RGD peptide, **OSCs** were first functionalized with azide groups, upon reaction of **OSCs** with 3-azidopropyltrimethoxysilane (AzTMS, see section 3.4.2. for its preparation), and the particles purification occurred by dialysis against an EtOH/H_2O (1:1 *v*/*v*) mixture for 12 h (Scheme 4). The amount of AzTMS was chosen to be 5 mol% in respect to TEOS used for the preparation of **OSCs**, which did not affect the final colloidal stability of **N_3-OSCs** as confirmed by DLS, which revealed an average hydrodynamic of 26±4 nm.

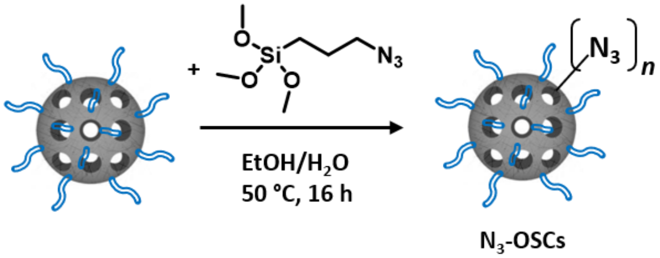

Scheme 4. Preparation of **N_3-OSCs**.

The presence of azide groups on the particle surface was determined by ATR-FTIR (Figure 15), which indicated the presence of an intense band at 2100 cm^{-1} corresponding to the characteristic asymmetric –N=N=N stretching vibration,[32] and was in agreement with spectra recorded on neat AzTMS.

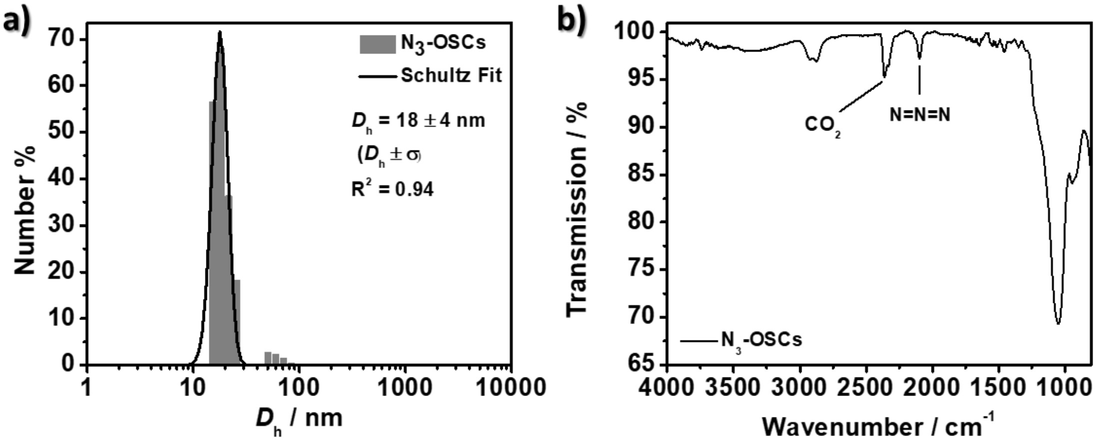

Figure 15. a) DLS size distribution of **N_3-OSCs** b) ATR-FTIR spectra recorded on **N_3-OSCs**.

Finally, the peptide was conjugated onto the particle surface upon the addition of Alkyne-RGD to a stirring **N_3-OSCs** particle dispersion, allowing to react overnight. The particle dispersion was then purified by means of dialysis in water for 48 h, yielding **RGD-OSCs** particles (see experimental section). The amount of peptide conjugated onto the particle´s surface was estimated via fluorimetric analysis using a previously reported fluorescence quantification method (see experimental section).[33] For this purpose an aliquot of **RGD-OSCs** was allowed to react with 9,10-phenantrenequinone (PQ), a reagent which specifically reacts with arginine in order to give a fluorescent reaction product after the addition of acid (Scheme 5).

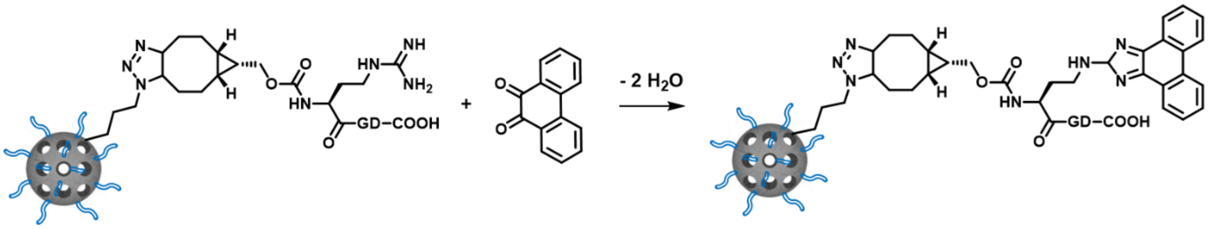

Scheme 5. Reaction of the guanidine group of arginine present on **RGD-OSCs**, with PQ, leads to the formation of a fluorescent addition product, used for the quantification of RGD onto the particles surface.

The amount of RGD covalently linked onto the particle surface was estimated upon measuring the fluorescence intensity of **RGD-COS** (Figure 16a) that have been derivatized with PQ (c=0.0107 mg/mL) at the wavelength of emission λ_{em}=424 nm (λ_{ex}=312 nm). Upon comparison of the measured emission with a previously established calibration curve based on the reaction of RGD with PQ at different concentrations (Figure 16b), a total amount of 25 µg per mg of particles was calculated (see section 3.4.5.).

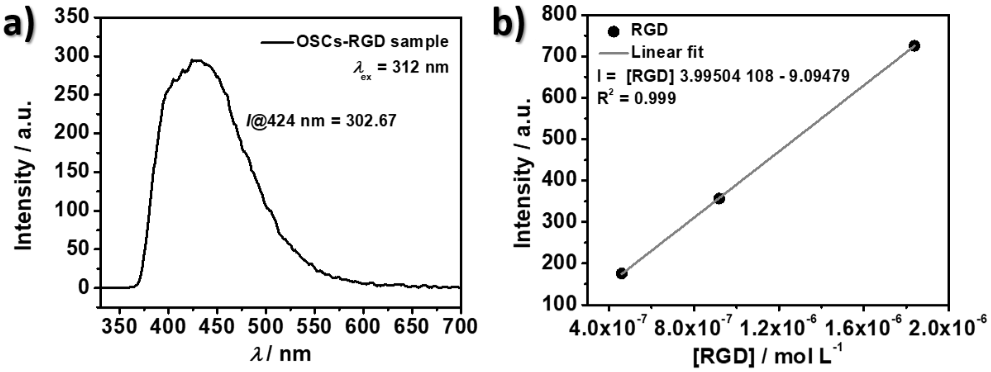

Figure 16. a) Fluorescence emission spectra of **RGD-OSCs** (c=0.0107 mg·mL^{-1}) which have been incubated with PQ (λ_{ex}=312 nm). b) Fluorescence emission calibration curve obtained from the reaction of RGD at different concentrations with PG (λ_{ex}=312 nm, λ_{em}=424 nm).

Herein, the possibility to functionalize these novel types of cage-like organosilica particles with a variety of bioactive small-molecules was proven, while maintaining their colloidal stability in aqueous dispersions. Future work will focus on the functionalization of the particles with specific cell surface receptors to evaluate the possibility to quantitatively cross the blood–brain-barrier (BBB), one of the major challenges for the development of nanomedicines for brain delivery applications.

3.2.4. Preliminary biological evaluation of cage-like organosilica particles

Once the physicochemical properties of **OSCs** have been assessed and their biodegradability successfully proven, the particle cytotoxicity was investigated. The preliminary biological evaluation was carried out by the group of Prof. Bigini (Mario Negri Institute). Although previously reported in vitro cytotoxicity studies on disulfide-bridged porous silica particles have shown good biocompatibility towards different cell-lines, the toxicity of **OSCs** were investigated to ensure safety during in vivo applications. Therefore, glioma C6 cells were incubated with **OSCs** at different concentrations (50, 100 and 200 µg·mL^{-1}) and the cell viability was evaluated using the trypan blue test, a dye-exclusion procedure that stains dead cells. As depicted in Figure 17,

OSCs showed no relevant cytotoxicity even at high concentrations after 24 and 48 h of incubation time, confirming the non-toxicity of disulfide-based organosilica particles.[7,34]

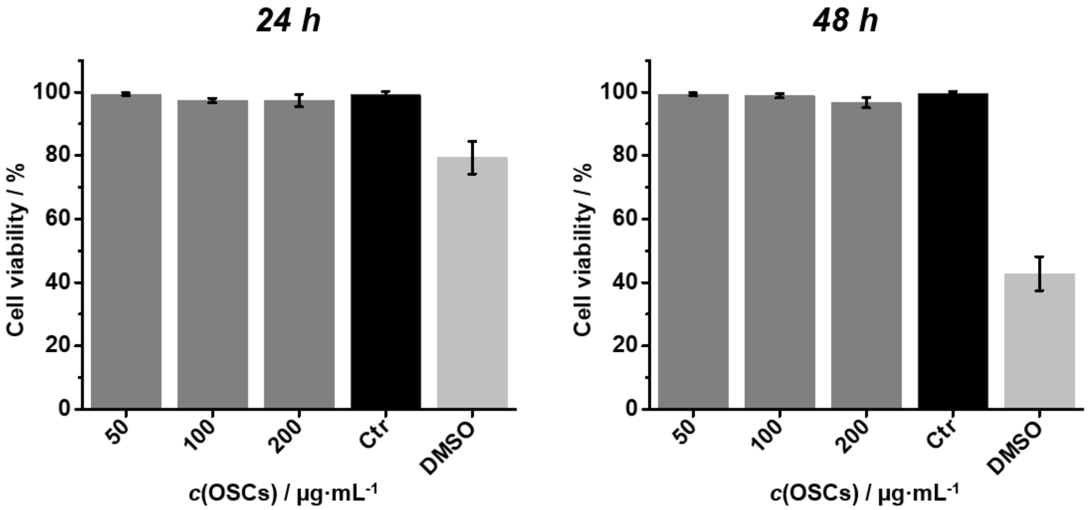

Figure 17. Trypan blue cell-viability results on glioma C6 cells obtained upon incubation with **OSCs** at different concentrations after 24 and 48 h of incubation.

With the positive cell-viability tests obtained the biodistribution of **OSCs** and **Sugar-OSCs** in healthy rodents was investigated. The biodistribution of small cage-like organosilica particles is still unexplored and a first evaluation of their in vivo behavior is therefore of interest, since distinct biodistribution behavior according to the size and shape nanomaterials has been reported.[15] The biodistribution studies included also the glucosamine functionalized particles, since the presence of the sugar moiety may enhance cellular uptake upon the interaction with GLUT-cell surface receptors present on the endothelial layer of the BBB, therefore having the potential to enable enhanced particle adherence on this biological barrier. Glucosamine was chosen considering that the C-2 position of the sugar can be modified without loss of receptor activity for the GLUT1-cell surface receptor.[35] In addition, glucosamine would provide a reactive amine group that could be easily used for **OSC** functionalization through alkoxysilane coupling. First biodistribution studies on **OSCs** were performed on healthy CD1 mice model, injecting **OSCs** via one-time intravenous tail injection (dose=7 mg particles per kg of mouse) and analyzing the animals after different time points (30 min, 1 h, 4 h and 24), using 6 animals for each experimental group (see section 3.4.9. for details). The presence of sCy5 on **OSCs** resulted to be ideal since the imaging occurs in the red region of the electromagnetic spectra, diminishing the autofluorescence signal from the mice bodies while further reducing the oxygen-induced attenuation. The results obtained from ex vivo optical imaging of the particles in various organs are shown in Figure 18; the fluorescent signals are normalized with respect to the mouse to which only a saline solution has been administered (vehicle).

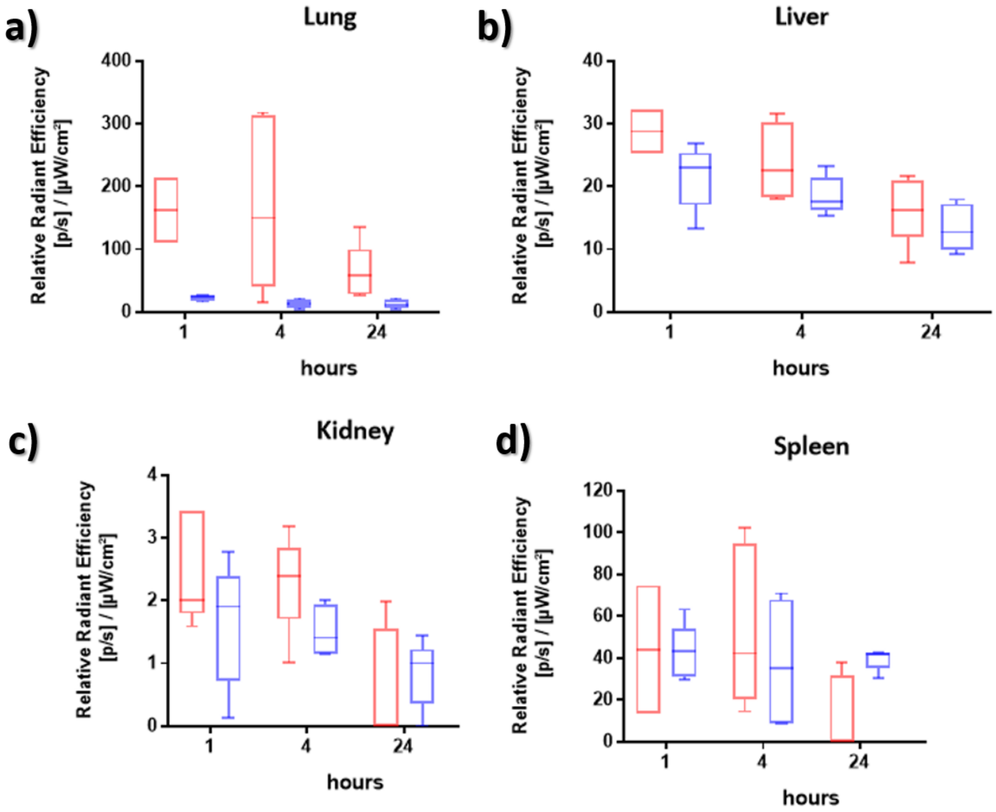

Figure 18. Ex vivo biodistribution of **OSCs** (red bars) and **Sugar-OSCs** (blue bars) at 1, 4 and 24 h. Relative radiant efficiencies for **OSCs** and **Sugar-OSCs** are shown in a) lung, b) liver c) kidney and d) spleen. Radiant Efficiency where all values are normalized to vehicle (saline solution injection) group=1.

The particles were found to accumulate in various organs well known for the elimination of nanoparticles. Interestingly, **OSCs** showed a 13-fold increased signal in the lung compared to **Sugar-OSCs**, which decreased by about 3 times after 24 h (Figure 18a). This behavior may be explained by the fact that **OSCs** possess a longer blood circulation lifetime compared to **Sugar-OSCs**, leading to their accumulation in the lungs. Similar results were previously reported for spherical nanoparticles of 20–30 nm that were shown to accumulate in the lungs within the first 30 min after intravenous administration.[18] This can be explained most probably by the fact that the PEG-chains protect the particles in the blood-stream from instability, while the presence of a sugar may decrease this ability of PEG stabilization in the blood-stream. To evaluate the uptake in the lung, histological analysis was done on lung sections (Figure 19). **OSCs** were only found in the lung parenchyma, whereas no signal related to the presence of **Sugar-OSCs** was observed.

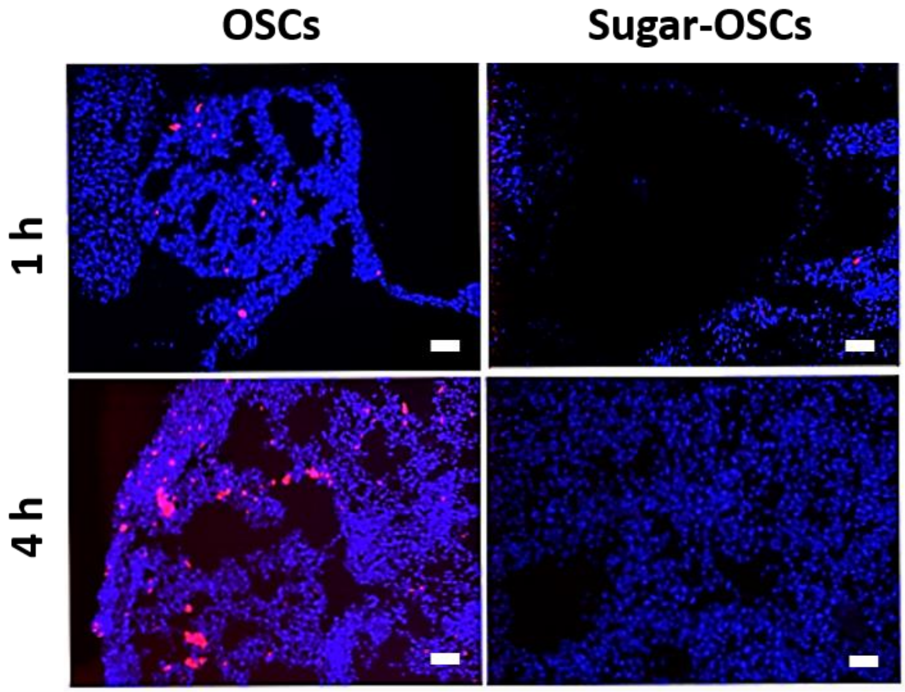

Figure 19. Histological analysis of **OSCs** and **sugar-OSCs** in lung sections 1 h and 4 h after the treatment obtained by fluorescent microscopy. The particles are visualized in red (sCy5 signal) and nuclei in blue (Hoechst 33258 staining). Scale bars=100 µm.

In the liver, a comparison between the accumulation of **OSCs** and **Sugar-OSCs** did not show a statistical difference, indicating that the presence of the sugar on the particle surface did not affect the kinetics or liver uptake (Figure 18b). Most interestingly, immunohistology of the liver indicated that **OSCs** and **Sugar-OSCs** did not accumulate in hepatic macrophages (Kupffer cells) usually involved in the clearance of nanoparticles from the liver. As depicted in Figure 20, no colocalization of the particles (red) with macrophages (green), which had been stained with fluorescein-labeled CD68 antibodies, was observed. This differentiated accumulation indicated the possibility that the particles are taken up by other cells of the liver, most likely epithelial cells. These findings suggest that the particles could serve for the development of drug-delivery carriers for the treatment of liver cancers.

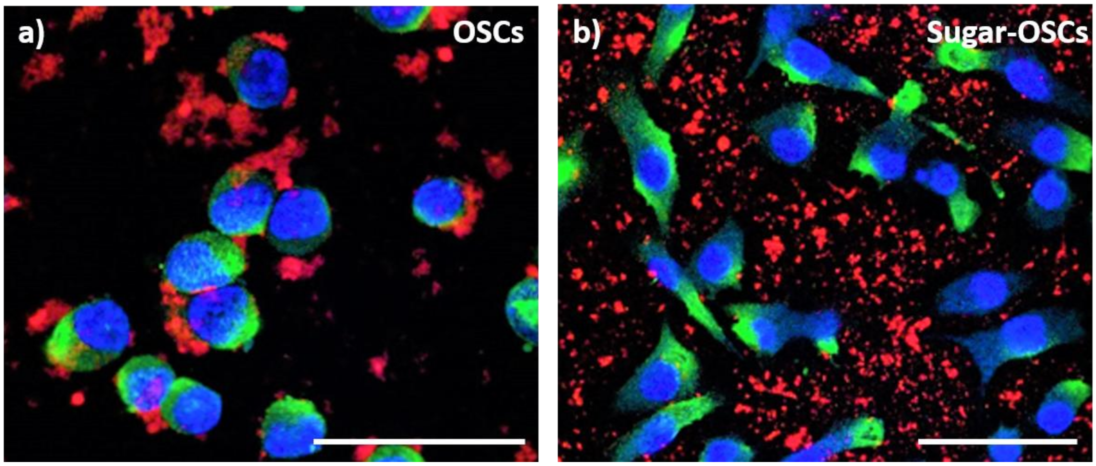

Figure 20. Immunohistology of the liver after 4 h of the treatment by fluorescence spectroscopy. Blue: nucleus stained with DAPI; red: **OSCs** and **Sugar-OSCs**; green: Kupffer cells. Scale bars=50 µm.

In the kidneys, the fluorescence signal of **OSCs** and **Sugar-OSCs** was relatively low, excluding a renal clearance of the particles (Figure 18c). It is known that renal clearance of nanoparticles is very strong for particles smaller than 5 nm, and the particles subjected in this study were too large to be excreted by the kidneys.[36] The particles were found to accumulate to a greater extend in the spleen than the liver and kidneys, which can be explained by the fact that the spleen is the main organ particle excretion (Figure 18d). Compared to **OSCs**, **Sugar-OSCs** seemed to be eliminated more slowly from this organ, which could be explained by the fact that sugar-functionalized particles form bigger aggregates in the blood that persist longer in the spleen. Histological analysis of spleen samples after 1 h and 4 h of the treatment indicated that the particles accumulated in the red pulp (RP), a region related to clearance of common antigens (Figure 21). Interestingly, no migration of the particles in other parts of the spleen, such as the marginal zone (MZ) or the white-pulp (WP), was observed.

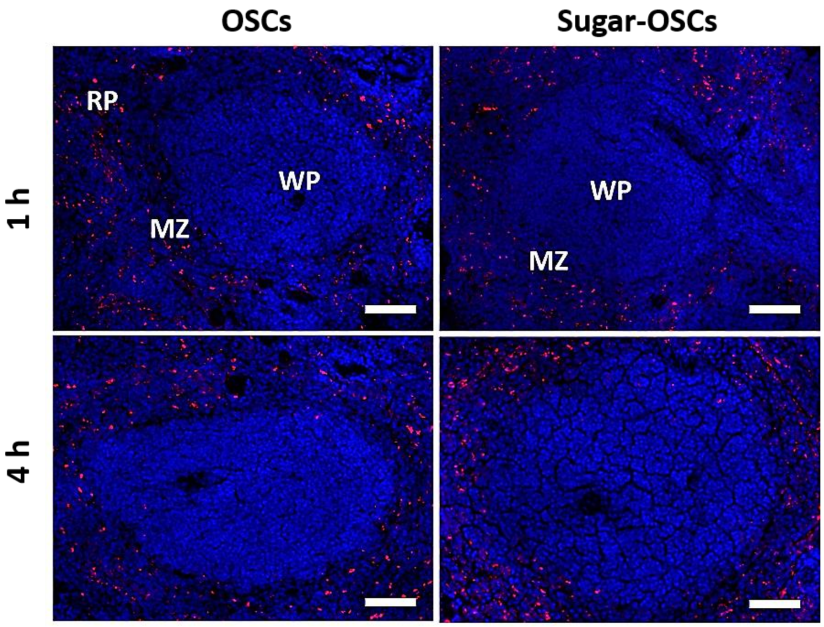

Figure 21. Histological analysis of **OSCs** and **Sugar-OSCs** in spleen sections at 1 and 4 h after the treatment obtained by fluorescent microscopy. NPs are visualized in red (sCy5 signal) and nuclei in blue (Hoechst 33258 staining). RP=red-pulp, MZ=marginal zone, WP=white-pulp. Scale bars = 100 µm.

The particle´s unique morphology, small size, and the presence of a sugar functionality may enhance the particle adherence on the epithelial layer of the BBB, possibility leading to enhanced BBB crossing. In Figure 22a, ex vivo fluorescent signals on the brain samples of mice treated with **OSCs**, revealed only a minor signal derived from the brain, which after 24 h was comparable to the intensities measured for the vehicle. Additionally, no significant statistical variation regarding the detected signal between **OSCs** and **Sugar-OSCs** was observed. To obtain a more quantitative information on the presence of the particles in the brain, inductively coupled plasma atomic emission spectroscopy (ICP-AES) was performed on the brain samples after 4 h of treatment. The ICP-AES results are shown in Figure 21b and indicate that a minor number of particles were able to cross the BBB, indifferently from the presence of a sugar moiety on the particles surface.

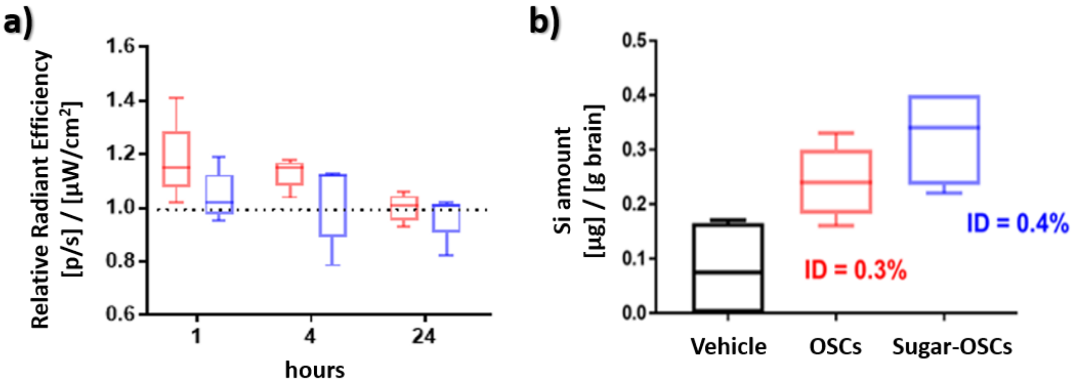

Figure 22. a) Ex vivo fluorescent emission analysis of mouse brain samples of **OSCs** (red bars) and **Sugar-OSCs** (blue bars) at 1, 4 and 24 h after treatment. Radiant Efficiency where all values are normalized to vehicle (injection of saline solution) group=1. b) ICP-AES results obtained from brain samples after 4 h of treatment; **OSCs** (red bars) and **Sugar-OSCs** (blue bars).

Similar results were obtained based on histological analysis of the brain after 4 h of treatment with **Sugar-OSCs** (Figure 23). The particles could be mainly detected in in the region of lateral ventricles of the brain and no inner penetration of brain areas, such as the caudate putamen (cPu)

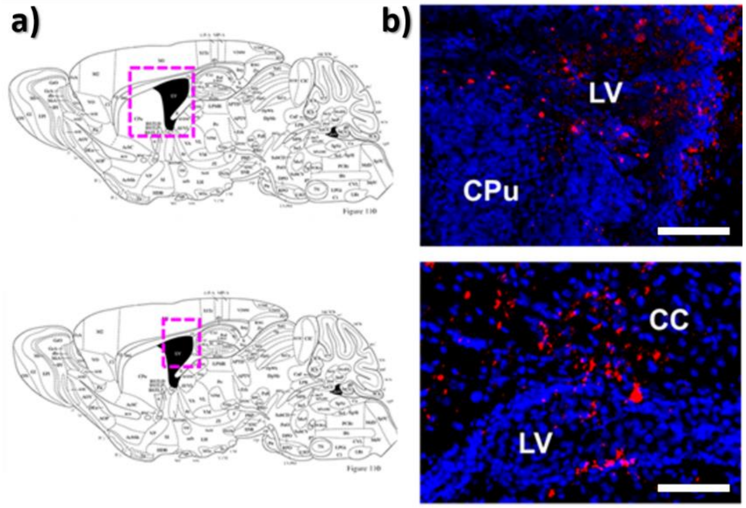

Figure 23. a) Sagittal sections of mouse brain. Dashed squares represent the field of view examined by histology. b) Representative images of brain sections of **Sugar-OSCs** treated mice at 4h obtained by fluorescent microscopy. NPs are visualized in red (Cy5 signal) and nuclei in blue (Hoechst 33258 staining). CC=corpus callosum, CPu=caudate putamen, LV=lateral ventricle. Scale bar=100 µm.

These results show that BBB crossing of **OSCs** and **Sugar-OSCs** is less than 1 % with respect to the total amount of injected particles (ID), that is, 0.2 % ID for **OSCs** and 0.3 % ID for **Sugar-OSCs** (Figure 22b). Although previously reported in-vitro experiments using BBB-models suggested an enhanced BBB crossing of sugar-functionalized gold and polymeric nanoparticles,[37,38] our experiments confirmed that this effect is negligible and almost absent in in vivo models, which is in agreement with recently results published by Kataoka and coworkers.[39,40] In fact, although it has been reported that the brain uptake of nanoparticles in healthy mice is somewhat size and shape dependent and that smaller particles are preferentially accumulated in brain regions, the amount that reaches the brain is generally low and below 1% ID.[39,41,42] Therefore, for future application in which brain accumulation of **OSCs** is desired, the particles must be functionalized with adequate cell targeting units to enhance the particles BBB crossing via transcytosis. Interesting cell-surface targeting ligands to be used for **OSCs** functionalization could be ganglioside targeting peptides such as the recently reported G23 peptide by Zuhorn and coworkers[43] or glycopeptide G7 reported by Tosi and coworkers.[44]

3.3. Conclusions

In this chapter, the preparation and characterization of novel porous cage-like organosilica particles was presented. The particles were found to be biodegradable due to the presence of a reducible disulfide moiety embedded within the silica framework and showed rapid rates of degradation due to their small size and highly accessible inner cavity. It has been also reported that the particles can be loaded with hydrophilic and hydrophobic molecules, demonstrating the stimuli-triggered cargo release upon the presence of a reducing agent, such as the endogenous tripeptide glutathione. Furthermore, facile and mild **OSCs** functionalization procedures for have been established, proving the successful covalent conjugation of bioactive molecules to the particle surface. Preliminary biological experiments indicated that the particles are nontoxic and the **OSCs** bioaccumulation was investigated upon intravenous injection in healthy mice. Interestingly, in the liver **OSCs** did not co-localized with macrophages, rendering these particles interesting for the development of drug-delivery carriers against liver-cancers. Strong accumulation of the particles in the lungs of mice have been observed when no sugar surface functionalization was present, which was explained by the fact that the particles possess good blood–serum circulation lifetimes. To enhance the BBB crossing of the particles, future experiments will focus on the ad hoc functionalization of **OCSs** with peptide-based ligands of cell surface receptors by using the functionalization procedures developed in this work.

3.4. Experimental section

3.4.1 Instruments

^{1}H, ^{13}C Nuclear magnetic resonance (NMR) spectra were recorded on a Bruker Avance 400 spectrometer. The ^{1}H NMR chemical shifts (δ) are given in ppm and refer to residual protons on the corresponding deuterated solvent. All deuterated solvents were used as received without any further purification. All coupling constants (J) are given in Hertz (Hz).

The attenuated total reflectance Fourier transform infrared (ATR-FTIR) spectrum and the Fourier transform infrared (FTIR) spectrum was measured with a Shimadzu IRAffinity-1 spectrometer. The transmittance spectrum was collected using a spectral resolution of Δ=1 cm^{-1}, accumulating 64 scans and the ATR-FTIR spectra were ATR corrected (penetration depth mode).

Absorption spectra were measured on a Shimadzu UV-3600 spectrophotometer double-beam UV–VIS–NIR spectrometer and baseline corrected. Quartz cuvettes with path length of 10 mm were used for the recording of UV-Vis absorption spectra.

Emission spectra were measured on a Horiba Jobin−Yvon IBH FL-322 Fluorolog 3 spectrometer equipped with a 450 W xenon arc lamp, double grating excitation, emission monochromators (2.1 nm mm^{-1} of dispersion; 1200 grooves mm^{-1}) and a TBX-04 single photocounting detector was used. Quartz cuvettes with path length of 10 mm were used for all recorded spectra.

Quantum yield measurements were performed with an absolute photoluminescence quantum yield spectrometer Quantaurus C11347 (Hamamatsu, Japan) exciting the sample at λ_{exc}=600 nm. For the measurement of colloidal dispersions, water was used as dispersion medium.

Fluorescence anisotropy measurements were performed on a PicoHarp300 or the Multi Channel Scaling (MCS) electronics NanoHarp 250 of the PicoQuant FluoroTime 300 (PicoQuant GmbH, Germany), equipped with a PDL 820 laser pulse driver. A pulsed laser diode LDH-P-C-510 (λ_{exc}=505 nm) was used to excite the sample and mounted directly on the sample chamber at 90°. The photons were collected by a PMA-C192 photomultiplier (PMT) single-photon-counting detector. The data were acquired by using the commercially available software EasyTau (PicoQuant GmbH, Germany), while data analysis was performed using the commercially available software FluoFit (PicoQuant GmbH, Germany).

Transmission electron microscopy (TEM) samples were analyzed on a FEI/PHILIPS CM120 system operating at 100 kV. Samples were prepared drop casting dispersions of particles in EtOH (0.1 mg·mL^{-1}) onto Formvar-coated Cu grids (400 mesh) and allowed to dry overnight prior visualization.

Nitrogen physisorption isotherms were obtained with a Micromeritics ASAP-2020 physisorption instrument. The particles sample was degassed at 100 °C for 12h. The N_2 adsorption–desorption measurement was performed at -196 °C. The surface areas were calculated by Brunauer–Emmett–Teller (BET) method in the relative pressure range p/p_0 0.06–0.3. The pore size distributions and pore volumes were calculated by classical method on the adsorption branch using a cylindrical model. The total pore volume was estimated at p/p_0 0.99.

X-Ray photoelectron spectroscopy (XPS) analysis was performed using a K-Alpha™+ X-ray Photoelectron Spectrometer (XPS) System (Thermo Scientific). Monochromatic Al K alpha X-rays were used (15 keV, 72 W, 200 mm spot diameter). Spectra were measured using pass energy of 200 eV for survey spectra and 50 eV for core level spectra. The analyzed samples were prepared by drop-casting an ethanolic dispersion (0.1 mg·mL^{-1}) of the particles onto a glass cover slip precoated with Au (Emitech K575X peltier cooled) for 3 min at 60 mA. The Advantage software was used for background subtraction (Shirley-type), and deconvolution of peaks.

Thermogravimetric analysis (TGA) was conducted on a Netzsch model STA 449 fi Jupiter instrument. The samples (0.5–2 mg) were kept at 100 °C for 30 mi for stabilization, then heated from 25 to 800 °C at a speed of 10 °C/min, before being held at this temperature for further 30 minutes, and finally cooled. The analyses were performed under a 20 $mL\cdot min^{-1}$ air flow.

ICP-AES analyses were performed with a Thermo Scientific instrument, ICAP 6500. Samples (1 mL) were diluted to a total volume of 10 mL using aqueous 2% nitric acid. All solutions were freshly prepared from UV sterilized deionized (about 18 MΩ) water and the samples were always handled in plastic falcon tubes. Standard Si solutions (0.01 ppm, 0.1 ppm, 1 ppm) were used for calibration. Reported measurements in each sample represent the average of 3 measurements and are back-calculated to offset the initial dilution. The individual measurements are typically obtained with a relative standard deviation of approximately 0.01 ppm per sample.

3.4.2. Preparation of alkoxysilanes for the functionalization of cage-like silica particles

General information. All solvents were purchased from Merck and used as received. Sulfo-cyanine5-NHS ester and sulfo-cyanine3-NHS ester were purchased from Lumiprobe. 3-(aminopropyl)triethoxy silane (APTES, 99%), 3-(triethoxysilyl)propyl isocyanate (ICPTES, 95%), triethylamine (TEA, >99%), (3-chloropropyl)trimethoxysilane (Cl–TMS, 95%), sodium azide (NaN_3, synthesis grade), D-(+)-glucosamine hydrochloride, tetrabutylammonium bromide (>99%) were purchased from Sigma–Aldrich

Preparation of sCy5-silane. A solution of sulfo-Cy5-NHS ester (0.5 mg, 0.643 µmol) in dry DMSO (200 µL) was prepared in in a 2 mL Eppendorf microtube . APTES (4.5 µL, 0.142 M in dry DMSO) was added and the reaction mixture was allowed to stir for 30 min in the dark. The reaction mixture was used for post-synthesis grafting of **OCSs** without further purification.

Preparation of sugar-silane. A solution of D-(+)-glucosamine hydrochloride (1.8 mg, 8.35 µmol) in DMSO (200 µL) was prepared in a 2 mL Eppendrof microtube. TEA (1.2 µL, 11.86 µmol) was added, followed by ICPTES (2.07 µL, 8.35 µmol), and the reaction mixture was allowed to react under stirring for 1 h. The reaction mixture was used for the post-synthetic grafting of **OCSs** without further purification. ^{1}H NMR (DMSO-d_6, 400 MHz): δ 6.42 (d, 1H, *J*=4 Hz), 6.10 (t, 1H, *J*=5.6 Hz), 5.60 (d, 1H, *J*=7.5 Hz), 4.90 (t, 1H, *J*=3.6 Hz), 4.87 (d, 1H, *J*=4.2 Hz), 4.70 (s broad, 1H), 4.40 (s broad, 1H), 3.63−3.50 (m, 2H), 3.49−3-27 (m, 5H), 3.09 (m, 1H), 3.01 – 2.87 (m, 9H), 1.35 (quint, 2H, *J*=7.1 Hz), 1,16 (t, 12 H, *J*=7.5 Hz), 0.82 ppm (t, 2H, *J*=7.4 Hz).

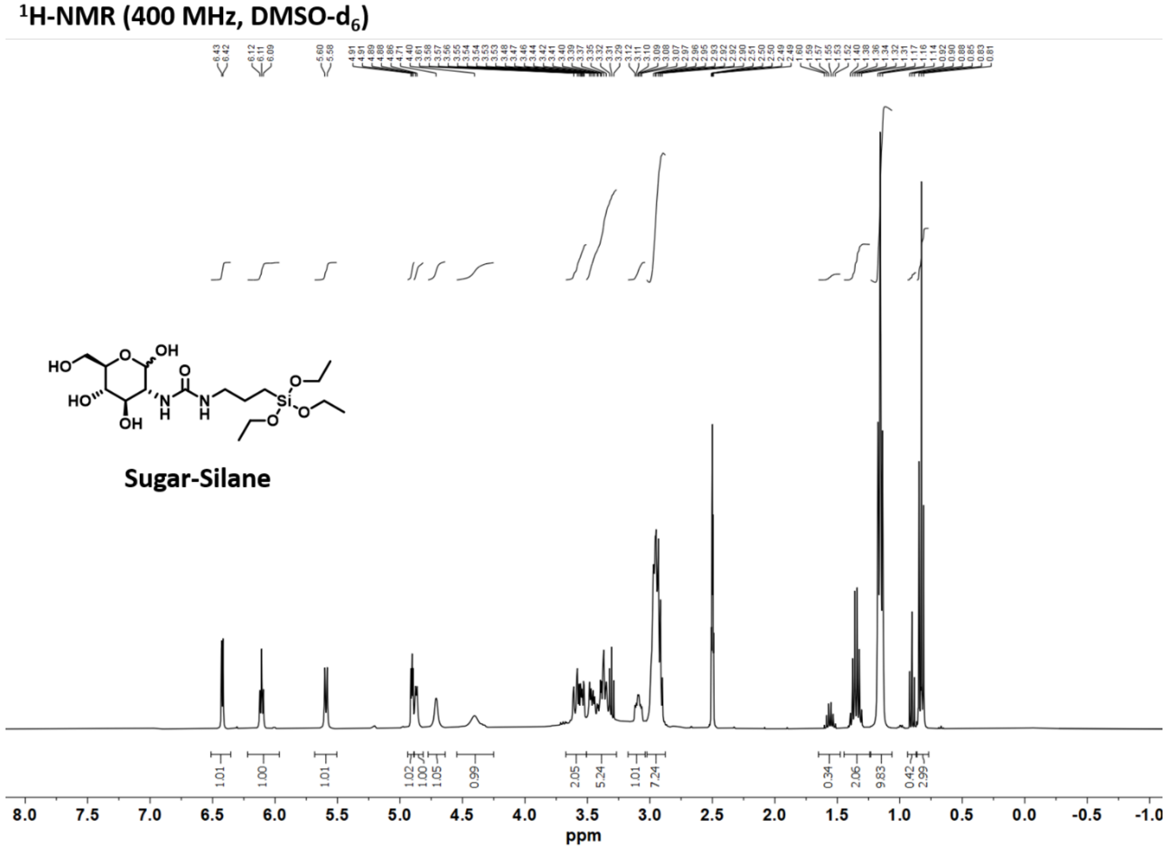

Preparation of AzTMS. To a stirring dispersion of NaN_3 (390 mg, 6 mmol) and tetrabutylammonium bromide (278 mg, 0.8 mmol) in acetonitrile (15 mL), Cl-TMS (964 µL, 4 mmol) was added dropwise and the reaction was subsequently allowed to stir for 24 at 80 °C under reflux conditions. The reaction mixture was allowed to cool down and subsequently Et_2O (5 mL) was added, which induced the formation of a white precipitate(NaBr). The reaction mixture was filtered from the precipitate and the organic solvents were evaporated from the filtrate under reduced pressure. The product was obtained as transparent, yellowish liquid (930 mg, 90%). ^{1}H-NMR ($CDCl_3$, 400 MHz): δ 3.57 (s, 9H), 3.26 (t, 2H, *J*=7.2 Hz), 1.76−1.70 (m, 2H), 0.75−0.63 (m, 2H) ppm. FTIR $\tilde{\nu}$ max [cm^{-1}]: 2941, 2843, 2092, 1463, 1190, 1078, 817, 775.

^{1}H-NMR (400 MHz, $CDCl_3$)

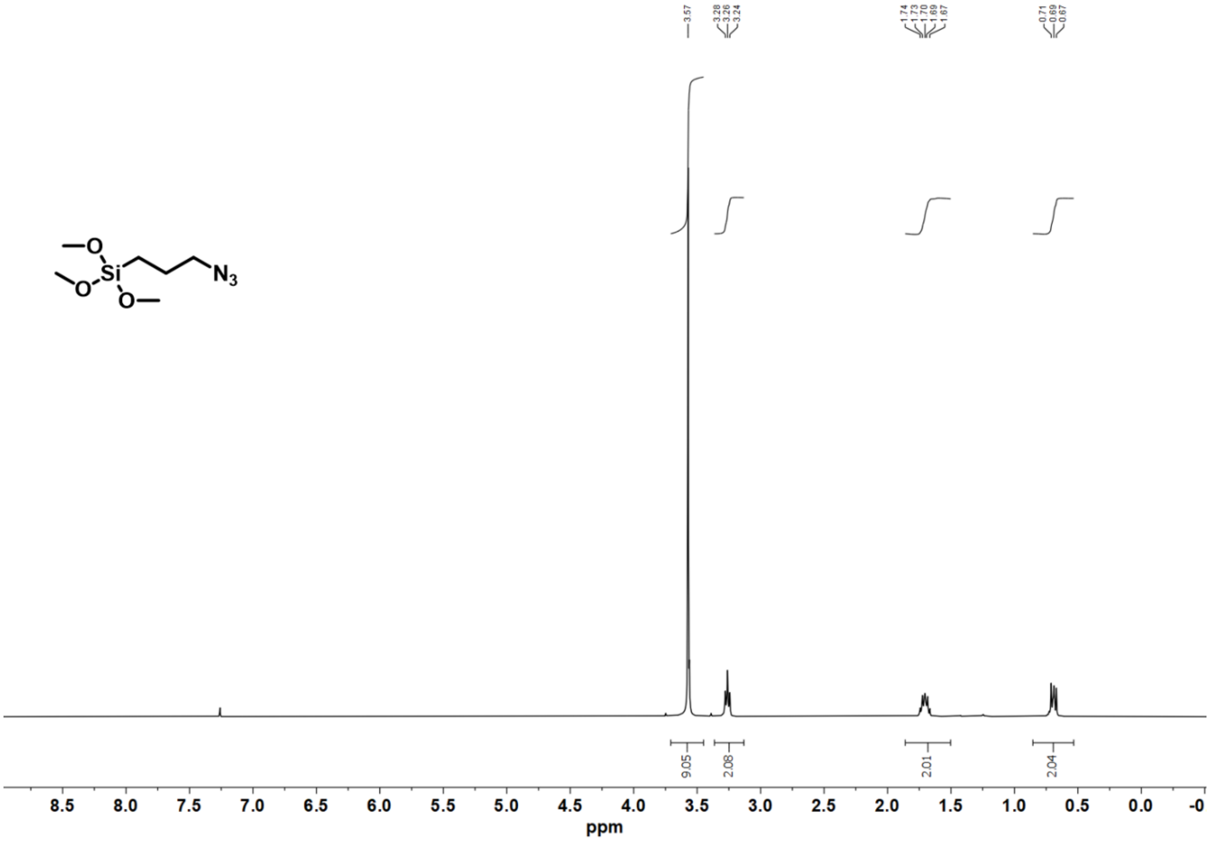

3.4.3. Preparation of alkyne-RGD

General information. The reaction was carried out under inert conditions and in the dark, using dry solvents. Dry DMF was purchased from Merck and used as received. Arg−Gly−Asp peptide (RGD, >97%), (1R,8S,9s)-bicyclo[6.1.0]non-4-yn-9-ylmethyl *N*-succinimidyl carbonate ester (BCN-NHS) and triethylamine (TEA, >99%) were from Merck.

Synthesis of Alkyne-RGD. To a RGD peptide solution (10mg; 28,88 µmol, 1eq) in DMF (3mL), placed in a 10 mL round-bottom flask, TEA (9.2µL, 68.1 µmol) and BCN-NHS (1.1 eq; 9.2 mg, 31.6 µmol) were added. The reaction mixture was stirred at room temperature, while kept in the dark, for 24 h. Subsequently, the reaction crude was dried under a constant nitrogen-flow. The product was finally washed with Et_2O (2 mL), centrifuged and dried under reduced pressure. After drying, the product was obtained ad waxy solid. HR-MS (ESI-TOF): *m/z* calcd for $C_{25}H_{35}N_6O_8$: 523.25 found 523.25.

3.4.4. Preparation of particles and their surface-functionalization

General information. All solvents were used as received. Hexadecyltrimethylammonium bromide (CTAB, 99+%) was purchased from ACROS ORGANICS. Bis(triethoxysilyl-propyl)disulfide (BTDS, 95%) was purchased from fluorochem. Methoxy-(poly-ethyleneoxy)-propyltrimethoxysilane (PEG-silane 6−9 units, 90%) was purchased from ABCR. Aqueous ammonia (NH_3, 28 wt.%) was purchased from VWR Chemicals. Tetraethyl orthosilicate (TEOS, ≥99.0 %, GC) was purchased from Sigma-Aldrich. Acetic acid (glacial, extra pure), hydrochloric acid (37%) and sodium carbonate were purchased from Fisher scientific. SnakeSkin dialysis tubing was purchased from ThermoScientific (MWCO 10.000, 22 mm). All reagents were used without further purification.

Preparation of non-surface-functionalized OSCs, OSCs and Sugar-OSCs. In a 100 mL round-bottom flask, equipped with a magnetic stirrer (Teflon; cylindrical geometry; 1 cm length), CTAB (408 mg, 1.12 mmol) was dissolved in freshly deionized water (50 mL) at 50^{o}C, while stirring the solution for 30 min at 250 rpm. Aqueous NH_3 (12.5 µL, 28 wt% in water) was added and the stirring speed was increased to 750 rpm. Subsequently a mixture of TEOS (448.1 µL, 2 µmol) and BTDS (102.8 µL, 0.223 µmol) was added and the mixture was stirred for 20 h at 50 ^{o}C, while stirring the reaction mixture at 750 rpm. Subsequently, PEG-silane (818 µL) was added to the stirring solution and the reaction mixture was stirred for 14 h at 50 °C. In the case were the dye and Sugar functionalization was desired, the sCy5-Silane solution and Sugar-silane solutions were added immediately after the addition of the PEG-silane and the mixture was stirred for further 14 h at 50^{o}C. The particle dispersion was purified by dialysis against $EtOH/H_2O/AcOH$ (1:1:0.007 *v*/*v*/*v*) mixture for 24 h and finally in an $EtOH/H_2O$ (1:1 *v*/*v*) mixture for another 24 h, whereby the dialysis solution was replaced every 2 h, when possible. Before conducting *in-vitro* and *in-vivo* experiments, the particle suspension was dialyzed against distilled water for 24 h.

Preparation of N_3-OSCs. To a stirring solution of surface extracted **OSCs** (5 mL, *c*=3mg mL^{-1}) which have been dialyzed against EtOH/H_2O (1:1 *v*/*v*), Az-Silane was added (11.1µL, 4.16µmol) and the mixture was allowed to stir for 12 h at 50 °C. Subsequently the particles were purified by means of dialysis against EtOH/H_2O (1:1 *v*/*v*) for 12 h.

Preparation of RGD-OSCS. To the purified **Az-OSCs** (2.5 mL, 3.94 mg·mL^{-1}) dispersion RGD-Alkyne (1 mg, 1.92 µmol) was added and the reaction mixture was stirred for 16 h at room temperature. Subsequently, the particle dispersion was dialyzed against water for 48 h.

3.4.5. Quantification of surface functionalization

Glucosamine quantification. To a dispersion of **Sugar-OSCs** (500 µL, *c*=2.3 mg/mL), 2-cyanoacetamide aqueous solution (500 µL, *c*=0.5 M) and borate-phosphate buffer (1 mL, composed of 0.3 M sodium borate and 0.3 M potassium dihydrogen phosphate, pH = 8) was added and the reaction mixture was heated for 30 min in a boiling water bath. The samples were allowed to cool down at room temperature and the fluorescence intensity was measured upon excitation at λ_{ex}=331 nm.

RGD quantification. To aqueous dispersion of **RGD-OSCs**, an ethanolic 9,10-phenantrenequinone solution (150 µL, 150 µM) and aqueous NaOH solution (25 µL, 2 M) was added. Subsequently the reaction mixture was heated at 60 °C for 3 h. Aqueous HCl (40 µL, 1.2 M) was added and the reaction mixture was kept at room temperature for 1 h before measuring its fluorescence (λ_{ex}=312 nm).

3.4.6. Loading protocols for OSCs

HOECHST 33258 (HE) loading of OSCs. In order to load non-functionalized **OSCs** with the hydrophilic dye Hoechst 33258, organosilica particles were prepared but no surface functionalization occurred. After CTAB removal via dialysis (as described above) the particle dispersion was lyophilized. Subsequently, 10 mg of particles were suspended via sonication (15 min, 30 W) in a solution of the dye (5 mg) in DMSO (300 µL). The suspension was briefly sonicated and allowed to stir for 24 h in the dark. Subsequently the organic solvent was removed by evaporation and the particles were washed once with a H_2O/EtOH mixture (500 µL, 1:1 *v*/*v*) and collected by centrifugation at 14.8 krpm for 30 min. Subsequently the particles were dispersed in EtOH (500 µL), TEA (1 µL) and finally PEG-Silane (64 µL) was added. The mixture was briefly sonicated and subsequently stirred for 12 h in the dark. The recovered particles were washed three times by dispersing the particles in a EtOH/H_2O (1:1 *v*/*v*) mixture (500 µL) and subsequent centrifugation and were finally dried under reduced pressure.

Docetaxel (DT) loading of OSCs. To load non-functionalized **OSCs** with the hydrophobic drug docetaxel (DT), **OSCs** were prepared but no surface functionalization occurred. After CTAB removal via dialysis (as described above) to an aliquot of the particle dispersion (784 µL, 4 mg of particles), EtOH (600 µL) and Doxotaxel (2mg) were added. The resulting suspension was briefly sonicated and subsequently allowed to stir over night at room temperature. The particles were then functionalized with PEG to reestablish the good colloidal stability and to physically entrap the drug into the organosilica cavity. Therefore, PEG-silane (6.4 µL) was added to the drug–particle dispersion. After 30 min, water (500 µL) was added and the particle dispersion was stirred over night at 50^{o}C to allow the PEG-to hydrolyze and condense on the particle surface. The particles were then collected by centrifugation (5 min, 14.8 krpm) and washed with an EtOH/H_2O (1:5 *v*/*v*) mixture by dispersing and centrifuging the particles, until no Docetaxel could be observed in the washing solutions. Therefore, the supernatant of the washing solution was collected, dried under reduced pressure, and the dried sample was solubilized in EtOH (100 µL) to record the UV-Vis absorption spectra. To evaluate the loading, an aliquot of the particles was taken (so that around 2 mg of loaded particles could be analyzed) and the sample was dried before the thermogravimetric analysis.

3.4.7. Degradability studies and HE release experiments

Degradability experiments of OSCs: To evaluate the degradability of **OSCs** upon the presence of GSH, particles (0.05 mg) were dispersed in 500 µL of a GSH solution in PBS (10mM, pH=7.4) and stirred at 37^{o}C. Separately, **OSCs** (0.05 mg) were dispersed in 500 µL of PBS (pH=7.4) and stirred at 37^{o}C. At different time intervals, an aliquot (6 µL) of each particle dispersion was taken and diluted with EtOH (1000 µL; the EtOH was filtered before use with a 25mm syringe filter with 0.2 µm nylon). The diluted samples were analyzed by STEM and TEM.

HOECHST 33258 release from OSC-He: 0.1 mg of **OSCs-He** were dispersed in 500 µL PBS buffer solution containing GSH (10mM, pH = 7.4) or solely in PBS (pH = 7.4) and the particle dispersion was allowed to stir at 37^{o}C. At different time point the particle dispersion was centrifuged (20 min, 14.5 krpm) and aliquots (20 µL) of supernatant were collected for subsequent, fluorescence measurements and a fresh aliquot of solution was added to the particle dispersion. The fluorescence measurement of the first sampled aliquot was performed by placing it in a quartz cuvette, adding subsequently PBS (2.48 mL) and measuring its fluorescence (λ_{ex}=350 nm). For each subsequent measurement, an aliquot from the cuvette was replaced by an aliquot of new supernatant solution from the centrifuged particle dispersion, obtaining therefore a cumulative release curve for HE. All The fluorescent emission spectra were recorded from 385−600 nm.

3.4.8. Cell viability experiments

5x10^4 Glioma C6 cells were seeded in two 24-well plates (culture media: DMEM supplemented with 10% FBS and 1% penicillin). After 5 hours incubation at 37°C 5% CO2, the spent cell culture media was discarded. After 20 minutes sonication, a certain volume of an aqueous stock solution of nanoparticles (1 mg·mL^{-1}) was withdrawn and added to the new complete culture media in order to have three different NPs concentrations, that is, 50, 100 and 200 µg·mL^{-1}. The positive control was represented by a solution of 10% DMSO in complete culture media, while simple complete culture media was used as negative control. The cells were incubated at 37°C for 24 and 48 h. In each plate, each test was performed in three replicates, in order to increase the statistical validity of the results. After 24 and 48 h the Trypan Blue exclusion test was performed.

The spent cell culture media was removed from each well and stored separately in different 2 mL Eppendorf tubes. The cells were washed using 100 µL of PBS in order to collect all the dead cells. The washing solution was added in the 2 mL Eppendorf tubes with the old media. The cells were detached using 100 µL of trypsin and incubated for 5 min. After trypsinization, 100 µL of pre-warmed complete growth medium were added and transferred in the 2 mL Eppendorf tubes with the old media and the PBS, the tubes were centrifuged at 18.000 rpm for 3 min. After discarding the supernatant, 100 µL of the new media were added and the cells resuspended. 50 µL of the cell suspensions were added to 50 µL of the Trypan Blue solution, and 10 µL from the above solution were placed in a cell counting slide. The cell viability was determined using a Countess automated cell counter. The whole experiment was performed twice,to increase the statistical validity of the results.

3.4.9. Biodistribution studies

Animal treatment: CD1 mice, ranging from 20 to 25 grams of weight, were recruited for biodistribution experiments. All studies were carried out with healthy, specific pathogen free and immunocompetent animals in compliance with welfare laws and according to the approval of the Italian ministerialresearch project number "669/2015-PR". For the first study, a single dose of NP (7 mg Silica/ kg of body weight) was administered by intravenous injection from the caudal vein (the same dose but in a volume of 5 µL). After NP administration, the mice did not show any evidence of stress and discomfort for the whole duration of the experiment. The study was carried out including at least 6 mice for each experimental group. Mice were randomly divided and received 200 µL of the following solutions: i) PBS alone; ii) PBS+**OSCs**; iii) PBS+**Sugar-OSCs**. Animals were sacrificed at different time-points (30 min, 1 h, 4 h, 24 h and 120 h) after the treatments with an overdose of anesthetic. Brain, lungs, spleen, liver and kidneys were removed and stored before ex vivo studies.

Optical imaging: The presence of a stable link connecting **OSC**s with a fluorescent dye enabled us to determine the distribution of **OSCs** in the body with a high sensibility and specificity. Briefly, living animals were anesthetized at different time-points and were positioned in prone position in a room connected with a source of light with a peak of emission at 630 nm (corresponding to the peak of excitation of the fluorophore attached to NPs). The instrument Lumina XRS was used for all scanning. Since the brain is anatomically well distinguishable from the other organs, it was possible to obtain reliable results using the images directly obtained from living mice. Opposite the scanning of toraco-abdominal region does not allow to discriminate among the different organs that overlaps among them. For this reason, the in vivo imaging is not reliable, and we decided to measure the fluorescence of lungs, liver, spleen and kidneys after sacrifice and organ removal. To avoid the background contribution associated with the autofluorescence of the tissues, spectral unmixing process was performed during the scanning. Spectral unmixing permits to distinguish between the dye and the background through the kinetics of extinction of the two different signals in the whole area of analysis. Both ex vivo and in vivo analyses are quantitative, and are expressed as relative radiant efficacy normalizing the average of signal originating from untreated mice to 1.

Ex vivo analysis. To determine the amount of silicon in brain and other organs samples were mineralized and processed by ICP-AES. Samples (1 mL) were diluted to a total volume of 10 mL using aqueous 2% nitric acid. All solutions were freshly prepared from UV-sterilized deionized (about 18 MΩ) water and the samples were always handled in plastic falcon tubes. Standard Si solutions (0.01ppm, 0.1ppm, 1 ppm) were used for calibration. Reported measurements in each sample represent the average of 3 measurements and were back-calculated to offset the initial dilution. In addition, micrometric sections from brain, spleen, liver, kidneys, and lungs were obtained from frozen samples of **OSCs**-treated and untreated mice. Hoechst 33258 (fluorescent nuclear dye with an excitation peak at 405 nm) was utilized to visualize the anatomy of tissues and to determine the localization cellular localization **OSCs** (detectable by a direct excitation at 635 nm) by confocal microscope.

3.5. References

(1) Hua, S.; de Matos, M. B. C.; Metselaar, J. M.; Storm, G. Current Trends and Challenges in the Clinical Translation of Nanoparticulate Nanomedicines: Pathways for Translational Development and Commercialization. *Front. Pharmacol.* **2018**, *9* (JUL), 1–14. DOI: 10.3389/fphar.2018.00790.

(2) Warther, D.; Jimenez, C. M.; Raehm, L.; Gérardin, C.; Durand, J. O.; Morère, A.; El Cheikh, K.; Gallud, A.; Gary-Bobo, M.; Maynadier, M.; Garcia, M. Small Sized Mesoporous Silica Nanoparticles Functionalized with Mannose for Retinoblastoma Cell Imaging. *RSC Adv.* **2014**, *4* (70), 37171–37179. DOI: 10.1039/c4ra05310a.

(3) Yu, L.; Chen, Y.; Lin, H.; Du, W.; Chen, H.; Shi, J. Ultrasmall Mesoporous Organosilica Nanoparticles: Morphology Modulations and Redox-Responsive Biodegradability for Tumor-Specific Drug Delivery. *Biomaterials* **2018**, *161*, 292–305. DOI: 10.1016/j.biomaterials.2018.01.046.

(4) Fatieiev, Y.; Croissant, J. G.; Alamoudi, K.; Khashab, N. M. Cellular Internalization and Biocompatibility of Periodic Mesoporous Organosilica Nanoparticles with Tunable Morphologies: From Nanospheres to Nanowires. *Chempluschem* **2017**, *82* (4), 631–637. DOI: 10.1002/cplu.201600560.

(5) Wei, Y.; Li, X.; Zhang, R.; Liu, Y.; Wang, W.; Ling, Y.; El-Toni, A. M.; Zhao, D. Periodic Mesoporous Organosilica Nanocubes with Ultrahigh Surface Areas for Efficient CO2 Adsorption. *Sci. Rep.* **2016**, *6* (September 2015), 1–11. DOI: 10.1038/srep20769.

(6) Maggini, L.; Travaglini, L.; Cabrera, I.; Castro-Hartmann, P.; De Cola, L. Biodegradable Peptide-Silica Nanodonuts. *Chem. - A Eur. J.* **2016**, *22* (11), 3697–3703. DOI: 10.1002/chem.201504605.

(7) Croissant, J. G.; Fatieiev, Y.; Almalik, A.; Khashab, N. M. Mesoporous Silica and Organosilica Nanoparticles: Physical Chemistry, Biosafety, Delivery Strategies, and Biomedical Applications. *Adv. Healthc. Mater.* **2018**, *7* (4), 1–75. DOI: 10.1002/adhm.201700831.

(8) Blanco, E.; Shen, H.; Ferrari, M. Principles of Nanoparticle Design for Overcoming Biological Barriers to Drug Delivery. *Nat. Biotechnol.* **2015**, *33* (9), 941–951. DOI: 10.1038/nbt.3330.

(9) Choi, H. S.; Liu, W.; Liu, F.; Nasr, K.; Misra, P.; Bawendi, M. G.; Frangioni, J. V. Design Considerations for Tumour-Targeted Nanoparticles. *Nat. Nanotechnol.* **2010**, *5* (1), 42–47. DOI: 10.1038/nnano.2009.314.

(10) Ma, K.; Werner-Zwanziger, U.; Zwanziger, J.; Wiesner, U. Controlling Growth of Ultrasmall Sub-10 Nm Fluorescent Mesoporous Silica Nanoparticles. *Chem. Mater.* **2013**, *25* (5), 677–691. DOI: 10.1021/cm303242h.

(11) Zhang, J.; Wang, X.; Wen, J.; Su, X.; Weng, L.; Wang, C.; Tian, Y.; Zhang, Y.; Tao, J.; Xu, P.;

Lu, G.; Teng, Z.; Wang, L. Size Effect of Mesoporous Organosilica Nanoparticles on Tumor Penetration and Accumulation. *Biomater. Sci.* **2019**, *7* (11), 4790–4799. DOI: 10.1039/c9bm01164a.

(12) Zhao, T.; Elzatahry, A.; Li, X.; Zhao, D. Single-Micelle-Directed Synthesis of Mesoporous Materials. *Nat. Rev. Mater.* **2019**, *4* (12), 775–791. DOI: 10.1038/s41578-019-0144-x.

(13) Toy, R.; Peiris, P. M.; Ghaghada, K. B.; Karathanasis, E. Shaping Cancer Nanomedicine: The Effect of Particle Shape on the in Vivo Journey of Nanoparticles. *Nanomedicine* **2014**, *9* (1), 121–134. DOI: 10.2217/nnm.13.191.

(14) Black, K. C. L.; Wang, Y.; Luehmann, H. P.; Cai, X.; Xing, W.; Pang, B.; Zhao, Y.; Cutler, C. S.; Wang, L. V.; Liu, Y.; Xia, Y. Radioactive 198Au-Doped Nanostructures with Different Shapes for in Vivo Analyses of Their Biodistribution, Tumor Uptake, and Intratumoral Distribution. *ACS Nano* **2014**, *8* (5), 4385–4394. DOI: 10.1021/nn406258m.

(15) Decuzzi, P.; Godin, B.; Tanaka, T.; Lee, S. Y.; Chiappini, C.; Liu, X.; Ferrari, M. Size and Shape Effects in the Biodistribution of Intravascularly Injected Particles. *J. Control. Release* **2010**, *141* (3), 320–327. DOI: 10.1016/j.jconrel.2009.10.014.

(16) Ma, K.; Gong, Y.; Aubert, T.; Turker, M. Z.; Kao, T.; Doerschuk, P. C.; Wiesner, U. Self-Assembly of Highly Symmetrical, Ultrasmall Inorganic Cages Directed by Surfactant Micelles. *Nature* **2018**, *558* (7711), 577–580. DOI: 10.1038/s41586-018-0221-0.

(17) Jimenez, C. M.; Rubio, Y. G.; Saunier, V.; Warther, D.; Stojanovic, V.; Raehm, L.; Frochot, C.; Arnoux, P.; Garcia, M.; Morère, A.; Bettache, N.; Maynadier, M.; Maillard, P.; Gary-Bobo, M.; Durand, J. O. 20-Nm-Sized Mesoporous Silica Nanoparticles With Porphyrin Photosensitizers for in Vitro Photodynamic Therapy. *J. Sol-Gel Sci. Technol.* **2016**, *79* (3), 447–456. DOI: 10.1007/s10971-016-3991-6.

(18) Dogra, P.; Adolphi, N. L.; Wang, Z.; Lin, Y. S.; Butler, K. S.; Durfee, P. N.; Croissant, J. G.; Noureddine, A.; Coker, E. N.; Bearer, E. L.; Cristini, V.; Brinker, C. J. Establishing the Effects of Mesoporous Silica Nanoparticle Properties on in Vivo Disposition Using Imaging-Based Pharmacokinetics. *Nat. Commun.* **2018**, *9* (1), 1–14. DOI: 10.1038/s41467-018-06730-z.

(19) Maggini, L.; Cabrera, I.; Ruiz-Carretero, A.; Prasetyanto, E. A.; Robinet, E.; De Cola, L. Breakable Mesoporous Silica Nanoparticles for Targeted Drug Delivery. *Nanoscale* **2016**, *8* (13), 7240–7247. DOI: 10.1039/c5nr09112h.

(20) Rohou, A.; Grigorieff, N. CTFFIND4: Fast and Accurate Defocus Estimation from Electron Micrographs. *J. Struct. Biol.* **2015**, *192* (2), 216–221. DOI: 10.1016/j.jsb.2015.08.008.

(21) Scheres, S. H. W. RELION: Implementation of a Bayesian Approach to Cryo-EM Structure Determination. *J. Struct. Biol.* **2012**, *180* (3), 519–530. DOI: 10.1016/j.jsb.2012.09.006.

(22) Pelaz, B.; Del Pino, P.; Maffre, P.; Hartmann, R.; Gallego, M.; Rivera-Fernández, S.; De La Fuente, J. M.; Nienhaus, G. U.; Parak, W. J. Surface Functionalization of Nanoparticles with Polyethylene Glycol: Effects on Protein Adsorption and Cellular Uptake. *ACS Nano*

2015, *9* (7), 6996–7008. DOI: 10.1021/acsnano.5b01326.

(23) Worthen, A. J.; Tran, V.; Cornell, K. A.; Truskett, T. M.; Johnston, K. P. Steric Stabilization of Nanoparticles with Grafted Low Molecular Weight Ligands in Highly Concentrated Brines Including Divalent Ions. *Soft Matter* **2016**, *12* (7), 2025–2039. DOI: 10.1039/c5sm02787j.

(24) Mekaru, H.; Yoshigoe, A.; Nakamura, M.; Doura, T.; Tamanoi, F. Biodegradability of Disulfide-Organosilica Nanoparticles Evaluated by Soft X-Ray Photoelectron Spectroscopy: Cancer Therapy Implications. *ACS Appl. Nano Mater.* **2019**, *2* (1), 479–488. DOI: 10.1021/acsanm.8b02023.

(25) Forman, H. J.; Zhang, H.; Rinna, A. Glutathione: Overview of Its Protective Roles, Measurement, and Biosynthesis. *Mol. Aspects Med.* **2009**, *30* (1–2), 1–12. DOI: 10.1016/j.mam.2008.08.006.

(26) Fernandes, P. A.; Ramos, M. J. Theoretical Insights into the Mechanism for Thiol/Disulfide Exchange. *Chem. - A Eur. J.* **2004**, *10* (1), 257–266. DOI: 10.1002/chem.200305343.

(27) Russell, L. M.; Hultz, M.; Searson, P. C. Leakage Kinetics of the Liposomal Chemotherapeutic Agent Doxil: The Role of Dissolution, Protonation, and Passive Transport, and Implications for Mechanism of Action. *J. Control. Release* **2018**, *269* (October 2017), 171–176. DOI: 10.1016/j.jconrel.2017.11.007.

(28) Beltrán-Gracia, E.; López-Camacho, A.; Higuera-Ciapara, I.; Velázquez-Fernández, J. B.; Vallejo-Cardona, A. A. *Nanomedicine Review: Clinical Developments in Liposomal Applications*; Springer Vienna, 2019; Vol. 10. DOI: 10.1186/s12645-019-0055-y.

(29) Ma, K.; Wiesner, U. Modular and Orthogonal Post-PEGylation Surface Modifications by Insertion Enabling Penta-Functional Ultrasmall Organic-Silica Hybrid Nanoparticles. *Chem. Mater.* **2017**, *29* (16), 6840–6855. DOI: 10.1021/acs.chemmater.7b02009.

(30) Honda, S.; Matsuda, Y.; Takahashi, M.; Kakehi, K.; Ganno, S. Fluorimetric Determination of Reducing Carbohydrates with 2-Cyanoacetamide and Application to Automated Analysis of Carbohydrates as Borate Complexes. *Anal. Chem.* **1980**, *52* (7), 1079–1082. DOI: 10.1021/ac50057a019.

(31) Wong, S.; Zhao, J.; Cao, C.; Wong, C. K.; Kuchel, R. P.; De Luca, S.; Hook, J. M.; Garvey, C. J.; Smith, S.; Ho, J.; Stenzel, M. H. Just Add Sugar for Carbohydrate Induced Self-Assembly of Curcumin. *Nat. Commun.* **2019**, *10* (1), 1–9. DOI: 10.1038/s41467-019-08402-y.

(32) Carpenter, W. R. Evidence of Overtone and Combination Bands in the Spectra of Organic Azides. *Appl. Spectrosc.* **1963**, *17* (3), 70–72.

(33) Ghosh, S.; Panja, P.; Dalal, C.; Jana, N. R. Arginine-Terminated, Chemically Designed Nanoparticle for Direct Cell Translocation. *ACS Appl. Bio Mater.* **2019**, *2* (1), 339–348. DOI: 10.1021/acsabm.8b00617.

(34) Croissant, J. G.; Mauriello-Jimenez, C.; Maynadier, M.; Cattoën, X.; Wong Chi Man, M.;

Raehm, L.; Mongin, O.; Blanchard-Desce, M.; Garcia, M.; Gary-Bobo, M.; Maillard, P.; Durand, J. O. Synthesis of Disulfide-Based Biodegradable Bridged Silsesquioxane Nanoparticles for Two-Photon Imaging and Therapy of Cancer Cells. *Chem. Commun.* **2015**, *51* (61), 12324–12327. DOI: 10.1039/c5cc03736k.

(35) Calvaresi, E. C.; Hergenrother, P. J. Glucose Conjugation for the Specific Targeting and Treatment of Cancer. *Chem. Sci.* **2013**, *4* (6), 2319–2333. DOI: 10.1039/c3sc22205e.

(36) Dreaden, E. C.; Austin, L. A.; MacKey, M. A.; El-Sayed, M. A. Size Matters: Gold Nanoparticles in Targeted Cancer Drug Delivery. *Ther. Deliv.* **2012**, *3* (4), 457–478. DOI: 10.4155/tde.12.21.

(37) Gromnicova, R.; Davies, H. A.; Sreekanthreddy, P.; Romero, I. A.; Lund, T.; Roitt, I. M.; Phillips, J. B.; Male, D. K. Glucose-Coated Gold Nanoparticles Transfer across Human Brain Endothelium and Enter Astrocytes in Vitro. *PLoS One* **2013**, *8* (12). DOI: 10.1371/journal.pone.0081043.

(38) Jiang, X.; Xin, H.; Ren, Q.; Gu, J.; Zhu, L.; Du, F.; Feng, C.; Xie, Y.; Sha, X.; Fang, X. Nanoparticles of 2-Deoxy-d-Glucose Functionalized Poly(Ethylene Glycol)-Co-Poly(Trimethylene Carbonate) for Dual-Targeted Drug Delivery in Glioma Treatment. *Biomaterials* **2014**, *35* (1), 518–529. DOI: 10.1016/j.biomaterials.2013.09.094.

(39) Anraku, Y.; Kuwahara, H.; Fukusato, Y.; Mizoguchi, A.; Ishii, T.; Nitta, K.; Matsumoto, Y.; Toh, K.; Miyata, K.; Uchida, S.; Nishina, K.; Osada, K.; Itaka, K.; Nishiyama, N.; Mizusawa, H.; Yamasoba, T.; Yokota, T.; Kataoka, K. Glycaemic Control Boosts Glucosylated Nanocarrier Crossing the BBB into the Brain. *Nat. Commun.* **2017**, *8* (1). DOI: 10.1038/s41467-017-00952-3.

(40) Min, H. S.; Kim, H. J.; Naito, M.; Ogura, S.; Toh, K.; Hayashi, K.; Kim, B. S.; Fukushima, S.; Anraku, Y.; Miyata, K.; Kataoka, K. Systemic Brain Delivery of Antisense Oligonucleotides across the Blood–Brain Barrier with a Glucose-Coated Polymeric Nanocarrier. *Angew. Chemie - Int. Ed.* **2020**, *59* (21), 8173–8180. DOI: 10.1002/anie.201914751.

(41) Betzer, O.; Shilo, M.; Opochinsky, R.; Barnoy, E.; Motiei, M.; Okun, E.; Yadid, G.; Popovtzer, R. The Effect of Nanoparticle Size on the Ability to Cross the Blood-Brain Barrier: An in Vivo Study. *Nanomedicine* **2017**, *12* (13), 1533–1546. DOI: 10.2217/nnm-2017-0022.

(42) Nowak, M.; Helgeson, M. E.; Mitragotri, S. Delivery of Nanoparticles and Macromolecules across the Blood–Brain Barrier. *Adv. Ther.* **2020**, *3* (1), 1900073. DOI: 10.1002/adtp.201900073.

(43) Georgieva, J. V.; Brinkhuis, R. P.; Stojanov, K.; Weijers, C. A. G. M.; Zuilhof, H.; Rutjes, F. P. J. T.; Hoekstra, D.; Van Hest, J. C. M.; Zuhorn, I. S. Peptide-Mediated Blood-Brain Barrier Transport of Polymersomes. *Angew. Chemie - Int. Ed.* **2012**, *51* (33), 8339–8342. DOI: 10.1002/anie.201202001.

(44) Tosi, G.; Costantino, L.; Rivasi, F.; Ruozi, B.; Leo, E.; Vergoni, A. V.; Tacchi, R.; Bertolini, A.;

Vandelli, M. A.; Forni, F. Targeting the Central Nervous System: In Vivo Experiments with Peptide-Derivatized Nanoparticles Loaded with Loperamide and Rhodamine-123. *J. Control. Release* **2007**, *122* (1), 1–9. DOI: 10.1016/j.jconrel.2007.05.022.

Chapter 4

Building organosilicas with oligonucleotides

In this chapter, the preparation of organosilica particles by using DNA and PNA oligonucleotides is described. To this purpose, novel DNA- and PNA-based bis-alkoxysilanes were synthesized and their hydrolysis and condensation by using sol–gel chemistry were investigated. In this regard, the influence of synthetic parameters, such as the length of the oligonucleotide, the presence of a secondary silica source or a surfactant serving as a structure-templating agent was assessed. The obtained particles are able to recognize other biomolecules, such as DNA, and to degrade upon enzymatic activity. Furthermore, inspired by supramolecular polymers and in particular by hybrid-bonding polymers, the possibility to self-assemble PNA-based mono-alkoxysilanes to their corresponding bis-alkoxysilanes through supramolecular interactions was investigated along with the use of the resulting supramolecular assemblies for the preparation of stimuli-responsive organosilicas. Spectroscopic characterization of the resulting material indicated the presence of PNA-based supramolecular aggregates within the polymerized alkoxysilane framework, proving therefore the possibility to form novel organosilica particles, which are constituted by both, supramolecular and covalent interactions.

The work presented in this chapter was carried out partially at the McGill University (Montréal, Canada) during a seven-month placement in the group of Prof. Hanadi Sleiman in the frame of the Nano-Oligomed project and received funding from the European Union's Horizon 2020 research and innovation program under the Marie Skłodowska-Curie grant agreement No 778133.

4.1. Introduction

Organosilica particles (OSPs) are hybrid organic–inorganic materials that find application in various fields such as catalysis,[1–3] photovoltaics,[4,5] separation sciences[6,7] and pollutant remediation [8–10]. Many different organic functional groups can be integrated within the silica structure of OSPs via sol–gel chemistry using organo-bisalkoxysilanes, thereby yielding particles endowed with specific physiochemical properties.[11] As mentioned in previous chapters, porous and stimuli-responsive OSPs that degrade upon exposure to external stimuli are attractive carriers for the development of future nanomedicines with improved biological safety. Examples of unexplored molecules for the preparation of OSPs include single-stranded deoxyribonucleic acid (ssDNA) and single-stranded peptide nucleic acid (ssPNA) based oligonucleotides. These molecules contain attractive organic functional groups for the preparation of OSPs that can ensure unique physicochemical properties, such as programmable base-pair complementarity and enzymatic degradability. Furthermore, by using specifically designed DNA sequences, such as aptamers, a variety of small molecules, metals, and even living cells can be sensed with high selectivity.[12,13] The integration of oligonucleotides within an inorganic framework can therefore lead to the preparation of hybrid materials with strong stimuli-dependent properties, ranging from stimuli-responsive degradation to selective binding of small molecules or even cells. Due to the precise programmability of DNA and PNA oligonucleotides regarding their hybridization with complementary strands, they were previously used in the preparation of self-assembled nanoparticles.[14–19] Aptamer-functionalized nanoparticles have been previously reported for either the detection of biomolecules,[20,21]cells[22,23] or for drug-delivery applications.[24,25] Porous silica particles have been previously reported as carriers for the delivery therapeutic DNA,[26–28] RNA[29–31] and PNA[32] oligonucleotides. Furthermore, the development of DNA-gated delivery systems[33,34] for biomedical applications was successfully reported, but the preparation of DNA or PNA-bridged organosilica particles has not yet been described in the literature. Integration of ssDNAs, such as aptamers, or ssPNAs would provide organosilicas with the ability to selectively bind biomolecules allowing for molecular recognition, accumulation and detection of disease-related biomarkers.[35–37] In order to prepare porous OSPs, in which the organic molecule serves as bridging group with the silica framework, typically organo bis-alkoxysilanes are hydrolyzed and condensed, beside a common silica source (e.g. tetraethyl orthosilicate), in the presence of a surfactant (e.g. cetyltrimethylammonium bromide).[11] Organoalkoxysilanes can also be thought to be used as monomers for the preparation of self-assembled structures, which can then be further hydrolyzed and condensed to form particles, consisting of supramolecular, that is non-covalent and covalent bonds. This approach would form materials which can be categorized as hybrid bonding polymers.[38] In this respect, the self-assembly of organoalkoxysilanes has been previously reported[39–43] and functionalized gold nanocrystals[44] as well as functionalized liposomes[45] have been reported by exploiting the self-assembly of such molecules. Nevertheless, the use of PNA oligonucleotides to form supramolecular assembled bis-alkoxysilanes, which can be further polymerized to prepare organosilica particles, has not been yet described.

In this chapter, the possibility to use various alkoxysilane derivatives of single–stranded DNA and PNA oligonucleotides to serve as novel stimuli-responsive building blocks for the preparation of stimuli-responsive organsilica particles was investigated. To this end, novel DNA and PNA bis-alkoxysilanes were synthesized and used to form organosilica particles by using a modified Stöber synthesis protocol. The ability of the particles to bind complementary ssDNA oligonucleotides and their degradation upon enzymatic activity was studied. Furthermore, inspired by the recent work reported on hybrid bonding polymers,[46] the possibility to self-assemble complementary PNA-based alkoxysilanes to prepare organosilicas was investigated. To this purpose, single-stranded complementary PNAs, which have been synthesized by Corradini's group (University of Parma), were derivatized to alkoxysilane derivatives and allowed to self-assemble to form supramolecular PNA-based bis-alkoxysilanes. These assembled alkoxysilanes were directly hydrolyzed and condensed to form organosilicas bearing a supramolecular bridging group within a covalent network of condensed alkoxysilanes. The presence of the supramolecular assembly within the particles was successfully characterized, indicating the possibility to form new types of stimuli-responsive organosilicas, which resemble some of the properties of hybrid bonding polymers.

4.2. Results and Discussion

4.2.1. Preparation of single-stranded DNA and PNA organosilica particles

As mentioned in the previous chapters, covalent integration of an organic functional group within a silica framework requires organo bis-alkoxysilanes to be hydrolyzed and condensed together with a common silica source, such as TEOS, in aqueous media. To integrate ssDNA within the framework of organosilica particles, ssDNA oligonucleotides were first prepared and subsequently derivatized to their corresponding bis-alkoxysilanes. ssDNA oligonucleotides and their backbone-modified analogues were prepared with a DNA synthesizer using a standard phosphoramidite protocol, yielding the diamino-modified and cyanine 3 (Cy3) labeled oligonucleotide **1** (see section 4.4.2. for details). Subsequent reaction of **1** with 2.1 eq of 3-(triethoxysilyl)propyl isocyanate (ICPTES) in the presence of the base TEA led to the successful preparation of its bis-alkoxysilane derivative **2** (Scheme 1, see section 4.4.3. for further information).

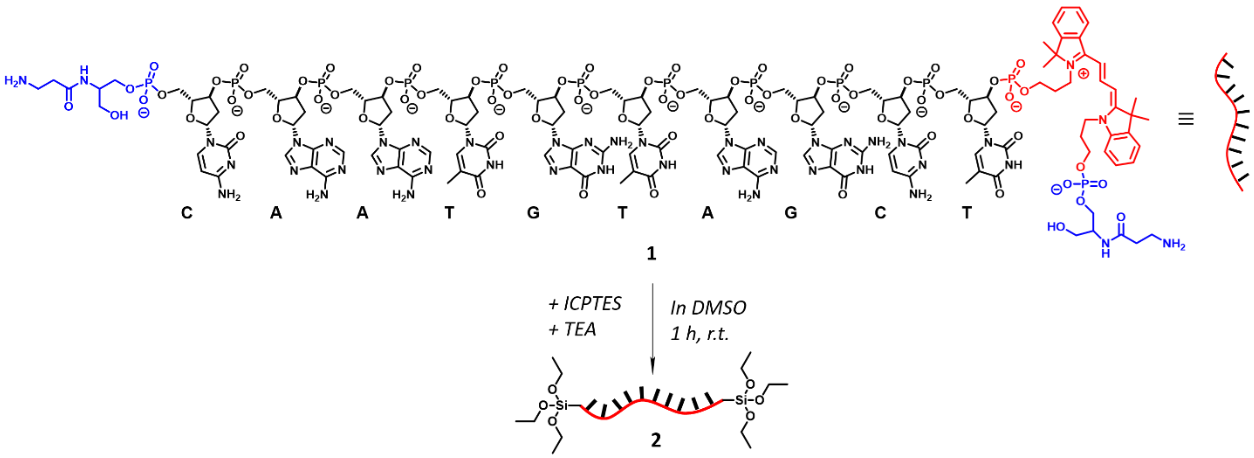

Scheme 1. Reaction scheme for the preparation of ssDNA alkoxysilane derivative **2**.

The use of a 10-mer oligonucleotide with its specific base-pair sequence was chosen because its hybridization with complementary DNA strands can occur at room temperature. To investigate the influence of the oligonucleotide length on the final particle morphology, a shorter 4-mer ssDNA bis-alkoxysilane was prepared analogously as described for the synthesis of **2** (see section 4.4.3.). Before using **2** to prepare organosilica particles, a protocol for the preparation of pristine mesoporous silica particles (MSPs) under slightly basic (pH=8.5) and low EtOH content conditions was optimized, to ensure the chemical stability of ssDNA during the particle preparation. By applying a modified Stöber synthesis and varying the H_2O/EtOH, the synthesis of MSPs was optimized to obtain 100 nm MSPs (see section 4.4.4.). TEM images (Figure 1), showed that the particle size distribution narrowed as the water content in the reaction mixture was increased, while the concentration of TEOS, CTAB and NH_3 concentrations were kept constant. The formation of smaller particles in reaction mixtures with a higher water content could be explained by the fact that the contact of water molecules with TEOS increased in such mixtures, leading faster to hydrolysis and nucleation of the silica source. The reactions were carried out at pH=8.5 where condensation rates are known to outcompete hydrolysis rates for alkoxysilanes, which further explains the fast formation of nucleation sites in reaction mixtures, possessing greater amounts of water.[47] Furthermore, TEM analysis suggested an increased porosity upon formation of smaller MSPs. A solvent ratio of 1:0.3 (*v*/*v*) was selected to prepare ssDNA-organosilica particles based on the formation of a narrow distribution of small (101±7 nm) MSPs (Figure 1b and d).

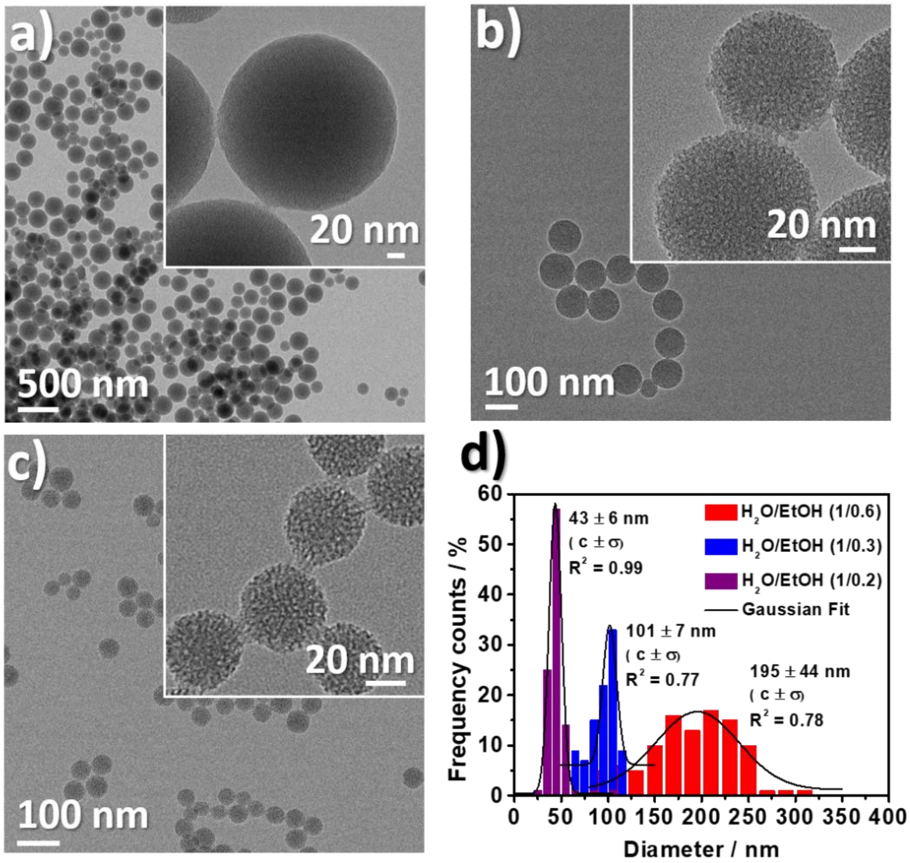

Figure 1. MSPs prepared at pH=8.5 with different H_2O/EtOH ratios: a) 1:0.6, b) 1/0.3 and c) 1.02. d) Calculated size distribution for MSPs prepared at different H_2O/EtOH ratios.

Once a suitable model synthesis for MSPs had been established, ssDNA-bridged organosilica particles (**ssDNA-OSPs**) were prepared by hydrolysis and condensation of compound **2** with TEOS (**2**/TEOS 0.007:1 molar ratio) in the presence of the surfactant CTAB and aqueous ammonia as the base. The particles were collected by centrifugation and the surfactant was removed upon extraction in EtOH under reflux for 24 h (see section 4.4.5.). As depicted in Figure 2, spherical particles with an average diameter of 387±88 nm (diameter calculated from TEM images) were obtained. Notably, the size of **ssDNA-OSPs** drastically increased compared to that of the model silica particles. This was most probably due to the presence of the charged DNA, which leads to electrostatic interactions with the surfactant, ultimately altering the assembly mechanism of the various reactants in the reaction mixture. TEM images showed a drastic loss porosity of **ssDNA-**

OSP compared to the model particles, which were prepared without the use of the organic linker. This loss in porosity can be explained by the high negative charge density and greater steric hindrance of the ssDNA, which interfere with the cooperative self-assembly mechanism of silanols and CTAB micelles, leading to a highly disordered pore arrangement. This hypothesis is supported by previously published work on porous organosilica particles in which a decrease in porosity and pore-order was observed when organoalkoxysilanes with greater structural flexibility were used to form OSPs.[48,49]

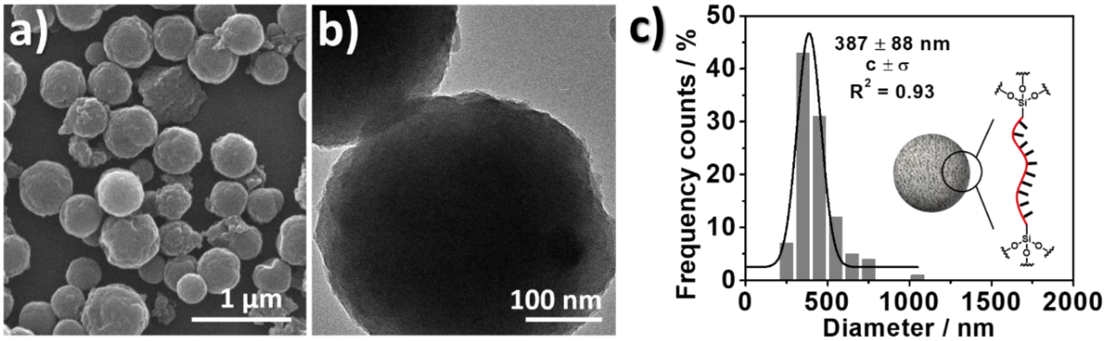

Figure 2. a) SEM and b) TEM images of **ssDNA-OSPs**. c) Size distribution of **ssDNA-MSPs** calculated from TEM images.

The use of a shorter ssDNA-silane composed of 4 nucleobases (GCGC) generated particles with increased porosity (Figure 3), confirming the hypothesis that negative charge density and sterically hindrance of the ssDNA organoalkoxysilanes can influence particle porosity.

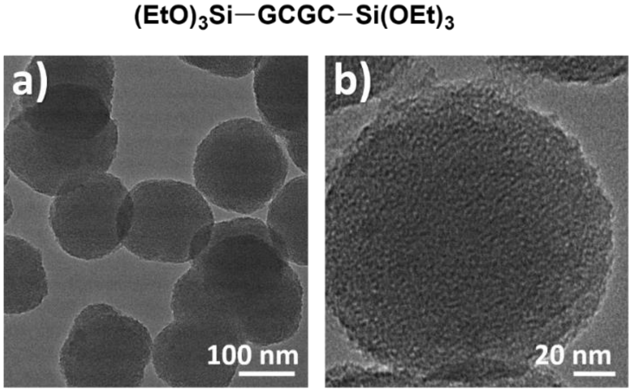

Figure 3. a) TEM image of organosilica particles prepared with a short ssDNA alkoxysilane (GCGC). b) TEM image of organosilica particles prepared with a short ssDNA alkoxysilane at higher magnification.

As depicted in Figure 4b, the SAXS pattern obtained from **ssDNA-OSPs** showed the presence of a broad signal at q=1.3 nm^{-1}, indicating the presence of an ordered structure within the particles. Analysis of the TEM images could not determine whether the SAXS pattern was produced by the presence of mesopores or a different ordered structure existing within **ssDNA-OSPs**. Interestingly, SEM images of **ssDNA-OSPs** at higher magnification (Figure 4a) show that the particles possess a rough surface and seem to be constituted from smaller spherical particles. Therefore, it cannot be excluded the possibility that the observed SAXS pattern was produced by this smaller-particles, which were arranged in either a hexagonally or face-centered closed packing. Analysis regarding the approximate size of the scatterer from the SAXS pattern observed, its size was calculated to be ca. 5 nm (see section 4.4.8. for calculation). This calculated value is in good agreement with the size of the small particles observed in Figure 4a, considering that the gold sputtering during the SEM sample preparation produced an additional gold-layer with thickness of ca. 8 nm. Further, when at a later stage the degradability of the particles in the presence of a hydrolase was assesses via SEM images (Figure 7b), it was evident that **ssDNA-OSPs** degraded into small spherical debris, suggesting further that the initial particle was composed of smaller silica particles. It was not possible to obtain amounts of **ssDNA-OSPs** large enough to analyze the particle porosity by N_2-adsorption–desorption measurements. The formation path of **ssDNA-OSPs** could be investigated via electron microscopy and SAXS measurements of the reaction mixture at different time intervals during particle formation. The way in which **ssDNA-OSPs** are formed could be significantly altered from the expected cooperative hydrolysis and assembly mechanism and rather follow altered formation pathways. Such an altered pathway could consist in the initial formation of silica particles of ca. 5 nm due to hydrolysis and condensation of TEOS and subsequent interparticle aggregation and further condensation with unreacted TEOS and **2**, leading to the formation of **ssDNA-OSPs**. Slower hydrolysis and condensation rates for **2** can be explained by the fact that slower reaction rates for sterically demanding organoalkoxysilanes were previously reported.[50]

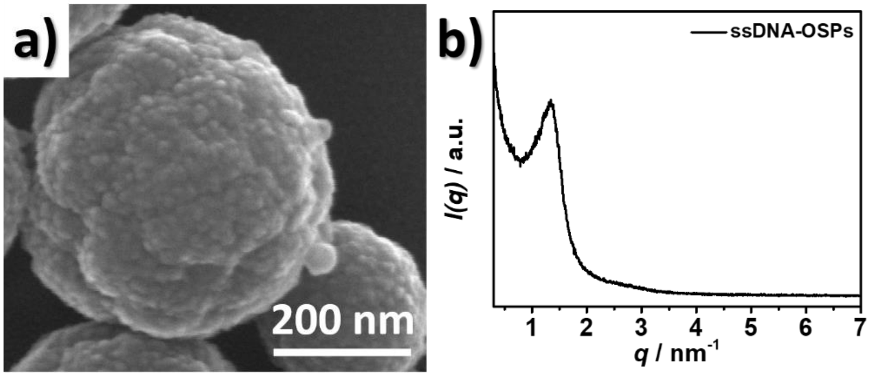

Figure 4. a) SEM image of **ssDNA-OSPs**. b) SAXS pattern obtained from **ssDNA-OSPs**.

The presence of the ssDNA moiety within the framework of **ssDNA-OSPs** was investigated by UV-Vis absorption spectroscopy, XPS analysis and ATR-FTIR spectroscopy. As depicted in Figure 5a, the UV-Vis absorption spectra of **ssDNA-OSPs** in H_2O showed a characteristic absorption band of compound **1** (Figure 5b) as indicated by the absorption band maxima centered at λ=260 nm and λ=550 nm, which can be attributed to purine and pyrimidine DNA nucleobases and the Cy3 moiety, respectively. The ATR-FTIR spectra indicated the presence of the organic functional group within **ssDNA-OSPs** (Figure 5c), showing the characteristic transmissions bands at 1474 cm^{-1} and 1649 cm^{-1}, both attributable to the presence of DNA.[51] The transmission bands occurring from 2848–2928 cm^{-1} can be attributed to C_{sp2}–H and C_{sp3}–H stretching vibrations of ssDNA and residual CTAB within **ssDNA-MSPs**. The survey XPS spectra recorded on **ssDNA-MSPs** indicated the presence of C(1s) and N(1s) signals at 285 and 403 eV, respectively (Figure 5d), confirming the presence of the organic functional group within **ssDNA-OSPs**. Although XPS analysis indicated the presence of residual CTAB within **ssDNA-OSPs**, ζ-potential measurements showed that the particles possessed an overall negative surface charge of -27±2 mV when dispersed in deionized water at pH=7.4. The latter result is important to exclude the possibility that the electrostatic interaction between positively charged particles and negatively charged DNA would result in false positive results when hybridization with a complementary ssDNA strand would be analyzed.

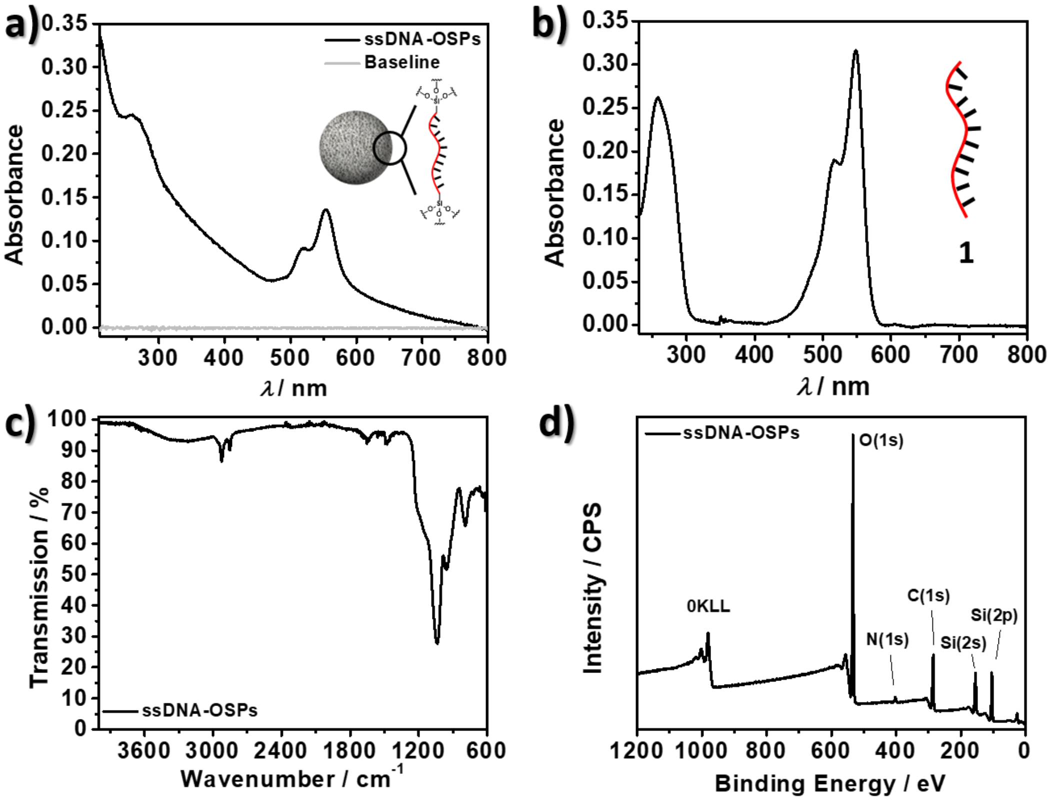

Figure 5. a) UV-Vis absorption spectra of **ssDNA-OSPs** in H_2O (c=0.02 mg·mL^{-1}). b) UV-Vis absorption spectra of **1** in H_2O (c=2.1 µM). c) ATR-FTIR spectra recorded on **ssDNA-OSPs**. d) XPS survey spectra recorded on **ssDNA-OSPs**.

The analysis of the HR-XPS scan of the C(1s), N(1s) and P(2p) core levels is shown in Figure 6. The deconvoluted HR scan for C (1s) peak (Figure 6a) shows the presence of three components C-1 (284.4 eV), C-2 (286.1 eV) and C-3 (287.5 eV) corresponding to C–C, C–O and C=O carbon species, respectively. The deconvoluted HR scan for the N(1s) peak (Figure 6b) shows the presence of three components N-1 at 399.7 eV, N-2 at 402.7 eV and N-3 at 405.9 eV. The component N-1 can be attributed to the nucleobase C–NH_2 and C=N-C species,[52] whereas the N-2 component can be attributed to residual CTAB within the particles.[53] The deconvoluted HR scan for the P(2p) peak (Figure 6c), indicates the presence of phosphorous at 133.2 eV, which can be explained by the presence of ssDNA in **ssDNA-OSPs**.

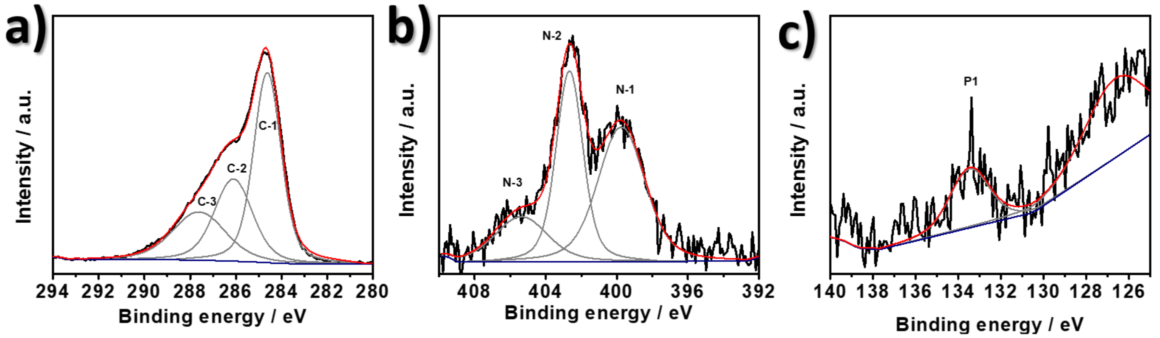

Figure 6. Deconvoluted XPS HR scan of C(1s) level recorded on **ssDNA-OSPs**. Deconvoluted XPS HR scan of N(1s) level recorded on **ssDNA-OSPs**. Deconvoluted XPS HR scan of P(2p) level recorded on **ssDNA-OSPs**

Once the presence of ssDNA within the particles structure was confirmed, the stimuli-responsive properties of **ssDNA-OSPs** upon the presence of external stimuli was investigated. First, the degradability of the particles structure upon activity of DNAse enzymes was investigated. A **ssDNA-OSPs** dispersion in Tris-buffer (c=0.04 mg·mL^{-1}, pH=7.6), DNase I enzyme was added to a particle dispersion and the particles were incubated for 1 h at 37 °C (see section 4.4.6.). DNase I enzymes are endonucleases able to hydrolyze single-stranded DNA oligonucleotides independently from the oligonucleotides sequence. The degradation of the particles was followed by SEM and DLS. As depicted in Figure 7, SEM images confirm the DNase-triggered degradation of **ssDNA-OSPs**, indicated by the loss of the initial particle morphology and the formation of small debris, most probable due to the particle disintegration. Particles that have been stirred in in the same conditions but in the absence of the enzyme did not indicated the formation of small degradation debris, confirming the role of the enzyme in the particle degradation. Degradation experiments suggested that the particles were composed of smaller silica particles (Figure 7b, SEM image with DNase). It can be therefore hypothesized that the ssDNA-silane would bridge the small spherical objects within **ssDNA-OSPs** and when hydrolyzed in the presence of DNase, the structure subsequently breaks apart and forms small debris.

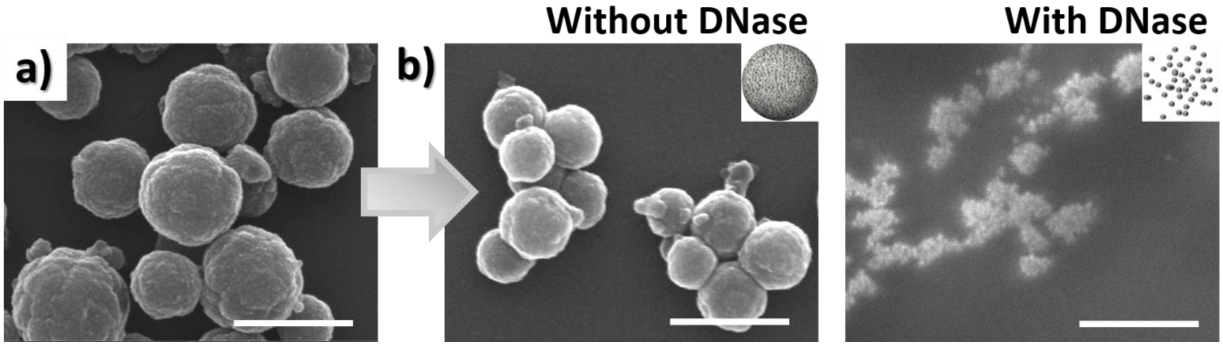

Figure 7. Degradation study via SEM of **ssDNA-OSPs** in the presence or absence of DNase I. a) SEM image of ssDNA-MSPs at t_0. b) SEM images of **ssDNA-OSPs** after 1 h without in the absence of DNase (left) or after being incubated 1 h with DNase I (right). Scale bars=500 nm.

Additional confirmation of the particle degradation upon enzymatic activity was obtained by DLS. As shown in Figure 8a, the hydrodynamic diameter of **ssDNS-OSPs** incubated with DNase for 1 h in Tris-buffer solution (see section 4.4.6) decreased significantly, while in the absence of DNase, no drastic particle degradation was observed. DLS analysis on **ssDNA-OSPs** showed that when the particles were stirred at 37 °C for 1 h in the absence of DNase, only a relatively small decrease of the hydrodynamic diameter was observed, most probably due to slow silica dissolution in the buffer at this temperature (Figure 8b).

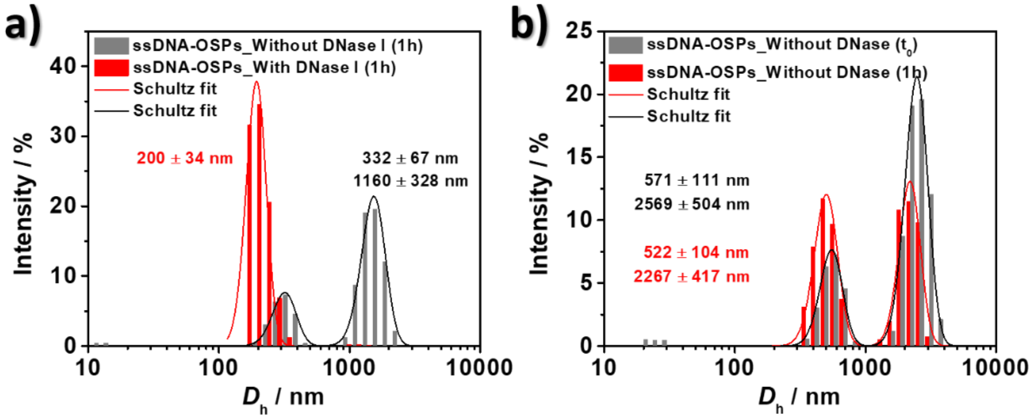

Figure 8. a) DLS intensity size distributions of **ssDNA-OSPs** in Tris buffer (pH=7.6) that have been stirred for 1 h with and without DNase. b) DLS intensity size distributions of **ssDNA-OSPs** at t_0 and that have been stirred for 1 h in the absence of DNase.

Next, **ssDNA-OSPs** were investigated regarding their ability to hybridize complementary ssDNA oligonucleotides by Förster resonance energy transfer (FRET) experiments (see section 4.4.7.). To this purpose, compound **3**, a Cy5-labeled ssDNA strand that can hybridize with the DNA in **ssDNA-OSPs** was synthesized (see section 4.4.2.). Cy3- and Cy5-labeled strands were chosen due to the partial spectral overlap of the Cy3 emission with the Cy5 absorption spectra, a necessary requirement for FRET to occur (Figure 9b), beside the need of close approximation of the FRET pair in space (max ca. 10 nm). As depicted in Figure 9a, only hybridized DNA strands can transfer the energy from the excited state of Cy3 in **ssDNA-OSPs** (FRET donor) to the Cy5 of **3** (FRET acceptor), resulting the quenching of Cy3 and sensitized emission from Cy5. FRET experiments were performed by adding different amounts of **3** to dispersions of **ssDNA-OSPs** ($c_{\textbf{ssDNA-OSPs}}$=0.96 µg·mL^{-1} in PBS containing Mg^{2+}) while monitoring the FRET process by exciting the donor moiety at λ_{ex}=520 nm while recording the emission spectra of the donor and acceptor moieties (see experimental section). As depicted in Figure 9c, upon the addition of **3** to the particle dispersion a concentration dependent quenched emission of the donor, while a sensitized emission of the acceptor was recorded, confirming therefore the occurrence of the FRET process due to DNA hybridization. Therefore, FRET experiments confirmed that **ssDNA-OSPs** possessed accessible ssDNA sites, which were recognized by complementary ssDNA strands, showing the particles ability to recognize other biomolecules through supramolecular interactions.

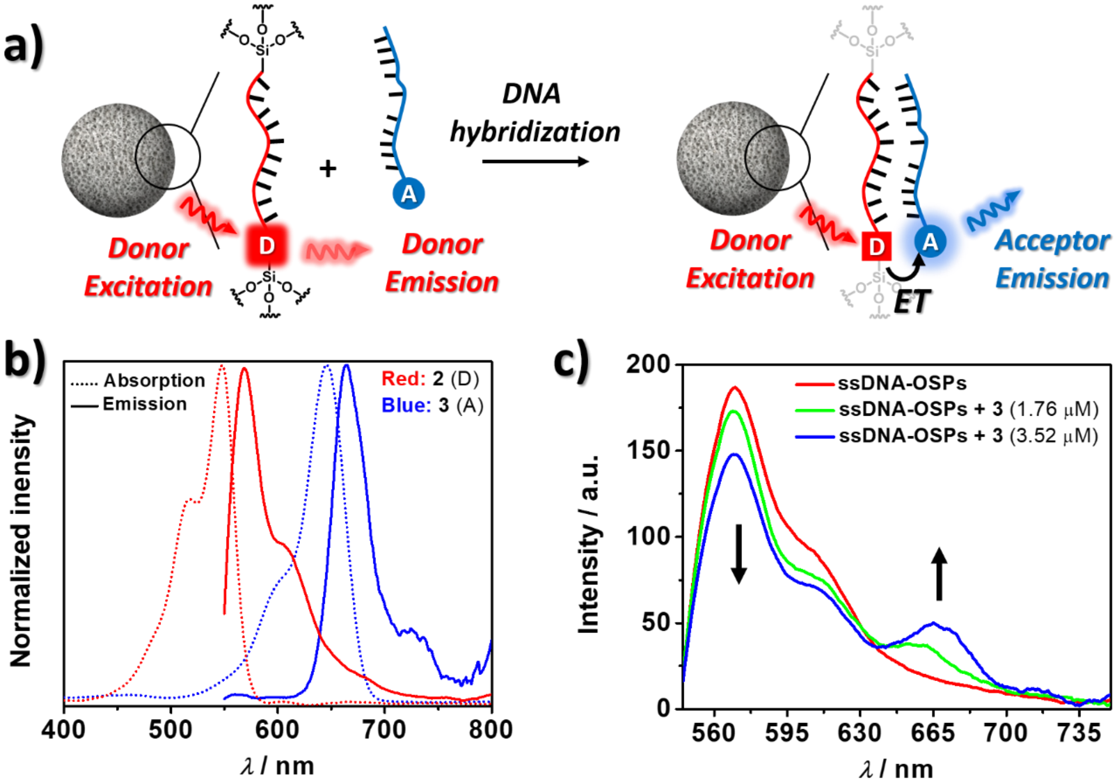

Figure 9. a) Schematic representation of the FRET process occurring upon hybridization of Cy3 (donor) and Cy5 (acceptor) labeled DNA strands. b) Normalized absorption and emission spectra of **1** and **3** in PBS; λ_{ex}(**1**)=520 nm and λ_{ex}(**3**)=650 nm. c) FRET experiment with **ssDNA-OSPs** ($c_{\mathbf{ssDNA\text{-}OSPs}}$=0.96 µg·mL^{-1}) and various concentrations of **3** (1.76 µM and 3.52 µM).

As previously mentioned, electron microscopy images of **ssDNA-OSPs** suggested that the presence of the DNA during the particles synthesis alters the formation pathway of the particles. The altered final morphology of **ssDNA-OSPs**, compared to model MSPs obtained with the same protocol, could be explained by the highly negatively charged DNA that strongly interacts with other charged species in during the Stöber synthesis protocol, while the role of the DNA length was confirmed to impact particle porosity. To prepare oligonucleotide-bridged organosilica particles with a uniform size distribution, the use of uncharged single-strand peptide nucleic acid (ssPNA) was investigated. ssPNA possess the same nucleobases as DNA, however the strand backbone is not composed of phosphodiester groups but instead of uncharged repeating N-(2-aminoethyl)-glycine units linked by peptide bonds. In order to prepare ssPNA-bridged organosilica particles (**ssPNA-OSPs**), a diamino and carboxytetramethylrhodamine (TAMRA) modified ssPNA (**4**) was provided by the group of Prof. Corradini (University of Parma). The bis-alkoxysilane ssPNA derivative **5** was obtained upon the reaction of the diamino-modified ssPNA strand **4** with 2.1 eq. of ICPTES in the presence of the base TEA (Scheme 2, see section 4.4.3.).

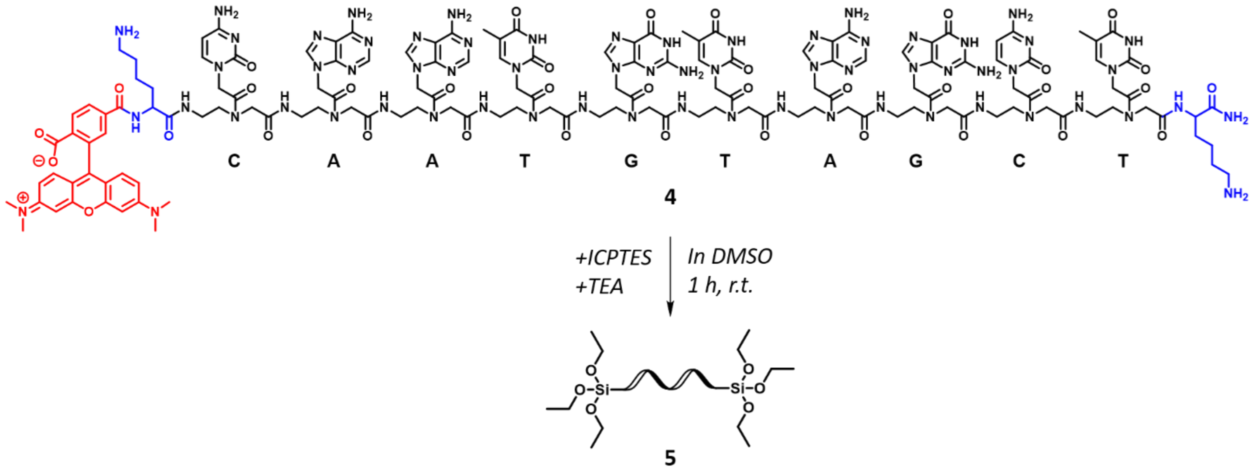

Scheme 2. Reaction scheme for the preparation of ssPNA alkoxysilane derivative **5**.

ssPNA-OSPs were prepared by hydrolysis and condensation of compound **5** with TEOS (**5**/TEOS 0.007:1 molar ratio) in the presence of the surfactant CTAB and by using aqueous ammonia as the base. The particles were collected by centrifugation and the surfactant was removed upon extraction in EtOH heated to reflux for 24 h (see section 4.4.5.). As depicted in Figure 10, SEM images of **ssPNA-OSPs** showed that spherical particles with an average diameter of 102±27 nm were obtained and were smaller than **ssDNA-OSPs**. The size distribution calculated from SEM images revealed the presence of two distributions of sizes close to each other (Figure 10c). Furthermore, SEM pictures of **ssPNA-OSPs** show that the particle surface still possessed smaller uneven silica structures, indicating that the presence of oligonucleotides, independently from their charge density, alters the formation mechanism when compared to the model synthesis (MSPs). Upon the use of a PNA, the particles morphology was exclusively spherical and less unordered smaller particles were observed when compared to the synthesis of **ssDNA-OSPs**, indicating that the use of a uncharged PNA oligonucleotide favors the formation of regular spherical particles.

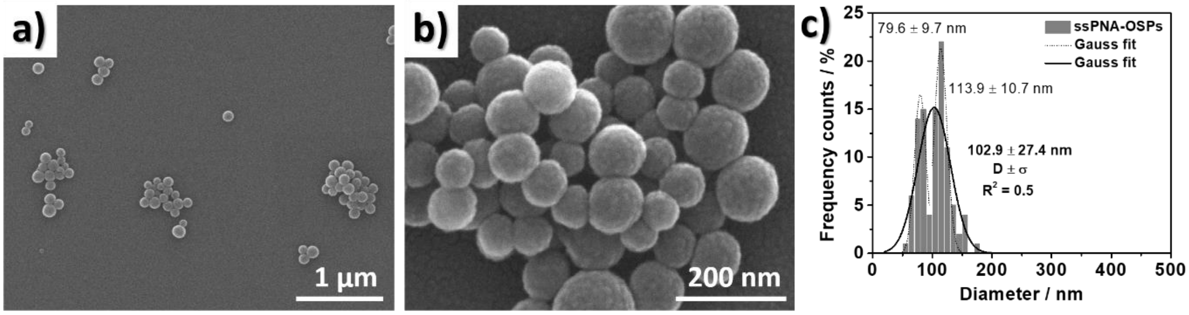

Figure 10. a) and b) SEM images of **ssPNA-OSPs**. c) Size distribution of **ssPNA-OSPs** calculated from SEM images.

4.2.2. Supramolecular assembled organoalkoxysilanes and their use for the preparation of organosilicas

4.2.2.1. PNA-based and supramolecularly assembled organoalkoxysilanes for the preparation of organosilicas

As mentioned in the introduction, the use of complementary ssPNA oligonucleotides to prepare supramolecular assemblies of bis-organoalkoxysilanes has been envisioned to produce novel hybrid bonding polymers (HBPs). The 10-mer ssPNA strands (**F-PNA** and **T-PNA**) used were designed to be complementary and to hybridize easily at room temperature in organic solvents, such as DMSO (Figure 11). The use of a 10-mer ssPNA was selected because it can form a helical structure already at rom temperatures, similar to that of DNA.[54]

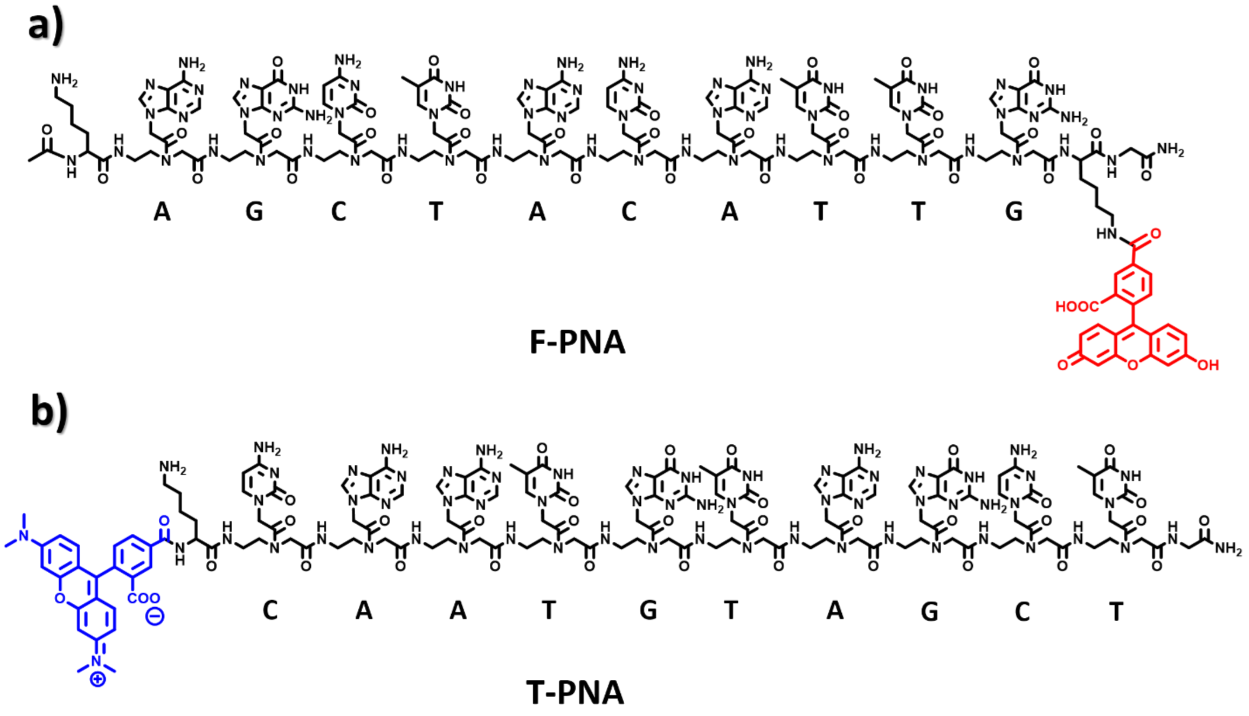

Figure 11. a) Structure of the 5-carboxyfluorescein labelled **F-PNA** strand. b) Structure of the carboxytetramethylrhodamine labelled **T-PNA**.

The ability of PNA strands to self-assemble was followed by FRET, since the 5-carboxyfluorescein-labeled PNA strand (**F-PNA)** and the 5-carboxytetramethylrhodamine-labeled PNA strand (**T-PNA)** possess an appropriate FRET donor–acceptor pair (5-carboxyfluorescein in **F-PNA**=FRET-donor and 5-carboxytetramethylrhodamine in **T-PNA**=FRET-acceptor). Experiments were first performed in aqueous mixtures containing a constant amount of **F-PNA** (c=1.14 µM) and variable amounts of **T-PNA**. As depicted in Figure 12a, upon hybridization of both PNAs, the FRET donor (**F-PNA**) was quenched (λ_{ex}=450 nm) by the FRET acceptor (**T-PNA**), resulting in the observation of acceptor emission at $\lambda_{em,T\text{-}PNA}$=600 nm. As depicted in Figure 12b, hybridization of the PNA strands occurred based on the observed quenching of the **F-PNA** emission concomitant with observation of **T-PNA** emission. The hybridization was proven with the PNA strands lacking alkoxysilane moieties, since these would hydrolyze in aqueous solutions, leading to unwanted precipitation. Neverthanless, the presence of the organosilane group at a later stage won´t affect the hybridization process, since the alkoxysilane group is located in positions where the nucleobases are and it has been previously shown that DNA amphiphiles, which possess even larger strand modifications can still hybridize.[55,56]

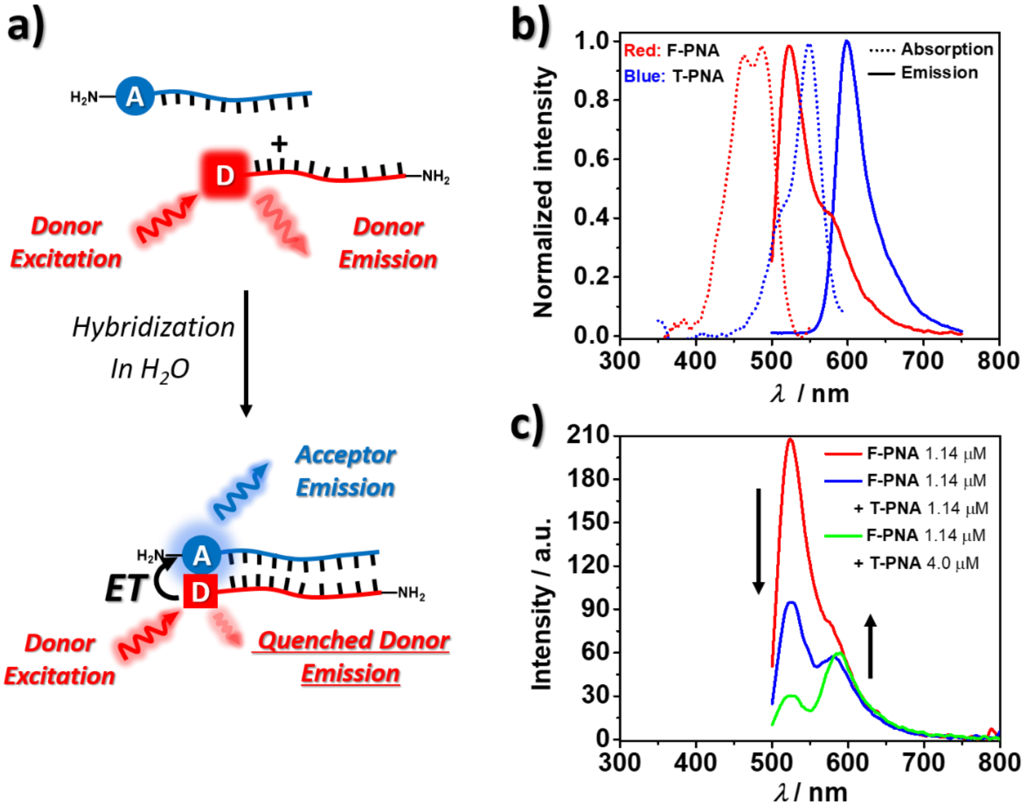

Figure 12. a) Schematic representation of the occurring FRET process. Only in the hybridized assembly the excited FRET donor can transfer its energy to the FRET acceptor, resulting in the acceptors sensitized emission, while a quenched emission for the FRET donor is observed. b) Normalized absorption and emission spectra of **F-PNA** (λ_{ex}=450 nm) and **T-PNA** (λ_{ex}=550 nm) in water. c) FRET experiments performed on a mixture of **F-PNA** (c=1.14 µM) in the presence of **T-PNA** in water at two different concentrations (c=1.14 and 4.0 µM) upon excitation at λ_{ex}=450 nm.

Having assessed the ability of the PNA strands to self-assemble, their alkoxysilane derivatives were prepared. To this purpose, **F-PNA** and **T-PNA** were allowed to react with 1.1 eq. of (triethoxysilyl)propyl isocyanate (ICPTES) in the presence of the base triethylamine, leading to the formation of the **F-PNA** and **T-PNA** monoalkoxysilane derivatives (**F-PNA-Si** and **T-PNA-Si**; Figure 13, see section 4.4.3.). Subsequently, both strands were mixed, resulting in the formation of the supramolecular PNA bis-alkoxysilane (**Supra-PNA-Si**; Figure 13).

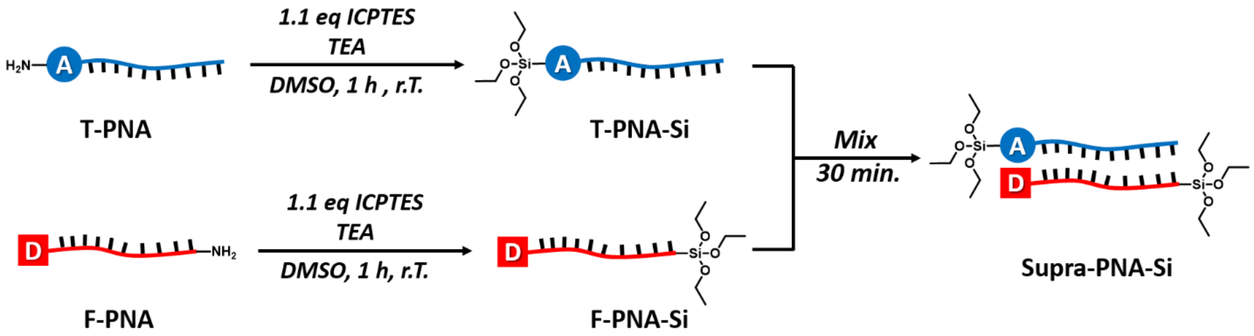

Figure 13. Schematic representation in the synthesis of alkoxysilane functionalized PNAs and their self-assembly leading to the formation of **Supra-PNA-Si**.

The **Supra-PNA-Si** was used for the preparation of organosilica particles, with or without the presence of the additional silica source tetraethyl orthosilicate (TEOS), upon its base-catalyzed hydrolysis and polycondensation in an H_2O/EtOH (1:0.3, *v/v* mixture), leading to the formation of organosilica particles **Supra-OSPs** (Figure 14, see section 4.4.5. for preparation details).

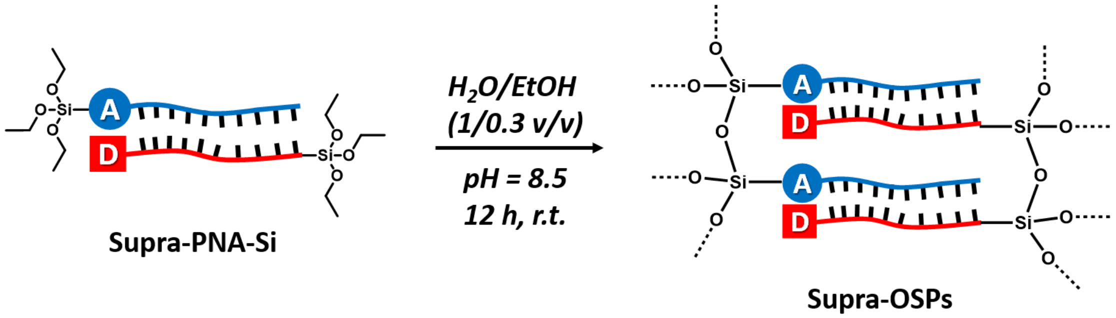

Figure 14. Schematic representation of the preparation of **Supra-OSPs**.

The morphological evolution during the formation of **Supra-PNA-Si** in the absence of an additional silica source was monitored via electron microscopy analysis by taking aliquots of the crude reaction mixture at 2 different time intervals. SEM images of the crude reaction at 3 h (Figure 15a and b) indicate the presence of silica structures, which appeared to be composed of smaller grain-like structures (Figure 15 b). The formation of grain-like particles may be explained by the structure of the **Supra-PNA-Si** itself, which can form a linear helical assembly,[54] thus representing an elongated hydrolysable alkoxysilane. Therefore, the formation of the structures observed in Figure 15 could be explained by the polymerization of **Supra-PNA-Si**, the subsequent formation of smaller grain-like structures which then assemble to form the final µm-sized structures through hydrolysis and condensation of uncondensed silanol groups (Figure 15c). The yield of these structures observed at 3 h of reaction time was low (less than 1 mg) and no quantitative amounts of the particles were recovered by centrifugation.

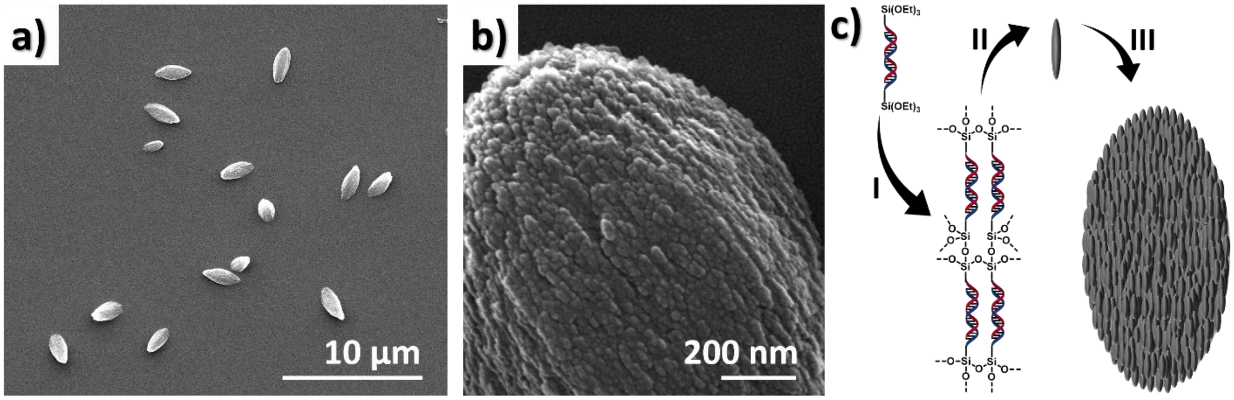

Figure 15. a) SEM images and b) SEM images taken at higher magnification of an aliquot taken from the reaction crude for the preparation of organosilica after 3 h of reaction time. c) Hypothesized formation mechanism of observed rice-grain-like structures observed; I) Hydrolysis and polycondensation of **Supra-PNA-Si** helix occurs; II) upon further condensation the organosilane may form sub-µm sized particles, which due to the presence of uncondensed silanol groups could further assemble to form III) µm sized grain-like structures.

After 12 h of reaction time, no grain-like structures were observed in the crude reaction mixture via SEM. Instead, a precipitate formed in the reaction mixture, which was collected via centrifugation and further washed through dispersion–centrifugation cycles in EtOH, yielding supramolecularly bridged organosilica particles (**Supra-OSPs**). Electron microscopy images of **Supra-OSPs** (Figure 16a and b) revealed the presence of smaller, sub-µm sized particulate. The absence of previously observed grain-like structures could be explained due to their instability over 12 h of reaction time. The instability of grain-like particles could derive from an incomplete condensation of the alkoxysilane groups of **Supra-PNA-Si**, leading to the formation of metastable structures, which due to prolonged exposure to water may further depolymerize and condense to form new and more stable organosilicas. Incomplete condensation degrees in organosilicas can be explained by the fact that hydrolysis and condensation rates of organosilanes are structure dependent, experiencing inductive and steric effects from the substituents.[57] In **Supra-PNA-Si** the Si-atoms possess one alkyl substituent, having a positive inductive effect on the Si atom. Therefore, the alkyl group in **Supra-PNA-Si** renders the Si atom less electrophilic compared to tetra alkoxy silanes, resulting in decreased hydrolysis rates and condensation degrees in basic solutions. The small particles observed for **Supra-OSPs** are hypothesized to represent degradation debris derived from previously formed grain-like structures. In this case, the formation of grain structures would represent a metastable morphology observed for **Supra-OSPs**.

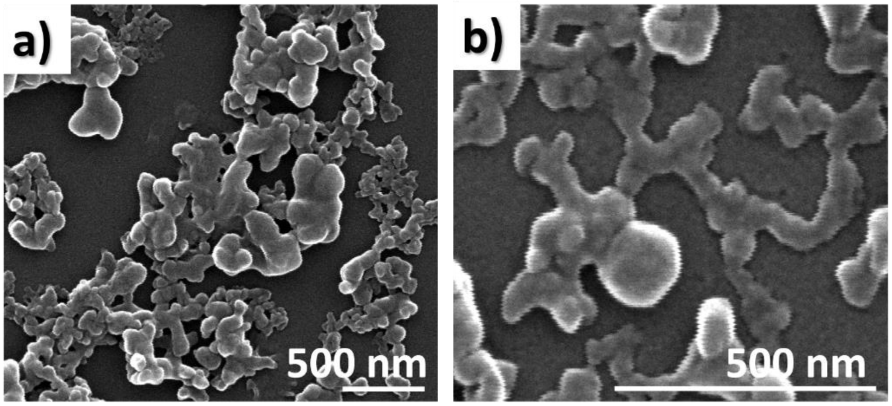

Figure 16. a) and b) SEM images recorded on **Supra-OSPs** after 12 h of reaction time.

To further investigate whether the particles degrade upon prolonged reaction time and to test the possibility to stabilize the grain-like structure of particles which were observed in the supernatant at 3 h of reaction time, hydrolysis and condensation of **Supra-PNA-Si** in the presence of an equimolar amount of tetraethyl orthosilicate (TEOS) was performed. A secondary silica source would increase the amount of highly condensed inorganic -Si–O–Si- bonds in the resulting organosilica, thus yielding more stable rice-grain-like structures. To follow the structural evolution of organosilica particles formed in the presence of TEOS, aliquots of the reaction mixture were analyzed at different time intervals by SEM. When TEOS was co-condensed to

Supra-PNA-Si, the presence of several µm-long fiber-like structures were observed after 1 h (Figure 17a,b and c), and they continued to grow when the reaction was allowed to proceed for 3 h (Figure 17d,e). Also in this case, the fibers were primarily composed of smaller, sub-µm structures, suggesting a similar formation pathway as it was previously hypothesized for the formation of rice-grain-like structures (Figure 15c). SEM images recorded on an aliquot of the crude reaction at 12 h indicated the absence of fibrous particles. Instead, the presence of smaller spherical-like particulate was imaged, suggesting again the instability of these fiber-like structures over prolonged reaction times (Figure 17f). Indeed, some of the very few remaining fiber-like structures present after 12 h confirmed the hypothesis of the material degradation. As depicted in Figure 18, these remaining fibers showed strong fragmentation and degradation, leading to the formation of sub-µm sized degradation products, which could be imaged (Figure 18). Therefore, the preparation of more resistant fiber-like structures by co-condensation of an equimolar amount of TEOS and **Supra-PNA-Si**, was not effective. In conclusion, co-condensation of an equimolar amounts of TEOS and **Supra-PNA-Si** did not increased the stability of fiber-like structures, suggesting that increasing the number of -Si–O–Si- bonds alone is not sufficient to obtain stable fibrous structures. Ultimately, the degradation of the organosilica materials could be explained by the dissolution of silicates in aqueous basic media, considering that no positively charged surfactants, which are known to stabilize the silicates through electrostatic interactions against hydrolysis,[58] were used for the preparation of **Supra-PNA-Si**. Future experiments will investigate the formation of organosilica particles from **Supra-PNA-Si** in the presence of the surfactant CTAB.

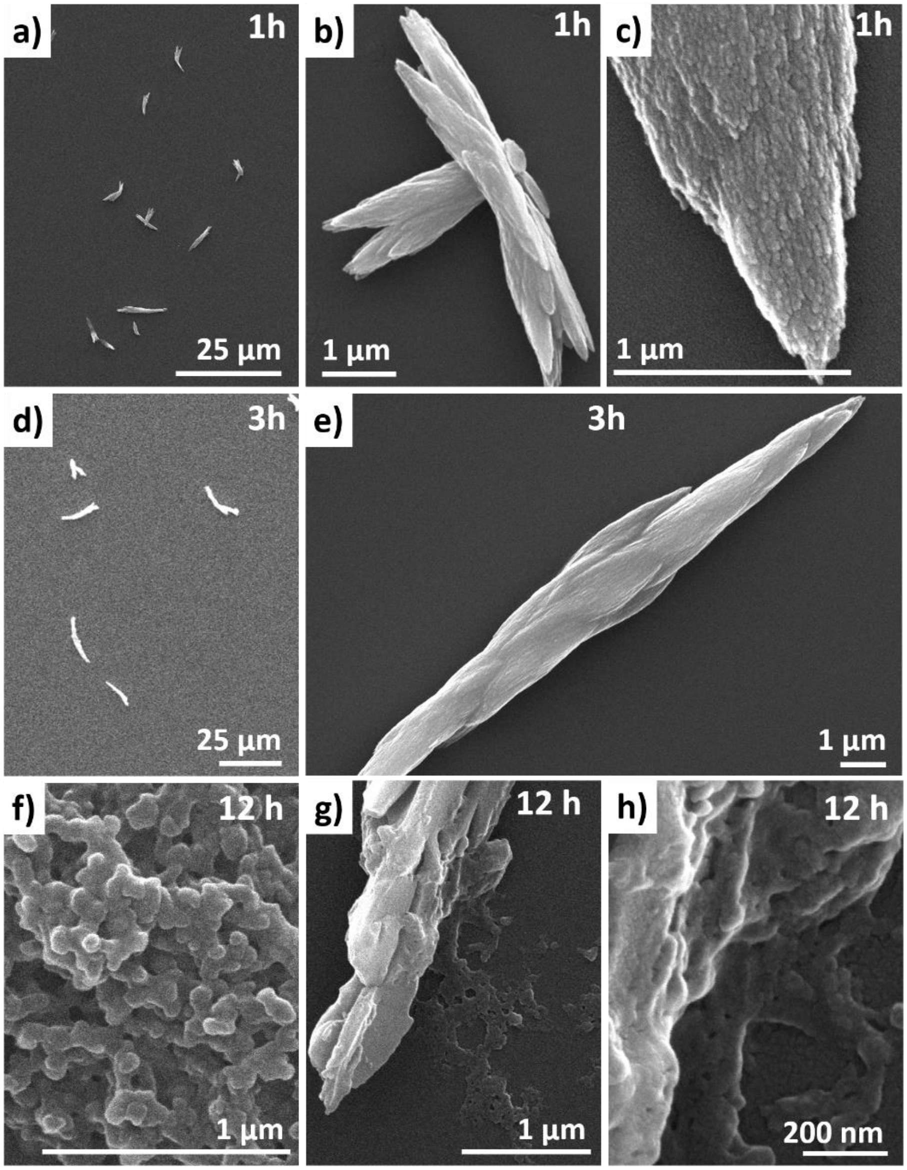

Figure 17. SEM images taken at different times on aliquots collected from reaction mixtures in which **Supra-PNA-Si** was co-condensed with TEOS. a-c) SEM images taken after 1 h of reaction time in which the formation of fiber-like structures was observed. d-e) SEM images recorded after 3 h of reaction time in which the grow of fiber-like structures was observed. f-h) SEM images recorded after 12 h of reaction time in which the formation of sub-µm sized spherical particulate was observed and the degradation of fiber-like structures was imaged as shown in panels g and h.

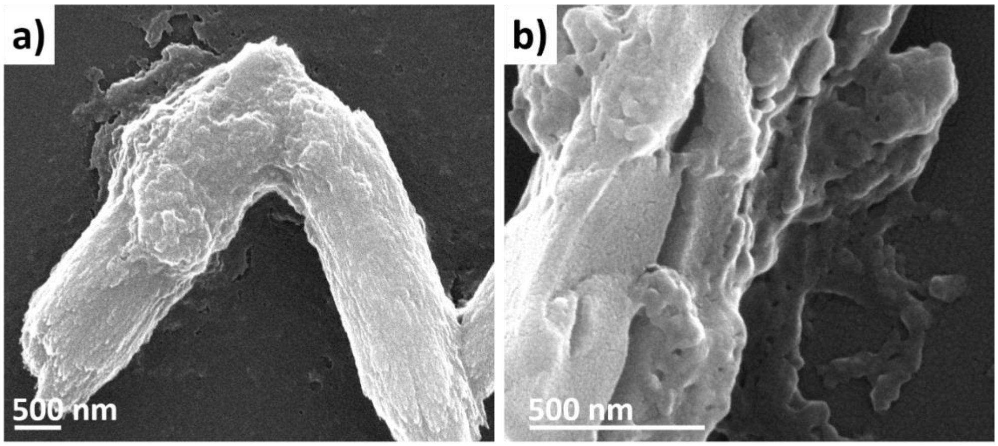

Figure 18. a) SEM image of degrading fibers observed at 3 h of reaction time. b) SEM image of degrading fiber at 12 h of reaction time.

The obtained precipitate of **Supra-OSPs** was further investigated by UV-Vis absorption and ATR-FIR spectroscopies to assess the presence of the supramolecular PNA moiety. The UV-Vis absorption spectra of a dispersion of **Supra-OSPs** (Figure 19a) in water (c=0.075 mg·mL^{-1}) showed the presence of the characteristic absorption bands centered at 270 nm, 470 nm and 510 nm, reflecting the presence of the PNA´s aromatic nucleobases and the PNA´s fluorescent labels (fluorescein and rhodamine), respectively. ATR-FTIR spectra recorded on **Supra-OSPs** (Figure 19b) showed the successful condensation of the alkoxysilane functional groups of **Supra-PNA-Si**, forming new siloxane bonds (-Si–O–Si-), as reflected by the transmission band at 1010 cm^{-1}. The presence of PNA was confirmed by the transmission bands at 1330 cm^{-1}, 1653 cm^{-1} and 1548 cm^{-1}, corresponding to the nucleobase =C–N- stretching vibration, the amide I and amide II bands, respectively. The broad transmission band observed from 2880 to 3650 cm^{-1} was ascribed to the presence of C_{sp2}–H, C_{sp3}–H and N–H stretching vibrations.

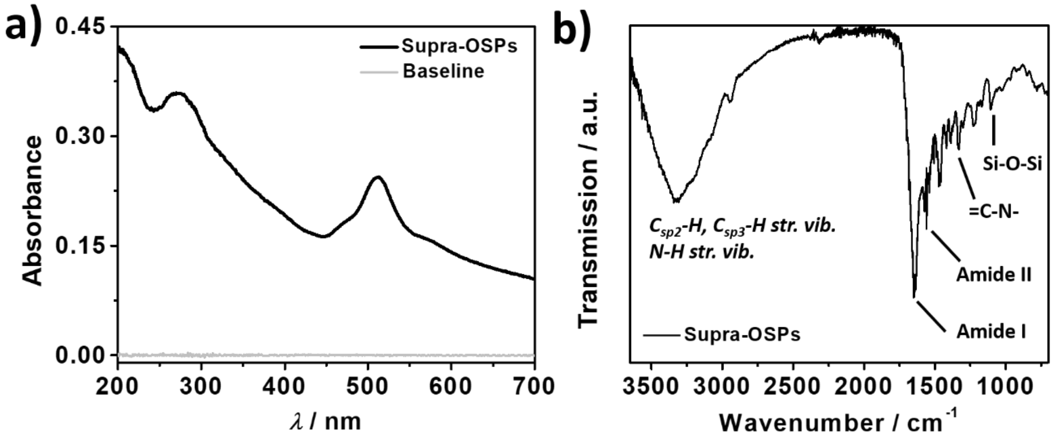

Figure 19. a) UV-Vis absorption spectra recorded on a **Supra-OSPs** dispersion in water (c=0.075 mg·mL^{-1}). b) ATR-FTIR spectra recorded on **Supra-OSPs**.

Next, the presence of the supramolecular PNA-bridge within **Supra-OSPs** was investigated via FRET analysis (Figure 20, see experimental section). A **Supra-OSPs** particle dispersion (c=0.008 mg·mL^{-1}) in PBS (pH=5.8) was excited at 450 nm and the photoluminescence was recorded. As depicted in Figure 20c, excitation of the FRET-donor moiety at λ_{ex}=450 nm (F-PNA moiety) saw the quenching of the donor emission ($\lambda_{em,F\text{-}PNA}$=517 nm), while emission from the FRET-acceptor (T-PNA moiety) $\lambda_{em,T\text{-}PNA}$=590 nm was observed, indicating the PNAs hybridization within **Supra-OSPs**. In addition, the possibility to dissociate the PNA hybridization within **Supra-OSPs** upon heating was also investigated by FRET-analysis. As depicted in Figure 20a, elevated temperatures can disrupt the supramolecular interactions between PNA strands in **Supra-OSPs**, and consequently disrupt FRET. A **Supra-OSPs** dispersion was heated at 60°C for 10 min and the particle dispersion was subsequently excited with light of 450 nm while monitoring the emission. As depicted in Figure 20d, heating was found to interrupt FRET between the donor and acceptor moieties, as indicated by the increased emission intensity observed for the donor strand (F-PNA). These experiments indicate that upon hydrolysis and condensation of **Supra-PNA-Si**, organosilica particles are formed that possess hybridized PNAs as bridging groups within their framework, which can be dissociated upon the presence of an external stimulus, for example, heat.

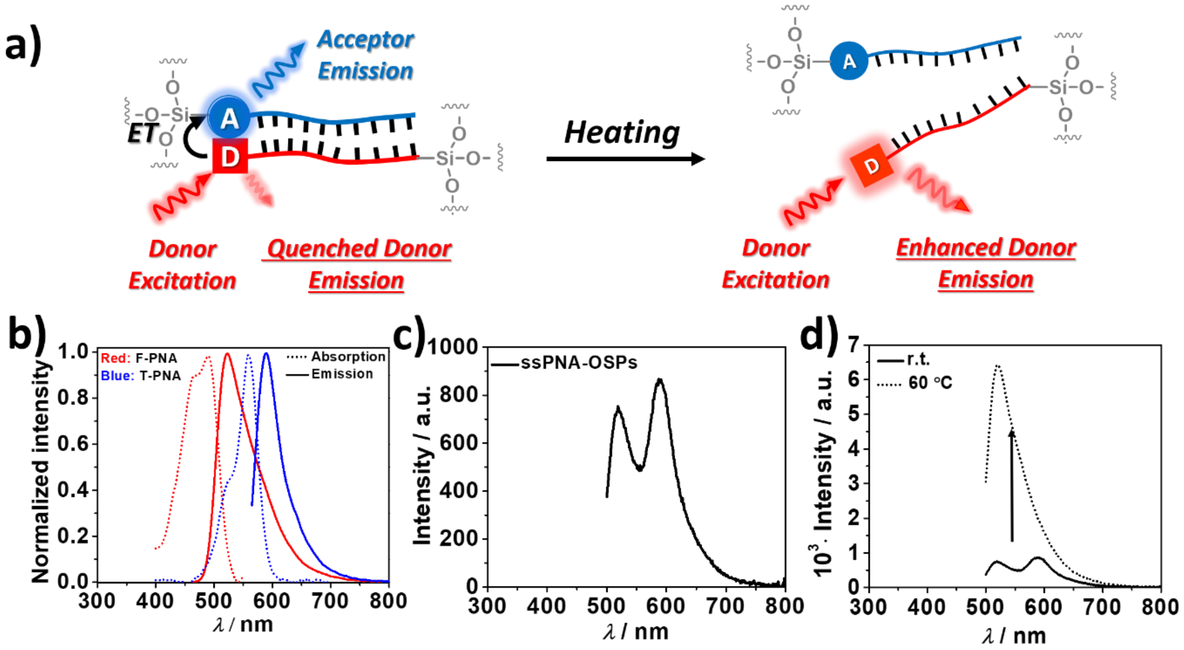

Figure 20. a) Schematic representation in the disruption of the FRET process upon heating a dispersion of **Supra-OSPs** due to PNA strand dissociation. b) Normalized absorption and emission spectra of F- and T-PNA strands in PBS buffer at pH=5.8. c) FRET experiment of on a dispersion of **Supra-OSPs** (c=0.008 mg·mL^{-1}) in PBS (pH=5.8) upon excitation at λ_{ex}=450 nm. d) Temperature dependent FRET experiments on dispersion of **Supra-OSPs** (c=0.008 mg·mL^{-1}) in PBS (pH=5.8) upon excitation at λ_{ex}=450 nm.

4.2.2.2. Organosilicas prepared through hybrid DNA–PNA supramolecular interactions

The successful preparation of PNA-based organosilicas prompted the preparation of stimuli-responsive organosilicas. Therefore, the possibility to use the self-assembly of a PNA-DNA-PNA assembly as stimuli-responsive bridging group for the preparation of organosilica particles has been investigated. The choice to combine of DNA and PNA interactions was due to the fact that the DNA moiety allows for precise interaction, depending on the DNA base-sequence, with biomolecules. As depicted in Figure 21, a supramolecular PNA-DNA-PNA bis-alkoxysilane **Supra-PDP-Si** is obtained by mixing of two single-stranded PNA-alkoxysilanes (**PNA-Si1** and **PNA-Si2**), which were designed to be complementary to 10-mer regions at the 5´and 3´end of a 45-mer single-stranded DNA (**ssDNA**). The 45-mer ssDNA was designed not only to hybridize with PNA-silanes, but also to possess an ATP binding sequence, as reported by Ricci and coworkers.[13] For this purpose the group of Prof. Ricci provided us the ATP-responsive ATP aptamer.

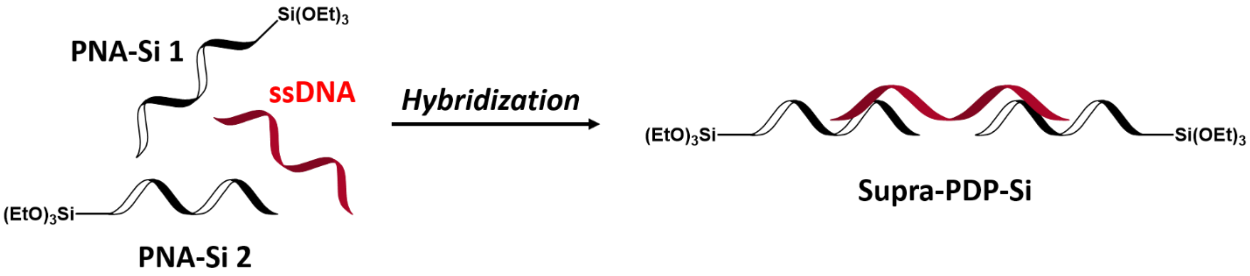

Figure 21. Schematic representation in the use of PNA-silanes, which bind to the ends of ssDNA to form the supramolecular assembly bis-organoalkoxysilane **Supra-PDP-Si**.

To prepare **Supra-PDP-Si**, the amino bearing PNA-strands were functionalized with ICPTES in the presence of the base TEA, forming their mono alkoxysilane derivatives (**PNA-S 1** and **PNA-Si 2**, see section 4.4.3.). Subsequently, an equimolar amount of **PNA-Si 1**, **PNA-Si 2** and **ssDNA** (see section 4.4.5 for its structure) were mixed to promote their hybridization, forming **Supra-PDP-Si**. Subsequent base-catalyzed hydrolysis and condensation of **Supra-PDP-Si** with and without the secondary silica source TEOS, in the presence of the surfactant CTAB was investigated in a H_2O/EtOH mixture (see section 4.4.5.). To follow the formation of organosilica particles, electron microscopy images were taken on aliquots of the reaction crude at different time intervals. Recorded SEM images of the reaction mixtures at 1 h, 3 h and 12 h of reaction time in the absence of TEOS are shown in Figure 22a–c. As depicted in Figure 22a, after 1 h sub-µm fiber-like structures (encircled in black) were observed, which further grew after 3 h of reaction time to form big fibrous structures, most probably due to a delayed hydrolysis and condensation of the bulky organoalkoxysilanes. After 12 h of reaction time, the fibrous structures started to degrade into smaller fibrous structures, most probably due to instability of the supramolecular interactions of the PNA-DNA-PNA supramolecular bridging groups. When organosilicas were prepared from **Supra-PDP-Si** with an equimolar amount of TEOS (Figure 22d–f), no fibrous structures could be imaged after 1 h of reaction time. After 3 h large fibrous structures were observed (Figure 22e), and stable fibrous structures were still observed at 12 h of reaction time (Figure 22f). The increased stability of the fibrous organosilica structures may be explained by co-condensation of TEOS to **Supra-PDP-Si** and the presence of CTAB, which stabilized the silicates in aqueous environments against depolymerization.

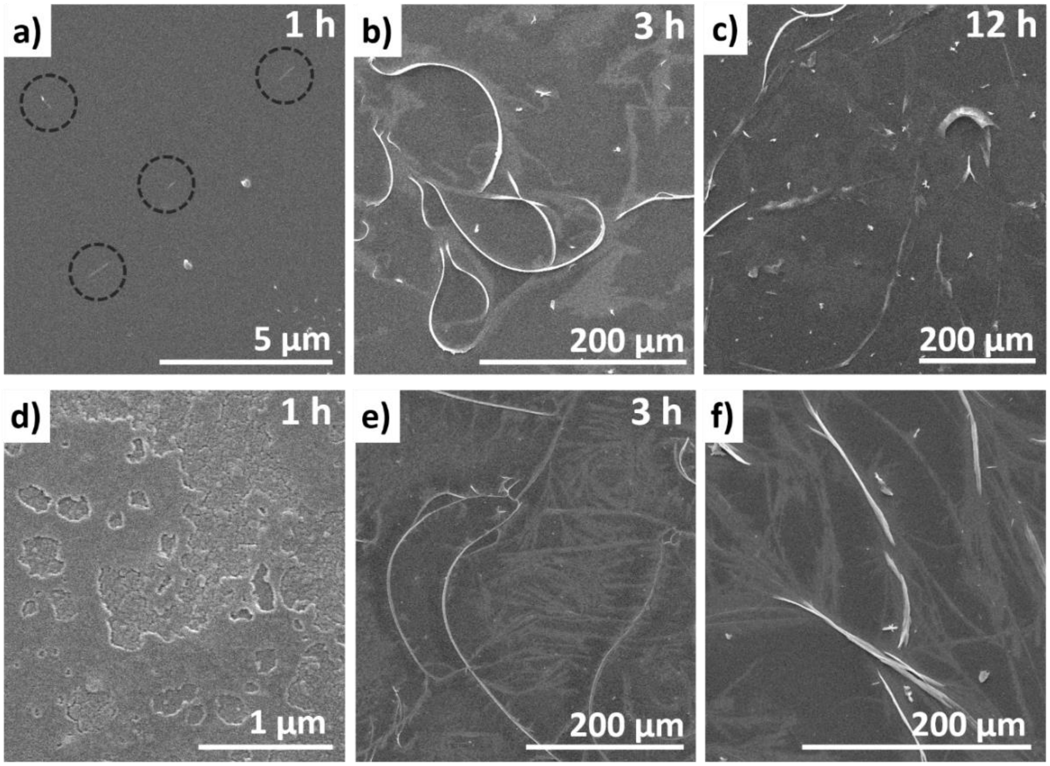

Figure 22. SEM images of the crude reaction mixtures for the formation of organosilicas from **Supra-PDP-Si**. a-c) SEM images of the reaction crude at different time intervals when no additional silica source was added in the hydrolysis and condensation reaction of **Supra-PDP-Si**. d-f) SEM images of the reaction crude at different time intervals when an equimolar amount of TEOS was added to the reaction.

The structure of fibers obtained from the polymerization reactions in which solely **Supra-PDP-Si** was used, varied from the fibers obtained when **Supra-PDP-Si** was polymerized in the presence of TEOS. Fibrous structures obtained from the polymerization of only **Supra-PDP-Si** at 3 h when possess rather smooth surfaces (Figure 23a), while the fibers obtained by co-condensing TEOS appeared to possess more layered internal structure (Figure 23b).

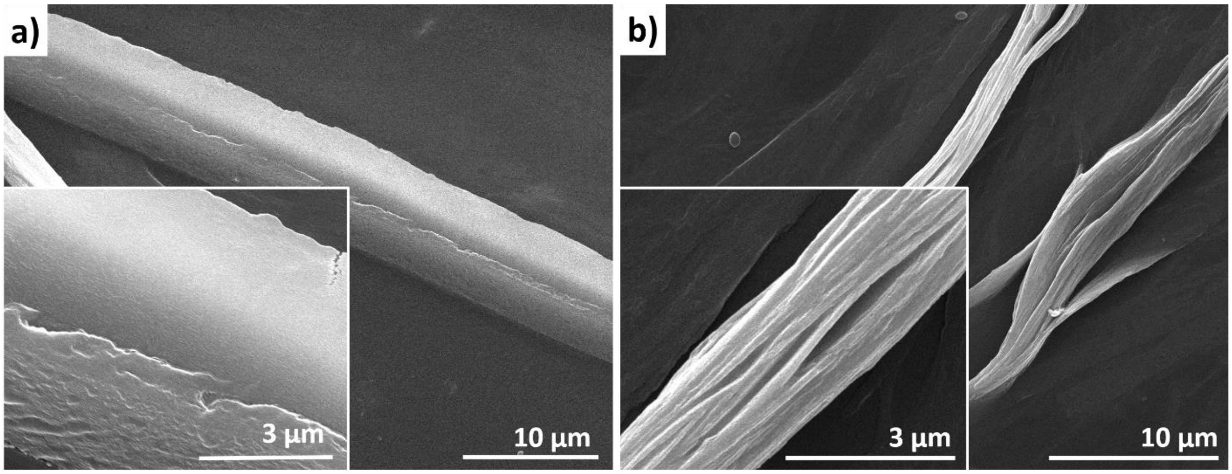

Figure X. a) SEM images of fibers obtained upon hydrolysis and condensation of **Supra-PDP-Si** after 2 h. b) SEM images of fibers obtained upon hydrolysis and condensation of **Supra-PDP-Si** with TEOS after 2 h.

The results obtained for the use of **Supra-PDP-Si** to prepare organosilicas are preliminary and future experiments will focus the thoroughly characterization of **Supra-PDP-Si.** Although these preliminary results show the presence of fiber/like structures, their composition must be further investigated to confirm their organosilica-based nature. Future experiments will investigate the stimuli-responsive behavior of the obtained fibers when ATP is present, since the DNA behaves as an ATP-aptamer, yielding to disassembly of the particles.

4.3. Conclusions

In this chapter, the possibility to use DNA and PNA-based building blocks to prepare stimuli-responsive organosilica particles was investigated. The synthesis of DNA and PNA organo bis-alkoxysilanes and their subsequent use to prepare organo-bridged silica particles was reported. DNA-bridged organosilica particles were prepared that possessed the ability to recognize complementary DNA molecules and to degrade in the presence of specific enzymes, such as hydrolyses. The advantage of using PNA bis-alkoxysilanes lies in the formation of more uniform particles. Moreover, the possibility to self-assemble complementary PNA alkoxysilanes to form a supramolecular PNA-based organo bis-alkoxysilane to be used for the preparation of hybridbonded polymers was shown. The successful integration of supramolecular bonds within a rigid silica-based structure was successfully proven via Förster resonance energy transfer experiments, showing the feasibility to prepare organosilicas possessing supramolecular bonds within their structure. Finally, the use of a PNA-DNA-PNA based organoalkoxysilane, held together by supramolecular interactions, to prepare organosilicas was investigated. The successful formation of fiber-like structures was confirmed, and future experiments will provide further insights into the physicochemical properties of PNA-DNA-PNA based organosilicas.

4.4. Experimental section

4.4.1. Instruments

Fourier transform infrared (FTIR) transmittance spectra were measured with a Shimadzu IRAffinity-1 spectrometer. The spectrum of **1** was recorded in $CHCl_3$ (ca. 1 mg mL^{-1}, 0.1 mm path length NaCl window cell). The attenuated total reflectance Fourier transform infrared (ATR-FTIR) spectra of the particle samples were collected using a spectral resolution of Δ=4 cm^{-1}, accumulating 64 scans and the ATR-FTIR spectra were ATR corrected (penetration depth mode).

Mass spectrometry (MS) experiments were performed on a Bruker Daltonics microToF spectrometer (Bruker Daltonik GmgH, Bremen, Germany) with the electrospray ionization (ESI) interface operating in a positive ion (for PNA) or negative mode (for DNA).

Absorption spectra were measured on a Shimadzu UV-3600 spectrophotometer double-beam UV–VIS–NIR spectrometer and baseline corrected. Quartz cuvettes with path length of 10.0 mm were used for the recording of UV-Vis absorption spectra.

Scanning electron microscopy (SEM) and scanning transmission electron microscopy (STEM) images were recorded with a FEI Quanta FEG 250 instrument (FEI corporate, Hillsboro, S3 Oregon, USA) with an acceleration voltage of 20 kV. The SEM sample were prepared by drop-casting the dispersion of particles in EtOH onto a glass cover slip, subsequently sputter coated with Au (Emitech K575X Peltier cooled) for 60 s at 60 mA prior to fixation on an Al support.

ζ-potential measurements were conducted on a DelsaNano C Particle Analyzer (Beckman Coulter, operative wavelength 655 nm). Measurements were performed on dispersions of the particles in EtOH (ca. 0.01 mg/mL).

Small-angle X-ray scattering (SAXS) set-up comprised the SAXSess mc2 instrument from Anton Paar GmbH, containing a slit collimation system, and the PW3830 laboratory X-ray generator (40 kV, 50 mA) with a long-fine focus sealed X-ray tube (CuKα wavelength of λ = 0.1542 nm) from PANalytical. Detection was performed with the 2D imaging-plate reader Cyclone® by Perkin Elmer. The measurement was performed on a powder sample for 5 min and the data collected up to a scattering vector q value of 7 nm^{-1}, where $q=(4\pi\sin\vartheta)/\lambda$ and 2ϑ is the scattering angle. The 2D data were converted to 1D data and background-corrected by using SAXSQuant software (Anton Paar GmbH, Austria).

X-ray photoelectron spectroscopy (XPS) analysis was performed using a K-Alpha™+ X-ray Photoelectron Spectrometer System (Thermo Scientific). Monochromatic Al K alpha X-rays were used (15 keV, 72 W, 200 mm spot diameter). Spectra were measured using pass energy of 200 eV for survey spectra and 50 eV for core level spectra. The samples were analyzed as powders. The Advantage software was used for background subtraction (smart mode), and deconvolution of peaks.

4.4.2. Preparation of ssDNA oligonucleotides

The oligonucleotides were synthesized on solid support using a BioAutomation Mer Made MM6 DNA synthesizer using a standard phosphoramidite protocol. Amino functionalities were introduced using the serinol aminomodifier (Am, GlenTech) and the fluorescent marker was introduced using Cyanine-3-phosphoramidite (Cy3, GlenTech) and Cyanine-5-phosphoramidite (Cy5, GlenTech). To this purpose, the phosphor amidite monomer modifier were dissolved in anhydrous CH_3CN to achieve a final concentration of 0.1 M and the coupling occurred on the resin in a glove box with inert atmosphere upon activating the phosphonamidites with 0.25 M 5-(ethylthio)tetrazole in anhydrous CH_3CN. For the introduction of oligonucleotide modifiers an extended coupling times of 10 min was used. 3% dichloroacetic acid in dichloromethane was used to remove DMT protecting group on the DNA synthesizer. After the synthesis was completed, CPG was treated with 28% aqueous ammonium hydroxide solution for 16–18 hours at 60°C. The crude mixture then was concentrated under reduced pressure at 60°C, dispersed in MilliQ water and subsequently filtered by 0.22µm centrifugal filter before purifying by RP-HPLC using CH_3CN/TEAA-buffer (3–50 % CH_3CN, pH = 8) as eluent mixture and freeze dried. Pure compound **1** was obtained as a pink solid (0.2 µmol, yield 20% compared to the initial CPG loading). The shorter 4-mer oligonucleotide was analogously prepared as the procedure described above, but not labeled with any fluorescent dye.

1: Am-CAATGTAGCT-Cy3-Am

MS (ESI-TOF negative mode): m/z $[M-3H]^{3-}$ calcd for $C_{139}H_{183}N_{43}O_{72}P_{12}$, 1326.00; found, 1326.06

Complementary strand to 1 = Cy5-Strand = Cy5-AGCTACATTG

MS (ESI-TOF negative mode): m/z $[M\text{-}3H]^{3-}$ calcd for $C_{141}H_{185}N_{43}O_{72}P_{12}$, 1332.63; found, 1332.65

Short 4mer diamino oligonucleotide: Am-GCGC-Am

MS (ESI-TOF negative mode): m/z $[M-2H]^{2-}$ calcd for $C_{50}H_{73}N_{20}O_{32}P_5$, 810.1694; found, 810.19

4.4.3. Preparation of ssDNA and ssPNA alkoxysilanes

General information. All solvents were purchased from Merck and used as received. DMSO (analytical reagent grade) was purchased from Fisher Chemical and dried over Na_2SO_4 prior to use. 3-(triethoxysilyl)propyl isocyanate (ICPTES, 95%), triethylamine (TEA, >99%), were purchased from Merck.

Preparation of 2. To a dispersion of **1** (2 mg, 0.5 µmol) in dry DMSO (50 µL), ICPTES (0.27 µL of a 4.04 M ICPTES solution in DMOS, 1.1 µmol ,2.2 eq) and TEA (0.5 µL) was added. The reaction mixture was stirred for 1 h at room temperature. The resulting reaction crude was used for the preparation of organosilica particles without further purification. MS (ESI-TOF negative mode): m/z $[M-7H]^{7-}$ calcd for C147H203N45O80P12Si2, 614.7321 found, 614.28.

Preparation of 5. The single stranded di-amino modified PNA strand **4** was prepared and provided by the group of Prof. Roberto Corradini (University of Parma). To a solution of **4** (0.5 mg, 0.15 µmol) in DMSO (30 µL), ICPTES (1.54 µL of a 0.2 M solution in DMSO; 0.315 µmol, 2.1 eq.) and TEA (0.2 µL) was added and the reaction mixture was stirred for 1 h at room temperature. The resulting reaction mixture was used for the preparation of organosilica particles without further purification. MS (ESI-TOF positive mode): m/z $[M+3H]^{3+}$ calcd for C153H203N66O44Si2, 1241.5071 found, 1241.18.

Preparation of F-PNA-Si and T-PNA-Si. To a solution of T- or F-PNA (0.1 µmol) in DMSO (50 µL), ICPTES (0.16 µmol; 0.4 µL of a 0.2 M ICPTES stock solution in DMSO, 1.2 eq.) and TEA (0.5 µL) was added and the reaction mixture was stirred 1 h at room temperature. The resulting reaction mixture was used for the preparation of organosilica particles without further purification. MS (ESI-TOF positive mode) for F-PNA-Si: m/z $[M\text{-Guanine-}CO_2\text{-}3xNH_3\text{+}4H]^{4+}$ calcd for C149H186N56O41Si, 860.8490 found, 860.85.

Preparation of PNA-S 1 and PNA-S 2. Two starting PNA strands were used: F-PNA, here referred as PNA-1, and a new PNA strand prepared by Dr. Marianna Rossetti from the research group of Prof. Francesco Ricci (University of Tor Vergata), named as PNA-2 and with the sequence 5'-GTGACCTT-Lys-3'. PNA-1 and PNA-2 (1.2×10^{-8} mol for each strand, taken from stock solutions of *c*(PNAs)=2.4 mM in DMSO) were placed in separate 2 mL Eppendorf tubes and to each PNA solution, ICPTES (1.32×10^{-8} mol, 2.6 µL from a 0.05 M stock solution in DMSO) and TEA (0.4 µL from a 0.07 M stock solution in DMSO) was added. The reaction mixtures were allowed to react for 1 h at room temperature. The crude reaction mixtures containing the silanized PNA-1 and PNA-2 were united and ssDNA (1.2×10^{-8} mol, 1.2 µL from a0.01 M ssDNA stock solution in MilliQ water containing 3 mM $MgCl_2$) was added and the reaction mixture was mixed and allowed to hybridize for 30 min at room temperature under static conditions, yielding **Supra-PDP-Si**.

4.4.4. Preparation of model mesoporous silica particles

General information. Hexadecyltrimethylammonium bromide (CTAB, Acros Organics, 99+%), ammonia solution (VWR, 28%), tetraethyl orthosilicate (TEOS, Sigma-Aldrich, ≥99% GC), 5-(ethylthio)tetrazole (TEOS, Sigma–Aldrich, 95%).

Preparation of MSPs. In a glass vial, CTAB (25 mg, 0.068 mmoL) was dissolved in a H_2O/EtOH mixture (0.739:0.26 *v*/*v*; 12.3 mL) at room temperature under stirring. Subsequently, NH_3 (28 wt% in H_2O, 5 µL) is added. Finally, TEOS (62.4 µL, 0.279 mmol) was added and the reaction mixture was stirred overnight at room temperature. The particles were collected by centrifugation and purified my means of re-dispersion and centrifugation in H_2O (1×) and EtOH (2×). The organic template was removed by extracting the particles in EtOH heated to reflux for 24 h, the particles were collected by centrifugation and dried under reduced pressure

4.4.5. Preparation of organosilica particles

General information. Hexadecyltrimethylammonium bromide (CTAB, Acros Organics, 99+%), ammonia solution (VWR, 28%), tetraethyl orthosilicate (TEOS, Sigma-Aldrich, ≥99% GC), 5-(ethylthio)tetrazole (TEOS, Sigma–Aldrich, 95%).

Preparation of ssDNA-OSPs. In a 2 ml Eppendorf tube equipped with a small magnetic stirrer, CTAB (6.25 mg, 17.15 µmol) was dissolved in a EtOH/H_2O mixture (0.26:0.739 *v*/*v*, 3.075 mL) and $NH_{3(aq)}$ (1.25 µL, 28 wt%) was added. Subsequently, TEOS (69.4 µmol, 15.5µL) was added to the crude reaction mixture of **2**, rapidly mixed and added to the stirring surfactant mixture and the reaction was stirred for further 12 h at room temperature. The precipitate was collected by centrifugation and wash with water (1) and EtOH (1×). The surfactant was extracted by dispersing the particles in 1 mL of fresh EtOH and refluxing the particle dispersion for 12 h. The extraction process was repeated one more time before finally collecting the particles by centrifugation. The collected precipitate was further washed with EtOH (1×) by means of dispersion and centrifugation and finally dried under reduced pressure.

Preparation of ssPNA-OSPs. In a 2 ml Eppendorf tube equipped with a small magnetic stirrer, CTAB (1.56 mg, 4.28 µmol) are dissolved in an EtOH/H_2O (0.26:0.739 *v*/*v*, 0.768 mL) mixture and aq. NH_{3aq} (0.3 µL, 28 wt%) was added. Subsequently, TEOS (17.33 µmol, 3.87 µL) was added to the crude reaction mixture of **5**, rapidly mixed and added to the stirring surfactant mixture and the reaction was stirred for further 12 h at room temperature. The precipitate was collected via centrifugation and wash with water (1×) and EtOH (1×). The surfactant was extracted by dispersing the particles in 1 mL of fresh EtOH and refluxing the particle dispersion for 12 h. The extraction process was repeated one more time before finally collecting the particles by centrifugation. The collected precipitate was further washed with EtOH (1×) by means of dispersion and centrifugation and finally dried under reduced pressure.

Preparation of Supra-OSPs. The crude mixtures of the synthesis of **F-PNA-Si** and **T-PNA-Si** were put in a single Eppendorf and allowed to self-assemble under static conditions for 30 min at room temperature. Subsequently the silane mixture was added to a stirring EtOH/H_2O (0.26:0.739 *v*/*v*, 0.615 mL) mixture containing $NH_{3(aq)}$ (0.25 µL, 28 wt%). and the reaction was stirred for further 12 h at room temperature. The precipitate was collected by centrifugation and wash with water (1×) and EtOH (1×) and dried under reduced pressure.

Preparation of Supra-OSPs with TEOS as secondary silica source. The final concentrations of alkoxysilanes used in this synthesis (F-and T-PNA as well as TEOS) were the same used for the preparation of **Supra-OSPs**. aliquots of the crude mixtures of the synthesis of **F-PNA-Si** (1.4×10^{-8} mol) and **T-PNA-Si** (1.4×10^{-8} mol) were put in a single Eppendorf and allowed to self-assemble under static conditions for 30 min at room temperature. Subsequently to the PNA-silane mixture, TEOS (2.8×10^{-8} mol, 1.25 µL from a 0.023 M TEOS stock solution in EtOH) was added and the mixture was rapidely mixed and added to a stirring EtOH/H_2O (0.26:0.739 *v*/*v*, 0.129 mL) mixture containing aq. NH_3 (0.25 µL, 28 wt% diluted 1:4 *v*/*v* in EtOH). and the reaction was stirred for further 12 h at room temperature. The precipitate was collected by centrifugation and washed with water (1×) and EtOH (1×), and finally dried under reduced pressure.

Preparation of Supra-PDP-Si based organosilicas. The ssDNA strand used for these experiments has the sequence 5’-ACCTGGGGGAGTATTGCGGAGGAAGGTCACTTTTTCAATGTAGCT-3’ and was bought from IDT Integrated DNA Technologies. The crude **Supra-PDP-Si** (preparation in section 4.4.3.) mixture was added to a stirring solution of CTAB (1.09 mmol, 0.4 mg) dissolved in EtOH/H_2O

(0.26:0.739 *v/v*, 0.187 mL)mixture, containing aq. NH_3 (0.4 µL, 28 wt% diluted 1:4 v/v in H_2O). The reaction mixture was stirred at room temperature for 12 h.

Preparation of Supra-PDP-Si based organosilicas with TEOS as secondary silica source. A **Supra-PDP-Si** (section 4.4.4. for its preparation) and TEOS ($2.4 \cdot 10^{-8}$ mol, 1.6 µL of a 0.089 M solution of TEOS in EtOH) mixture was added to a stirring solution of CTAB (1.09 mmol, 0.4 mg) dissolved in an EtOH/H_2O (0.26:0.739 *v/v*, 0.187 mL) mixture, containing $NH_{3(aq)}$ (0.4 µL, 28 wt% diluted 1/4 v/v in H_2O). The reaction mixture was stirred at room temperature for 12 h.

4.4.6. DNAse I-triggered degradation of ssDNA-OSPs

ssDNA-OSPs (0.02 mg) were dispersed in Tris-buffer (0.5 mL see below the composition of the buffer) and DNase I solution (10 µL of a solution with 9563 units/mL)was added and the mixture was stirred at room temperature.

Tris buffer composition. Prepared from distilled water. Contains: Tris(hydroxymethyl)aminomethane (10mM), Calcium chloride (0.5 mM), magnesium chloride (2.5 mM). The pH of the buffer solution was 7.6.

4.4.7. FRET experiments

FRET experiments with **ssDNA-OSPs** and **Cy5-Strand.** In three different cuvettes, three samples were prepared by dissolving both **ssDNA-OSPs** and **Cy5-Strand in PBS**; the final concentrations of the Cy5-Strand were 0 µM, 1.76 µM and 3.52 µM, respectively, whereas the final concentration of **ssDNA-OSPs** was in all three samples 0.96 $\mu g \cdot mL^{-1}$. After mixing the particle dispersion with the **Cy5-Strand** solution, the system was let to stand for 30 min under static conditions at room temperature. Subsequently, the emission spectra of the sample solution were recorded upon light excitation at λ_{ex}=520 nm.

FRET experiments with F- and T-PNA. In three different cuvettes, three samples were prepared by dissolving **F-PNA** and **T-PNA** in PBS; the final concentrations of the **T-PNA** were 1 µM, 2 µM and 4 µM, whereas the final concentration of **F-PNA** was 1.143 µM in all three samples. After mixing the PNA solutions, the system was let to stand for 30 min under static conditions at room temperature. Subsequently, the emission spectra of the sample solution was recorded upon light excitation at λ_{ex}=450 nm.

FRET experiments with Supra-OSPs. In a quartz cuvette a particle dispersion of *c*(**Supra-OSPs**)=0.008 mg·mL^{-1} in PBS (pH = 5.8) was placed and the emission spectra was recorded upon light excitation at λ_{ex}=450 nm. To evaluate the strand melting at elevated temperatures, the same quartz cuvette with the particle dispersion was placed in a water bath and kept at 60 °C for 10 min. Subsequently the emission spectra of the warm particle dispersion were measured upon light excitation at λ_{ex}=450 nm.

4.4.8. SAXS-based analysis of ssDNA-OSPs

Assuming that an ordered hexagonally arranged structure composed of small silica particles exists within **ssDNA-OSPs** and that the observed SAXS pattern centered at q=1.3 nm^{-1} corresponds the (100) diffraction plane of a hexagonally arranged phase, then the mean size of the scatterers can be calculated as:

$$d = \frac{2\pi}{q} = 4.8\, nm$$

4.5. References

(1) Yu, L.; Pan, P.; Zhang, Y.; Zhang, Y.; Wan, L.; Cheng, X.; Deng, Y. Nonsacrificial Self-Template Synthesis of Colloidal Magnetic Yolk–Shell Mesoporous Organosilicas for Efficient Oil/Water Interface Catalysis. *Small* **2019**, *15* (14), 1–9. DOI: 10.1002/smll.201805465.

(2) Himiyama, T.; Waki, M.; Maegawa, Y.; Inagaki, S. Cooperative Catalysis of an Alcohol Dehydrogenase and Rhodium-Modified Periodic Mesoporous Organosilica. *Angew. Chemie - Int. Ed.* **2019**, *58* (27), 9150–9154. DOI: 10.1002/anie.201904116.

(3) Shi, J. Y.; Wang, C. A.; Li, Z. J.; Wang, Q.; Zhang, Y.; Wang, W. Heterogeneous Organocatalysis at Work: Functionalization of Hollow Periodic Mesoporous Organosilica Spheres with MacMillan Catalyst. *Chem. - A Eur. J.* **2011**, *17* (22), 6206–6213. DOI: 10.1002/chem.201100072.

(4) Li, Y.; Auras, F.; Löbermann, F.; Döblinger, M.; Schuster, J.; Peter, L.; Trauner, D.; Bein, T. A Photoactive Porphyrin-Based Periodic Mesoporous Organosilica Thin Film. *J. Am. Chem. Soc.* **2013**, *135* (49), 18513–18519. DOI: 10.1021/ja4082028.

(5) Auras, F.; Li, Y.; Löbermann, F.; Döblinger, M.; Schuster, J.; Peter, L. M.; Trauner, D.; Bein, T. A Zinc Phthalocyanine Based Periodic Mesoporous Organosilica Exhibiting Charge Transfer to Fullerenes. *Chem. - A Eur. J.* **2014**, *20* (46), 14971–14975. DOI: 10.1002/chem.201404169.

(6) Bilo, M.; Lee, Y. J.; Fröba, M. Millimeter-Sized Micellar-Templated Silica Beads and Phenylene-Bridged Mesoporous Organosilica Beads. *Microporous Mesoporous Mater.* **2019**, *284* (March), 327–335. DOI: 10.1016/j.micromeso.2019.04.028.

(7) Rebbin, V.; Schmidt, R.; Fröba, M. Spherical Particles of Phenylene-Bridged Periodic Mesoporous Organosilica for High-Performance Liquid Chromatography. *Angew. Chemie - Int. Ed.* **2006**, *45* (31), 5210–5214. DOI: 10.1002/anie.200504568.

(8) Jayasundera, S.; Burleigh, M. C.; Zeinali, M.; Spector, M. S.; Miller, J. B.; Yan, W.; Dai, S.; Markowitz, M. A. Organosilica Copolymers for the Adsorption and Separation of Multiple Pollutants. *J. Phys. Chem. B* **2005**, *109* (19), 9198–9201. DOI: 10.1021/jp051435h.

(9) Ganiyu, S. O.; Bispo, C.; Bion, N.; Ferreira, P.; Batonneau-Gener, I. Periodic Mesoporous Organosilicas as Adsorbents for the Organic Pollutants Removal in Aqueous Phase. *Microporous Mesoporous Mater.* **2014**, *200*, 117–123. DOI: 10.1016/j.micromeso.2014.07.047.

(10) Dai, J.; Zou, H.; Wang, R.; Wang, Y.; Shi, Z.; Qiu, S. Yolk-Shell Fe3O4@SiO2@PMO: Amphiphilic Magnetic Nanocomposites as an Adsorbent and a Catalyst with High Efficiency and Recyclability. *Green Chem.* **2017**, *19* (5), 1336–1344. DOI: 10.1039/c6gc02926d.

(11) Croissant, J. G.; Fatieiev, Y.; Almalik, A.; Khashab, N. M. Mesoporous Silica and

Organosilica Nanoparticles: Physical Chemistry, Biosafety, Delivery Strategies, and Biomedical Applications. *Adv. Healthc. Mater.* **2018**, *7* (4), 1–75. DOI: 10.1002/adhm.201700831.

(12) Keefe, A. D.; Pai, S.; Ellington, A. Aptamers as Therapeutics. *Nat. Rev. Drug Discov.* **2010**, *9* (7), 537–550. DOI: 10.1038/nrd3141.

(13) Del Grosso, E.; Ragazzon, G.; Prins, L. J.; Ricci, F. Fuel-Responsive Allosteric DNA-Based Aptamers for the Transient Release of ATP and Cocaine. *Angew. Chemie - Int. Ed.* **2019**, *58* (17), 5582–5586. DOI: 10.1002/anie.201812885.

(14) Jin, J. O.; Kim, H.; Huh, Y. H.; Herrmann, A.; Kwak, M. Soft Matter DNA Nanoparticles Hybridized with CpG Motifs and Peptide Nucleic Acids Enable Immunological Treatment of Cancer. *J. Control. Release* **2019**, *315* (October), 76–84. DOI: 10.1016/j.jconrel.2019.09.013.

(15) Berger, O.; Adler-Abramovich, L.; Levy-Sakin, M.; Grunwald, A.; Liebes-Peer, Y.; Bachar, M.; Buzhansky, L.; Mossou, E.; Forsyth, V. T.; Schwartz, T.; Ebenstein, Y.; Frolow, F.; Shimon, L. J. W.; Patolsky, F.; Gazit, E. Light-Emitting Self-Assembled Peptide Nucleic Acids Exhibit Both Stacking Interactions and Watson-Crick Base Pairing. *Nat. Nanotechnol.* **2015**, *10* (4), 353–360. DOI: 10.1038/nnano.2015.27.

(16) Fakih, H. H.; Fakhoury, J. J.; Bousmail, D.; Sleiman, H. F. Minimalist Design of a Stimuli-Responsive Spherical Nucleic Acid for Conditional Delivery of Oligonucleotide Therapeutics. *ACS Appl. Mater. Interfaces* **2019**, *11* (15), 13912–13920. DOI: 10.1021/acsami.8b18790.

(17) Bujold, K. E.; Hsu, J. C. C.; Sleiman, H. F. Optimized DNA “Nanosuitcases” for Encapsulation and Conditional Release of SiRNA. *J. Am. Chem. Soc.* **2016**, *138* (42), 14030–14038. DOI: 10.1021/jacs.6b08369.

(18) Berger, O.; Gazit, E. Molecular Self-Assembly Using Peptide Nucleic Acids. *Biopolymers* **2017**, *108* (1), 1–6. DOI: 10.1002/bip.22930.

(19) Jones, M. R.; Seeman, N. C.; Mirkin, C. A. Programmable Materials and the Nature of the DNA Bond. *Science (80-.).* **2015**, *347* (6224). DOI: 10.1126/science.1260901.

(20) Pavlov, V.; Xiao, Y.; Shlyahovsky, B.; Willner, I. Aptamer-Functionalized Au Nanoparticles for the Amplified Optical Detection of Thrombin. *J. Am. Chem. Soc.* **2004**, *126* (38), 11768–11769. DOI: 10.1021/ja046970u.

(21) Dou, B.; Xu, L.; Jiang, B.; Yuan, R.; Xiang, Y. Aptamer-Functionalized and Gold Nanoparticle Array-Decorated Magnetic Graphene Nanosheets Enable Multiplexed and Sensitive Electrochemical Detection of Rare Circulating Tumor Cells in Whole Blood. *Anal. Chem.* **2019**, *91* (16), 10792–10799. DOI: 10.1021/acs.analchem.9b02403.

(22) Song, Y.; Shi, Y.; Huang, M.; Wang, W.; Wang, Y.; Cheng, J.; Lei, Z.; Zhu, Z.; Yang, C. Bioinspired Engineering of a Multivalent Aptamer-Functionalized Nanointerface to Enhance the Capture and Release of Circulating Tumor Cells. *Angew. Chemie - Int. Ed.*

2019, *58* (8), 2236–2240. DOI: 10.1002/anie.201809337.

(23) Chen, Y.; Tyagi, D.; Lyu, M.; Carrier, A. J.; Nganou, C.; Youden, B.; Wang, W.; Cui, S.; Servos, M.; Oakes, K.; He, S.; Zhang, X. Regenerative Nanooctopus Based on Multivalent-Aptamer-Functionalized Magnetic Microparticles for Effective Cell Capture in Whole Blood. *Anal. Chem.* **2019**, *91* (6), 4017–4022. DOI: 10.1021/acs.analchem.8b05432.

(24) Dhar, S.; Gu, F. X.; Langer, R.; Farokhza, O. C.; Lippard, S. J. Targeted Delivery of Cisplatin to Prostate Cancer Cells by Aptamer Functionalized Pt(IV) Prodrug-PLGA - PEG Nanoparticles. *Proc. Natl. Acad. Sci. U. S. A.* **2008**, *105* (45), 17356–17361. DOI: 10.1073/pnas.0809154105.

(25) Xu, L.; He, X. Y.; Liu, B. Y.; Xu, C.; Ai, S. L.; Zhuo, R. X.; Cheng, S. X. Aptamer-Functionalized Albumin-Based Nanoparticles for Targeted Drug Delivery. *Colloids Surfaces B Biointerfaces* **2018**, *171* (April), 24–30. DOI: 10.1016/j.colsurfb.2018.07.008.

(26) Roy, I.; Ohulchanskyy, T. Y.; Bharali, D. J.; Pudavar, H. E.; Mistretta, R. A.; Kaur, N.; Prasad, P. N. Optical Tracking of Organically Modified Silica Nanoparticles as DNA Carriers: A Nonviral, Nanomedicine Approach for Gene Delivery. *Proc. Natl. Acad. Sci. U. S. A.* **2005**, *102* (2), 279–284. DOI: 10.1073/pnas.0408039101.

(27) Xia, T.; Kovochich, M.; Liong, M.; Meng, H.; Kabehie, S.; George, S.; Zink, J. I.; Nel, A. E. Polyethyleneimine Coating Enhances the Cellular Uptake of Mesoporous Silica Nanoparticles and Allows Safe Delivery of SiRNA and DNA Constructs. *ACS Nano* **2009**, *3* (10), 3273–3286. DOI: 10.1021/nn900918w.

(28) Dengler, E. C.; Liu, J.; Kerwin, A.; Torres, S.; Olcott, C. M.; Bowman, B. N.; Armijo, L.; Gentry, K.; Wilkerson, J.; Wallace, J.; Jiang, X.; Carnes, E. C.; Brinker, C. J.; Milligan, E. D. Mesoporous Silica-Supported Lipid Bilayers (Protocells) for DNA Cargo Delivery to the Spinal Cord. *J. Control. Release* **2013**, *168* (2), 209–224. DOI: 10.1016/j.jconrel.2013.03.009.

(29) Möller, K.; Müller, K.; Engelke, H.; Bräuchle, C.; Wagner, E.; Bein, T. Highly Efficient SiRNA Delivery from Core-Shell Mesoporous Silica Nanoparticles with Multifunctional Polymer Caps. *Nanoscale* **2016**, *8* (7), 4007–4019. DOI: 10.1039/c5nr06246b.

(30) Ngamcherdtrakul, W.; Morry, J.; Gu, S.; Castro, D. J.; Goodyear, S. M.; Sangvanich, T.; Reda, M. M.; Lee, R.; Mihelic, S. A.; Beckman, B. L.; Hu, Z.; Gray, J. W.; Yantasee, W. Cationic Polymer Modified Mesoporous Silica Nanoparticles for Targeted SiRNA Delivery to HER2+ Breast Cancer. *Adv. Funct. Mater.* **2015**, *25* (18), 2646–2659. DOI: 10.1002/adfm.201404629.

(31) Choi, E.; Lee, J.; Kwon, I. C.; Lim, D. K.; Kim, S. Cumulative Directional Calcium Gluing between Phosphate and Silicate: A Facile, Robust and Biocompatible Strategy for SiRNA Delivery by Amine-Free Non-Positive Vector. *Biomaterials* **2019**, *209* (January), 126–137. DOI: 10.1016/j.biomaterials.2019.04.006.

(32) Bertucci, A.; Prasetyanto, E. A.; Septiadi, D.; Manicardi, A.; Brognara, E.; Gambari, R.;

Corradini, R.; De Cola, L. Combined Delivery of Temozolomide and Anti-MiR221 PNA Using Mesoporous Silica Nanoparticles Induces Apoptosis in Resistant Glioma Cells. *Small* **2015**, *11* (42), 5687–5695. DOI: 10.1002/smll.201500540.

(33) Schlossbauer, A.; Warncke, S.; Gramlich, P. M. E.; Kecht, J.; Manetto, A.; Carell, T.; Bein, T. A Programmable DNA-Based Molecular Valve for Colloidal Mesoporous Silica. *Angew. Chemie - Int. Ed.* **2010**, *49* (28), 4734–4737. DOI: 10.1002/anie.201000827.

(34) Zhang, P.; Cheng, F.; Zhou, R.; Cao, J.; Li, J.; Burda, C.; Min, Q.; Zhu, J. J. DNA-Hybrid-Gated Multifunctional Mesoporous Silica Nanocarriers for Dual-Targeted and MicroRNA-Responsive Controlled Drug Delivery. *Angew. Chemie - Int. Ed.* **2014**, *53* (9), 2371–2375. DOI: 10.1002/anie.201308920.

(35) Pavlovic, M.; Kats, A.; Cavallo, M.; Chen, R.; Hartmann, J. X.; Shoenfeld, Y. Pathogenic and Epiphenomenal Anti-DNA Antibodies in SLE. *Autoimmune Dis.* **2010**, *1* (1). DOI: 10.4061/2010/462841.

(36) Yu, Q.; Liu, M.; Wei, S.; Wu, S.; Xiao, H.; Qin, X.; Su, H.; Li, P. Characterization of SsDNA Aptamers Specifically Directed against Trachinotus Ovatus NNV (GTONNV)-Infected Cells with Antiviral Activities. *J. Gen. Virol.* **2019**, *100* (3), 380–391. DOI: 10.1099/jgv.0.001226.

(37) Vilaivan, T. Fluorogenic PNA Probes. *Beilstein J. Org. Chem.* **2018**, *14*, 253–281. DOI: 10.3762/bjoc.14.17.

(38) Stupp, S. I.; Clemons, T. D.; Carrow, J. K.; Sai, H.; Palmer, L. C. Supramolecular and Hybrid Bonding Polymers. *Isr. J. Chem.* **2020**, *60* (1–2), 124–131. DOI: 10.1002/ijch.202000005.

(39) Shimizu, I.; Okabayashi, H.; Hattori, N.; Taga, K.; Yoshino, A.; O'Connor, C. J. 13C- And 1H-NMR and FTIR Spectroscopic Evidence for Aggregate Formation of Organosilanes in Toluene. *Colloid Polym. Sci.* **1997**, *275* (3), 293–297. DOI: 10.1007/s003960050084.

(40) Parikh, A. N.; Schivley, M. A.; Koo, E.; Seshadri, K.; Aurentz, D.; Mueller, K.; Allara, D. L. N-Alkylsiloxanes: From Single Monolayers to Layered Crystals. The Formation of Crystalline Polymers from the Hydrolysis of n-Octadecyltrichlorosilane. *J. Am. Chem. Soc.* **1997**, *119* (13), 3135–3143. DOI: 10.1021/ja963284p.

(41) Ni, L.; Chemtob, A.; Croutxé-Barghorn, C.; Brendlé, J.; Vidal, L.; Rigolet, S. Kinetics, Thermodynamics, and Dynamics in Organosilane Self-Assembly. *J. Phys. Chem. C* **2012**, *116* (45), 24320–24330. DOI: 10.1021/jp307274d.

(42) Dieudonné, P.; Man, M. W. C.; Pichón, B. P.; Vellutini, L.; Bantignies, J. L.; Blanc, C.; Creff, G.; Finet, S.; Sauvajol, J. L.; Bied, C.; Moreau, J. J. E. In Situ X-Ray Measurements to Probe a New Solid-State Polycondensation Mechanism for the Design of Supramolecular Organo-Bridged Silsesquioxanes. *Small* **2009**, *5* (4), 503–510. DOI: 10.1002/smll.200800254.

(43) Han, J. T.; Lee, D. H.; Ryu, C. Y.; Cho, K. Fabrication of Superhydrophobic Surface from a Supramolecular Organosilane with Quadruple Hydrogen Bonding. *J. Am. Chem. Soc.* **2004**, *126* (15), 4796–4797. DOI: 10.1021/ja0499400.

(44) Fan, H.; Chen, Z.; Blinker, C. J.; Clawson, J.; Alam, T. Synthesis of Organo-Silane Functionalized Nanocrystal Micelles and Their Self-Assembly. *J. Am. Chem. Soc.* **2005**, *127* (40), 13746–13747. DOI: 10.1021/ja053795o.

(45) Hashizume, M.; Kawanami, S. I.; Iwamoto, S.; Isomoto, T.; Kikuchi, J. I. Stable Vesicular Nanoparticle "Cerasome" as an Organic-Inorganic Hybrid Formed with Organoalkoxysilane Lipids Having a Hydrogen-Bonding Unit. *Thin Solid Films* **2003**, *438–439* (03), 20–26. DOI: 10.1016/S0040-6090(03)00745-4.

(46) Yu, Z.; Tantakitti, F.; Yu, T.; Palmer, L. C.; Schatz, G. C.; Stupp, S. I. Simultaneous Covalent and Noncovalent Hybrid Polymerizations. *Science (80-.).* **2016**, *351* (6272), 497–502. DOI: 10.1126/science.aad4091.

(47) Brinker, C. J. Hydrolysis and Condensation of Silicates: Effects on Structure. *J. Non. Cryst. Solids* **1988**, *100*, 31–50.

(48) Burleigh, M. C.; Markowitz, M. A.; Spector, M. S.; Gaber, B. P. Direct Synthesis of Periodic Mesoporous Organosilicas: Functional Incorporation by Co-Condensation with Organosilanes. *J. Phys. Chem. B* **2001**, *105* (41), 9935–9942. DOI: 10.1021/jp011814k.

(49) Travaglini, L.; Picchetti, P.; Totovao, R.; Prasetyanto, E. A.; De Cola, L. Highly Degradable Imine-Doped Mesoporous Silica Particles. *Mater. Chem. Front.* **2019**, *3* (1), 111–119. DOI: 10.1039/c8qm00438b.

(50) Chemtob, A.; Ni, L.; Croutxé-Barghorn, C.; Boury, B. Ordered Hybrids from Template-Free Organosilane Self-Assembly. *Chem. - A Eur. J.* **2014**, *20* (7), 1790–1806. DOI: 10.1002/chem.201303070.

(51) Mello, M. L. S.; Vidal, B. C. Changes in the Infrared Microspectroscopic Characteristics of DNA Caused by Cationic Elements, Different Base Richness and Single-Stranded Form. *PLoS One* **2012**, *7* (8), 1–12. DOI: 10.1371/journal.pone.0043169.

(52) Volkov, I. L.; Smirnova, A.; Makarova, A. A.; Reveguk, Z. V.; Ramazanov, R. R.; Usachov, D. Y.; Adamchuk, V. K.; Kononov, A. I. DNA with Ionic, Atomic, and Clustered Silver: An XPS Study. *J. Phys. Chem. B* **2017**, *121* (11), 2400–2406. DOI: 10.1021/acs.jpcb.6b11218.

(53) Hubert, F.; Testard, F.; Spalla, O. Cetyltrimethylammonium Bromide Silver Bromide Complex as the Capping Agent of Gold Nanorods. *Langmuir* **2008**, *24* (17), 9219–9222. DOI: 10.1021/la801711q.

(54) Wlttung, P.; Nlelsenh, P. E.; Buchardtt, O.; Egholm, M.; Norden, B. DNA-like Double Helix Formed by Peptide Nucleic Acid. **1994**, *368* (April), 561–563.

(55) Albert, S. K.; Thelu, H. V. P.; Golla, M.; Krishnan, N.; Chaudhary, S.; Varghese, R. Self-Assembly of DNA-Oligo(p-Phenylene-Ethynylene) Hybrid Amphiphiles into Surface-Engineered Vesicles with Enhanced Emission. *Angew. Chemie - Int. Ed.* **2014**, *53* (32), 8352–8357. DOI: 10.1002/anie.201403455.

(56) Roh, Y. H.; Lee, J. B.; Kiatwuthinon, P.; Hartman, M. R.; Cha, J. J.; Um, S. H.; Muller, D. A.;

Luo, D. DNAsomes: Multifunctional DNA-Based Nanocarriers. *Small* **2011**, *7* (1), 74–78. DOI: 10.1002/smll.201000752.

(57) Tan, B.; Rankin, S. E. Study of the Effects of Progressive Changes in Alkoxysilane Structure on Sol-Gel Reactivity. *J. Phys. Chem. B* **2006**, *110* (45), 22353–22364. DOI: 10.1021/jp060376k.

(58) Fang, X.; Chen, C.; Liu, Z.; Liu, P.; Zheng, N. A Cationic Surfactant Assisted Selective Etching Strategy to Hollow Mesoporous Silica Spheres. *Nanoscale* **2011**, *3* (4), 1632–1639. DOI: 10.1039/c0nr00893a.

Acknowledgements

First of all, I would like to thank Prof. Luisa De Cola for having given me the possibility to conduct research in her working group. During this time, I was able learn and grow as a chemist in many aspects. I am especially grateful for the possibility to have worked independently on research problems and never experiencing any financial or instrumental related shortcomings – essentially to thrive in research labs and enjoying experimentation. I will remember the vivid and inspiring scientific discussions we had in the lab.

I would like to thank Leana Travaglini and Brian DiMarco for their adamant support and helpful discussions, contributing to the successful conclusions of the work presented in chapter 2. Thanks also to Etienne Piantanida and Simone Silvestrini for their support regarding XPS analysis and Yang Zhang for in-vitro experimentation presented in chapter 2.

I would like to thank collaborators of the Mario Negri Institute, especially Dr. Laura Talamini, Prof. Paolo Bigini and Dr. Giovanni Sitia, which helped with in vitro and in vivo experiments presented in chapter 3. I would like to thank Adrien Mourgout, which as part of his Master's internship, worked excellently under my supervision on the functionalization of cage-like silica particles. I thank Alexander Frechat, Corinne Crucifix and Prof. Patrick Schultz for their help during the 3D structure reconstruction of cage-like particles using Relion® and assistance during long TEM sessions at the IGBMC.

I would like to thank also Prof. Hanadi Sleiman for her enthusiastic support and motivating discussions we had during my placement at the McGill University. Big thanks to Michael Dore, Tuan Trinh, Aurélie Lacroix, Donatien de Rochambeau and Nicole Avakyan for the time we spend together in Montréal and for fantastic assistance to any research-related problem/discussion. Further members of the Sleiman lab and faculty members that I want to thank are: Dr. Johans Fakhoury, Xin Luo, Christophe Lachance-Brais, Daniel Saliba, Dr. Alexander Whaba and Dr. Violetta Toader. Many thanks also to Dr. Alessandro Porchetta, Dr. Marianna Rossetti, Prof Roberto Corradini and Dr. Stefano Volpi for their helpful discussions regarding the work presented in chapter 4 and for the preparation of the PNA strands.

Thanks also to Prof Marta Cerruti and Prof. Fiorenzo Vetrone for their participation and support of scientific project which originated in discussion with Vivienne Tam, during my stay at the McGill University. I would like to thank Vivienne for her enthusiastic and hard work related to this collaboration.

Guillermo Moreno Alcantar, Simone Silvestrini and Alessandro Aliprandi are thanked for their precious scientific advice, support and readiness for occasional experiments – True to the motto: *let us try out what happens if… .* Further, I would like to thank also Atena, Fred, Aline and Adrien for their kind support.

I want to thank past academic supervisors for their training and teaching, particularly Prof. Harry Martin, Prof. Luca Gentilucci, Dr. Enrico Rampazzo and Dr. Rossella De Marco.

I would also like to thank Fabrizio Ballerini and Daniela Eisendle, which whom I lived and worked with during my teenage years in the most beautiful (to me at least) place I know of on this earth. Much I have learned from you, from which I very thankful of.

I would like to thank further Peter Wurzer, Martin Oberparleiter, Carmen Gatterer, Bernhard Kronbichler, Luca Ciscato and Erica Rossetti for their kind visits to Strasbourg.

Und zin Schluss nou, gonz nochn Motto: “Die Letschtn san die Beschtn“- -I thank my family for the unimaginable support I receive from you. There are no words which can describe my profound gratitude and joy I experience because of you. Thank you very much.

Axa Research Found, L’Òreal and Biologia et Naturalia association are thanked for financial support. Furthermore, I thank the European Union for financial support, which financed the project presented in Chapter 4 through the European Union’s Horizon 2020 research and innovation programme under the Marie Skłodowska-Curie grant agreement No 778133.

Financial support was obtained from:

Fonds AXA pour la Recherche
Chercher pour protéger

European Commission

MARIE CURIE ACTIONS

NEB
Association
NATURALIA & BIOLOGIA
Au service de la recherche scientifique et médicale

Pierre PICCHETTI

Design and Preparation of Degradable Organosilica Particles for Biomedical Applications

Résumé

Les travaux présentés dans cette thèse se sont concentrés sur la préparation et la caractérisation de nouvelles particules d'organosilice sensibles aux stimuli. À cet égard, une série d'organoalkoxysilanes ont été synthétisés et utilisés pour préparer des organosilices possédant des groupes fonctionnels organiques liés de manière covalente ou supramoléculaire dans leur structure de silice. Il a été démontré qu'il est possible de préparer des organosilices poreuses et photodégradables qui sont capables, sous irradiation lumineuse, de libérer quantitativement des molécules hydrophobes. De plus, certains oligonucléotides, tels que l'ADN et l'ANP, peuvent être intégrés dans la structure des particules afin de préparer des matériaux pouvant interagir avec des molécules biologiques telles que des enzymes ou des ADN complémentaires. Enfin, la possibilité de préparer des particules d'organosilice sous forme de cage et sensibles à l'oxydoréduction a été mis en évidence et leur utilisation potentielle pour le développement de nouvelles techniques de nanomédecine a été évaluée et discutée.

Résumé en anglais

The work presented in this thesis focused on the preparation and characterization of novel stimuli-responsive organosilica particles. In this respect, a series of organoalkoxysilanes have been synthesized and used to prepare organosilicas, which possess either covalently or supramolecularly linked organic bridging-groups within their silica framework. It has been shown that porous and light-degradable and organosilicas can be prepared which are able to quantitatively release hydrophobic molecules upon light-irradiation and that oligonucleotides, such as DNA and PNA can be integrated into the particles framework in order to prepare materials, which can interact with biological molecules such as enzyme or complementary DNAs. Finally, the possibility to prepare redox-responsive cage-like organosilica particles, a novel type of morphology for organosilicas, was shown and their potential use for the development of novel nanomedicines was evaluated and discussed.